THESE

Pour l'obtention du grade de
DOCTEUR DE L'UNIVERSITÉ DE POITIERS
UFR des sciences fondamentales et appliquées
Pôle poitevin de recherche pour l'ingénieur en mécanique, matériaux et énergétique - PPRIMME
(Diplôme National - Arrêté du 7 août 2006)

École doctorale : Sciences et ingénierie en matériaux, mécanique,
énergétique et aéronautique - SIMMEA
Secteur de recherche : Mécanique des milieux fluides

Présentée par :
Jian Wu

Contribution to numerical simulation of electrohydrodynamics flows: application to electro-convection and electro-thermo-convection between two parallel plates

Directeur(s) de Thèse :
Hubert Romat, Philippe Traoré

Soutenue le 17 septembre 2012 devant le jury

Jury :

Président	**Michel Visonneau**	Directeur de recherche - CNRS, École centrale de Nantes
Rapporteur	**Michel Visonneau**	Directeur de recherche - CNRS, École centrale de Nantes
Rapporteur	**Alberto Perez**	Profesor - Universidad de Sevilla
Membre	**Hubert Romat**	Professeur - École nationale supérieure d'ingénieurs de Poitiers, Université de Poitiers
Membre	**Philippe Traoré**	Maître de conférences - Université de Poitiers
Membre	**Christophe Louste**	Maître de conférences - Université de Poitiers
Membre	**Dantchi Koulova**	Associate Professor - Bulgarian Academy of Sciences
Membre	**Fengquan Li**	Professor - Dalian University of Technology, China
Membre	**Pédro Vazquez**	Profesor asociado - Universidad de Sevilla

Pour citer cette thèse :
Jian Wu. *Contribution to numerical simulation of electrohydrodynamics flows: application to electro-convection and electro-thermo-convection between two parallel plates* [En ligne]. Thèse Mécanique des milieux fluides. Poitiers : Université de Poitiers, 2012. Disponible sur Internet <http://theses.univ-poitiers.fr>

THESE

POUR L'OBTENTION DU GRADE DE

DOCTEUR DE L'UNIVERSITE DE POITIERS

(Faculté des Sciences Fondamentales et Appliquées)
(Diplôme National – Arrêté du 7 août 2006)
Ecole Doctorale Sciences et Ingénierie en Matériaux, Mécanique, Energétique et Aéronautique

Secteur de Recherche : Génie électrique / Mécanique des milieux fluides

Présentée par :

Wu Jian

CONTRIBUTION TO NUMERICAL SIMULATION OF ELECTROHYDRODYNAMICS FLOWS: APPLICATION TO ELECTRO-CONVECTION AND ELECTRO-THERMO-CONVECTION BETWEEN TWO PARALLEL PLATES

(EXEMPLAIRE PROVISOIRE)

Directeur de Thèse : ***Romat Hubert***
Co-Directeur : ***Traoré Philippe***

Soutenue le 17 Septembre 2012 devant la Commission d'Examen

Jury

Perez Alberto	Professor, University of Seville, Spain	Reporter
Visonneau Michel	Dr., Ecole Centrale de Nantes, France	Reporter
Vasquez Pédro	Associate Professor, University of Seville, Spain	Examiner
Koulova Dantchi	Associate Professor, Bulgarian Academy of Sciences, Bulgarian	Examiner
Li Fengquan	Professor, Dalian University of Technology, China	Examiner
Louste Christophe	Associate Professor, University of Poitiers, France	Examiner
Traoré Philippe	Associate Professor, University of Poitiers, France	Examiner
Romat Hubert	Professor, University of Poitiers, France	Examiner
Atten Pierre	Dr., G2Elab, Joseph Fourier University, France	Invited

THESE

POUR L′OBTENTION DU GRADE DE

DOCTEUR DE L′UNIVERSITE DE POITIERS

(Faculté des Sciences Fondamentales et Appliquées)
(Diplôme National – Arrêté du 7 août 2006)
Ecole Doctorale Sciences et Ingénierie en Matériaux, Mécanique, Energétique et Aéronautique

Secteur de Recherche : Génie électrique / Mécanique des milieux fluides

Présentée par :

Wu Jian

CONTRIBUTION TO NUMERICAL SIMULATION OF ELECTROHYDRODYNAMICS FLOWS: APPLICATION TO ELECTRO-CONVECTION AND ELECTRO-THERMO-CONVECTION BETWEEN TWO PARALLEL PLATES

(EXEMPLAIRE PROVISOIRE)

Directeur de Thèse : ***Romat Hubert***
Co-Directeur : ***Traoré Philippe***

Soutenue le 17 Septembre 2012 devant la Commission d′Examen

Jury

Perez Alberto	Professor, University of Seville, Spain	Reporter
Visonneau Michel	Dr., Ecole Centrale de Nantes, France	Reporter
Vasquez Pédro	Associate Professor, University of Seville, Spain	Examiner
Koulova Dantchi	Associate Professor, Bulgarian Academy of Sciences, Bulgarian	Examiner
Li Fengquan	Professor, Dalian University of Technology, China	Examiner
Louste Christophe	Associate Professor, University of Poitiers, France	Examiner
Traoré Philippe	Associate Professor, University of Poitiers, France	Examiner
Romat Hubert	Professor, University of Poitiers, France	Examiner
Atten Pierre	Dr., G2Elab, Joseph Fourier University, France	Invited

ACKNOWLEDGEMENTS

I would like to express my sincere gratitude to my supervisors, Prof. Hubert Romat and Associate Prof. Philippe Traoré for their continuous interest, support and guidance during this study.

I am also indebted to my friends and colleagues in the Groupe Electrofluidodynamique, particularly to Jean Charles Laurentie who helps me a lot in programming. I wish to thank Dr. Mohamed EL-Adawy (my officemate), Associate Prof. Christophe Louste, Associate Prof. Thierry Paillat, Professor Li Fengquan and Dr. Yang Le for some interesting discussions.

I would like to thank Prof. K. Adamiak and Associate Prof. Li Xiangyu. Prof. K. Adamiak is the first world-class scientist I worked with. I learned a lot from his attitude to work and wide range of knowledge in EHD field. Associate Prof. Li Xiangyu is only several years older than me but he is a rising research star in the field of solid mechanics. I always enjoy the cooperation with him. Both of them are my valuable examples in my scientific research career.

I would also like to thank Associate Professor Yi Hongliang and Mr. Lu Sicong who are my guarantee for my studying abroad. Thank them for their trust.

Some friends I made in Poitiers: Wang Chenan, Zeng Tengfei, Wang Dingyong, Luo Qiong, Zhang Wansheng, Cong Weiming Liu Fei, Wang Jia, Lao Yu and his wife and their daughter Shanshan, Zhang Qinghua and his wife Xiu Juan and their daughter Xinxin, Tran Thanh Tung, Xiang Guojin, Fan Yu and Qiu Sha, Xu Yan, Xie Tao, Yan Zelu …. Thank them so much as my life abroad is great because of you.

My sincere thanks to Miss Li Huijie (JOJO) and Miss Hou Liwei who has always been interested and concerned with my everyday life.

Thank all jury members for their interest in this study and attendance at my thesis defense.

The financial support provided by the China Scholarship Council is gratefully acknowledged.

Dedicated to my parents and little brother

Wu Lugen, Yu Mei'e and Wu Qiang

University of Poitiers, France

September 2008 – September 2012

ABSTRACT

In this thesis, a new numerical approach is presented for the dynamic simulation of the electro- and electro-thermo convective phenomena that occur in a dielectric liquid subjected to unipolar injection and a thermal gradient. The main difficulty of computation comes from the determination of the electric field and charge density distribution, as the space charge modifies the electric field which in turn, controls the space charge distribution. This nonlinear coupling has prevented obtaining analytical solutions, especially in complex geometry configurations. An efficient algorithm is proposed to simulate electric field-space charge coupled problems. In the first step, the governing equations of the system are rewritten in the form of a so-called generic transport equation describing a general unsteady convection-diffusion transport of a conserved quantity. Then a finite volume approach is used to discretize the generic transport equation. The total variation diminishing (TVD) type high-resolution (HR) scheme and improved deferred correction (IDC) scheme of surface decomposition method are used to compute the convective and diffusive fluxes separately. The application of TVD scheme prevents non-physical oscillations and allows capturing accurately the possible high gradients in the charge density distribution.

The first part of this thesis is some fundamental research with the TVD and IDC schemes. A unified approach for TVD-type bounded high-resolution convection scheme is presented and various limiter functions are applied to the unsteady pure convection problem to compare the effectiveness, accuracy and computational cost. The connection among three widely used methods for the calculation of diffusive flux, i.e., the coordinate transformation method, the surface decomposition method and direct gradient evaluation method has been revealed. The original IDC scheme is improved by the application of 2^{nd} order gradient evaluation method (Gauss formula or the Least-squares approach).

After the description of the computational process and numerical validation of the electric field-space charge coupled module, our numerical solvers have been applied to several classic EHD and ETHD problems. The simulation begins with the electro-convection in insulting liquids between two parallel plates induced by unipolar injection. Both weak and strong injection cases are considered. The methodology was assessed by the determination of the linear and nonlinear stability criterion in the finite amplitude regime. By continuous increasing the driving parameter (T) of the system, the successive instabilities and the route to the chaotic state with the strong injection case has been defined. Then, the effect of the diffusion mechanism for charge density transport and vertical walls on hysteresis loop (including T_C and T_f) and flow structure of finite amplitude convection is investigated.

To improve the performance of our numerical algorithm, some numerical aspects, like injection boundary condition treatment, optimal time marching and TVD schemes and performance with non-uniform grids, are discussed.

The last section of this thesis is concerned by the electro-thermo-convection when a dielectric liquid layer is simultaneously subjected to unipolar injection and a thermal gradient. Our numerical ETHD solver was firstly verified with a stationary and an overstable stability problem which have been tackled with the linear stability analysis approach. The model problem that both heating and injection are from the bottom electrode has been analysed in details. The neutral stability curve which separates the stable and unstable regions was reproduced. The existence of nonlinear phenomenon, finite-amplitude bifurcation behaviour and the flow structure are highlighted.

Keywords: Dielectric liquid, finite volume method (FVM), charge-coupled system, total variation diminishing (TVD) scheme, improved deferred correction (IDC) scheme, electro-convection, electro-thermo-convection, unipolar injection.

ACRONYMS

AC	*Alternating-Current*
CBC	*Convection Boundedness Criterion*
CD	*Central Differencing*
CFD	*Computational Fluid Dynamics*
CFL	*Courant-Friedrichs-Levy*
CN	*Crank-Nicolson*
CTM	*coordinate transformation method*
CV	*Control Volume*
DC	*Direct-Current*
DFC	*Deferred Correction*
DGEM	*Direct Gradient Evaluation Method*
DL	*Dielectric Liquids*
EDL	*Electrical Double layer*
EE	*Euler Explicit*
EHD	*Electro-Hydrodynamics*
ETHD	*Electro-Thermo-Hydrodynamics*
FCT	*Flux Corrected Transport*
FDM	*Finite Difference Method*
FEM	*Finite Element Method*
F(S)UD	*First(Second) order Upwind*
FVM	*Finite Volume Method*
GT	*Gauss Theorem*
HR	*High Resolution*
IBVP	*Initial Boundary Value Problem*
IDC	*Improved Deferred Correction*
IE	*Euler Implicit*
IVF	*Imposing Velocity Field*
I3L	*Implict three-level*
LS	*Least Squares*
MIM	*Momentum Interpolation Method*
MOL	*Method of Lines*

NHT	*Numerical Heat Transfer*
NDM	*Normal Decomposition Method*
NVD	*Normalized Variable Diagram*
PDE	*Partial Differential Equation*
PIC	*Particle In Cell*
RBC	*Rayleigh – Bénard Convection*
RK	*Runge-Kutta*
SCL	*Space-Charge-Limited*
SIMPLE	*Semi-Implicit Method for Pressure-Linked Equations*
SSP	*Strong Stability Preserving*
FFT	*Fast Fourier Transform*
TSE	*Taylor Series Expansion*
TVD	*Total Variation Diminishing*
VAC	*Voltage-Ampere Characteristic*
1D /2D/3D	*One/ Two /Three Dimensional*

NOMENCLATURE

Symbol	Description	Units
A	*Coefficient matrix*	
	Amplitude of velocity field	[m/s]
AM	*Angular momentum*	[N.m.s]
b	*Thickness*	[m]
c	*CFL coefficient*	
c_p	*Specific heat capacity*	[J/kg.K]
D	*Ion diffusion coefficient*	[m^2/s]
e_0	*Electro Charge*	[C]
e_1	*Derivative of permittivity to temperature*	
$\vec{E}$	*Electric field*	[V/m]
f	*Frequency*	[Hz]
$\vec{f}$	*Force field vector*	[N/m^3]
$\vec{f}_e$	*Electric force field vector*	[N/m^3]
I	*Electric current*	[A]
I_d	*Displacement current*	
$\vec{j}$	*Electric current density*	[A/m^2]
k	*Boltzmann constant*	[J/K]
k_C	*Critical wave-length*	
k_D	*Dissociation constant*	
k_R	*Recombination constant*	
K	*Ionic mobility*	[m^2/V.s]
k_1	*Derivate of mobility to temperature*	
L	*Horizontal length*	[m]
$\vec{n}_k$	*Unit normal vector*	
P	*Actual pressure*	*[Pa]*
$\tilde{P}$	*Modified pressure with electrostrictive force*	
$P(f)$	*Power spectral*	
q	*Ionic charge density*	[C/m^3]
q_0	*Charge density at emitter electrode*	
Q	*Heat flux*	[W/m^2]
r	*Gradient ratio*	
S	*Surface area*	[m^2]
t	*Time*	[s]
$\vec{U}$	*Velocity vector*	[m/s]
V	*Voltage*	[V]
V_p	*Volume of control cell*	[m^3]
α_U	*Under-relaxation factor for velocity*	

α_p	*Under-relaxation factor for pressure*	
θ	*Temperature*	[K]
θ_0	*Reference temperature*	
ρ	*Mass density*	[kg/m^3]
ϕ	*Scalar*	
	Electric potential	[V]
ε	*Permittivity*	[F/m]
ε_0	*Permittivity of vacuum/air*	
μ	*Dynamic viscosity*	[kg/m.s]
ν	*Kinematic viscosity*	[m^2/s]
σ	*Electrical conductivity*	[S/m]
δ	*Growth rate*	
κ	*Thermal diffusivity*	[m^2/s]
η	*Injection coefficient*	
Φ	*Limiter function*	

NON-DIMENSIONAL PARAMETERS

T	*Electric Grashof number*
C	*Injection strength*
M	*Non-dimensional mobility number*
Re	*Reynolds number*
R	*Electrical Reynolds number*
Ra	*Rayleigh number*
Pr	*Prandtl number*
α	*Non-dimensional ionic diffusion number*
L	*Non-dimensional temperature derivate of dielectric constant*
N	*Non-dimensional temperature derivate of ion mobility*
Nu	*Nusselt number*
Ne	*Electric Nusselt number*
A	*Aspect Ratio, non-dimensional geometry parameter*

Table of content

Chapter 1 Introduction

1.1 Background

Electrohydrodynamics (EHD) is an interdisciplinary science dealing with the interaction of fluids and electric fields or charges [1]. There is a strong nonlinear coupling between electric field and fluid field. The effect of fluid motion on electric fields as well as the influence of the fields on the motion should be considered simultaneously [2].

Flow control and optimization is increasingly incorporated in the design of engineering devices ranging from aircraft and space vehicles to micro-fluidic devices [3]. Comparing with traditional pressure-driven mechanism, flow driven through electric fields has the following advantages:

1. The devices are simple, as only power supply and electrodes are necessary. No complex mechanical structures and moving partes are needed;
2. The size of the device is small and the shape and the size of electrode can be easily adjusted, indicating strong mobility;
3. The flow responds rapidly to the applied electric fields;
4. Low power consumption and noise.

In addition, for the application of the EHD technique in heat transfer or heat exchanger design, there are two extra advantages,

5. The technique can be applied to the environment with zero or low gravity, while buoyancy-driven mechanism may not work;
6. High efficiency in the case of small temperature difference.

Considering all above advantages, the EHD technique presents some promising opportunities in flow control, enhancement of heat and mass transfer, micro-electromechanical system (MEMS) and some other industrial processes. However, at present stage, there are few mature commercial products or applications purely based on the EHD technique. Two very recent conceptual designs can be found in [4] and [5] with applications in the cooling of laptop and devices on a flight in space separately. The relative backwardness of such applications with the EHD technique can be attributed to the lack of complete mastering the characteristics of flow motion.

Since the first observation according to which water can be attracted by “electrics” rubbed with a cloth by William Gilbert during the 16th century [6], there had been wide and deep studies on the interaction between fluids and electric fields. Nowadays, the knowledge of most processes involved in EHD field has reached a stage where a modeling may be done with a certain confidence. Some widely known phenomena with EHD and their explanations can be found in [7] and [8]. For more general theoretical studies on EHD, three monographs [1][9][10] are strongly recommended.

To fully understand the behavior of dielectric liquids under the effect of external electric fields, the first task is to classify the acting forces involved. Luckily, in dielectric liquids characterized by low values of conductivity, Maxwell equations reduce to the electroquasistatic limit [10, p.123]. In other words, the magnetic effects can be neglected in the realm of EHD. According to the theory of Laudau [11], the electric (body) force acting on dielectric liquids mainly contains Coulomb

force, dielectric force and electrostrictive force. Early work in EHD mainly concerned the dielectric and electrostrictive forces [12-17], as there was no efficient method to introduce charge carriers into dielectric liquids. It should be noted that the temperature field analysis is always needed when considering the dielectric force because of the close physical properties relationship between them.

Along with the development of physical chemistry, the technique which can reproduce injections of ions has come of age. At present, there are two classes of methods to introduce ions into dielectric fluids. The first class is to cover the electrodes with electrodialytic membranes or varnishes [18]. This method won wide application in the early EHD experiments [19-22]. However, the membranes and varnishes are easily degraded under mechanical and thermal stresses [23]. With the other class, only applied for nonpolar liquid, weak and moderate injection can be achieved by adding some specific salts to the liquid [24]. For the latter method, bare electrodes can be directly used. The details of the injection mechanism will be explained in Chapter 2.

In addition, dissociation of impurities can be considered as a third way for ions creation in dielectric liquids. This dissociation is governed by the physical and chemical processes. The details of the dissociation process are linked with the nature of impurities and dielectric liquids [1, p.24-27]. Generally, there is no difference between the injected and dissociated ions [25, 26], though P. Atten once showed a different opinion [27]. More importantly, with plentiful experiments, it is proved that the injection process is the dominant one comparing with dissociation for both polar liquid [28] and nonpolar ones [29] with different electrodes [30-33].

Once some ions appear in the fluids, the flow will be driven by the ion-induced Coulomb forces. The complex coupling relationship between the flow field and the charge density distribution usually brings great difficulties to determine their values [34]. On the one hand, the flow field is influenced by the charge distribution through the Coulomb forces in the Navier-Stokes equations; on the other hand, the charge density (the Coulomb forces) is updated via the conservation equation of charge. In addition, the change of charge density distribution also affects the local electric fields through the electric potential equation.

In a word, Coulomb-driven convection in insulating liquids shows more non-linear characteristics comparing with the buoyancy-driven convection. The strong nonlinear interaction precludes the possibility of using analytical methods to determine the charge distribution, even with extremely simple geometry configurations.

When applying the EHD technique to enhance heat transfer, the temperature field must be taken into account. The formed electro-thermo convection leads to more complex interaction among fluid, heat and electric fields. Generally speaking, heat field has at least three types of direct effects on EHD convections: (1) buoyancy force in momentum equations; (2) dielectric force and electrostrictive force; (3) temperature-dependent physical properties (like fluid density, ionic mobility and permittivity).

Since the solutions of EHD and ETHD are not readily amenable to an exact mathematical analysis, these problems have been tackled by several alternative methods. The Galerkin method and the small disturbances method are widely used in linear stability analysis [35-37]. By the analogy with

thermal plumes, some authors utilize a self-similar analysis and an integral model to analyze EHD plumes [38][39]. However, there are distinct limitations for all these methods. For example, the linear stability analysis methods generally can only be applied to problems with strict assumptions. The Galerkin method could not provide satisfactory description of the convective flow in slightly supercritical and subcritical conditions.

Since the governing equations of EHD problems have been obtained with a certain confidence, a natural idea is to directly solve the whole system with numerical methods. In the present study, we try to build an efficient numerical tool which can be applied to Coulomb-driven convection and electro-thermo-convection both in two- and three-dimensional problems with unipolar ion injection. The essence of numerical calculation is converting the (coupling and nonlinear) partial differential equations (PDEs) which govern a problem into discrete calculations which can be solved on a high-performance computer. In principle, all EHD problems can be solved by appropriate numerical methods as the governing equations are deduced based on continuum model, which can avoid the difficulties met by theoretical methods. However, developing an efficient numerical tool for EHD problems would meet some practical difficulties.

In the study of fluid mechanics, an important idea is to refine the essences of fluid flow by focusing on some classical problems, like Rayleigh-Bénard convection, lid-driven cavity flow, Taylor vortex, Couette flow between concentric spheres and so on. In the present study, we follow the same thought by considering some fundamental problems in EHD: the convection induced by unipolar injection in a plane layer of dielectric field. In addition, the effect of the thermal gradient on the instability phenomena and the heat transfer enhancement by the Coulomb-driven convection are the other two research topics of the present study.

With the relatively simple geometry problem, we would like to gain some basic understandings of physical models, charge conduction process, flow structures and bifurcation of stability in an electrical-hydrodynamic (EHD) or electro-thermo-hydrodynamics (ETHD) nonlinear dynamical system.

1.2 Previous and related studies

1.2.1 Finite volume method

Based on iterative segregated methods, a numerical simulation of a complete EHD problem contains two or three modules depending on whether the temperature field is included or not: the electrostatics module, the velocity-pressure module and the energy module. These three modules correspond to Maxwell's equation, Navier-Stokes equations and energy equation respectively.

There is no doubt that numerical methods based on finite volume method (FVM) are dominant in the field of Computational Fluid Dynamics (CFD). Even with problems of very complex geometry structure, finite volume method can work well. A very good example can be found in [40], which was published in 1998. In this paper, a parallel finite volume method for unstructured grids, combining local grid refinement and efficient linear system solver, is applied to a direct numerical simulation of the flow around a sphere at Reynolds number (Re = 5000). The good agreement of

flow structure between numerical solutions and visualization experiments shows the ripeness and stability of FVM with fluid simulation.

In fact, the application of FVM has been successfully extended to some other fields, like solid stress analysis [40-43], fluid-solid interaction [44][45], radiation heat transfer [46][47, chapter 13] and others.

As for numerical techniques for electrostatics, traditionally, Finite Difference Method (FDM) and Finite Element Method (FEM) are the dominant ones, see [10, chapter 6] and [48]. Only during the past 10-15 years, the FVM has started to be used to solve electromagnetic problems. Various discretization schemes and algorithms have been developed [49-53]. Recently, N. Neimarlija, et al. applied the FVM to calculate electrostatic fields in electric precipitators and made a systematical explanation of the practical implementation process [54]. In a subsequent paper, N. Neimarlija et al. incorporated the calculation of electrostatic fields into a much complex system including the flow of gas, particle dynamics and electrostatics [55]. The core idea of [54] and [55] is to employ an iterative segregated solution procedure of the resulting set of algebraic equations. Traoré et al. have successfully developed a direct numerical simulation based on FVM to solve the EHD [56] and ETHD equations [57].

The present study follows a similar algorithm as the one proposed by N. Neimarlija et al. [54][55] and the one by Traoré et al. [56][57] with an iterative segregated solution procedure. The main difference between our numerical algorithm and the one in [54][55] includes two aspects:

1. ***Transient calculation.***

All the examples provided in [54] and [55] were based on the assumption of steady state. This assumption would help decreasing the computational cost by the neglect of the formation or developing process of various fields. However, for EHD simulation, the formation or developing process may play an important role in understanding the flow structures. For example, an important observation in EHD experiment with unipolar injection in a plane layer of dielectric liquid is the fluctuations of the electrical current once the liquid is in motion. In addition, for bifurcation study, the steady state may not exist. Thus, temporal terms (in charge density equation, Navier-Stokes equations and energy equation) and transient process will be considered in our numerical solvers. The transient SIMPLE algorithm is used to solve both steady and unsteady Navier-Stokes equations. However, including the temporal term, the charge conservation equation without diffusion transport mechanism turns to be a hyperbolic partial differential equation. This conversion brings some new difficulties in the construction of numerical algorithms.

2. ***Discretization schemes.***

One key difficulty in numerical modeling of the Coulomb-driven convection in insulating liquids is the method of adequately computing charge density distribution with steep gradients. The problem arises from the fact that diffusion mechanism of charge transport is negligible comparing with other charge conduction mechanisms. It has been proved by numerical results in [58] that a second upwind differencing (SUD) scheme turned out to be inefficient when computing the charge distribution because of its severe numerical diffusion [59].

In [54] and [55], the authors use a kind of hybrid scheme by blending the second-order central differencing (CD) scheme and the first-order upwind scheme (FUD). The problem of the hybrid scheme is the determination of the blending factor. In addition, this scheme can't guarantee the positivity of the obtained charge density field.

The numerical diffusion can be reduced by decreasing the size of the mesh or using local grid adaptive technique. Howeverm, the computational cost or the complexity of the numerical algorithm increases dramatically.

There is a clear similarity between the hyperbolic charge conservation equation and the unsteady advection equation. The advection equation has been extensively studied as the model problem or combining with other fluid dynamical equations [60]. One survey of Rood [61] mentioned that over 100 algorithms for discretizing the convective terms were found. An extensive bibliography was summarized in [61]. In EHD field, some numerical methods were specially designed while some others were borrowed from other areas to solve charge conservation equation. Two widely used methods are the particle in cell (PIC) method [62][63] and the flux corrected transport (FCT) method [64][65]. Both methods have been used to simulate the development of electro- convection between two parallel plates [66][67] and their abilities to deal with transport problems in the presence of steep gradients were demonstrated. Some differences showing in the prediction of small oscillations of the velocity and the electric current are highlighted and explained [66]. Generally, the computational cost of FCT method is much lower than the one with PIC method, especially with the weak injection case.

In the present study, the so-named high-resolution (HR) schemes [66-70] will be used to tackle the difficulty. Considering the development history, both FCT and TVD-type schemes are designed for the shock capturing when solving compressible Euler equations. The basic ideas of the two algorithms are similar to each other. Both of them use a low order, oscillation-free scheme and a higher order, oscillatory scheme to reconstruct the optimal solution. The difference is the flux limiting procedure: FCT contains two steps while TVD scheme uses an adaptive limiter function. Thus, we may expect TVD schemes to be more efficient than FCT schemes in solving the charge conservation equation from the viewpoint of the simplicity of the algorithm.

Normally researches based on CFD technique are some kind of systematic engineering. It is clearly impossible to give a complete survey of all aspects with CFD here. Instead, we will briefly describe some key techniques involved in our practical developing process.

It's also worth pointing out that our numerical algorithm employs the same discretization and data structure for both fluid flow and electrostatic equations which facilitates the formulation of an efficient solution algorithm. In other words, all governing equations will be written in the form of a generic transport equation, which helps explaining the discretization methods. More significantly, the consistency between the convective flux and charge density equation and the consistency between diffusive flux and Poisson equation are highlighted. This kind of research strategy puts more emphasis on the common ground of governing partial differential equations (PDEs) from different physical processes.

High-Resolution schemes

The charge density equation and Navier-Stokes equations contain convection terms, though with different names and meanings. For CFD researchers in both compressible and incompressible fluid fields, the discretisation method of the first-derivative advection term attracts much attention from practical application requests. The essential reason is that the majority of fluid flows encountered in nature and industry are characterized with high Reynolds numbers (even at turbulent state), which means that convection term is at a dominant position [68, page 46]. The study aims to obtain several schemes of good properties (e.g. stability, convergence, boundedness, and accuracy, etc.) with low computational cost. It is difficult to design a scheme to meet all the requirements of the above-mentioned properties and only the major requirements should be considered. In addition, different properties may conflict with each other. For example, high-order linear schemes (like second-order upwind, QUICK and k-scheme [69]) can lead to high accuracy but unphysical, oscillatory behavior, especially in regions of steep gradients, while the solution obtained with the first-order upwind (FUD) and other low-order schemes often suffer from severe artificial diffusion.

However, boundedness is an extremely important property for some problems. For example, in the absence of sources, some equations (e.g. heat equation for temperature) require the minimum and maximum values of the variable to be limited on the boundaries of the domain [70, page 33], and the pollution concentration to lie between 0% and the value of its initial moment. Another representative example is with $k-\varepsilon$ turbulent models, a negative value of turbulent dissipation would results in negative turbulent viscosity, usually with disastrous effects on the solution algorithm [71]. In compressible fluid field, the goal of efficient shock-capturing methods is to capture discontinuities in the solution automatically and reduce smearing to a minimum, and not to introduce nonphysical oscillations near the discontinuities [72, page 6]. In all cases, the convection term in its differential form does not violate the bounds of the variable given by its initial distribution. Therefore, this property should also be preserved in the discretised form of the term.

A formal definition of boundedness can be described as the one with which the numerical solution will never surpass the maximum or minimum values inherently determined by the physical process [73]. It is essentially equivalent to the demand of avoiding numerical under- and overshoots in regions of strong variation [74].

Considering the importance of boundedness property, sustained effort has been made to find or design schemes which can lead to accurate and bounded solutions. However, the road to find a linear high-order scheme which can also lead to oscillation-free results has been blocked by Godunov's famous theorem [75] which states that no linear convection scheme of second-order accuracy or higher can be monotonic. It is now well-known that the use of a non-linear convection schemes can lead to solutions of oscillation-free and high-accuracy. The fundamental idea behind the non-linear schemes is straightforward. These schemes can be viewed as blending schemes of high and low order approximations. In other words, based on local information, the actual used scheme would switch between high-order oscillatory schemes and low-order bounded schemes. To achieve the goal, two typical questions need to be answered:

1. How to recognize the regions where the switch is required;
2. What kind of switch should be introduced ;

Different answers to above questions lead to two well-known types of high-resolution (HR) schemes: Total Variation Diminishing (TVD) schemes [76][77] and Normalized Variable Diagram schemes (NVD) [78][79]. TVD schemes emphasize the mathematical properties, while NVD schemes are based on appropriate translation with physical meanings of boundedness property. The first TVD scheme has been designed for unsteady equations. Later, Roe [80] and Z. Wang & B.E. Richards [81] extended it to steady-state equation. Despite the different starting points, TVD and NVD schemes share some commons. For example, both of them use some sort of "unboundedness indicators" to recognize the regions where interventions are needed and the definition of the indicator requires at least three local points. In addition, some switching functions were designed to include lots of established schemes. The essential connection between TVD and NVD schemes has been firstly revealed in [82]. In simple terms, the two types of schemes can convert to each other through some simple formulae.

Till recently, the complete numerical tools have not been widely used to tackle EHD problems. By careful examination, the demand of solving charge density equation is quite similar to the example of pollution concentration mentioned above. In details, it is always desired that the numerical solutions of charge density containing no non-physical negative values. To achieve the goal, a unified approach which has been clearly explained by in [81-84] will be adopted.

The main features of the unified approach can be summarized as,

1. The expression of the unified approach follows the flux-limiting algorithm, which are more convenient than NV methods, since a deferred correction (DFC) approach can easily be adopted [85][86]. In fact, all five-point schemes can always be transformed into the unified expression [73, page 132], which has greatly facilitated the implementation of new schemes.
2. The schemes may be applied to transient problems when they are combined with an appropriate time marching method and obey the time-step restriction condition [84].
3. The approach employs two more general boundedness criteria: positivity and the convection boundedness criterion (CBC). The change of the boundedness criteria from TVD has a vital significance for understanding the performance of schemes in multidimensional cases. The TVD condition has been proved for one-dimensional case, but never in multiple dimensions, though there are quite a lot of success applications based on the time splitting approach. In the "dimensional splitting", 2D or 3D implementation consists of one-dimensional schemes applied separately along each direction. The unified approach can be successfully applied to multi-dimensional problems. The detailed proof process can be found in [79] and [87, chapter 5].

It is worth pointing out the relationship between the above mentioned TVD-type high-resolution and the FCT method, which has already been applied in EHD set of equations [66][67][88]. The basic idea of the FCT method is the same with the TVD schemes which also uses a low order scheme (that includes serious numerical diffusion) and a higher order scheme (that includes unphysical oscillation) to reconstruct the optimal solution. The key difference is the limiting procedure: the FCT method contains two steps while all TVD schemes need only one step with an inherent adaptive limiter function. Though there is no clear conclusion about the accuracy comparison, the computational efficiency of TVD schemes is obvious. Then it explains why we introduce the TVD schemes rather than the FCT methods to solve the charge density equation.

Our final goal is to build an efficient numerical tool for EHD problems, which can be applied to arbitrary complex geometry configurations. In recent years, the unstructured grid methodology is quickly evolving in CFD field mainly due to its inherent flexibility for discretization of complicated geometries [89][90]. However, most HR schemes cannot be applied to unstructured grids directly. The main difficulty is the lack of far-upwind cell information [91]. To circumvent this difficulty various methods have evolved [71][91-93]. There are two main thoughts to apply the HR schemes on unstructured meshes. The first is to avoid explicitly using far-upwind points, like GAMMA scheme [71] and Bruner's approach [92]. GAMMA scheme uses an 'unbounded indicator' without far-upwind information, whereas it uses the CD scheme as the high order base scheme. However, GAMMA scheme requires that the nodal point locating in the centre of the control volume, which is not always the case for unstructured meshes. The second is to construct the virtual far-upwind points, like Darwish's r-factor algorithm [91] and Lian-xia Li's new r-factor algorithm [93]. Both algorithms need to calculate nodal gradients and to use extra memory for virtual points. The most serious problem of all above mentioned methods is all of them show minor oscillations, even if the grid size is sufficiently small.

Besides some implementation details of the unified approach, in the present study, we will mainly focus on the following two aspects of HR schemes,

1. The performance of different limiter functions, i.e., different TVD schemes and their effect on complete EHD problems;
2. The reason of the minor oscillations when extending TVD schemes to unstructured grid system and the possible solutions;

Temporal schemes

In order to match with the application of high-resolution of hyperbolic charge density equation, the discretisation method for temporal term should also be paid extra attention. There are two standard ways to derive numerical algorithms for multi-dimensional flow problems [94]: either by the method of lines (MOL) approach, where space and time discretization are considered separately, or with the dimensional splitting approach, starting from a fully discrete one-dimensional method. Both approaches have been combined with HR schemes and are being widely used in CFD fields. Generally speaking, dimensional splitting often leads to more accurate solutions in wide Courant number range when one-dimensional high-resolution methods are applied in each direction separately [95]. The main advantage of MOL approach is its simple algorithm and straight extension to nonlinear conservation laws. In addition, the generic transport equation solver can be directly applied to the charge density equation when following the MOL approach.

If we assume that the time dimension is the same as the space dimension, it is not difficult to understand the fact that some time marching schemes may potentially introduce oscillations. Taking the well-known three time level (I3L) scheme for example, the essence of its construction is to make a linear interpolation among solutions at three time levels, just like the linear high-order spatial schemes. Thus, it possibly leads to oscillating results. A typical test example can be found in Chapter 3.

In fact, in recent years, it has been a hot research topic in designing the so named TVD [96][97] or Strong Stability Preserving (PPS) time schemes [98][99]. The SSP schemes are used to match with higher-order oscillation-free schemes, like TVD, essentially nonoscillatory (ENO) [100] and weighted ENO (WENO) methods [101][102]. The essential requirement for these schemes is the ability of avoiding oscillatory solutions.

Since excellent up-to-date reviews of the previous studies on this subject have been documented in the literature [103][104], they are not repeated here. Some content closely related to the present study can be found in Chapter 3. In this thesis, we will not go deep into the design process of each time scheme. On the contrary, we are more concerned with the performances (accuracy, robustness, computational cost and so on) of these schemes when combining with TVD-type high-resolution schemes and their effects in numerical solutions of complete EHD problems.

Surface-decomposition method

The solving methods of Poisson equation or all partial differential equations containing the diffusion term is another research point in the present study. Considering its broad utility in electrostatics, mechanical engineering and theoretical physics, quite a lot of methods have been developed, both numerically and theoretically.

Starting from our CFD and NHT background, an efficient finite volume Poisson solver based on surface decomposition approach [107, page 33] and a recent proposed improved deferred correction (IDC) scheme [105][106] was developed.

Normally, it is not difficult to use 2^{nd} - or 4^{th}- order Central Differencing (CD) scheme to solve Poisson equations numerically when control volumes are regular and orthogonal. However, when control volumes are unstructured or non-orthogonal, the accuracy of CD schemes degrades. It should be emphasized that 'unstructured' represents the data storage ordering while non-orthogonal represents the geometry property of grid. There is no essential connection between them. There exist some types of unstructured orthogonal meshes, like regular-triangle, regular polygon and admissible meshes [108]. However, in general cases, unstructured meshes are also non-orthogonal. Thus, we put them together here to highlight the fact that the IDC scheme can also be directly applied to arbitrary unstructured meshes.

When the grid is non-orthogonal, the discretization of diffusive flux is indeed less straightforward than with orthogonal ones. A variety of methods have been developed to take the non-orthogonal contribution into account, like the coordinate transformation method, CTM [109][110], the normal decomposition method, NDM [68][105][107] and the direct gradient evaluation method, DGEM [111][70, page 234-235]. Some other methods are summarized in [73, page 194-197] [112][113]. Although these three above mentioned methods have been invented independently with different conceptual bases, all of them have gained wide applications from CFD or NHT community. In the present study, we are concerned about two aspects:

1. The similarity and relationship among the above mentioned three methods for diffusive flux computation on nonorthogonal meshes;
2. Some implementation details and further development of the IDC scheme;

The first aspect aims at providing some constructive answers to the following questions,

1. Can all these methods lead to the converged solution on extremely skewed meshes?
2. Based on the converged solution, how to evaluate the advantages and disadvantages of these approaches in terms of accuracy and computational cost?
3. What are the main factors affecting the accuracy and computational cost of these different approaches?

The second aspect is to increase the accuracy of the scheme by carefully selecting gradient evaluation method and implementing numerical boundary conditions and to extend it to three-dimensional problems.

SIMPLE algorithm and its improvement

For incompressible fluid, the pressure-based approach is the mainstream choice. Among the pressure-based approaches, the pressure-correction method is the most widely-used one because of its simplicity and straightforwardness in physical concept [114]. Patankar and Spalding proposed the first pressure-correction method in 1972 [115] and named it SIMPLE algorithm. There are two major approximations made in the SIMPLE algorithm,

1. The initial pressure and velocity field are assumed independently, hence the interconnection between pressure and velocity is neglected, leading to some inconsistency between them;
2. The effects of the velocity corrections of the neighboring grids are arbitrarily dropped in order to simplify the solution procedure, thus making the algorithm semi-implicit.

Though the two approximations will not affect the final solutions when the solution process converges [116], they do affect the convergence speed and the stability of the solving process. Therefore, a number of variants have been developed to overcome the two approximations. In 1981, Patankar proposed the SIMPLER algorithm [117], which successfully gets rid of the first approximation. In the SIMPLER algorithm, the initial pressure is determined by a pressure equation. Many variants of the SIMPLE algorithm are available, like SIMPLEC [118], SIMPLEX [119], PISO [120] and Yen and Liu's explicit correction step method [121] and so on, but none of them have successfully overcome the two assumptions simultaneously.

Until very recently, Tao Wenquan's group of Xi'an Jiaotong University, China, uses a sophisticated technique to overcome the second assumption of SIMPLE algorithm. They directly improve the pressure, rather than introducing the pressure correction and proposed the CLEAR algorithm [122][123]. To improve the robustness of the CLEAR (coupled and linked equations algorithm revised) algorithm, a modified algorithm, named CLEARER was designed [124]. In addition, another algorithm named the IDEAL algorithm (Inner Doubly-iterative efficient Algorithm for Linked-equations) [125][126], which is also on the basis of the CLEAR algorithm, was proposed to retain the fully-implicit feature and to further enhance the robustness and convergence characteristics. The Implementation details of the IDEAL algorithm on 3D collocated grid system and its performance for three-dimensional incompressible fluid flow and heat transfer problems can be found in [114][127].

In the present study, the more advanced but complicated CLEAR(ER) or IDEAL have not implemented into our EHD or ETHD solvers, as the original SIMPLE algorithm can fully meet our current needs. The above short review indicates the direction of future extension of velocity-pressure coupling algorithm. Instead, we try to make another contribution to CFD field by tacking the problem of pressure-velocity coupling on extremely non-orthogonal grids. In [128], Peric studied the property of the pressure correction equation in a non-orthogonal grid system. By comparing the simplified equation (neglecting the non-orthogonal terms) with the complete equation, he found that the iteration process never converges with the simplified equation if the grid is extremely non-orthogonal (with typical angle $\beta \geq 135°, \beta \leq 45°$). In addition, the range of the relaxation factors was seen to become narrower for higher skewness of the grid. Though the problem can be solved by using the full 9-point pressure-correction equation for 2D flow, the method is not efficient from the viewpoint of computational cost. For 3D flow, the full pressure-correction equation contains 19 diagonals, which bring great troubles for selection of the linear system solver and considering computational cost.

To alleviate or solve this problem, Cho and Chung [129] proposed a way of incorporating effects of non-orthogonality in the pressure-correction without extending the computational molecule. However, an additional user defined parameter is needed. T. Lenhause and M. Schafer designed a new linear interpolation method based on a muti-dimensional Taylor series expansion (TSE) [130], and applied it to the pressure-correction equations on non-orthogonal grids and found its effectiveness in improving overall performance of Navier-Stokes solvers [131]. The main ideas of the above two methods are to adjust the coefficient of the neighboring points directly to take into account the non-orthogonality of the grid system on the condition that no far near points are used. In the present study, we follow another approach by the application of IDC scheme to pressure-correction equations. The essence of the IDC scheme is to introduce the angle information into the discrete equation, and the angle information represents non-orthogonal information to a great extent.

1.2.2 Coulomb-driven convection

In single-phase liquid flow and under DC electric field, the Coulombic component of the electrical body force exerted on the fluid by collisions between ions and neutral molecules is the main driving force. There are various physico-chemical processes that may result in the production of free charge carriers inside fluids. Considering the very reactive chemical property of the liquid, electrolytic impurities can undergo chemical reactions giving rise to ionic pairs [132-134]. Another more direct and effective method is the injection of ions by electrochemical reactions at metallic electrodes [135-137]. The second mechanism tends to dominate at large field [30-32]. However, the electric force of all charge carriers are of the same type, though with different generation mechanisms. Typically, the fluid will be set in motion under the action of Coulomb force, thus changes the distribution of charges that in turn modifies the electric field. The two ways coupling makes the EHD convection a difficult subject.

Generally speaking, researches with EHD are closely linked with the type (shape and size) of electrodes. In early experiments, focus was put on the relative importance of different components of the electrical body force and the ion injection process. Needle-plane, knife-plane and

blade-plane [138][139] electrode configurations are favorable because they feature locally high electric fields that enhance charge generation. However, the complex geometry structures bring a lot of difficulties in the theoretical analysis. Only until very recently, EHD flow of a dielectric liquid around a blade electrode was systematically explained with the aid of a simple injection law [140-142].

On the other hand, another class of relatively simple electrodes (parallel planes) attracts much attention. The physical model is quite simple: the initially still dielectric fluid was put between two parallel plane (circular) electrodes. By external electrical field, the free charger carriers (i.e., ions) are formed in the medium due to an intense electric field in the vicinity of one of the electrodes (the emitter). While these charges move towards the other electrode (the collector), they impose momentum to the neutral molecules of the medium, thus 'dragging' them along and producing a net of flow of the medium. However, the above mentioned two ways coupling brings serious obstructions for accurate determination of charge density distribution and flow field. In a simple word, the final purpose is to well understand the voltage-current characteristic of dielectric liquids under different types of applied electric field. Just like most fluid problems, all three tools, i.e., theoretical analysis, physical experiment and numerical simulation are used.

Theoretical analysis and physical experiment

For two plane parallel electrodes geometry, there are some analogies between unipolar injection and Rayleigh-Bénard (fluid layer heated from below) problems. In both cases, the state of rest is potentially unstable and the viscous dissipation prevents the disturbances from growing for low enough motive forces (buoyancy force for RB flow and Coulomb force for electro-convective flow). At a certain threshold the fluid layer becomes unstable and turns into a regular pattern of convective cells. The certain threshold is named the critical linear stability value. The first linear stability analysis has been performed by Schneider and Watson [143] in the case of space-charge-limited (SCL) injection. Two important assumptions were made: (1) perfectly insulating medium and (2) negligible diffusion. The stability values of the general case of any injection level were reported in [144], which requires a third assumption of zero charge density perturbation on the injector (autonomous). To verify the theoretical criteria, physical experiments were taken by Watson, et.al, and the agreement was satisfactory [145]. It should be noted that there is a difference between the problems tackled by Schneider and Watson and the core problems of the present study. In [143] and [145] the dielectric liquid layer had a free surface and the present study only considers the case with rigid boundaries. A closer physical experiment can be found in [19]. In this paper, the authors considered two asymptotic states of convection: viscosity and inertial effects dominated. The figures of the electric Nusselt number versus the stability parameters in different liquids are provided, which is of great help to understand the general features of electro-convection.

However, there is a main difference in the transport of the scalar quantity between RB flow (heat) and unipolar injection (charge density). Heat is transferred by diffusion alone whereas the charge carriers migrate under the action of the electric field with a fixed mobility, their diffusion being mostly negligible. The drift velocity and the liquid velocity can compete: for instance, a laminar liquid motion prevents the ions from entering regions in which their velocity component along the

electric field direction at least balances the ionic velocity *KE* [146]. Thus, it is possible to have some regions strictly free of charges that bring a completely new nonlinear phenomenon for unipolar injection. In fact, for double injection case, a similar nonlinear phenomenon has also been observed experimentally [147].

The main feature of the nonlinear phenomena is the existence of two criteria, one being the classical linear stability criteria T_c associated with perturbations of infinitely small amplitude, the other, T_f , corresponding to finite amplitude velocity disturbances. Considering $T_f < T_c$, there is a hysteresis loop and jumps of the steady values of both the velocity amplitude and the current between the two critical values [148].

The most important features of the nonlinear instability mechanism have been derived by Félici [149]. Later, P.Atten and J.C. Lacroix investigated the phenomena that occurred at the onset of instability of unipolar injection based on a simplified model and obtained some more detailed conclusions [148]. Experiments with various liquids under SCL conditions have also been performed [146][148]. The existence of the hysteresis loop in the electrical current-voltage figure has been highlighted.

As for flow structure in three-dimensions (3D), it is experimentally observed that convection sets in the form of hexagonal cells when the driving parameter was slightly above the onset of instability. In details, when the applied voltage is suddenly increased to a level above the critcal value, the liquid layer initially at rest starts to move and a pattern consisting of nearly prismatic cells is detectable at a very short time. After some reorganisation, the polygonal cells become very regular and stable hexagonal cells.

Numerical modeling

When numerically simulating the problem, the first task is to separate the injection problem in liquids from the one in gases. Taking air at atmospheric pressure as an example, the ions created by the electrodes generally have a drift velocity much higher than the air velocity. In that case the motion has but negligible effects and the ion trajectories are the electric field lines. The coupling of electric field and velocity field can be considered as one way, which greatly simplifies the EHD problem [150].

In 1987, A. Castellanos and P.Atten developed the mathematical model of unipolar injection, explained the ion generation process and some preliminary researches on numerical stability analysis were performed [151]. In 1989, A. T. Perez, et al., investigated the influence of charge diffusion upon the nonlinear stability criterion and subsequent finite amplitude electro-convection of an isothermal liquid layer subjected to weak injection [152]. It was found that a new non-dimensional parameter (the ratio of the Coulombic repulsion to the charge diffusion) played a major role.

In 1991, the physical model including electrical boundary conditions and governing equations of unipolar injection were further described by A. Castellanos [153]. In addition, the bifurcation behavior of the nonlinear system was also introduced primarily. Then, P. Atten explored the effects of space charge density and the geometry of the electrodes on fluid. In 1997, R. Chicon, et.al, used

a method of superparticles to solve the unipolar injection problem [34]. A good agreement between their numerical results and experimental observations is obtained for both weak and strong injection cases. In 2006, P. A. Vazquez et al. used both FCT and PIC methods to deal with the distribution of electric charge [66]. In 2008, P. A. Vazquez et al. considered the full model by incorporating the computation of the velocity [67]. In addition, they did the analysis of time scales. Very recently, Ph. Traoré et al. also solved the whole set of electrohydrodynamic equations using a finite volume method [154][56]. Their emphasis was put on the strong injection problem. In 2011, P. A.Vazquez and A. Castellanos performed the stability analysis of the 3D electro-convective charged flow between parallel plates using the PIC method and imposing velocity roll structure [155]. The traditional QUICK scheme with a novel boundary condition treatment method has been used to solve charge density equation in [289]. With this new method for the charge density equation and a commercial software FLUENT, they studied the turbulent electro-convection between two parallel square electrodes.

Comparing with the accurate calculation of the velocity field, the technique which is capable of capturing the steep gradients of the electric charge is the primary concern. Very often, the velocity field can be provided through some models. There are some obvious shortcomings with this velocity field imposing technique. Firstly, it cannot be applied to complex geometry cases. Secondly, even with simple geometry configuration, the self-similar flow structure may not always work. For example, the fact of possible non-existence of a stable roll with weak injection is mutually conflicted with the imposed assumption [67]. Thirdly, the technique can only be applied to flow near stability criterion. If we want to have some insights of flow with stronger destabilizing force or forced flow, the velocity field must be obtained by solving simultaneously the Navier-Stokes equations.

In addition, though injection induced by unipolar injection in a plane layer of dielectric has been the object of research for several decades, there are still many basic questions to be answered. For example,

1. There is a discrepancy between the theoretical (also verified numerically) and measured values for the onset of instability;
2. Experimental observations showed that the electrical current is always time-dependent once the liquid is in motion. The fluctuations of the electrical current have a well defined average value but present a chaotic state [59];
3. What will happen to the system with higher potential difference;

In the present study, with our newly developed numerical tool, we would like to provide some new understandings of above questions.

1.2.3 Electro-Thermo-hydrodynamics (ETHD)

Heat and mass transfer enhancement through external forces is an important subject of fluid mechanics research. Electro-Thermo-Hydro-Dynamics (ETHD) is a relatively new inter-disciplinary subject. The major contents of the subject are to use electrical forces to enhance mixing heat transfer within the fluid (both gas and liquid). The earliest experiment of this topic was accomplished by Ahsmann and Kronig [156] in 1950. Over the past half century, the heat transfer enhancement by external electric field has been continuously studied and large number of work has

been published. Several reviews [17][157-160] are available, the most noteworthy being that of Jones [160]. In [160], the author classified the various theoretical and experimental studies and provided a complete bibliography.

In the present study, we mainly focus on the coupling effects of heat, velocity and electric fields in a simple configuration of a horizontal dielectric liquid layer between two parallel plates subject to an arbitrary unipolar injection and a thermal gradient. It is necessary to distinguish the present work from some published results.

1. Coupling mode. As listed in [161], there are at least four distinct EHD coupling modes: Columbic forces, electrostriction, dielectric gradients and Joule heating. In preliminary researches, researchers mainly considered the effect of the synergism between the permittivity gradient and the imposed temperature gradients [162-165]. In the present study, the Coulomb force is the main driving force.
2. Working medium. Though some other works also considered the Coulomb force, they generally took the ohmic or quasi-ohmic liquids as the work medium. For these liquids, the generation of free charge is through the conductivity gradient, which can be induced through a temperature gradient. For these classes of problems, some results about stability analysis and evaluation of heat transfer effect can be found in [12][166-171]. However, for dielectric liquid of low conductivity, more intense process of charge creation is ion injection. More significantly, this charge injection and corresponding Coulomb force may be considered as being independent of temperature gradients [172].

Following the above distinction, we found that only few work have been done on this particular problem. Some related and worth referring works are summarized below.

Fernandez et al. [173] performed experiments with an EHD-enhanced oil heater in tubes. The results showed that a radial motion of the fluid was strongly generated and that the heat transfer rate increased of more than 20 times over the fully developed laminar flow when a high DC voltage was applied. T. Mizushina, et al. [174] experimentally investigated the effect of radial electrical fields on heat and momentum transfer in dielectric liquid through concentric annuli. They found that EHD enhancement was less pronounced at higher Reynolds number forced flows. Similar conclusion has been obtained by A. Castellanos and N. Agrait through theoretical analysis [175]. The experimental results obtained by Bradley and Hoburg [178] highlighted the increase in Nusselt number due to injection. Paschkewitz and Pratt [179] investigated the effects of fluid properties on EHD heat transfer enhancement. Both viscous and electrically dominated flow regimes were considered. It was found that EHD had more important effect in lower viscosity liquids at the same low Reynolds number.

An interesting coincidence is that all above works were done with forced flow. However, as pointed out in [22] and [172] the convection state was mainly determined by the Coulomb force. Thus, heat transfer can be viewed as the passive transfer, a similar case in force flow condition. Thus, the conclusion obtained with forced flow may also for initially still fluids.

The most relevant experiments and theoretical analysis were performed by P. Atten, et.al [22][173]. Considering the importance of these two papers, some key ideas are summarized here.

In the experiments, the case of weak injection case was considered. It is interesting to find that the typical test case is different from all previous experiments used for hydrodynamic stability analysis [19][146][148].The reason is that the membranes used to generate strong injection were particularly poor thermal conductors. Thus, the ion injection is introduced by adding some salts to non-polar liquids, which limited its strength. Through the experiment, all four possible situations: (i) heating and injection from below or (ii) from above, (iii) heating from below and injection from above or (iv) heating from above and injection from below, were conducted. All results verified the dominant role of the Coulomb force compared to the buoyancy force.

In theoretical analysis, the author started from the experiment observations which stated that natural convection played a very minor role in heat transfer with electro-convection. Then, the non-dimensional Nusselt number (Nu) was assumed to be individually dependent on the Reynolde number (Re), like in the forced flow case. Then the left job was to estimate the velocity field. With the energy argument proposed by Felici [180], the formulas of velocity expressed by different parameters were obtained for two asymmetric cases: viscously and inertially dominated regimes. Though the author obtained the relevant parameters which governed the electrical forces for the two regimes, the problem was still far from the complete solution. On the one hand, the exact power law coefficients which relate the Nu and Re numbers have not been obtained. In fact, in some cases, like the transition range between viscously and inertially dominated regimes, it is impossible to get the law, as the estimation of the velocity field is extremely difficult. On the other hand, some possible error sources should be taken into account, like the modification of charge injection level during experiments and the effect of temperature on the conductivity of the working liquid.

Besides the above two experiments, more works have been done on the stability analysis. Through the systematic analysis of published references, the stability analysis with the typical problem is complete. The completeness means the problem with arbitrary unipolar injection and temperature-dependent state equations (ionic mobility and permittivity). The detailed information can be found in a series of papers [15][16] [181-183].

For the same problem, we are interested in these aspects: stability analysis and heat transfer enhancement effect. Rather than traditional linear stability analysis, we carry out a direct numerical study of the problem. Though Yan, et al. provided a numerical modeling of EHD effect on natural convection in an enclosure in [184], the full coupled ETHD problem has not been performed in a satisfactory way. In [184], the author concerned more about purely mathematical calculation, rather than combining together with the physical meaning of the problem. Thus, the roles of electrical parameter, mobility parameter and charge strength in heat transfer enhancement did not show up.

On the contrary, Traoré et al. [57][185] developed a numerical tool with FVM, which has been successfully applied to solve the full coupled ETHD problem. The numerical procedure is based on the Augmented Lagrangian method [188]. In [185], the author used the numerical method to systematically analyze the stability parameter with a typical problem of a planar layer of dielectric liquid heating and injection both from below. Some other applications of their numerical approach can be found in [186][187].

In the present study, we developed another similar tool but on collocated grid systems. The SIMPLE algorithm is used for the pressure-velocity coupling instead of the Augmented Lagrangian algorithm. Some effects are made to improve the accuracy and reduce the computational costs. With the newly developed tool, we firstly investigated some other problems like various heating and injection modes. In addition, we try to introduce the time-dependent state equations (both ionic mobility and permittivity).

1.3 Present contributions

This study makes the following specific contributions to the fields of computational fluid dynamics and electrohydrodynamics:

1. A unified approach of the TVD-type high-resolution convective scheme coupled with various temporal schemes has been detailed and successfully applied to solve the charge density equation. Numerical performances of various TVD limiter functions were compared with steady and unsteady convection equations.
2. The extension of TVD schemes to unstructured meshes has been reviewed. We proved the equivalence of two widely used extension methods, named Jasak's type [69] and Darwish's type [89].
3. The relationship among three widely used diffusive flux discretization methods has been built. Some implementation details of the IDC scheme, like numerical boundary condition treatment and the selection of gradient evaluation methods, have been considered to improve the accuracy and robustness of the scheme. In addition, the IDC scheme has been successfully extended to three-dimensional problems

Based on the above improvement of the FVM approach, an efficient numerical tool has been developed for EHD and ETHD problems. With this tool, some interesting problems have been investigated numerically,

4. A systematical bifurcation study of a two-dimensional EHD nonlinear system has been done. The critical values of stability parameter with linear stability, non-linear stability has been obtained numeically. For both weak and strong injection cases, the numerical values we obtained are very close to the ones predicted by the stability analysis.
5. The optimal choices, like TVD schemes, time scheme, Poisson equation solving frequency and implementation on the non-uniform grid, has been discussed with the numerical solutions of strong unipolar injection case.
6. The role of the charge diffusion in finite-amplitude electro-convection is revisited, especially with strong injection case.
7. The effect of wall boundary conditions on both linear and nonlinear stability criterion has been discussed in details with 2D problems.
8. The continuous bifurcation and route to chaotic state with the two-dimensional strong injection problem has been defined.
9. Some preliminary numerical results have been obtained for three-dimensional unipolar injection between two parallel square electrodes.

10. A new numerical approach for electro-thermal-convection was proposed. The solver was used to analyze the linear and nonlinear stability characteristics of the 2D mode that both heating and injection are from the bottom electrode.
11. The heat transfer enhancement effect by charge injection has been demonstrated.

1.4 Thesis outline

In Chapter 2, the EHD theory background is firstly explained. Then the physical model and governing equations of continuum mechanics (Electrostatic, Navier-Stokes and Energy equations) are summarized.

Chapter 3 presents a second-order discretisation approach of the Finite Volume Method. Discretisation of a general scalar transport equation is examined. The temporal, convective and diffusisve schemes are discussed separately.

In Chapter 4, a numerical tool for EHD problems is assessed and validated by applying it to some simple problems for which either analytical or well-known empirical solution exist.

In Chapter 5, the problem of finite-amplitude electro-convection in dielectric liquids induced by unipolar injection is studied in details. Both weak and strong injections are considered.

In Chapter 6, some numerical aspects which help improving the performance of our numerical solvers in electro-convection simulation are discussed in details.

In Chapter 7, the flow structures of electro-convection due to strong charge injection are described in details. The route to chaotic state is defined numerically. In addition, the effects of vertical walls and diffusion mechanism for charge density transport on the hysteresis loop and flow structure are also discussed.

In Chapter 8, the problem of electrohydrodynamic stability in the presence of a thermal gradient and heat transfer enhancement is analyzed with the numerical simulation approach.

Finally, conclusions and suggestions for future development are given in the last chapter.

Chapter 2 Governing equations in Electro-Hydrodynamics and Electro-Thermo-Hydrodynamics flow

2.1 Electrohydrodynamics (EHD) theory background

This thesis mostly discussed about electro-convection and electro-thermal-convection between two parallel plates immersed in a single-phase dielectric liquid subjected to unipolar injection and a thermal gradient. Two typical problems will be:

1. An isothermal thin dielectric liquid layer subjected to an electric liquid and unipolar injection;
2. A planar layer of non-isothermal dielectric liquid subjected to both an injection of ions and temperature difference;

In simple terms, when a strong DC electric field is applied, charge injection occurs and the electric body force sets the liquid into motion. Meanwhile, the charge density distribution and electric field are modified by the velocity field via the conservation equation of charge density. If a thermal gradient is simultaneously applied, a more complex interaction among velocity field, charge density distribution, electric potential and temperature fields can be expected. Before presenting the complete physical models and their governing equations, some theoretical background will be introduced in this section firstly.

According to the theory of Landau [11], the electric body force per unit volume can be expressed as,

$$\vec{f}_e = q\vec{E} - \frac{1}{2}\left(\vec{E}\cdot\vec{E}\right)\nabla\varepsilon + \frac{1}{2}\rho\nabla\left[\left(\frac{\partial\varepsilon}{\partial\rho}\right)_\theta \vec{E}\cdot\vec{E}\right] \qquad (2\text{-}1)$$

where $\vec{E}$ is the electric strength, q is the free (or space) charge density, ε is the permittivity, ρ is the mass density and θ is the temperature.

The first term on the right hand side of (2-1) represents the Coulomb force exerted by an electric field upon the free charge within the bulk liquid. The second and third terms represent dielectrophoretic (or dielectric) and electrostrictive forces that depend on the nature and spatial distribution of $\vec{E}$ and ε. Generally speaking, the Coulomb force is the strongest term and usually dominates when DC electric fields are applied. The dielectric force is usually weaker than the Coulomb force and only dominates when the action of AC electric fields with a period much shorter than the charge relaxation time and/or the ionic transient time, is imposed [10, p.126]. The electrostrictive force is a conservative vector. Thus this term can be included into the pressure term. To estimate its value, the partial derivative, $\left(\partial\varepsilon/\partial\rho\right)_\theta$, can be expressed with the Clausius- Mosotti relationship, i.e.

$$\rho\left(\partial\varepsilon/\partial\rho\right)_\theta = (\varepsilon-\varepsilon_0)(\varepsilon+2\varepsilon_0)/2\varepsilon_0$$

In EHD field, one key problem is the understanding of the passage of electric current. Numerous studies determined the main features of the mechanisms of conduction, which are fairly better understood. A simple schematic drawing of the experiment to obtain the voltage-ampere characteristic (VAC) of dielectric liquids (DL) is plotted in Figure 2-1 (a). Though the final current-voltage curve depends on various factors, like the nature of the electrodes, the number of runs or the growth rate of the voltage [189], it generally exhibits three distinct parts (see Figure 2-1b) [1, page 105-107][189-191]:

(i) At low fields ($E = V/d < 1kV/cm$), the current appears to be a linear function of the applied voltage *V*, and obey Ohm's law. This quasi-ohmic behavior corresponds to the electrolytic conduction.

(ii) Increasing the voltage to the range $40-100kV/cm$ (moderate field), the current tends to rise usually proportionally to V^2. This range is named as the sub-ohmic part and corresponds to the tendency towards current saturation.

(iii) At high fields there is a strong increase in the current ($I \propto V^{\alpha}, \alpha > 1$). The current increases sharply for comparatively small increments of the field. This final region corresponds to the dominance of the injection process.

Finally, the liquids will break down at a sufficiently high magnitude of electric strength.

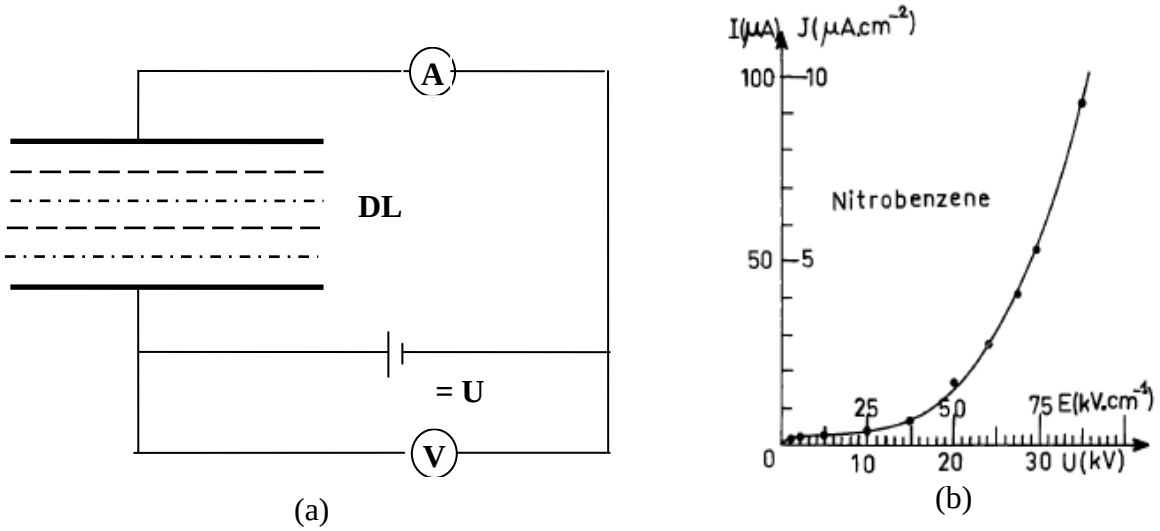

(a) (b)

Figure 2- 1 (a) A schematic drawing of experimental circuit to determine the Volt-ampere characteristics (VAC) of dielectric liquids (b) the VAC for Nitrobenzene [192]

In the next paragraphs, we make a brief introduction of the creation mechanisms of free charges in dielectric liquids. There are mainly three possible origins of net space charge: the conductivity model [193], dissociation of impurities in the bulk and ion injection. The ion injection is also named 'mobility models' of charge transport in some literature. Both dissociation and injection can be enhanced by the external electric fields, giving rise to the typical nonlinear current-voltage characteristics, common to most of the insulating liquids.

The conductivity model

The conductivity model states that a temperature gradient will give rise to a conductivity gradient and the charge density q_{cm} can be expressed with [168],

$$q_{cm} = -\frac{\varepsilon}{\sigma}\vec{E}\cdot\nabla\sigma \qquad (2\text{-}2)$$

where σ is the electrical conductivity of the liquid. Apparently, the model can only work for non-isothermal fluids, which means it fails to show the instability mechanism in the limit of small temperature gradient. In addition, this type of space charge production is more relevant to ohmic or quasi-ohmic liquids [172]. For dielectric liquids with low conductivity, other sources of free charge are more important than this. In the present study, it is wise to neglect this mechanism.

Dissociation of impurities

Dissociation of impurities in liquids is normally governed by complicated physical and chemical processes. In real world, perfectly pure dielectric liquids do not exist, the impurities or the liquid itself contribute to their conductivity. Two typical dissociation processes with ionophore and ionogen electrolytes are explained below.

Ionophore electrolytes are mostly ionic salts. Within the solvent, the ion-dipole interactions will break the ionic lattice, and free ions (positive and negative in pairs) are generated. It should be noted that not all ionophore molecules will break up [26],

$$(A^+B^-) \underset{k_R}{\overset{k_D}{\rightleftharpoons}} A^+ + B^-$$

where (A^+B^-) represents a ionic-pair and A^+ and B^- represent the free ions. According to the Onsager theory [194], the dissociation constant may be expressed as

$$k_D = k_D^0 F(E)$$

where k_D^0 is the dissociation constant of the thermodynamic equilibrium ionic pair/free ions, and $F(E)$ is a well-known tabulated function of the electric field [194]. In contrast, the recombination constant k_R is independent of the electric field strength in a wide range, and it can be computed with the theoretical Langevin expression,

$$k_R = 2e_0\mu/\varepsilon$$

under the assumption that the anions and cations have the same mobility μ (for liquids, this assumption is generally well respected). In above equation, ε and e_0 denote the permittivity of the liquid and the absolute electronic charge separately.

The direct dissociation process cannot be applied to ionogen electrolytes, which are formed by covalent bonds. Generally, the production of free ions with ionogen electrolytes contains two steps. The first step is the chemical reaction between the impurity molecules and /or another impurity species or solvent, which produce some ionic pairs. Then, the reaction products dissociate into free ions, just like ionophore electrolytes. Though the physicochemical process with dissociation is clear, the essential difficulty is the evaluation methods for reaction rate coefficients, like the dissociation and recombination coefficients and kinetic rate constants. In general, all the impurities

in polar liquids will be dissociated into free ions, while there is a dynamic equilibrium between free ions and ionic pairs. Some assumptions were made and different models were proposed, like Debye model for the combination constant [195], Fuoss formula for the ionic association constant [196], the Thomson model [197] and so on. Qualitatively, the rate of generation of free ions is modified by the presence of an external electric field, and an exact evaluation of the effect has been provided by Onsager [194]. In addition, the recombination constant is almost unaffected by the external electric field. In present study, the ions produced by dissociation will not be considered temporary for its small amount comparing with ion injection mechanism.

Polar and Non-Polar liquids

Before the explanation of ion injection process in dielectric liquids, we need to distinguish polar and nonpolar liquids. To strictly distinguish between them, one needs to compare the size of the ions with Bjerrum distance. From molecular structure point of view, the structure of polar liquid is asymmetrical in space while the structure of non-polar liquid is symmetrical. The difference in the molecular structure leads to the difference in electronegavity. The ability to attract electrons of polar liquids is stronger than non-polar liquids because of their higher electronegavity. In the experiments, the unipolar and strong injection can be obtained by covering the electrodes with electrodialytic membranes which then behave as injector of ions [198]. In nonpolar liquids, weak and moderate injection can also be obtained by adding some specific salt to the liquid [24].

Charge injection

When dielectric fluids contact with metal, another ion generation mechanism may become dominant. The ion injection process can be divided into two processes: ions with same polarity as the electrode are created and then entering into fluid. There are various physical mechanisms that can be used for ion injection. First of all, the injection mechanism in liquids and in vacuum or air are different. The well-known Schotky injection and field emission don’t apply for dielectric liquids. In the present study, we focus on the injection through electrochemical reactions in dielectric liquids. A brief introduction of this type of injection in both nonpolar and polar liquids will be made below and the emphasis is on the possible effects of electric fields.

At the interface between a solid (like metal) and a liquid, a physio chemical process takes place and an electrical double layer is created. Different models were proposed to describe the electrical double layer (EDL), like Helmotz model [199], Gouy and Chapman model [200][201], Stern model [202] and so on. Some more recent theoretical developments of EDL are reviewed by J. Lyklema [203]. Here, we use the Stern model to qualitatively describe the injection process in nonpolar and polar liquids.

The neutral molecules, ions and ionic pairs attach to the metal surface because of the chemical and/or electrostatic image forces. Then electrons are transferred between the metal and the attached microscopic particles, giving rise to an EDL.

There is a first layer of absorbed solvent molecules and to a less extend also molecules, ions and ionic pairs originated from the dissolved impurities. The second layer is formed with solvated ions of polarity opposed to the electrode. Both layers define the double charged sublayer with a

width, l_H, of the order of the solvated ionic radius. Another region is defined by the distance $l_B/4$, where l_B is the Bjerrum distance. In this region, the ions are subjected to their image force. When the electric field is applied, a potential barrier is formed.

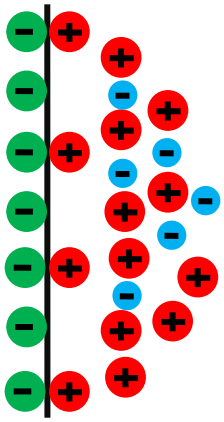

Figure 2-2 Stern double layer model on electrode, the figure is reproduced following [7]

For polar liquids, the Bjerrum distance, l_B, is equal or lesser than the width of DBL, l_H, and therefore the ions, once produced, are immediately injected into the liquid. For nonpolar liquids, the ions have to overcome the potential barrier created by the image fore and the external electric field before injecting into the bulk of fluid. In the following, the creation of charge carriers in polar and nonpolar liquids is present in a succinct way and highlights the function of external electric field. We assume that an electron transfer from a molecule of the fluid to the metal electrode.

Injection in polar liquids [191] [1, page 29-30]

In [191], N. J. Felici modeled the ions injection in polar liquids with the following reaction,

$$\mathbf{M + A} \underset{\alpha_{rd}}{\overset{\alpha_{ox}}{\rightleftharpoons}} \mathbf{M(e)^-} + \mathbf{A^+}$$

where M and A represent the metal and the electron donor molecule separately, and α_{ox} and α_{rd} are the oxidation and reduction constants. If there is no external field, a dynamical equilibrium state can be reached. The presence of an external field will bring different effects to the oxidation and reduction processes, which can be precisely described in terms of oxidation and reaction constants [1, page 29],

$$\alpha_{ox} = \alpha_{ox}^{o} \exp\left[\frac{eEl_H}{k_B T}\right], \qquad \alpha_{rd} = \alpha_{rd}^{o} \exp\left[-\frac{eEl_H}{k_B T}\right] \tag{2-3}$$

where α_{ox}^{o} and α_{rd}^{o} are the oxidation and reaction constants at thermodynamic equilibrium, k_B is the Boltzmann constant and T is the temperature. It is easy to find from Eqns. (2-3) that the ion generation process is enhanced with the external electric field. All the extra ions are injected into

the bulk of the liquid. Using $n^i_{A^+}$ to represent the number density of the extra ions, we obtain the following equation from charge conservation law.

$$en^i_{A^+}\mu_+ E = e\alpha_{ox}n_A - e\alpha_{rd}n_{A^+} \tag{2-4}$$

where n_A and n_{A^+} are the species concentration per unit area of neutral molecules and positive ions separately, and μ_+ is the mobility of positive ions. Assuming that n_A is constant with the value of n^0_A during the reaction, the concentration of the number density of the total positive ions and injection ions can be simply expressed as $n_{A^+} = Cn^0_A$ and $n^i_{A^+} = Cn^0_A$. By the definition formula of the injected charged density, $q_i = en^i_{A^+}/l_H$, and the injected current density, $J_i = q_i\mu_+ E$, we obtain [1],

$$\frac{J_i}{J_S} = \frac{\exp(\vartheta E/E_S)}{E/E_S + \exp(-\vartheta E/E_S)}\frac{E}{E_S} \tag{2-5}$$

with $E_S = \alpha^o_{rd}l_H/\mu_+$ and $\vartheta = el_H E_S/k_B T$.

Two limiting cases can be used to simply Eqn.(2-5).

Case I: $\vartheta E/E_S << 1$

$$\frac{J_i}{J_S} \approx \frac{\vartheta E/E_S}{1+E/E_S} \quad , \quad q_i \approx \frac{J_S/E_S}{\mu_+(1+E/E_S)} \tag{2-6}$$

Only with $E << E_S$, the widely used 'autonomous injection' hypothesis can be guaranteed. The hypothesis means that the injected charge density is constant and independent of electric field. However, in practical situations, the requirement might appear harder to satisfy.

Case II: $\vartheta E/E_S >> 1$

$$\frac{J_i}{J_S} \approx \exp(\vartheta E/E_S), \qquad q_i = \frac{J_i}{\mu_+ E} \approx \frac{J_S\exp(\vartheta E/E_S)}{\mu_+ E_S} \tag{2-7}$$

Both the current and the injected charge density increase exponentially with external electric field.

Injection in nonpolar liquids [33][1, page 30-32]

In nonpolar liquids, the ion injection process may be separated into two steps. In the first step, the ions are created at the electrodes. Then, the ions escape into the bulk of fluid after overcoming the potential barrier. The complete reaction may be described as,

$$\alpha_{ox}$$

$$\mathbf{M + (A^+B^-)} \underset{\alpha_{rd}}{\overset{}{\rightleftharpoons}} \mathbf{M(e)} + \mathbf{A^+B} \xrightarrow{\alpha_{\text{ext}}} \mathbf{A^+_{free}}$$

The first part of the above chemical equation is similar to injection in polar liquids. In the latter part, α_{ext} is the extraction constant of the ion from the image force. The first equation can be obtained based on the assumption that the density of ionic pairs is constant [1],

$$\frac{dn_+^{free}}{dt} = \alpha_{ext} \frac{\alpha_{ox}}{\alpha_{rd} + \alpha_{ox}} n \tag{2-8}$$

The final object of the analysis of injection process is to determine the injected charge current and density. The injected current density is:

$$J_i = e\alpha_{ext} n_+ = \alpha_{ext} \frac{\alpha_{ox}}{\alpha_{rd} + \alpha_{ext}} en \tag{2-9}$$

where n and n_+ are the surface density of ionic pairs and ions formed by electron transfer at the electrode. Firstly, oxidation and reaction constants, i.e., α_{ox} and α_{rd}, can be expressed in a similar equations as in Eqn. (2-3). Then, the rest task to decide the rate of extraction of ions, α_{ext}, though , will be not easy. An accurate and complete expression requires the understanding the transport mechanisms participating at the interface: ionic migration and diffusion. A detailed analysis can be found in [33] and a simple version in [1, page 31]. Here, we directly give the final expression,

$$\alpha_{ext} = \frac{\mu_+ E}{l_H} \frac{\exp\left(e\phi(l_H)/k_B T\right)}{bK_1(b)} \tag{2-10}$$

where $b = l_B / l_O$, $l_O = \sqrt{e/16\pi\varepsilon E}$, and K_1 is the modified Bessel function of the second kind and order one. Function $\phi(x)$ denotes the potential barrier. It should be noted that the diffusion coefficient, which account for the diffusion transport mechanisms, is expressed with the ionic mobility by the aid of Einstein's relation. Two situations can be distinguished by the comparison of chemical reaction rate of the two steps.

Case I: The second step of extraction process is much faster than the first step of the oxidation-reduction reaction. The exponential law of injection for the polar liquid, i.e., Eqn. (2-7) is recovered.

Case II: However, the reverse situation that the extraction speed is slower than the ion generation is more common in real world. Then, the current density equation Eqn.(2-9) may be simplified to,

$$J_i = \alpha_{ext} \frac{\alpha_{ox}}{\alpha_{rd}} en \tag{2-11}$$

Taking Eqn.(2-10) and formula of α_{ox} and α_{rd} into Eqn.(2-9), the final expression for the injected current can be obtained [1, page 32].

$$q_i = \frac{J_i}{\mu_+ E} = \frac{en}{l_H}\frac{\alpha_{ox}^o}{\alpha_{rd}^o}\frac{\exp(-e^2/16\pi d_H k_B T)}{bK_1(b)} = \frac{q_i^0}{bK_1(b)} \qquad (2\text{-}12)$$

with q_i^0 a constant that depends on the liquid and electrolyte nature. The electric field only appears in b parameter and it is found that the 'autonomous injection' hypothesis works well for values of $10^5 \le E \le 4\times10^6 V/m$ [1][153].

Once the free ions were generated and injected into the bulk of fluids, the electric field will exert a force on these free charges. Then, the force is transmitted on the neutral molecules by collisions. Typically, the liquid will be set in motion. The distribution of charges will follow constantly changing and the electric field will be modified. Further, the amount of ions injected into the fluids may change if conditions for autonomous injection are not satisfied. The complete coupling makes the EHD problem difficult to understand and solve.

2.2Electro-Thermo-Hydrodynamics (ETHD) theory background

In recent years, the complex interactions that occur when an electric field and a thermal gradient are simultaneously applied across a dielectric liquid containing space charge have received much attention. Two apparent research motivations of electro-thermo-hydrodynamics are:

1. Scientific point: the underlying nature of the instability and the rich subsequent nonlinear development or bifurcation of electro-thermal convection;
2. Engineering and industrial point: The promising way to increase or control the heat transfer by means of electric forces;

In general, the thermal field dramatically increases the complexity of the EHD system. This complexity shows itself through the following factors:

Firstly, the possibilities of free charge carrier generation due to the conductivity model.

Secondly, the buoyancy driving force in the momentum equations. The buoyancy force is induced by the variation of the fluid density with temperature. The classical Boussinesq approximation will be used in the present study to simplify the effect of non-constant fluid density. Boussinesq approximation states that the density differences are sufficiently small to be neglected, except where they appear in the terms multiplied by the acceleration due to gravity.

Thirdly, various temperature-dependent properties. Strictly speaking, besides density, kinematic viscosity, thermal diffusivity, electrical permittivity and ionic mobility may also vary with the temperature field. However, in the present study, it is assumed that the kinematic viscosity and thermal diffusivity remain constant. We neglect such variations to highlight the effects of buoyancy force, temperature dependence of mobility and permittivity.

Since the electrical permittivity gradient would be induced by the imposed temperature gradient, the dielectric force should also be taken into account. However, under DC condition with space charge generation in the liquid, the force never becomes dominant when comparing with the Coulomb force.

In addition, the Joule heating and other dissipation effects in energy equation provide other couple modes between EHD and ETHD systems.

The equation of the temperature in EHD has been obtained by A. Castellanos with the classical procedure of thermodynamics of irreversible process [1, chapter 5][204]. In addition, the Boussinesq approximation is also introduced into EHD to simplify the temperature equation. In the present study, we will use the simplified temperature equation. For more details of derivation, please refer to [1, chapter 5][204].

2.3 Physical model and governing equations

Consider an incompressible and perfectly insulating liquid of density ρ, permittivity ε, constant kinematic viscosity ν and constant thermal diffusivity κ, enclosed between two parallel planar electrodes at a distance d from one to the other. For EHD problems, only an electric potential is applied between the electrodes so that injection of charge can occur. Though double injection is possible and can be well controlled in some liquids [205], the case of unipolar injection is the main concern in the present study. After applying an external electric field, electric charges are injected into the system from the electrode of higher potential.

For ETHD problem, the two horizontal metallic electrodes are assumed to be rigid perfectly heat conducting plates and maintained at fixed different temperatures θ_0 and θ_1 respectively.

As for vertical sidewalls, both symmetric boundary condition and rigid wall boundary conditions will be applied to velocity variables according to the physical problems of interest. Symmetric boundary stands for infinite domain, while no-slip wall boundary indicates the problems are in enclosures. In addition, the polarities of electrodes and the relative magnitude of θ_0 and θ_1 are not fixed, which allows the four possible situations for stability analysis in 2D and other six configurations for heat transfer enhancement evaluation, see Figure 2-3.

2.3.1 Basic assumptions

Before the introduction of the physical model, some basic assumptions need to be made. The following should be satisfied with all problems under consideration in this dissertation.

1. Incompressible Newtonian liquid;
2. DC electric field and unipolar injection;
3. One kind of ion in the fluid;
4. Negligible magnetic effects;
5. Negligible electrical double layer;

Unipolar injection means ion injection occurs at one electrode only. It should be pointed out that unipolar injection is more classical than double injection (ambipolar). This was verified by electro-optic measurement. Certainly, numerical simulation of double injection is a bit more complicated than unipolar injection, as the recombination process must be taken into account [206], a similar situation with injection under AC fields [207][208] .

Some extra assumptions are needed for individual problems. For pure EHD problems,

1. Isothermal fluids;
2. The electrical conductivity σ, the permittivity ε and ion mobility k are constant;

For ETHD problems,

3. The Boussinesq approximation;
4. The permittivity ε and ion mobility k are constant or vary linearly with temperature;
5. Viscous dissipation and Joule heating is neglected;

Typical 2D and 3D problems with some well-defined boundary conditions are plotted in Figure 2-3, 2-4 and 2-5.

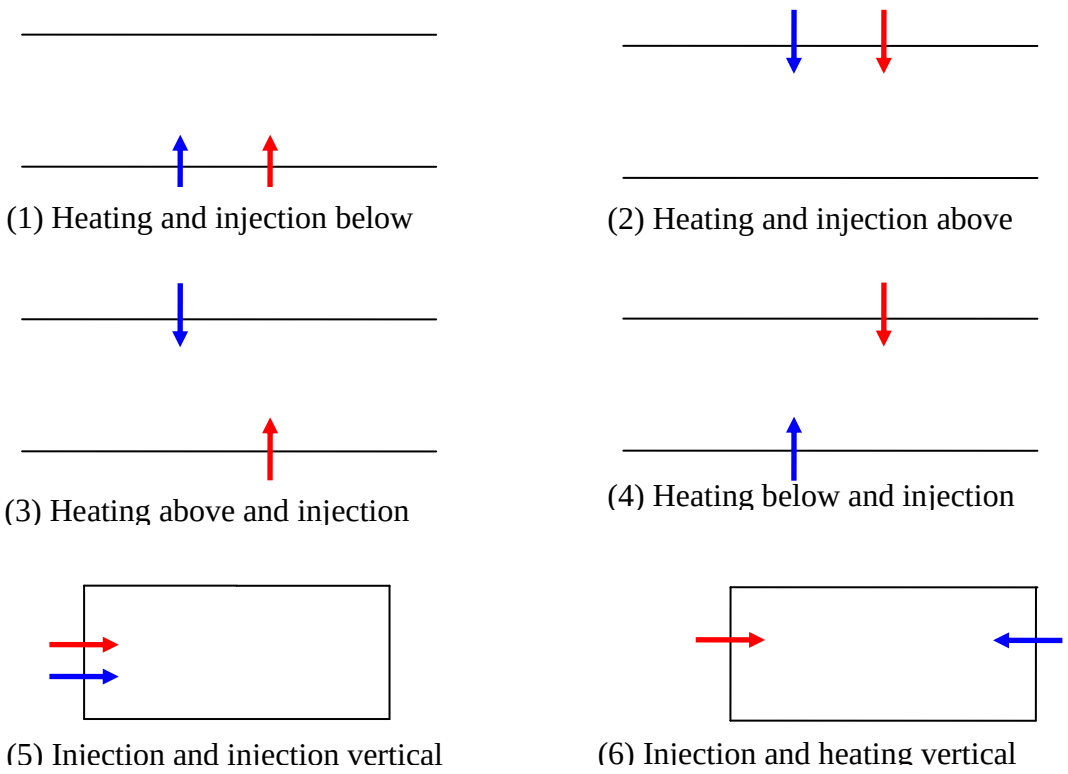

Figure 2-3. Different heating and injection modes (blue arrows - heat; red arrows – injection)

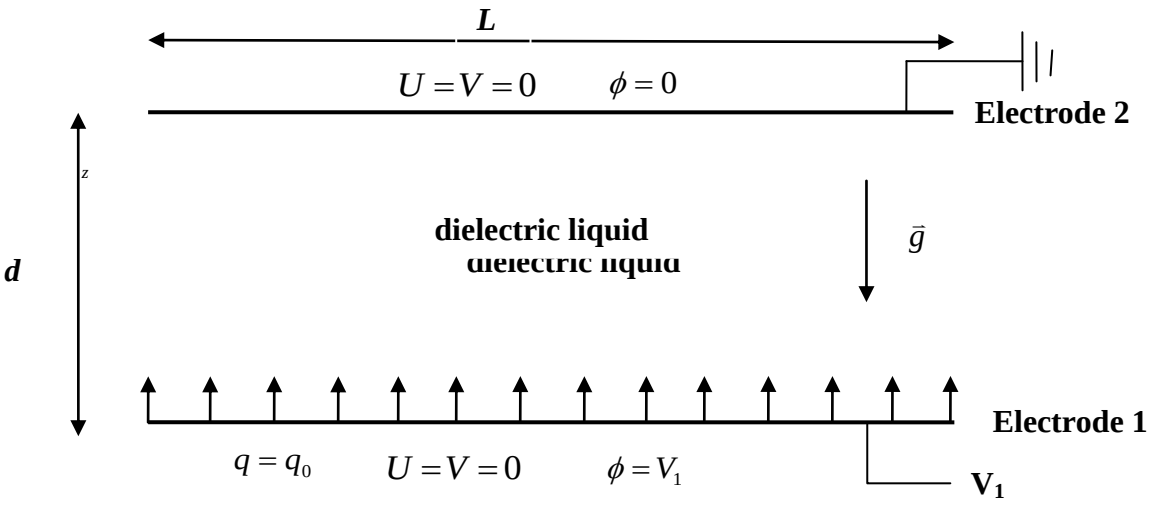

Figure 2-4. The dielectric liquid layer and parallel plane electrodes configuration in 2D

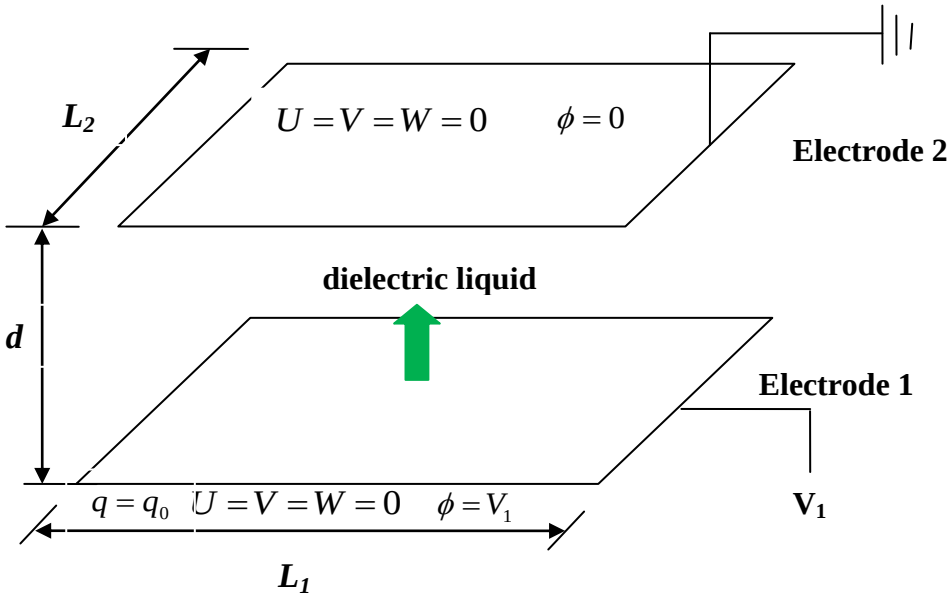

Figure 2-5. The dielectric liquid layer and parallel plane electrodes configuration in 3D

2.3.2 Governing equations

Electrical Equations

For dielectric liquids of low conductivity, Maxwell equations reduce to the electroquasistatic limit ($\vec{E} > c\vec{B}$, where c is the velocity of light and $\vec{B}$ represents the magnetic fields), thus falling in the realm of EHD [1, page 5-8]. In other words, the electrical equations in EHD are,

$$\nabla \cdot \vec{\vartheta} = q \qquad \nabla \times \vec{E} = 0 \qquad \frac{\partial q}{\partial t} + \nabla \cdot \vec{J} = 0$$

where $\vec{\vartheta}$ is the displacement vector, $\vec{\vartheta} = \varepsilon \vec{E}$ and $\vec{J}$ is the current density;

For unipolar injection with only one species injected into a perfectly insulating liquid, $\sigma = 0$, the constitutive law for the current density is :

$$\vec{J} = qK\vec{E} - D\nabla q + q\vec{U}$$

The first term gives the contribution due to the drift of ions that move relatively to the liquid with a velocity $K\vec{E}$, with K the ionic mobility. The second term accounts for molecular diffusion, with D the charge diffusion coefficient. The Einstein's relation $D/K = k\Theta/e$ (k the Boltzmann constant and e the elementary charge) can be used to estimate the order of D. The third term of above equation is due to convection of charge density by the liquid velocity field $\vec{U}$.

To conclude, the complete electrical equations for unipolar injection can be summarized as,

$$\nabla \cdot (\varepsilon \mathbf{E}) = q \tag{2-13}$$

$$\mathbf{E} = -\nabla \phi \tag{2-14}$$

$$\frac{\partial q}{\partial t} + \nabla \cdot \left(qK\vec{E} - D\nabla q + q\vec{U}\right) = 0 \tag{2-15}$$

where ϕ stands for the electric potential.

Mechanical Equations

Following the assumption of incompressible Newtonian liquid, the mechanical equations (the conservation of mass and momentum) are,

$$\nabla \cdot \vec{U} = 0 \tag{2-16}$$

$$\rho_0 \left(\frac{\partial \vec{U}}{\partial t} + \vec{U} \cdot \nabla \vec{U} \right) = -\nabla p + \mu \nabla^2 \vec{U} + \vec{f}_b + \vec{f}_e \tag{2-17}$$

where μ denotes the dynamic viscosity. $\vec{f}_b$ and $\vec{f}_e$ are the possible buoyancy and electrical forces. The complete expression for $\vec{f}_e$ is given by Eqn.(2-1). However, we consider the Coulomb force and dielectric force in the present study and put the electrostrictive force into the pressure term,

$$\vec{f}_e = q\vec{E} + \frac{1}{2}\left(\vec{E}\cdot\vec{E}\right)\nabla\varepsilon \tag{2-18}$$

As for buoyancy force, the final expression can be obtained by applying the Boussinesq approximation,

$$\vec{f}_b = \left(\rho - \rho_0\right)\vec{g}_i = \rho_0\vec{g}_i\beta(\theta - \theta_0) \tag{2-19}$$

where g_i is the component of the gravity acceleration vector in x_i-direction, β is the coefficient of thermal expansion and θ_0 is the reference temperature at which ρ_0 and other physical properties.

Energy Equation

In [1, page 62-82][204], A. Castellanos firstly derived the entropy equation for dielectric fluids in movement from the first principle. Then, the temperature is derived from the entropy equation with the entropy definition equation. However the energy equation he provided contains too many variables and some further simplifications are needed for the practical situations we are concerned about.

1. For frequencies below the microwave region, the molecular polarization is in equilibrium with the field, and dielectric heating is not present [1, page 81].
2. Small temperature difference. It should be pointed out that there are two functions of this assumption. First, it is used to neglect the reversible variations of temperature with the electric field [1, page 80]. Second, it helps making use of the Boussinesq approximation, which means that the contribution from viscous dissipation can also be neglected safely.

Under above two conditions and with the Boussinesq approximation, the temperature equation in EHD reduces to,

$$\frac{\partial\theta}{\partial t} + \vec{U}\cdot\nabla\theta = \kappa\nabla^2\theta \tag{2-20}$$

where κ denotes thermal diffusivity.

In principle, there are two extra terms on the right hand side of above equation,

The Joule heating term: $\vec{J}\cdot\vec{E}/c_p$

The viscous dissipation term: $\mu\vec{V}\cdot\nabla^2\vec{V}$

For most attempts to solve ETHD problem numerically, the effects of Joule heating and viscous dissipation can be neglected based on some order (dimensional) analysis with the fact the electric current is of μA or less with highly insulating liquids. The validity of neglecting both heat sources in space-charge-limited-current regime has been proved with an illustrative example in [209]. The authors estimated that the energy dissipation of a typical dielectric liquid (like silicone oil) due to Joule heating and viscous dissipation would increase the temperature at a rate $\sim 10^{-4} K/s$.

In addition, its neglect can be understood in another way. It is well-known that Joule heating for forced convection can be safely neglected. Remembering the experimental results of [22][172], heat transfer within ETHD system can be viewed as the similar case of forced flow. Thus, Joule heating should be small enough to justify its neglect.

The state equations

The first state equation is for fluid density,

$$\rho = \rho_0 \left[1 - \beta(\theta - \theta_0)\right] \tag{2-21}$$

Similar with density, it is possible that the ionic mobility and the electrical permittivity vary with temperature. Some models are needed to describe the specific relationship. In present study, a linear model is used. The same model has been widely used for stability analysis with ETHD systems [15][16][26][181-183],

$$\varepsilon = \varepsilon_0 \left[1 - e_1(\theta - \theta_0)\right] \tag{2-22}$$

$$K = K_0 \left[1 + k_1(\theta - \theta_0)\right] \tag{2-23}$$

In Eqns. (2-21) ~ (2-23), a subscript 0 denotes a reference value which for later convenience, will be taken as $y = 0$. The coefficients e_1 and k_1 denote the corresponding derivatives of ε and K with respect to temperature separately. If we want to freeze ε and K to be constant, we just have to set $e_1 = 0$ and $k_1 = 0$.

It should be pointed out that the above 'linear model' is just an approximation of an elaborate model. Taking the ionic mobility as the example, its temperature-dependent relationship is usually expressed by the Arrhenius-type equation [15],

$$K(T) = K_0 \exp\left[-W_k\left(\frac{1}{\theta} - \frac{1}{\theta_0}\right)\right] \tag{2-24}$$

where W_k is the ratio of an activation energy to the Boltzmann constant [210, chapter 1], so Eqn.(2-23) is equivalent to a Taylor expansion of Eqn.(2-24) to first order in $(\theta - \theta_0)$, which means that the 'linear model' can work well only with small thermal gradient ($\leq 1^o / mm$) [36]. Some quadratic and higher-order approximations are also available.

2.3.3 Boundary conditions

A coordinate system is chosen to express boundary conditions easily. With the parallel plane electrodes, we set (x, y)-plane to coincide with the electrode. For velocity, electrical potential and temperature, the physical and corresponding numerical boundary conditions can be easily defined.

Considering the rigidness of electrodes, the velocity boundary conditions at the electrodes are assumed to be non-slip. The electric potential is usually fixed at the electrodes, so that $\phi_{electrodes} = \phi_{given}$. For other vertical sides, symmetric, periodic and wall boundary conditions are possible. In addition, in some cases, inflow and outflow boundary conditions may be used. In the present study, all other sides (i.e., all physical boundaries except electrodes) are set as Neumann boundary condition for potential equation.

As for energy equations, only two types of boundary conditions will be considered: isothermal and adiabatic. Both of them can be easily transferred to corresponding mathematical expressions. It should be pointed out here the lack of constant heat flux boundary condition makes it impossible to completely reproduce the physical experiments of [22] [172] with our numerical tools. In the coming future, heat flux boundary condition treatment will be incorporated.

The boundary condition for the charge density is regarded as one of the most complicated problem of EHD-related problems considering the complex electro-chemical reactions on the electrode surfaces (both emitter and collecting electrodes) [208].

For the emitter electrode, the accurate value of charge density is not easy to determine. Theoretically, its value can be computed by extracting the injected current from the measured value. The detailed method is explained in [211], or a simple one in [171]. Another possible method is to use the definition of chemical kinetics, which makes it possible to express the charge density on the injection electrode in terms of the physical constants of the fluid [208]. However, in numerical studies, the injection strength is a control parameter, thus its value should be given in advance as boundary condition. The next question is whether the charge density on emitter electrode adjusts itself during the calculation process or not. Physically speaking, ion injection process may be affected by many factors. A complete analysis is beyond the scope of the present study. By the assumption of autonomous injection, we can avoid the problem. Autonomous injection means that the charge density at injectors remains constant during the whole simulation process, neither influenced by the electric field nor by the liquid motion. In [1, p. 29-32], unipolar injections in both polar and nonpolar liquids were analyzed in detail. The final conclusion is that the autonomous injection assumption is more likely to be satisfied with nonpolar liquids. However, the autonomous injection assumption has been widely used to reduce the complexity of problem. To get closer to the real physical problems, some non-autonomous injection laws should be incorporated into the numerical solvers. Taking the field-dependent law given by Felici and Gosse [212] (see also in [141]) for example, the non-autonomous injection can be expressed as,

$$q_0 = \frac{q_*}{2bK_1(2b)} \tag{2-25}$$

where K_1 is the modified Bessel function of second kind and order one. The constant q_* is linearly dependent with the residual conductivity δ of the liquid. The parameter b is the ratio of two physical distances,

$$b = l_B / l_E$$

$$l_B = e^2 / 4\pi\varepsilon k\theta \quad : \quad \text{the Bjerrum distance}$$

$$l_E = \left(e / 4\pi E(0)\right)^{1/2}$$

where k is the Boltzmann constant, θ is the absolute temperature and $E(0)$ is the electric field at the injector. For simplicity, the electrode conditions can also be formulated as [213],

$$q_0 = \eta E F_i(E) \tag{2-26}$$

where η is the injection coefficient. The form of the function F_i is determined by the emission properties of the electrodes and the specifics of the electrochemical reaction. When $F_i(E) \equiv 1$, the injection law becomes linear. The linear injection law has been used in several cases, to see [214] and [215].

For the collecting electrode, we assume that the injected charge carriers are instantaneously discharged once they arrive at the electrodes (a typical ejection law). This assumption is also named 'the completely open condition' in literature. The hypothesis indicates that we impose a boundary condition which is equivalent to the supersonic outflow boundary condition in aerodynamics [152]. Either the zero-slope method or the extrapolation method can be used to express the boundary condition.

The zero-slope method

$$\frac{\partial q}{\partial y} = 0 \quad \text{at} \quad y = d \tag{2-27}$$

The extrapolation method

$$\frac{\partial q}{\partial y} \quad \text{continuous at} \quad y = d \tag{2-28}$$

For simplicity, in present study we will adopt the zero-slope, i.e., Neumann condition, except where some special statements are made.

If we neglect the diffusion mechanism, the charge density equation becomes hyperbolic. Then we need not to specify any physical boundary condition at the collecting electrodes (and in fact cannot, since the charge density is entirely determined by the data given already) [72, page 19]. However, for numerical implementation method of high-resolution TVD schemes in present study, a mathematical boundary condition is necessary. To avoid or reduce the possibility of the noise that

generated at the outflow boundary propagate back into the inner domain, some numerical skill is needed to treat the mathematical boundary condition. A detailed analysis can be found in section 5.

2.3.4 Initial conditions

The complete system is an initial-boundary-value problem (IBVP). Thus, besides the boundary condition, the initial data is also necessary for final numerical solutions. Generally, three types of initial conditions are used in present study according to the purposes of simulation.

1. Zero field

All variables (like velocity, pressure, charge density, electric potential and temperature field) are set to be zero. This type of initial condition stands for the computation starting from the still state of the fluid or a sudden step pulse is applied.

2. Hydrostatic solutions

Quite a lot of hydrostatic or electro-thermal hydrostatic equilibrium solutions are available in literature, as these solutions are the starting point for linear instability analysis. Hydrostatic solutions means the velocity field keeps zero and other variables (like charge density, electric potential and temperature) are in a dynamic balance. For numerical simulation, these solutions can be used to shorten the computational time. In addition, it is important to damp out the fluctuations introduced by step pulse injection.

3. Previous simulation results

Quite a lot of computational cost may be saved if we start the computation from one steady state. In addition, this kind of restart and continuation computation is a key component for numerically determining the nonlinear stability criteria and hysteresis loop.

2.3.5 Non-dimensional form

For EHD and ETHD problems, it is difficult to foresee how electrical, mechanical and thermal effects will interact [10, page 99]. Another equally serious problem is the existence of several time scales. Thus, it is not easy to define the best non-dimensional scales. Some detailed analysis can be found in [1, page 54-60], [10, chapter 7], [216] and [217].

However, several non-dimensional forms have already been applied to a fair amount of numerical work. In present study, we follow the same expressions. Two non-dimensional forms will be used to keep consistent with some published literature for the comparison purpose.

EHD problem

Taking d, ϕ_0, $\varepsilon\phi_0 / d^2$ and $K\phi_0 / d$ as the scales for distance, potential, charge density and velocity respectively, the governing equation of EHD problem can be written as,

$$\nabla \cdot \vec{U}^* = 0 \qquad (2\text{-}29)$$

$$\frac{\partial \vec{U}^*}{\partial t} + \left(\vec{U}^* \cdot \nabla\right)\vec{U}^* = -\nabla\tilde{p} + \frac{M^2}{T}\Delta\vec{U}^* + M^2 q^* \vec{E}^* \tag{2-30}$$

$$\Delta\phi^* = -q^* \tag{2-31}$$

$$\frac{\partial q^*}{\partial t} + \nabla \cdot \left(q\left(\vec{E}^* + \vec{U}^*\right)\right) = \alpha\nabla^2 q^* \tag{2-32}$$

where $\tilde{p}$ includes the non-dimensional pressure and electrostrictive force term. The name, expression and physical meanings of the non-dimensional parameters newly appearing above can be found in Table 2-1.

Another non-dimensional expression will also be used in present study for extremely strong injection to approximate the 'space charge limited (SCL) injection' $C \to \infty$. With this new style, the scale for charge density is q_0, the charge density at the injection electrode. Some modification should be done with Navier-Stokes equations and potential equation,

$$\frac{\partial \vec{U}^*}{\partial t} + \left(\vec{U}^* \cdot \nabla\right)\vec{U}^* = -\nabla\tilde{p} + \frac{1}{R}\Delta\vec{U}^* + CM^2 q^* \vec{E}^* \tag{2-30-2}$$

$$\Delta\phi^* = -Cq^* \tag{2-31-2}$$

ETHD Problem

If now length, time, liquid velocity, charge density, electric potential, electric field temperature, pressure field, mass density, permittivity and ionic mobility are made dimensionless by making the following transformations:

$$U_i^* = \frac{U_i}{\nu/d},\ \phi^* = \frac{\phi - \phi_1}{\phi_0 - \phi_1},\ E_i^* = \frac{E_i}{(\phi_0 - \phi_1)/d},\ x_i^* = \frac{x_i}{d},\ t_0 = \frac{d^2}{\nu},\ \theta^* = \frac{\theta - \theta_1}{\theta_0 - \theta_1}$$

$$\rho^* = \frac{\rho}{\rho_0},\quad \varepsilon^* = \frac{\varepsilon}{\varepsilon_0},\ K^* = \frac{K}{K_0}$$

the resulting governing equations of this thermo-electrohydrodynamic system are:

$$\nabla \cdot \vec{U}^* = 0 \tag{2-33}$$

$$\frac{\partial \vec{U}^*}{\partial t} + \left(\vec{U}^* \cdot \nabla\right)\vec{U}^* = -\nabla\tilde{p} + \Delta\vec{U}^* + RTCq^*\vec{E}^* - RT\frac{E^{*2}}{2}\nabla\varepsilon^* + \frac{Ra}{\mathrm{Pr}}\theta^* \cdot \vec{e}_z \tag{2-34}$$

$$\Delta\phi^* = -Cq^* \tag{2-35}$$

$$\frac{\partial q^*}{\partial t} + \nabla \cdot \left(q^*\left(RK\vec{E} + \vec{U}^*\right)\right) = 0 \tag{2-36}$$

$$\frac{\partial \theta^*}{\partial t} + \left(\vec{U}^* \cdot \nabla\right)\theta^* = \frac{1}{\mathrm{Pr}}\nabla^2\theta* \tag{2-37}$$

and the update equations for fluid properties,

$$\varepsilon = 1 - L\,R\theta \tag{2-38}$$

$$K = 1 + NRa\,\theta \tag{2-39}$$

The difference between above two non-dimensional expressions is the unit scale of new scales of charge density and liquid velocity. An interesting point is that the above non-dimensional form implicitly uses the viscous time as the time scale, which is recommended by P. A. Vaequez in [67] after a systematic comparison of the viscous time, the drift time and the Coulomb repulsion time.

Note: 1. the above expression can be also used for pure EHD problem by setting Ra = 0;

2. The diffusion term has been neglected temporarily;

3. $L = e_1 \beta d / Ra$ and $N = k_1 \beta d / Ra$

Along with the non-dimensional forms, boundary conditions also need to be nondimensionalized. Special attention should be paid to the non-dimensional charge density at the injection electrodes with the two different non-dimensional styles.

Table 2-1. Some important non-dimensional numbers and their physical meanings

Name	Nomenclature	Expressions	Meaning
Electric Grashf parameter	T	$\frac{\varepsilon\phi_0}{\eta K}$	The ratio of the destabilizing Coulomb force to the stabilizing viscous force
Injection strength	C	$\frac{q_0 d^2}{\varepsilon\phi_0}$	A measure of the injection strength
Mobility parameter	M	$\frac{1}{K}\left(\frac{\varepsilon}{\rho}\right)^{1/2}$	The ratio of hydrodynamic mobility, $(\varepsilon/\rho)^{1/2}$ and the ionic mobility
Electrical Reynolds number	R	$\frac{T}{M^2}$	The ratio of the ionic drift timescale to the viscosity timescale
Rayleigh number	Ra	$\frac{g\beta\Delta\theta d^3}{\nu k}$	The ratio of the destabilizing buoyancy force to the stabilizing viscous force
Prandtl number	Pr	$\frac{\nu}{k}$	The ratio of momentum diffusivity to thermal diffusivity
Diffusion number	α	$\frac{D}{K\phi_0}$	The parameter represent the charge-diffusion effects
The nondimensional temperature derivate of dielectric constant	L	$\frac{e_1\nu\kappa}{\beta g d^3}$	The non-dimensionalised first derivative with repsect to temperature of dielectric constant
The nondimensional temperature derivate of mobility	N	$\frac{k_1\nu\kappa}{\beta g d^3}$	The non-dimensionalised first derivative with repsect to temperature of mobility

Some other non-dimensional parameters can also be defined, for example an electrical Grashof number (the Coulombic body force to the viscous body force) and an electric Prandtl number appear in [1, page 83-162].

2.4 Physical range of non-dimensional parameters

Through the above non-dimensional analysis, a large number of inherent parameters appear. On the one hand, various controlling parameters indicate the diversity of the fluid structures. On the other hand, these variables and their possible ranges bring a certain difficulty for systematical analysis. Considering our concerns are limited to dielectric liquids and under the action of unipolar injection, some physical ranges could be obtained for above non-dimensional parameters.

The stability number T and Rayleigh number Ra are the two control parameters which are proportional to the potential and temperature difference separately, thus they could vary in a wide range. Some attention should be made to the Rayleigh number. We need to distinguish the stabilizing and destabilizing effects of buoyancy force when heating is from the above or the below side.

C parameter represents the strength of charge injection. For weak injection, the electric field within the fluid is mainly determined by the applied electric potential difference. On the contrary, for strong injection, the electric field within the fluid would be seriously affected by the space-charge distribution [216, page 21]. Following Tobazéron's classification [218], three injection regimes of C are possible, see below

- Strong injection: $5 < C < \infty$
- Medium injection: $0.2 < C < 5$
- Weak injection: $0 < C < 0.2$

The typical values for the non-dimensional diffusion number α range between 10^{-3} and 10^{-4}[152]. This range can be determined through the Einstein relation for liquids [9], which relate the ionic diffusion to mobility of the fluid.

In [150], Atten et al., highlighted the difference between liquid and gas systems using M parameter. Typical values for gases usually obey $M << 1$ and for liquid $M > 3$. The parameter implicates the closeness between the electric module and velocity module. For gas system, low M value indicates that the electric module can be solved independently without information from velocity field. Some values of M for different dielectric liquids are given by [152] and listed in Table 2-2.

As for Prandlt number, there is also a wide range. For example, in [219], the three working dielectric liquids (Polyalphaolefin, ECO-C and Beta fluid) have quite different Prandlt number: 75, 12.1 and 830.

Parameters N and L are derived from the thermal dependence of ionic mobility and electrical permittivity respectively. Both N and L have similar signs. Negative (positive) N means injection from upper (lower) electrode.

Table 2-2. Values of M for different liquids [152].

Liquid	Ions	M
Methanol	H^+	4.1
Chlorobenzene	Cl^-	4.9
Ethanol	H^+	8.8
Ethanol	Cl^-	26.5
Nitrobenzene	Cl^-	22
Propilene carbonate	Cl^-	51
Chlorinated diphenyls	Cl^-	60~475

2.5 Closure

In this chapter, the typical problems and their physical models and governing equations have been introduced. Some brief descriptions of charge generation mechanism and injection laws are summarized. Two dimensionless forms and non-dimensional parameters for EHD and ETHD systems are detailed. Some physical ranges of non-dimensional parameters are made considering the working mediums are dielectric liquids. After the establishment of the mathematical framework, the discretisation of the general transport equation in spatial and temporal domain is the next step in achieving the numerical solutions. This is the subject of the next chapter.

Chapter 3 Finite volume discretisation

3.1 Introduction

In the previous chapter the general mathematical model of Newtonian fluid flow and the equations defining the electrostatic field in EHD and ETHD system have been explained. In this chapter, the numerical discretisation method will be described. The purpose of the discretisation is to transform the partial differential equations into a corresponding system of algebraic equations. The whole discretisation process includes two parts: the discretisation of the solution domain and the discretisation of the equation.

The discretisation of the solution domain is to define a numerical grid, which replaces the continuous spatial and temporal domain by a finite number of computational cells (control volume (CV)) and time steps where the numerical values of the dependent variables will be determined. Discretisation process consists in replacing partial differential operators in the governing equations by algebraic expression of the unknown function at given connected nodes. In the present study, the finite volume method (FVM) will be used integrate the equations. This discretisation method has the following features:

1. All PDE equations (Navier-Stokes equations, energy equation and Maxwell's equations) are solved with a fixed grid system.

2. The collocated grid system where all variables share the same CVs is adopted. It is more suitable to treat problems of complex geometries than staggered arrangements.

3. Due to the strong nonlinearity of the underlying equations, the PDEs systems are solved with a segregated iterative algorithm. This algorithm means that all PDEs are solved one at a time, with the inter-equation coupling treated in the explicit way.

4. The method can be applied to both steady and transient calculations. The time marching method is incorporated for transient problems.

The reminder of this chapter is organized as follows. Firstly, in section 3.2 the grid system is described. Section 3.3 presents the discretisation procedure for a generic scalar transport equation. The discretisations of the convective terms, diffusive terms and temporal terms are presented in Section 3.3.1, 3.3.2 and 3.3.3 separately. The generalized segregated approach with SIMPLE algorithm for pressure-velocity coupling is outlined in Section 3.4. Numerical examples, illustrating the behavior of the discretised terms are presented in Section 3.5. Finally, some closing remarks are given in the last section.

3.2 Discretisation of the computational domain

The main purpose when discretizing the solution domain is to generate the computational mesh on which the governing equations will be solved subsequently. It also determines the positions of spatial nodes and temporal instants where the solutions are sought. The typical procedure can be split into two parts: the discretisation of space and time. Space discretisation will be explained in this section, while the temporal discretisation will be discussed in Section 3.3.3.

The discretisation of spatial domain for FVM requires a subdivision of the domain into a number of contiguous, non-overlapping control volumes (CVs) which completely fill the computational domain. Under the collocated arrangement, all computational nodes are located in the CV's centroids. The detailed process includes two main aspects: (1) the shape of the control volumes; (2) the topology of the control volumes. Both aspects are closely linked with the geometrical configuration of the problem to be solved. For simple geometry, the structured regular or non-orthogonal meshes are the best choices. For complex geometry, there are two options with different considerations: multi-block structured meshes and unstructured meshes. The primary advantage for the unstructured grid methodology is its inherent flexibility for discretization of complicated geometries. By comparison, the main advantages of the multi-block method are:

1. It can resolve the topological complexity of a complicated geometry by permitting grid components to be generated individually and more easily fitted with the local boundary geometry.

2. The wide variety of linear system solvers for structured grids can be directly used or with slight modification.

3. It provides a natural way for parallel computation. Ideally, the computation in each block is assigned to a separate processor (domain decomposition in space).

It should be pointed out that the grid generation for very complex geometries with multi-block method becomes very difficult. However, for the present study, multi-block method is a very appropriate choice as the geometry of study problems is not too complicated.

For 2D problems, we use structured orthogonal and non-orthogonal quadrilateral meshes for simple and complex geometry cases separately. For 3D problems, one approach which uses non-overlapping multi-block hexahedral meshes is adopted. Two examples of the general quadrilateral mesh and hexahedral mesh, with characteristic geometry quantities, are shown in Figure 3-1.

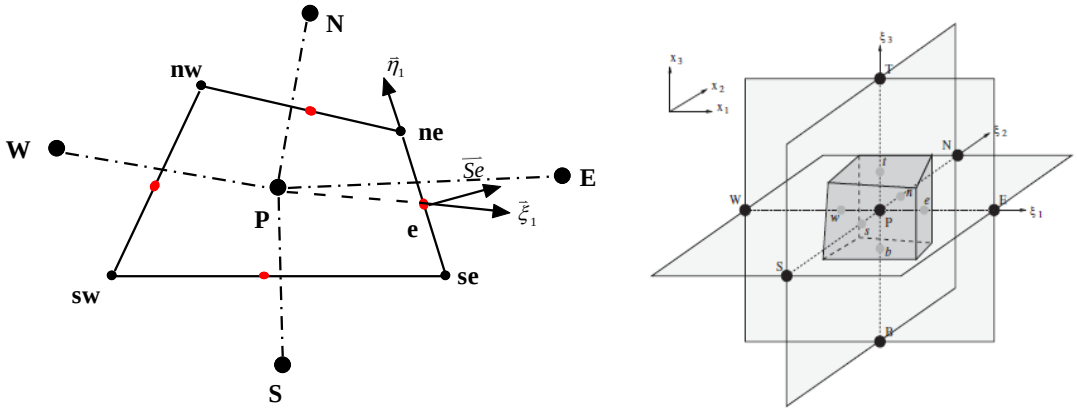

Figure 3-1. (left) Non-orthogonal quadrilateral mesh and (right) general hexahedral mesh

3.3 Discretisation of the generic transport equation

Before further discussions on numerical methods, it is indeed a happy coincidence that the spatial discretization schemes for charge density equation and Poisson equations correspond to convection and diffusion schemes in Navier-Stokes equation separately. In order to simplify the presentation of the numerical method, the form of a so-called generic transport equation which represents a general convection-diffusion transport of a conserved quantity is first described:

$$\frac{\partial \xi\psi}{\partial t} + \nabla \cdot (\vec{U}\psi) = \nabla \cdot (\Gamma \nabla \psi) + S(\psi) \qquad (3\text{-}1)$$

The two terms of left hand side (LHS) are transient and convection term, while the diffusion and source terms are listed on the right hand side (RHS) of above equation. The meaning of the generic variable and the coefficients for governing equations in EHD system are given in Tab.3-1.

Table 3-1. The meaning of ξ, ψ, Γ_ϕ and $S(\phi)$ in generic equation (3-1)

Equation	ξ	ψ	$\vec{U}$	Γ_ϕ	$S(\phi)$
Poisson equation	0	ϕ	0	ε_0	$-q$
Charge density equation	1	q	$\vec{u} + K\vec{E}$	D	0
Mass conservation equation	1	ρ	$\vec{u}$	0	0
Momentum equation [*]	1	$\rho\vec{u}$	$\vec{u}$	η_0	$-\nabla\tilde{p} + q\vec{E} - \frac{1}{2}(\vec{E}\cdot\vec{E})\nabla\varepsilon + (\rho-\rho_0)\vec{g}_i$
Energy Equation	1	ρT	$\vec{u}$	κ	$(q\vec{u} + K\vec{E}q)\cdot\vec{E}/c_p$

Noting (1) The electrostrictive force term is included in the pressure term;

(2) The source term in energy equation is the viscous dissipation and Joule heating;

(3) [*] means term $\nabla\cdot\left(\mu\nabla\cdot\vec{u}^{\,t}\right)$ should be added into the source term in the momentum equation to take into account the contribution due to the spatial variability of the viscosity

3.3.1 Discretisation of the convective term

Though convection term is represented by a simple first-order derivative, its numerical representation remains one of the central issues in CFD community. Applying the Gauss Theorem, the discretisation of the convection term follows,

$$\int_{V_P} \nabla \cdot (\rho \vec{U} \phi) dV = \int_S \left(\rho \vec{U} \phi\right) \cdot \vec{n} ds = \sum_f \vec{S} \cdot \left(\rho \vec{U} \phi\right)_f = \sum_f \vec{S} \cdot \left(\rho \vec{U}\right)_f \phi_f = \sum_f F_f \phi_f \tag{3-2}$$

where $\vec{S} = S\vec{n}$, S is the aera of the surface and F_f in above equation represents the mass flux through the face:

$$F_f = \vec{S} \cdot \left(\rho \vec{U}\right)_f \tag{3-3}$$

The calculation of these face fluxes will be later discussed separately in Section 3.4.3.

So equation (3-2) requires the face value of the variable ϕ represented with the values in the cell centres, which is obtained using the convection differencing scheme. The first order upwind (FUD) scheme and the second Central Differencing (CD) scheme are the two simplest but widely used schemes.

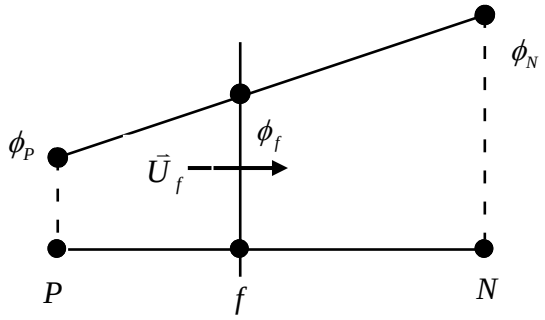

Figure 3-2. Face Interpolation

FUD

$$\phi_f = \begin{cases} \phi_P & \text{for } F > 0 \\ \phi_N & \text{for } F < 0 \end{cases} \tag{3-4}$$

CD

$$\phi_f = f_x \phi_P + (1 - f_x)\phi_N \quad \text{with} \quad f_x = \frac{\overline{fN}}{\overline{PN}} \tag{3-5}$$

In fact, FUD scheme and CD scheme represent two general types of linear convection schemes.

First order upwind (FUD), HYBRID and Power-Law: algorithmic simplicity, fast convergence and lead to plausible looking results; these methods can give reasonably accurate solutions for steady, quasi-one-dimensional flow. However, when used for flows oblique or skew to the grid, inherent artificial viscosity (or diffusivity) seriously degrades the solution, especially in

the case of recirculation flows. They are known to generate excessive artificial viscosity or numerical diffusion.

Central Differencing (CD), Second Order Upwind (SUD) and QUICK): high accuracy in smooth region but with convergence difficulties and a tendency to generate unphysical overshoots near sharp, monotonic transitions. The convergence difficulties are rooted in whether the coefficient matrix of the discrete equation is diagonally dominant or not. If the spectral radius of the coefficient matrix is close to unit, it is not easy to obtain convergent solutions. This kind of difficulty can be overcome by the deferred correction (DFC) technique, which will be described in the next section. However, the possibility to generate unphysical oscillation solution belongs to the inherent property of schemes, which can't be changed by DFC technique.

The reasons we put emphasis on the boundedness properties of the convection schemes are,

1. There is a direct relationship between the boundedness and stability property of the schemes. The solutions may display unphysical oscillations in regions of steep gradients, which can be sufficiently serious to cause numerical instability and code divergence.

2. Physically speaking, the purpose of numerical simulation is to obtain the numerical solutions which are close to the real physical solutions. Taking the charge density distribution in EHD problems, the real physical solutions require the charge density to lie between zero and the value of the injection strength. Therefore, it is necessary to avoid the appearance of some negative values or values higher than the maximum charge density in the numerical solution. In other words, if the convection term in its differential form does not violate the bounds of the variable given by its initial distribution, this property should be also preserved in the discretised form of the term.

It is necessary to mention the Blended scheme of Peric [220], as the construction process of the scheme is quite similar to the following high-resolution schemes. Peric represents an attempt to suppress the dispersive nature of CD scheme by a linear combination with FUD.

BLENDED SCHEME

$$\phi_f = (1-\gamma)(\phi)_{FUD} + \gamma(\phi)_{CD} \tag{3-6}$$

where γ is the blending factor with a value between 0 and 1, and determines how amount of both schemes to be introduced. The core question is how to decide the value of the blending factor. Perić proposed a constant value of γ for all faces of the mesh.

All the convection schemes mentioned above are linear schemes. The linear schemes can be analyzed in terms of Taylor series expansion,

1. If the leading term of the truncation error is odd-order derivative, the solution will be affected by numerical diffusion,

2. If the leading truncation term is even-order derivative, numerical dispersion occurs, causing unphysical and bounded oscillations. In addition, the sign of the even-order

derivative is directly linked to the area where the oscillation is expected [221], and this phenomenon has been observed in the numerical tests in [222].

TVD and NVD Schemes

It is impossible to design a linear scheme which is of second order or higher accuracy, but removing above two limitations. That is, the linear schemes could not hold the high accuracy and oscillation-free property simultaneously. This limitation is predicted by Godunov's theorem [75] which states that no linear convection scheme with greater than first-order truncation error can be monotonic.

To achieve this goal, the nonlinear discretization schemes were designed, nonlinear which means that the schemes adjust themselves in some way according to the local solution values so as to maintain the bounded behaviour. Various methods based on some different but related concepts were proposed, such as the Normalised Variable Approach (NVA) [78][79], the Total-Variation Diminishing (TVD) methods [75][76], Local Extremum Diminishing methods (LED) [223], positive schemes [74], and Essentially Non-Oscillatory (ENO) schemes [96]. The relationship among these concepts can be seen in Yee's diagram [224], which is also showed in [83].

It should be pointed out that in the present study we confine ourselves to stencils with five points per (spatial) direction, though the idea of constructing nonlinear bounded schemes can be extended to the case of larger computational cell. The five-point stencil has following advantages,

1. The five-point stencil is still relatively compact, which is easy for the implementation of boundary conditions.

2. The five-point stencil allows orders of consistency up to 3 and comprises a number of potentially interesting spatial discretization schemes, like QUICK, SUD and *k*-scheme;

3. All five-point stencils, which are of second or third order, can be rewritten as a function of a single variable. The conversion brings great convenience for the design of nonlinear high-resolution schemes.

It is clearly impossible to give a complete survey of all nonlinear discretizations schemes here, and we mainly focus on two kinds of schemes which are being widely used in the numerical simulation of incompressible flow: NVD-type and TVD-type high-resolution schemes. The basic thoughts under the two types of schemes are to mix the first order upwind and high-order linear scheme, using a measure of the local monotonicity in the predicted field to switch to FUD approximation whenever and wherever non-monotonicity is identified. A direct result is that the numerical diffusion, induced by the lower-order scheme, dissipates the genesis of a spurious oscillation before it can damage the quality of the solution.

Reconsidering the BLENDED scheme, high-resolution schemes essentially provide methods to define the γ value.

In details, designing an efficient high-resolution scheme requires answers to the following three questions:

1. Which high-order schemes?

2. How to recognise the regions where switching to FUD is needed?

3. What kind of intervention should be introduced?

Generally speaking, following the normalized variable approach, linear and nonlinear schemes can be constructed rather easily and the conditions for a scheme to be bounded can be clearly identified. However, flux-limiting algorithms are more convenient in practical implementation than NV method since a defect correction approach can easily be adopted.

In the next section, we will make a brief introduction a unified approach of high-resolution schemes recently proposed by Waterson and Deconinck [84]. The unified approach follows the idea of flux limiting and well includes most already existing HR (both TVD-type and NVD-type) schemes. The cell-face value of the convected variable, predicted by the unified HR approach, may be written, using the notation outline in Figure 3-3.

$$\phi_f = \phi_C + \frac{\Delta x_C}{2}\varphi(r)\left(\frac{\partial \phi}{\partial x}\right)_f \tag{3-7}$$

where $\varphi(r)$ is named as the limiter function of the gradient ratio r,

$$r = \left(\frac{\partial \phi}{\partial x}\right)_u \Big/ \left(\frac{\partial \phi}{\partial x}\right)_f \tag{3-8}$$

With a uniform grid system, the ratio can be simplified to,

$$r = \frac{\phi_C - \phi_U}{\phi_D - \phi_C} \tag{3-9}$$

It should be noted that the above definition of r is the reciprocal of the corresponding expression in [84]. Thus, the final expressions of HR schemes may need some modification if they are not symmetric [225].

Through the selection of limiter functions $\varphi(r)$, Eqn.(3.1) could stand for various linear and nonlinear schemes. Some classical linear schemes are summarized in Table 3-2, while some high-resolution schemes are listed in Table 3-3 or Appendix A, including a recently developed third order TVD scheme [226]. Some other schemes can be found in reference [84] which did the excellent summarization.

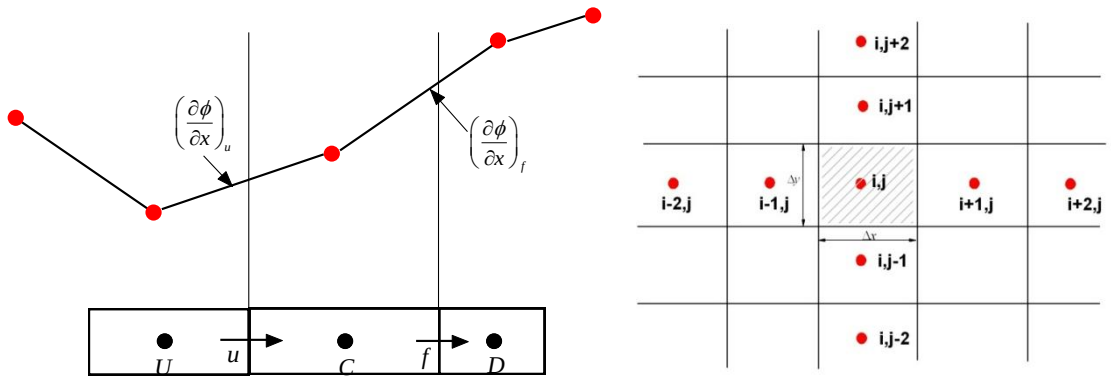

Figure 3-3. Sketch of upwind-biased stencil and notation in 1D (left) and 2D (right) grid system

Table 3-2. Limiter functions of Linear Schemes

Scheme	Limiter function
FUD	0
CD	1
SUD	r
QUICK	$\frac{3}{4}+\frac{r}{4}$

The main idea of constructing bounded schemes is first to define the possible regions or the conditions of high-resolution schemes. Then the specific formulas of the schemes are designed considering accuracy, convergence, computational cost and other. As shown in [84], the Total–variation diminishing (TVD), Positivity and the Convection-Boundedness Criterion (CBC) are three most widely used criteria. Here we adopted the Spekreijse's positivity region [226] which is more flexible and general than the other two. A complete description of the conditions for the Spekreijse's positivity region can be described as,

$$\alpha \le \varphi(r) \le M \qquad \text{and} \quad -M \le \frac{\varphi(r)}{r} \le 2+\alpha \tag{3-10}$$

where $\alpha \in [-2,0]$ and $M \in (0,\infty)$ are two constants. The positivity region on a $r-\varphi$ diagram is shown in Figure 3-4 (left). In fact, there are some interior relations among different criteria and they could be converted to each other easily. For example, the Spekreijse positivity region can be converted to Normalized-variable Diagram via the relationship $\tilde{\phi}_C = \frac{r}{1+r}$, as showed in Figure 3-4 (right). The bounded criteria used here is not very important, as most of schemes listed in Appendix A can satisfy both CBC and the Spekreijse's positivity region. A number of TVD-type HR schemes are shown in Figure 3-5, and the formulations are in Table 3-3.

Table.3-3. Limiter functions of classical TVD-type HR schemes

Name	Limiter function $\varphi(r)$	Source
van Leer	$\varphi(r)=\frac{r+\lvert r\rvert}{1+r}$	Van Leer(1974)
Superbee	$\varphi(r)=\max(0,\min(1,2r),\min(2,r))$	Roe(1985)
Min-mod	$\varphi(r)=\min\text{mod}(1,r)$	Roe(1985)
van Albada	$\varphi(r)=\frac{r+r^2}{1+r}$	van Albada et al. (1982)
MC	$\varphi(r)=\max(0,\min((1+r)/2,2,2r)$	Van Leer(1977)
UMIST	$\varphi(r)=\max\left[0,\min\left(2r,\frac{1+3r}{4},\frac{3+r}{4}2\right)\right]$	Lien and Leschziner (1993)
SMART	$\varphi(r)=\max(4r,\min((0.75+0.25r),2)$	P.H. Gaskell and A. K. C. Lau (1988)

Note: only the van Albada limiter function is not equal to zero when $r<0$.

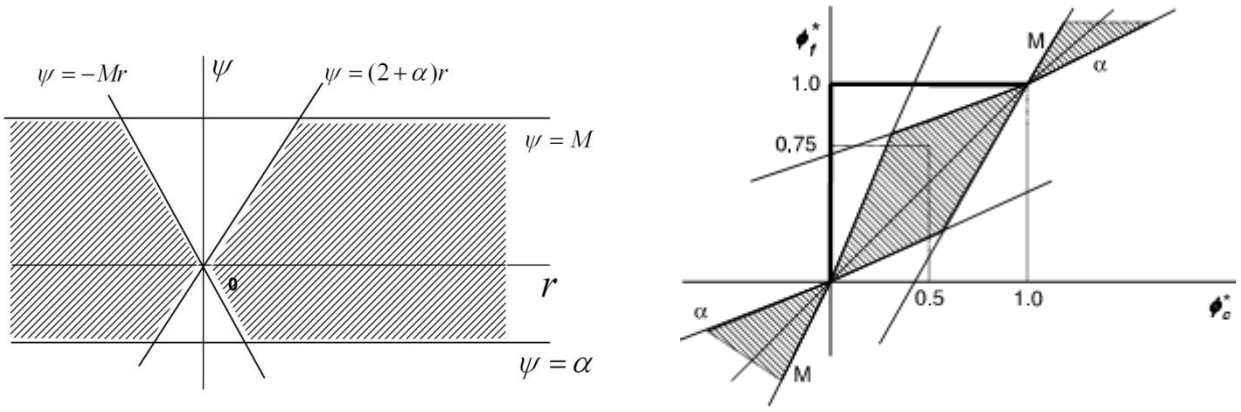

Figure 3-4. The Spekreijse positive region in Flux-Limiter Diagram (left) and Normalized-Variable Diagram (right) [84]

The conditions with Eqn. (3-10) are not sufficient and necessary conditions for a scheme to lead to oscillation-free solutions. Some schemes violate the requirement of Eqn.(3-10), like the van Albada scheme [227] and Čada & Torrilhon's new third-order scheme [226], can also lead to bounded solutions. A summarization of other boundedness criteria can be found in [228]. In the present study, we care more about the performances of different schemes, rather than the construction process.

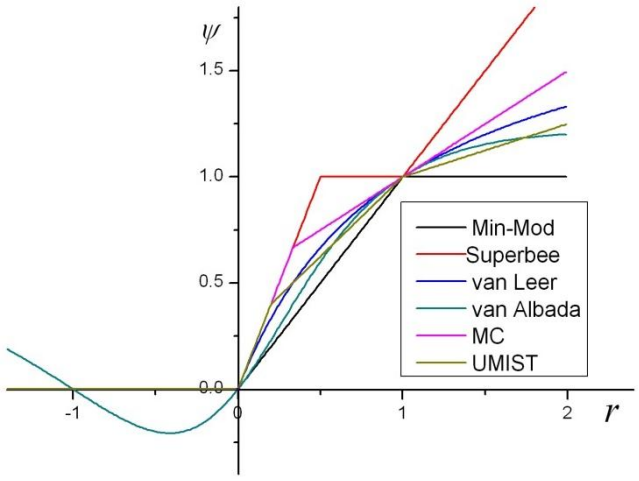

Figure 3-5. Flux-limiter diagram: six flux limiters function of Table 3-3.

On the extension of HR schemes to multi-dimensional grid

In the present study, the so-named "dimensionally split" method which means that the 2D and 3D implementations are obtained by applying one-dimensional schemes separately along each of the other directions, is used to treat multi-dimensional problems. Gaskell and Lau [79] has proved that this method combined with the high order schemes which satisfy the CBC could always lead to bounded solutions. When a scheme which only satisfies the positive criterion is used in multi-dimensional problems through this method, do the results still remain bounded? The numerical tests carried out in the present study give a positive answer to this question.

On the extension of HR schemes to unstructured meshes

From the construction process of HR schemes, it is easy to find that most HR schemes cannot be applied to unstructured grids directly. The major obstacle is the lack of far-upwind cells information. The far-upwind cells information will appear both in 'unbounded indicator' and high-order schemes. Several methods have been proposed to circumvent this difficulty [71][91-93]. Generally, there are two natural thoughts to apply HR schemes to unstructured meshes. The first one is to avoid explicitly using far-upwind points, like GAMMA scheme [71] and Bruner's approach [92]. GAMMA scheme uses an 'unbounded indicator' without explicitly using far-upwind information, meanwhile takes CD scheme as the high order base scheme. However, GAMMA scheme needs the locating of the nodal point in the middle of the control volume, which is not always the case for unstructured meshes. The second is to construct the virtual far-upwind points, like Darwish's r-factor algorithm [91] and Lian-xia Li's new r-factor algorithm [93]. Both algorithms need to calculate nodal gradients and to use extra memory for virtual points. In fact, through the comparison of the expression of Jasak's 'unbounded indicator', (eqn(20). in [71]) and Darwish's r-factor (eqn(16). in [91]), we can view them as the same method. Recently, Qin Qian, et al. [229] proposed a new approach which uses the upwind approximation as the 'unbounded indicator". During the computation, the actual scheme switches between QUICK scheme and 1st-order upwind (FUD) scheme, according to whether the indicator locates in the range of physical bounds or not. To avoid the use of far upwind information in high-order scheme, we use

the CD instead of QUICK scheme [230]. However, little over-shoot is required to activate the schemes and a small amount of non-monotonicity is inevitable [229], which is the cost of using simple indicator. Thus, the problem of the extension of HR to unstructured grid has not been fully solved.

Some preliminary research about this topic was done in the present study. Firstly, we will briefly introduce the extension algorithm based on auxiliary point method. Then, we will analyze the reason why the algorithms cannot lead to completely oscillation-free solutions.
When switching to unstructured grid system, it is clear that the main difficulty in implementing TVD schemes in unstructured meshes lies in the need of defining a 'virtual' far-upwind U point, see Figure 3-6.

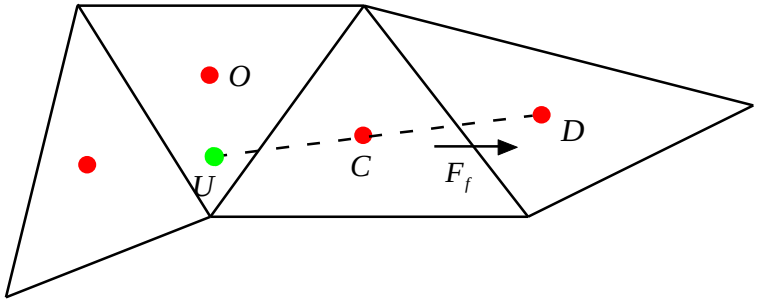

Figure 3-6. Unstructured triangle meshes

In order to get rid of non-uniform grid problem, it is commonly advised to locate the virtual far-upwind point at the position that, $\left|\overrightarrow{CD}\right| = \left|\overrightarrow{UC}\right|$, where $|\cdot|$ means the distance between two points. Some words should be said about the application of HR schemes to non-uniform grid, as unstructured grid systems are also normally non-uniform system. Strictly speaking, HR schemes of Eqn.(3-9) are derived on uniform grid system. For non-uniform grid system, some spatial parameters should be introduced to extend the applicability of the normalized variable formulation (NVF) methodology. Meanwhile, the boundedness criteria and accuracy conditions need to be updated too. The normalized variable and space formulation (NVSF) methodology is developed by Darwish and Moukalled [231] to extend HR schemes to non-uniform grid system. However, in unstructured grids, it is not easy to define accurately the extra spatial parameters needed for NVSF methodology. Moreover, almost all HR schemes need to be updated separately. Thus, an opportunistic question is: can the original expression of Eqn.(3-9) be directly applied to non-uniform grid system without any modification? From our numerical test results and some other numerical results in [232] and [234], the answer is positive. This conclusion can be understood in this way: firstly, the boundedness criteria, like CBC, do not depend on the uniformity of grid system; secondly, the accuracy of high-order component of HR schemes is linked to the uniformity of the grid. In other words, the original expressions of HR, i.e., TVD-type limiter functions still satisfy the boundedness criteria. However, their accuracy will be affected. It should be noted that the reduction of accuracy is not dramatic with most second-order schemes [232]. Only with third-order schemes (like SMART and STOIC [231]) and big expansion ratio, the improvement with NVSF is clear. The statement of HR schemes with non-uniform grid system is

very important for finding the essential reasons why the following two extension approaches tend to lead to slightly unphysical oscillations.

1. (Darwish and Moukalled, 2003) [91]

In this approach, the value of the virtual point is defined through information at point C and D,

$$\phi_U = \phi_D - 2\left(\nabla\phi\right)_C \cdot \overrightarrow{CD} \tag{3-11}$$

and the r-factor is expressed as,

$$r_{f,D\&M} = \frac{2\left(\nabla\phi\right)_C \cdot \overrightarrow{CD}}{\phi_D - \phi_C} - 1 \tag{3-12}$$

2. (Li, et al., 2008) [93]

In this approach, the value of the virtual point is defined through information at CV node which contains the virtual point, U, see Figure 3-6.

$$\phi_U = \phi_O + \overrightarrow{OU} \cdot \left(\nabla\phi\right)_O \tag{3-13}$$

and the r-factor is expressed as,

$$r_{f,Li} = \frac{\phi_C - \left(\phi_O + \overrightarrow{OU} \cdot \left(\nabla\phi\right)_O\right)}{\phi_D - \phi_C} \tag{3-14}$$

Both methods have been tested in [92] over a problem of pure convection with a double-step profile in an oblique uniform velocity field. The superiority of Li's method in terms of convergence speed and accuracy has been demonstrated. But, in this test case, both methods tend to generate unphysical oscillations, which is undesirable.

To analyze the reason of this behavior, Li, *et al.*, attribute it to 'the original TVD definition in uniform and one-dimensional grids that may not be directly extended to multi-dimensional and unstructured one'. In our opinion, this should not be the real reason. Goodman and Leveque [233] showed that on general grids in two space dimensions TVD schemes cannot be more than first order, though, as noted by Leveque [234], this does not prevent one-dimensional TVD schemes to be applied quite successfully in multiple dimensions through the use of "dimensional splitting" along individual grid directions, though such schemes are not technically TVD. In fact, when extending the TVD scheme to 2D and 3D, we just use its expression. We are not seeking the numerical solutions which satisfy the Total Variation Diminishing property, but a weaker restriction, like positive property.

By comparison with multi-dimensional slope limiter methods, we attribute the oscillation to the introduction of gradient evaluations. As seen in Eqns. (3-11) and (3-13), gradient values have been used to compute the values of the virtual far-upwind points. It is possible that the obtained

far-upwind point value is out of range of the maximum and the minimum variable values around the working cell.

To solve the problem, there are two possible ideas. The first one is to limit the gradient value. Mathur and Muthy [235] pointed out that the gradient at the cell could be limited to ensure the reconstructed value at each of the nodes bounded by the maximum and minimum values of ϕ over all the cells that share the node. The other one is to limit the obtained value of far-upwind point. A similar technique has been used in [236]. In our case, the final value of the virtual points can be decided as,

$$\phi_{U,\text{final}} = \max\left[\phi_{\min}^{neighbours}, \min\left(\phi_U, \phi_{\max}^{neighbours}\right)\right] \tag{3-15}$$

where *neighbors* mean the CV cells sharing the faces of the working cell.

In addition, for general structured meshes, the above algorithms can also be used. Moreover, the above algorithms are recommended for the implementation of TVD-type high-resolution schemes in extremely distorted structured meshes. The difference between structured and unstructured meshes is only the data storage, not in expressing the velocity field information. A nominal far-upwind cell (see from the storage order) may not offer the appropriate 'upwind' velocity information with a structured grid.

An example is provided in Figure 3-7, following the structured storage, the point U will be used as the far-upwind point of cell face, f, which is obviously inappropriate. By examining the numerical test results, when using U as the far-upwind point, the solution is oscillation-free but with a fairly low accuracy [237].

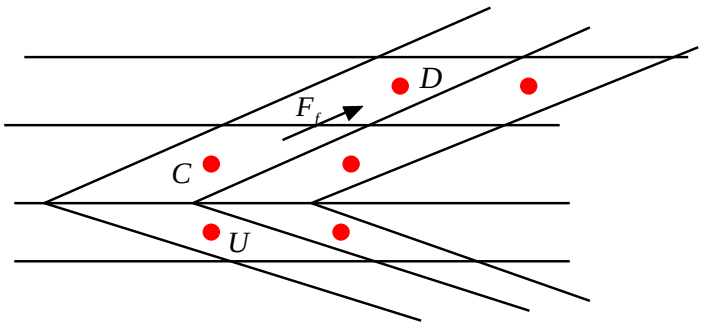

Figure 3-7. An extremely distorted structured mesh

3.3.2 Discretisation of the diffusive term

Based on finite volume method, the discretization of the diffusive flux for a scalar quantity ϕ through a surface can be expressed as,

$$\int_{V_p} \nabla\cdot(\Gamma\nabla\phi)d_V = \int_{S_p} (\Gamma\nabla\phi)\cdot\vec{n}d_S \tag{3-16}$$

with the Gauss' theorem, where S_p represents the surface around the control volume V_p and $\vec{n}$ is the unit normal vector to this surface.

The approximation of the term in the left hand side of Eqn. (3-16) is equivalent to the evaluation of the quantity of Eqn. (3-17), on each face *k* of the control volume.

$$S_k^P \left(\nabla\phi\right)_k^P \cdot \vec{n}_k^P \tag{3-17}$$

Where S_k^P and $\vec{n}_k^P$ represent respectively the area of the surface k and the unit vector normal to this face. Then the new problem is to find a consistent approximation of $\left(\nabla\phi\right)_k^P \cdot \vec{n}_k^P$ by using values of adjacent control volume nodes. If the mesh is non-orthogonal, the fact that the gradient $\left(\nabla\phi\right)_f$ cannot be directly expressed by the values of ϕ at centroids P and K brings a lot of difficulties. In order to obtain the higher accuracy, different approaches were proposed, like coordinate transformation method, CTM [109][110], direct gradient evaluation method, DGEM[111][70, page 234-235] and normal decomposition method, NDM [68][105][107]. Though these three above mentioned methods have been invented independently with different conceptual bases, all of them are widely used in computational fluid dynamic or numerical heat transfer fields.

As mentioned earlier, the diffusion scheme will be applied to both the viscous term in Navier-Stokes equations and Poisson equation. Thus, it is always worth spending time to select an efficient discretization scheme among considerable variety of choices. We started from NDM and tried to complete the method. In addition, we also successfully revealed some relationship among CTM, DGEM and NDM. In the following, we make a brief introduction of NDM and several specific schemes.

The normal decomposition method in its first version was initially proposed by Muzaferija in [107]. This version was called SDC, which stands for Standard Deferred Correction (see [105]). The basic idea of the method contains two steps: firstly, the surface vector is decomposed into two parts:

$$\vec{n} = \vec{n}_1 + \vec{n}_2 \tag{3-18}$$

where $\vec{n}_1$ is defined in the PK direction , see Figure 3-8. Taking Eqn. (3-18) into Eqn.(3-17),

$$S_k \left(\nabla\phi\right)_k \cdot \vec{n}_k = S_k \left(\nabla\phi\right)_k \cdot \vec{n}_1 + S_k \left(\nabla\phi\right)_k \cdot \vec{n}_2 \tag{3-19}$$

The first part of the right-hand side of Eqn.(3-19) can be easily approximated by a centered formula, while the second part will be explicitly computed using the values of the previous iteration, which is the core thought of deferred correction method [238]. Numerical tests show that there is a limitation of possible angle θ_k (the exact maximum value is 38^o) for Muzaferijia's method [68] [105].

In fact, there are many possible decomposition schemes, as Eqn.(3-18) and Eqn.(3-19) are always valid. Three approaches named Minimum Correction (the same with Muzaferija's approach), Orthogonal Correction ($\vec{n}_1 = \frac{\overrightarrow{PK}}{|PK|}$, where $\overrightarrow{PK}$ represents the vector from point P to K, and $|\cdot|$ stands for the distance between the two points, the same representation will be used below) and

Over-relaxed Correction (the same with Traoré's approach, see below) separately are listed in [68]. Recently, Traoré's et al. [105] proposed another decomposition scheme, which is named Improved Deferred Correction (IDC) scheme. In this new approach, $\vec{n}_2$ is parallel to the surface, see Fig.3-8. Considering the superiority of IDC scheme in the maximum possible angle θ_k and smoother convergence process, it is recommended for further application.

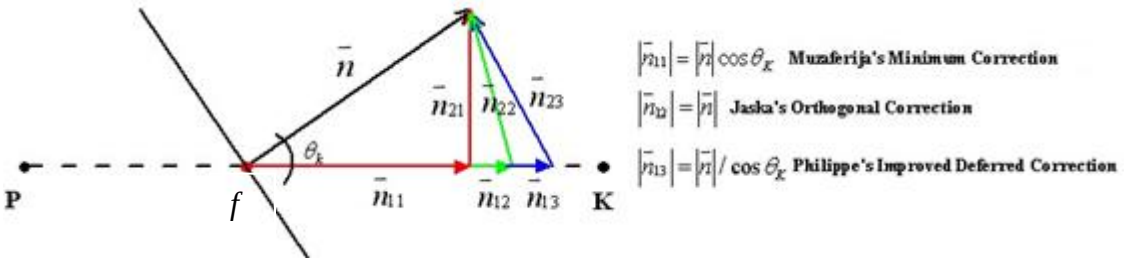

Figure 3-8. Normal surface vector decomposition method and specific schemes

To compute the second part of the right-hand side of Eqn. (3-19), the usual practice is to compute the dot product of vector $(\nabla\phi)_f$ and $\vec{n}_2$ directly. The vector $\vec{n}_2$ can be chosen between:

$$\vec{n}_2 = \vec{n} - \vec{n}_1 = \vec{n} - \frac{1}{\cos\theta}\vec{e}_1 \tag{3-20}$$

or

$$\vec{n}_2 = \vec{e}_2 \cdot \tan\theta \tag{3-21}$$

where $\vec{e}_1$ and $\vec{e}_2$ are depicted on Figure 3-9.

The gradient at the intersection point f' should be determined from the gradients of the two cells sharing the face. A simple method is carried out in the present paper,

$$(\nabla\phi)_f = f_x(\nabla\phi)_P + (1 - f_x)(\nabla\phi)_K \tag{3-22}$$

where f_x is the interpolation factor and is defined as $f_x = \frac{|fK|}{|PK|}$, see Figure 3-9.

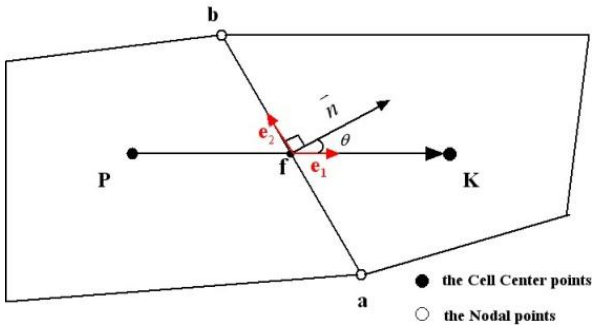

Figure 3-9. The geometric relationship of two adjacent cells

Taking Eqn.(3-20) into Eqn.(3-19), then we get,

$$S_f(\nabla\phi)_f \cdot \vec{n}_f = \frac{S_f}{\cos\theta}(\nabla\phi)_f \cdot \vec{e}_1 - S_f(\nabla\phi)_f \cdot \left(\vec{n} - \frac{1}{\cos\theta}\vec{e}_1\right)$$

$$= S_f \frac{\phi_K - \phi_P}{\xi\cos\theta} - S_f(\nabla\phi)_f \cdot \left(\vec{n} - \frac{1}{\cos\theta}\vec{e}_1\right) \qquad (3\text{-}23)$$

The $(\nabla\phi)_f$ in the last term of Eqn.(3-23) will be explicitly computed from the values of the previous iteration. Obviously, IDC leaves out the consideration of skewness-induced error. Comparing with CTM, IDC needs no interpolation of nodal point values. On the contrary, the approximation of gradients at cell center points is necessary. And as we will show it later the accuracy of the gradient evaluation methods has great impact on the final solution accuracy.

We could also put Eqn.(3-21b) into Eqn.(3-20) and reach another effective expression.

$$S_f(\nabla\phi)_f \cdot \vec{n}_f = \frac{S_f}{\cos\theta}(\nabla\phi)_f \cdot \vec{e}_1 - S_f \tan\theta(\nabla\phi)_f \cdot \vec{e}_2$$

$$= S_f \frac{\phi_K - \phi_P}{\xi\cos\theta} + S_f \frac{\phi_b - \phi_a}{\eta}\tan\theta \qquad (3\text{-}24)$$

Before further discussion, the concepts of skewness on surfaces and non-orthogonality on boundaries are explained. Skewness on surfaces means that the intersection point between line PK and surface doesn't coincide with the midpoint of the surface, to see Figure 3-10 (left). Non-orthogonality on boundaries is the situation that the lines connecting boundary nodes and near-boundary CV nodes are not normal to physical boundaries; to see Figure 3-10 (right). These are two main error sources for the calculation of diffusive flux on non-orthogonal meshes using surface decomposition method. Numerical experiments show that the methods for the treatment of the two error sources can significantly affect the final accuracy and convergence rate.

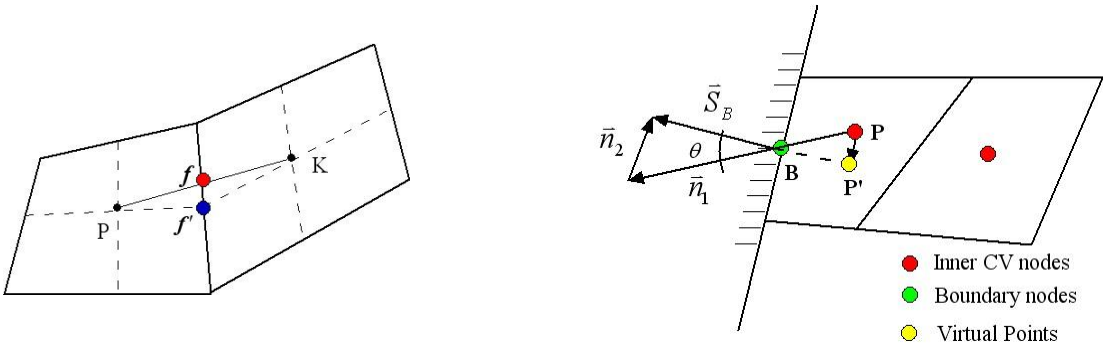

Figure 3-10. (Left) Skewness on the surface and (right) non-orthogonality on the boundary

3.3.2.1 On gradient evaluation methods

We have noticed that the gradient values of CV nodes appear in convective flux estimation, diffusive flux and pressure source term (see next section) evaluation expressions when

unstructured or non-orthogonal grid systems are utilized. Thus, it is necessary to estimate the influence of different gradient evaluation methods on the accuracy, computational cost and convergence process. Five different approaches for gradient evaluation are explained in Appendix B. In the numerical test section of 3.5.3, all the approaches are tested to highlight the difference between their performances.

By summarization of numerical results, it is found that there is obvious difference between the accuracy and the computational cost. The present study firstly highlights the importance of the selection of an appropriate and accurate gradient evaluation method for diffusive flux calculation when using normal decomposition method in non-orthogonal meshes. Secondly, some advices are given for the selection of the gradient evaluation method.

3.3.2.2 Boundary condition treatment

There are two types of numerical boundary conditions. Dirichlet boundary condition prescribes the value on the boundary, while Von Neumann boundary condition prescribes the gradient of the variable normal to the boundary. Following the normal decomposition approach, the core issue with the implementation of Dirichlet boundary condition is the lack of the gradients at boundary nodes. If the grid is orthogonal, the gradients at boundary nodes can be decided by the value of nodes on the boundary and in the internal domain. No difficulty appears. However, if there is non-orthogonality on boundaries, no simple method for the computation of gradients on boundaries is available. Compared with Dirichlet boundary condition, the treatment of Neumann boundary condition seems easier, as the Neumann boundary condition can be introduced directly into the discretized equation. With Neumann boundary condition, the real problem now is how to compute the values of variables on boundaries, which is usually needed for gradient evaluation of nearest grid nodes.

In the present study, different approaches have been implemented in our solvers and the performances have been compared with different numerical examples. In the following, we firstly explain the possible methods to implement both Dirichlet and Neumann boundary conditions.

To implement the Dirichlet boundary condition, two natural ways can be followed. The first way is to avoid the explicit use of the gradients based on some simplifying assumptions. The other way is to extrapolate from the gradients of inner nodes.

In [68], Jasak provided a simple method, which is essentially equivalent to giving up the non-orthogonal correction at the boundary surfaces.

$$\textbf{Simple:}\quad \vec{S}_B \cdot (\nabla\phi)_B \approx \frac{\phi_B - \phi_P}{|BP|\cos\theta} \tag{3-25}$$

where ϕ_B is the value on the boundary, given by Dirichlet Boundary condition.

Apparently, the above equation is not accurate when the non-orthognality on boundaries is serious, i.e., the angle θ is big. Two methods which take the non-orthogonal contribution into account are

reported in [113]. The first method is to use a simple linear extrapolation method to obtain the gradient at the boundary, to see Figure 3-10:

$$\textbf{First:}\quad (\nabla\phi)_B \approx (\nabla\phi)_P + \frac{\left|\overrightarrow{PB}\right|}{\left|\overrightarrow{KB}\right|}\left((\nabla\phi)_P - (\nabla\phi)_K\right) \tag{3-26}$$

The above extrapolation method is only first order when Point B, P and K are not on the same line, which is always the case for non-orthogonal meshes.

The other method is to construct a virtual point P'. The virtual point is the orthogonal projection of CV node P onto the mid-perpendicular line of the boundary surface. Then the diffusive flux on the boundary can be approximated as,

$$\textbf{Second:}\quad \vec{S}_B \cdot (\nabla\phi)_B \approx S_B \frac{\phi_B - \phi_{P'}}{|BP'|} = S_B \frac{\phi_B - \phi_{P'}}{|BP|\cos\theta} \tag{3-27}$$

The second method can be viewed as a simplified version of the first method. The derivation process is given as follows.

For the first method, a simplified extrapolation method is based on the assumption that the gradient at the boundary is the same as the nearest grid nodes, $(\nabla\phi)_B \approx (\nabla\phi)_P$. Then the diffusive flux on the boundary can be expressed as,

$$\begin{aligned}\vec{S}_B \cdot (\nabla\phi)_B &\approx \vec{S}_B \cdot (\nabla\phi)_P = S_B (\nabla\phi)_P \cdot (\vec{n}_1 + \vec{n}_2) \\ &= S_B \frac{\phi_B - \phi_P}{|BP|\cos\theta} + S_B (\nabla\phi)_P \cdot \vec{n}_2\end{aligned} \tag{3-28}$$

For the second method, a common way to approximate the value of the virtual point is,

$$\phi_{P'} = \phi_P + (\nabla\phi)_P \cdot \overrightarrow{PP'} \tag{3-29}$$

Taking Eqn.(3-29) into Eqn.(3-28), the final expression is,

$$\vec{S}_B \cdot (\nabla\phi)_B \approx S_B \frac{\phi_B - \phi_P}{|BP|\cos\theta} + S_B (\nabla\phi)_P \cdot \frac{\overrightarrow{PP'}}{|BP|\cos\theta} \tag{3-30}$$

Considering the geometric relationship, $|PP'| / |BP| = \sin\theta$ and $\overrightarrow{PP'} // \vec{n}_2$.

Eqn.(3-28) and Eqn.(3-30) are exactly the same.

To implement the Neumann boundary condition, three methods to update the values of variable on boundaries are provided. The first one is to assume that the value is the same at the the nearest grid nodes,

Simple: $\phi_B \approx \phi_P$ (3-31)

A better approximation which uses a Taylor expansion can be expressed as,

First: $\phi_B \approx \phi_P + (\nabla\phi)_P \cdot \overrightarrow{PB}$ (3-32)

In principle, an iteration loop is necessary for Eqn.(3-32) as ϕ_B will be used for computing $(\nabla\phi)_P$. A simple way is to use the value of the previous iteration.

It is noticed that the Neumann boundary condition doesn't work in the updating process. This is against the rule of accelerating convergence of boundary value problems, which requires transferring the boundary information into inner domain as soon as possible. Following the idea, the third method is proposed,

Second: $\phi_B \approx \phi_{P'} = \phi_P + (\nabla\phi)_P \cdot \overrightarrow{PP'}$ (3-33)

The Neumann boundary condition is implicitly taken into account in the above equation in the first symbol of approximate equal.

As it will be seen in the numerical test section, there is a clear difference in solution accuracy and convergence cost of the performance of different boundary condition treatment methods.

3.3.2.3 Similarity and interconnection among CTM, DGEM and NDM

Inspired by the idea of [239], which discussed the equivalence of three approaches of building shape-preserving advection schemes in one-dimensional system, we are interested in the relationship between CTM, DGEM and NDM for the calculations of diffusive fluxes. For the first step, we deduce the final formula for diffusive flux estimation with CTM and DGEM, to see Appendix C.

The first observation is that Eqn.(3-24) is strictly equivalent to Eqn.(C-7) (in Appendix C). It indicates that with this implementation, the two methods CTM and IDC are mathematically identical. The subsequent discussion will focus now on the connection between IDC scheme and the DGEM method. The analysis contains two cases.

Case 1. No Skewness situation

Firstly, we will discuss the case when there is no skewness. Here no skewness means that f and f' coincide with each other, see Figure.3-11.

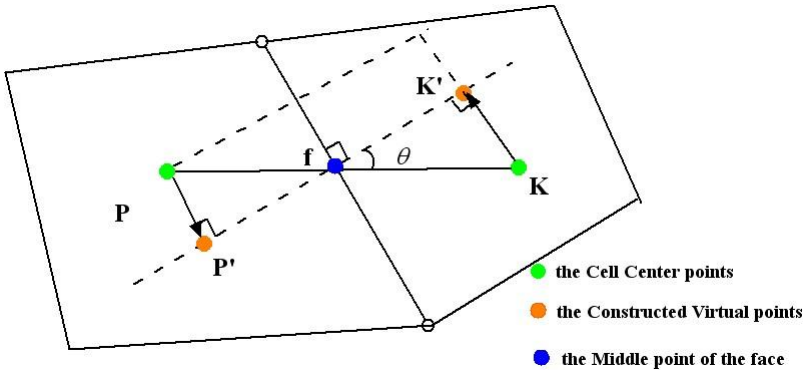

Figure 3-11. No skewness on the surface

The unit vector from f to the top nodal point is defined as $\vec{l}$. The relationship $\overrightarrow{PP'}//\overrightarrow{KK'}//\vec{l}$ is valid. From Figure 3-11, it is easy to demonstrate that the triangle $PP'f$ is similar to $KK'f$. So

$$\frac{\left|\overrightarrow{PP'}\right|}{\left|\overrightarrow{KK'}\right|}=\frac{\left|\overrightarrow{Pf}\right|}{\left|\overrightarrow{Kf}\right|}=\frac{\left|\overrightarrow{P'f}\right|}{\left|\overrightarrow{K'f}\right|}=p \tag{3-34}$$

where p is a ratio coefficient.

Due to the following geometric relationships,

$$|Pf|+|Kf|=|PK|=\xi \tag{3-35}$$

$$|KK'|=|Kf|\sin\theta,\ |PP'|=|Pf|\sin\theta \tag{3-36}$$

and the interpolation formula,

$$(\nabla\phi)_f=\frac{|fK|}{|PK|}(\nabla\phi)_P+\frac{|Pf|}{|PK|}(\nabla\phi)_K \tag{3-37}$$

the second term of the right-hand side of Eqn.(24) can be rewritten as,

$$\begin{aligned}S_f\frac{(\nabla\phi)_K\cdot\overrightarrow{KK'}-(\nabla\phi)_P\cdot\overrightarrow{PP'}}{\xi\cos\theta}&=S_f\frac{(\nabla\phi)_K\cdot\vec{l}|KK'|-(\nabla\phi)_P\cdot\vec{l}|PP'|}{\xi\cos\theta}\\&=S_f\frac{\left(|fK|(\nabla\phi)_K-|Pf|(\nabla\phi)_P\right)\cdot\vec{l}\sin\theta}{\xi\cos\theta}\\&=S_f\tan\theta(\nabla\phi)_f\cdot\vec{l}\end{aligned} \tag{3-38}$$

The above equation is strictly identical to the cross diffusion term in Eqn. (3-23). Summarizing Eqn.(C-13) and Eqn.(3-38), we can reach the conclusion that the coordination transformation method (CTM), the improved deferred correction (IDC) of the normal decomposition method

(NDM) and the Perić's direct gradient evaluation method (DGEM) lead to equivalent schemes for diffusion flux computations, when no skewness arises in the mesh.

Case 2: Skewness situation

Unfortunately, no skewness is more the exception than the rule. In most of arbitrary meshes or with no special care in the grid generation process, grid skewness arises. In that case, the equivalence between the IDC scheme, DGEM and CTM vanishes.

Before further discussion, we shall design another version of DGEM. To derive it, we first draw the line L_2 which is perpendicular to the surface S_f and crosses it at the intersection point f'. Then, the locations of virtual points K'' and P'' are defined following the relationship, $\overrightarrow{KK''} \perp L_2$ and $\overrightarrow{PP''} \perp L_2$, see Figure 3-12. The interpolation of ϕ at these virtual points is still based on Eqn.(C-11a) and Eqn.(C-11b). Thus the final diffusive flux is computed as,

$$S_f (\nabla\phi)_f \cdot \vec{n} = S_f \frac{\phi_K - \phi_P}{\left|\overrightarrow{K''P''}\right|} + S_f \frac{(\nabla\phi)_K \cdot \left|\overrightarrow{KK''}\right| - (\nabla\phi)_P \cdot \left|\overrightarrow{PP''}\right|}{\left|\overrightarrow{K''P''}\right|} \tag{3-39}$$

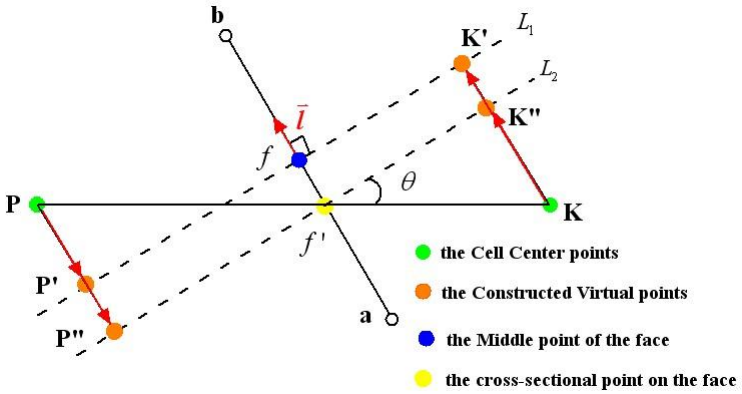

Figure 3-12 Skewness and virtual points of modified direct gradient evaluation (MDGE) method

We should name this new version as modified direct gradient evaluation (MDGE) method. Through similar analysis of the previous section of no skewness situation, we found that this new method is exactly equivalent to IDC scheme in any case.

To compare the accuracy of IDC scheme and DGEM method, we investigate the difference between the two methods. By subtracting Eqn.(3-39) from Eqn.(C-12), the following expression is obtained,

$$\varpi = S_f \frac{(\nabla\phi)_K \cdot \overrightarrow{KK'} - (\nabla\phi)_P \cdot \overrightarrow{PP'}}{\left|K'P'\right|} - S_f \frac{(\nabla\phi)_K \cdot \overrightarrow{KK''} - (\nabla\phi)_P \cdot \overrightarrow{PP''}}{\left|K'P'\right|} \tag{3-40}$$

Considering $\left|\overrightarrow{K'P'}\right| = \left|\overrightarrow{K''P''}\right| = \left|\overrightarrow{KP}\right|\cos\theta = \xi\cos\theta$, and $\overrightarrow{PP'} // \overrightarrow{PP''} // \overrightarrow{KK'} // \overrightarrow{KK''} // \vec{l}$, the above equation can be simplified as,

$$\varpi = S_f \frac{(\nabla\phi)_K \cdot \overrightarrow{K''K'} - (\nabla\phi)_P \cdot \overrightarrow{P''P'}}{\xi \cos\theta} = \frac{\left((\nabla\phi)_K - (\nabla\phi)_P\right) \cdot \vec{l}\,|ff'|}{\cos\theta} \tag{3-41}$$

Dividing the difference ϖ with the whole non-orthogonal correction term, we obtain the relative error ε_r:

$$\varpi = \frac{\left((\nabla\phi)_K - (\nabla\phi)_P\right) \cdot \vec{l}\,|ff'|}{(\nabla\phi)_K \cdot \overrightarrow{KK'} - (\nabla\phi)_P \cdot \overrightarrow{PP'}} = \frac{\left((\nabla\phi)_K - (\nabla\phi)_P\right) \cdot \vec{l}\,|ff'|}{\left((\nabla\phi)_K \cdot |KK'| + (\nabla\phi)_P \cdot |PP'|\right) \cdot \vec{l}} \tag{3-42}$$

It is straightforward to show that the difference is much smaller than the whole non-orthogonal correction. It means that the accuracy of the IDC scheme and the Peric's DGEM is almost similar and that the accuracy is directly driven by the accuracy of the gradient evaluation method.

We should specially point out that the link between the three methods is very deep. With the link we established between the three methods we can expect that the CTM and the Peric's DGEM can also be successfully applied for extremely skew meshes.

Through numerical tests we presented in test section, we obtained the following conclusions:

(i) The coordinate transformation method (CTM) is mathematically equivalent to the improved deferred correction (IDC) but the particular implementation of IDC performs better than CTM especially in terms of accuracy.
(ii) The only advantage of CTM on its counterparts is its lower computational cost.
(iii) CTM which is widely used in modern CFD is turned out to be the most ineffective one on highly skewed grid.
(iv) In the case of no skewness, the CTM, the IDC and the Perić's direct gradient evaluation method DGEM lead to equivalent schemes for diffusion flux calculation.
(v) In presence of skewness there is a slight difference between IDC and DGEM in favour of IDC. But the accuracy and computational cost of the two methods are very close to each other.

It should be pointed out that the origins of error sources for the three above mentioned methods are different. For CTM, the main errors are (1) skewness-induced error, (2) nodal value interpolation error while for IDC and DGEM, the lack of accuracy of the gradient computation method is the main error source. In addition, all above derivation process is based on 2D general meshes, and the relationship among these methods with 3D non-orthogonal is one future research point.

3.3.2.4 Extension of the IDC scheme to 3D problems

Before to present some 3D results, we shall first describe in details how the 3D extension of IDC must be handled. The starting point of the method is based on the normal vector decomposition (see section 3.2.2.1) such as:

$$\vec{n}_f = \vec{n}_1 + \vec{n}_2 \tag{3-42}$$

with $\vec{n}_1 = \frac{1}{\cos\theta_f}\vec{\hat{e}}_1$ and $\vec{n}_2 = \tan\theta_f \vec{\hat{e}}_2 = \vec{n}_f - \frac{1}{\cos\theta_f}\vec{\hat{e}}_1$

For an efficient implementation the cosine of angle θ_f between $\vec{n}_f$ and $\vec{\hat{e}}_1$ is determined from the dot product between these to unit vectors which are obtained from the metrics.

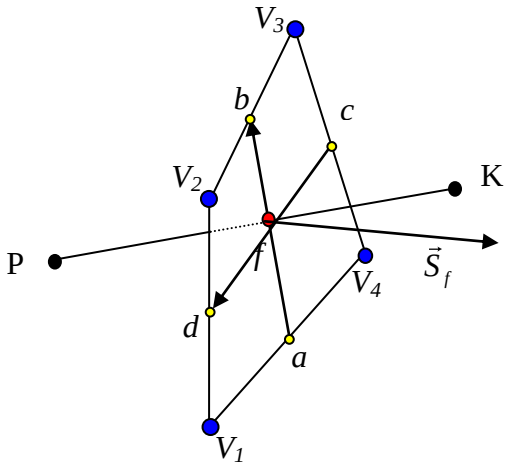

Figure 3-12. 3D metrics calculations

$\vec{n}_f = \frac{\vec{S}_f}{\|\vec{S}_f\|}$ with $\vec{S}_f = \overrightarrow{ab} \wedge \overrightarrow{cd}$ where the coordinates of points *a,b,c,d* are deduced from the coordinates of the vertices V_1, V_2, V_3, V_4

$$\vec{\hat{e}}_1 = \frac{\overrightarrow{PK}}{\|\overrightarrow{PK}\|}$$

Thus finally the deferred correction term $S_f \left(\nabla\phi\right)_f^{old} \cdot \vec{n}_2$ takes the form:

$$S_f \left(\nabla\phi\right)_f^{old} \cdot \left(\vec{n}_f - \frac{\vec{\hat{e}}_1}{\vec{n}_f . \vec{\hat{e}}_1} \right)$$

And at this stage all the needed quantities are known to compute this term in 3D.

In the numerical test sections, several 3D Poisson problems with well selected non-orthogonal grids are used to evaluate the effects of gradient evaluation methods, compare different boundary condition implementation methods and verify the effectiveness of the extension approach.

3.3.3 Temporal discretisation schemes

There are two kinds of time marching approaches for unsteady EHD problems. For Navier-Stokes equations, the implicit formulation is preferred considering the convergence speed.

The first-order Euler implicit (IE) method and the implicit three level (I3L) second-order method are implemented within our Navier-Stokes flow solver. The second-order approximation of the temporal derivative is [70, p142]:

$$\frac{\partial \phi}{\partial t} = \frac{3\phi^n - 4\phi^o + \phi^{oo}}{2\Delta t} \tag{3-43}$$

Note that we need to use other methods to start the calculation, which is the role of the Implicit Euler method in our solver.

For charge conservation equation which is a classic hyperbolic equation if neglecting the diffusion mechanism, the selection of temporal scheme is not straightforward. To solve this equation, the method of line (MOL) approach is considered for its robustness and algorithmic simplicity when extending to multi-dimensional problems.

The MOL approach means the space and time discretization are considered separately. Following this approach, the time-dependent partial differential equations (PDEs) is first discretized with regard to the spatial variables to obtain a semi-discrete form,

$$\frac{\partial \phi}{\partial t} = L(\phi) \tag{3-44}$$

Here, L is a spatial operator.

This is then an ordinary differential equation (ODE) system regarding time, which can be solved by any ODE method. However, the selection of an appropriate time scheme is faced by the following considerations:

1. The time discretization is able to maintain the strong stability in the same norm as the first order forward Euler version. In other words, when combining with some suitable non-linear spatial schemes, like TVD, ENO and WENO, the numerical solution obtained typically does not exhibit nonlinear instabilities (oscillation-free).

2. The influence of temporal discretisation on the accuracy of the solution should be as small as possible. It is well known that accuracy of the solution for time-dependent problems does not only depend on the spatial formulation but also on the way the rate of unsteady term is represented [241]. To put in simple terms, we need to find a higher order time scheme.

3. The time step restriction should not be too tight. For Euler Explicit, an important drawback is the Courant number limit (Courant et al. [242]). The Courant number is defined as:

$$C_O = \frac{\vec{U}_f \cdot \vec{d}}{\Delta t} \tag{3-45}$$

where $\vec{U}_f$ is the velocity vector at a cell face, while $\vec{d}$ is the distance vector between the two control volumes sharing the face. If the Courant number is larger than unity, the explicit system becomes unstable. For a given velocity field and grid system, this condition sets the biggest possible time step Δt_{FE}.

4. The computational cost and memory requirement. For large scale scientific computing in three space dimension, storage is an important consideration.

It is difficult to design a scheme satisfying all requirements listed above. In the present study, we mainly focus on accuracy and computational cost. The special consideration for computational speed is because, in EHD system simulation, like ionic injection, gas discharge, the real physical time is very short. For low stage RK methods, which only require 2 or 3 storage units per ODE variable, please refer to [104] and [243].

3.3.3.1 Explicit Euler, Implicit Euler, Crank-Nicolson and Implicit Three-Level schemes

To perform a systematic comparison, we introduce various time integration schemes whose performance regarding the accuracy, time step restriction and computational cost will be examined in the following sections. In [68, page 87-92], the author did some preliminary analysis and compared the numerical diffusion induced by four widely used time schemes, i.e., Explicit Euler (EE), Implicit Euler (IE), Crank-Nicolson (CN) and the implicit three time level (I3L). Here, we are more concern with the property which can guarantee that the final solutions are oscillation-free (i.e., strong stability preserving, SSP).

Explicit and Implicit methods for form (3-44) can be written in general as,

$$\frac{\phi^{n+1}-\phi^{n}}{\Delta t}=\eta L(t^{n+1},\phi^{n+1})+(1-\eta)L(t^{n},\phi^{n}) \qquad (3\text{-}46)$$

where t^n represents the n^{th} time step. With different choices, one obtains several schemes which are given in Table 3-4.

Table 3-4. Various time marching schemes

η	**Scheme**	**Order**	**Type**
0	Explicit Euler (EE)	1	Explicit
1	Implicit Euler (IE)	1	Implicit
1/2	Crank-Nicolson (CN)	2	Implicit

Firstly, we summarized some useful conclusions about the SSP property for these four schemes.

1. Euler Explicit

When the TVD-type monotonic scheme is first proposed by Roe [75] and Harten [76] for hyperbolic equations, it appears as a mixture form with Euler Explicit as the time scheme. The well-known flux-limiter form and the $r-\psi$ diagram [76] (region of limiters for explicit TVD scheme, see Figure a) are based on Euler Explicit scheme. In other words, using the Euler Explicit as the time scheme is a natural choice when applying TVD schemes.

2. Euler Implicit

For steady flow computation, implicit schemes are preferred. In [80], the spatial terms are divorced entirely from the temporal discretization and the basic flux-limiter formulation is derived for the convective term. In [85], Zijlema and Wesseling systematically analyzed the conditions and region of limiters for implicit (Euler Implicit) TVD scheme and found that Sweby's TVD region in the Flux-Limiter diagram is entirely contained in the new region, see Figure 3-12. That is, all TVD schemes which are designed based on the Euler Explicit scheme can also be used together with the Implicit Euler scheme to obtain oscillation-free results. Same conclusion was reached from theoretical mathematics field [244][245].

3. Crank-Nicolson and Implicit Three-Level

The Crank-Nicholson temporal scheme is unconditionally stable, but does not guarantee boundedness of the solution [66, p89]. For the Implicit Three-Level, (3-43), again, the boundedness of the solution cannot be guaranteed [110, p.142, 66, p91]. This point can be understood in this way: if we view time as a special space dimension, the I3L scheme is some kind of linear high-order scheme, which can lead to oscillating results. However, all numerical tests results of next sections do not support the claim that 'CN method does not guarantee boundedness of the solution'.

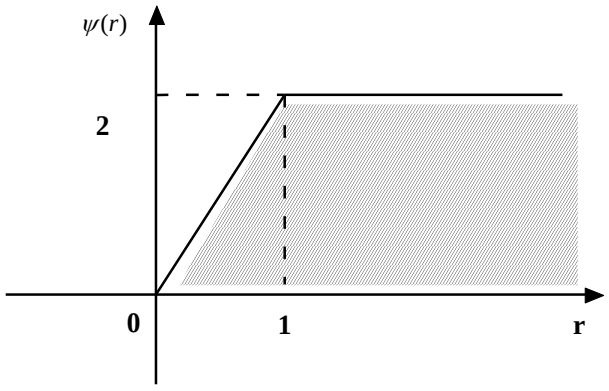

Figure 3-13. Region of limiters for explicit TVD schemes

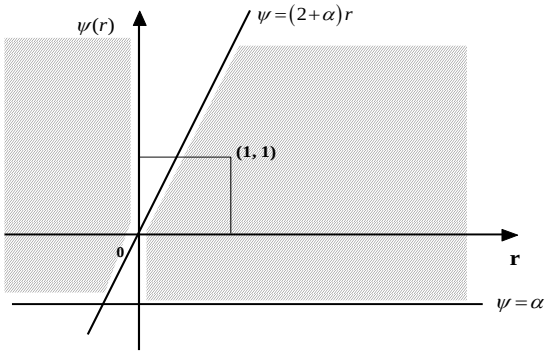

Figure 3-14. Region of limiters for implicit TVD schemes

3.3.3.2 Strong stability preserving (SSP) high order time scheme

From a stability analysis point of view, to obtain oscillation-free solution is equivalent to preserve the strong stability of the solution. The strong stability preserving (SSP) methods are specially designed for hyperbolic problems with discontinuous solutions. When a spatial nonlinear scheme

and the forward Euler scheme are applied to the convective and temporal terms, if the solutions are guaranteed to be bounded, we can expect that when the same convective scheme and a SSP scheme are applied to the same problem, the solutions will also be well bounded.

These time schemes were first developed in [96] and [97] and were called TVD time discretizations. They were further developed in [246]. Ref. [104] is the latest review which summarizes optimal explicit and implicit SSP Runge-Kutta and multistep methods, for linear and nonlinear problems. In fact, along the discovery of connections between SSP theory and contractivity theory, new optimal and efficient SSP methods were developed [104]. However, considering the accuracy order of Finite Volume method and spatial discretisation schemes, it is no necessary to combine a time scheme higher than 3rd order.

The essential idea of SSP methods can be explained with two steps. Firstly, with the method of lines, it is assumed that the first order forward Euler time discretisation of ODE is strongly stable under a certain norm when the time step Δt is suitably restricted. Then, the task is to try to find a higher order time discretization (Runge-Kutta or multistep) that maintains strong stability for the same norm, perhaps under a different time step restriction.

$$\Delta t \le c\Delta t_{EF} \tag{3-47}$$

where Δt_{EF} is the time step dictated by the Courant-Friedrichs-Levy (CFL) condition for EE method and c can be considered as a CFL coefficient.

In the present thesis, two best known explicit SSP Runge-Kutta methods were implemented in our charge density solver, the two-stage second-order and three-stage third-order optimal explicit SSPRK schemes [104]. These two schemes are optimal among all Runge-Kutta methods with their respective order and number of stages [247].

SSPRK (2, 2): The optimal second order TVD Runge- Kutta method is given by,

$$\phi^{(1)} = \phi^n + \Delta t L\left(\phi^n\right)$$

$$\phi^{n+1} = \frac{1}{2}\phi^n + \frac{1}{2}\phi^{(1)} + \frac{1}{2}\Delta t L\left(\phi^{(1)}\right),$$

with a CFL coefficient $c = 1$ in Eqn.(3-45).

SSPRK (3, 3): The optimal third order TVD Runge- Kutta method is given by,

$$\phi^{(1)} = \phi^n + \Delta t L\left(\phi^n\right)$$

$$\phi^{(2)} = \frac{3}{4}\phi^n + \frac{1}{4}\phi^{(1)} + \frac{1}{4}\Delta t L\left(\phi^{(1)}\right)$$

$$\phi^{n+1} = \frac{1}{3}\phi^n + \frac{2}{3}\phi^{(2)} + \frac{2}{3}\Delta t L\left(\phi^{(2)}\right),$$

with a CFL coefficient $c = 1$ in Eqn.(3-45).

The latter method is widely known as the Shu-Osher method, and is probably the most commonly used SSP RK method. It is an explicit scheme, of third order and the algorithm is simple. It should be pointed out that fourth-order accuracy has only been obtained at the additional expense of introducing two additional evaluations of a related operator, leading to suboptimal efficiency, both in terms of time-step restriction and memory usage.

Another relevant question is: can we find an efficient implicit high-order scheme to obtain oscillation-free solution, without time step limitation? The answer is negative. Even for optimal implicit SSP Runge-Kutta methods, there is some finite time step restriction for schemes to be unconditionally strongly stable [104]. However, implicit SSP method may have significantly large upper limit for time step than those of explicit methods with the same order and number of stages. The question is the computational cost required in the implicit solution is much bigger than explicit solution, especially combined with deferred correction (DFC) technique.

In the next sections, three numerical test cases will be first introduced. Then, some numerical tests were performed for two goals: (1) the need for careful selection of time scheme to obtain completely oscillation-free solution; (2) the comparison of different time schemes coupled with TVD-type high resolution schemes.

3.4 Algorithms for velocity-pressure coupling

The discretisation of all terms in the generic transport equation, Eqn.(3-1), have been described in the preceding sections. The same principles would apply to the terms of the Navier-Stokes equations with some additional problems which require further treatment.

Without any loss of generality, we use the two-dimensional case to describe the algorithm for the coupling between the pressure and velocity fields. Let us consider a laminar steady flow of an incompressible Newtonian fluid in an arbitrary two-dimensional domain described by the well-known Navier-Stokes equations:

$$\frac{\partial u_i}{\partial x_i} = 0 \tag{3-48}$$

$$\frac{\partial u_i}{\partial t} + u_j \frac{\partial u_i}{\partial x_j} = \frac{\partial}{\partial x_j}\left[\nu\left(\frac{\partial u_i}{\partial x_j} + \frac{\partial u_i}{\partial x_i}\right)\right] - \frac{1}{\rho}\frac{\partial p}{\partial x_i} \tag{3-49}$$

where u_i are the velocity vector components with respect to the Cartesian co-ordinates x_i, p is the pressure, ν is the kinematic viscosity and ρ is the density.

In the segregated approach, the above equations are solved in sequence. However, some attention is required for the calculation of the pressure field. On the one hand, pressure field makes contribution to the momentum equations by its gradient. On the other hand, the continuity equation does not have a dominant variable. A specific way should be used to deal with inter-equation coupling in calculation of the Navier-Stokes equations. This is done by modifying the continuity

equation into an equation for pressure [115]. Derivation of the pressure equation for the collocated variable arrangement is well explained in [70].

The SIMPLE Algorithm

In the present study, the approach used to handle the velocity-pressure coupling is SIMPLE algorithm proposed by Patankar [115]. SIMPLE stands for Semi-Implicit Method for Pressure-Linked Equations. The SIMPLE algorithm is widely used for both steady-state and transient calculations. Here, we neglect an extensive description of the algorithm, as it can be found in standard text books, like [47] and [70]. Only the basic idea and an outline of the sequence of calculations are provided. The solution procedure consists of three main steps:

Step 1: **Momentum predictor**. The velocity field is computed from the momentum equation by using the pressure and velocity from the previous iteration or the initial guess. For transient computation, the solution of previous time step is the natural choice for the initial guess. The equation should be under-relaxed with a factor, α_U $(0 < \alpha_U < 1)$, in an implicit manner.

Step 2: **Pressure solution**. The pressure correction equation is formulated and solved in order to obtain the new pressure distribution.

Step 3: **Velocity and pressure correction**. With the new pressure field, a new field of conserved fluxes is calculated using Eqn.(3-51). The associated velocity field which satisfies continuity is updated with the pressure gradient at the new iteration, but does satisfy the momentum equation until the overall process has converged. The solution of the pressure field also needs to be under-relaxed with the pressure-relaxation factor, $\alpha_p (0 < \alpha_p < 1)$, but in an explicit style,

$$p^{new} = p^{old} + \alpha_p (p^p - p^{old}) \qquad (3\text{-}50)$$

where p^p is the solution of the pressure equation, p^{old} is the solution from previous iteration or an initial guess. p^{new} stands for the pressure field for the next iteration.

After the third step, a checking of the convergence criterion for all equations is needed. If the system has not converged, we go back to step 1 and a new iteration continue.

For transient flows, an extra time stepping loop is needed. In each time step, the SIMPLE loop starts with the previous values of velocity and pressure and iterates till the convergent condition is met. The energy equation can be solved after step 3, using the corrected fluxes and velocities. It can also be solved after the whole procedure of velocity and pressure field.

Pressure correction equation for non-orthogonal meshes

The SIMPLE-algorithm needs to be modified when the grid is non-orthogonal and/or unstructured [70, page 247]. A complete derivation of the pressure-correction with non-orthogonal meshes in collocated grid system can be found in [128] and [70, page 247-250].

A one step method (Eqn.(8.61) in [70]) is incorporated in our solver. However, the IDC scheme we developed originally for the discretisation of diffusion terms is also used to solve the pressure correction equation on extremely distorted meshes. It is expected this application can reduce the convergence time for problem with non-orthogonal grids. The SIMPLE algorithm with IDC scheme for pressure correction equation may works for extremely skewed non-orthogonal meshes. Some preliminary comparisons with different surface decomposition schemes for the pressure correction equation have been done in [248].

Rhie-Chow Interpolation

Evaluating cell face velocity simply by arithmetic averaging neighbour cell velocities may lead to unphysical checker-boarder pressure field for collocated grid systems. To overcome the difficulty, Rhie-Chow [249] proposed a momentum interpolation method (MIM) with subsequent refinements by Perić [220]. Some improvements were made to alleviate or solve the drawbacks of original MIM of Rhie and Chow, like under-relaxation factor-dependence [250][251][253] and time step size-dependence [252][253][254]. However, the original MIM works well for most of the situations and will be adopted in the present study.

The formula proposed by Rhie and Chow is to express the mass flux at a cell as

$$F_j = \rho_j A_j \overline{\vec{u}_j} \cdot \vec{n} + \rho_j A_j \overline{\left(\frac{\Delta V}{A_p^u}\right)} \left(\left(\overline{\nabla p}\right)_j \frac{\overrightarrow{PK}}{\left|\overrightarrow{PK}\right|} - \frac{p_P - p_K}{\left|\overrightarrow{PK}\right|} \right) \frac{\left|\overrightarrow{PK}\right|}{\vec{n} \cdot \overrightarrow{PK}} \tag{3-51}$$

where the overbar denotes the interpolation from the neighbor cell values. The detail derivation procedure for above equation is referred to in Rhie and Chow [249].

Under-relaxation

To reduce the variation between two consecutive iterated solutions, under-relaxation is a common practice in all iterative process. Considering its importance, a short introduction is made below. For example, once the final discretised equations from the generic equation is obtained,

$$A_P \phi_P + \sum_{j=neighbours} A_j \phi_j = B$$

where A_P and A_j are the coefficients, B is the source term. The above equations was under-relaxed in an implicit manner,

$$A_P{}^* \phi_P + \sum_{j=neighbours} A_j \phi_j = B + \frac{1-\alpha}{\alpha} A_p \phi_P^0 \qquad \text{and} \qquad A_P{}^* = \frac{1}{\alpha} A_P$$

where α is the under-relaxation factor and ϕ_P^0 is the value from previous iteration.

Perić [128] analyzed the under-relaxation process and recommended the following relationship,

$$\alpha_p = 1.1 - \alpha_U$$

$\alpha_p = 0.2$ for the pressure and $\alpha_U = 0.8$ for momentum.

This relationship is valid for both orthogonal and nonorthogonal grids when the full pressure-correction equation is employed. When the one step method is applied to the pressure correction with nonorthogonal grids, the optimum α_p should be smaller than 0.2 [128].

3.5 Numerical Tests

In this section, numerical results will be presented. We shall start with the comparison of various high-resolution convection differencing schemes. A comparison of the HR schemes coupled with various time marching algorithms will be given in Section 3.5.2. The importance of gradient evaluation method for surface decomposition scheme is highlighted in Section 3.5.3. The numerical verifications of new methods for both Dirichlet and Neumann boundary condition treatment with IDC scheme are presented in Section 3.5.4. Finally, an example to show the extension of IDC scheme to three-dimensions is given.

3.5.1 Comparison of various high-resolution schemes with flux limiters

A number of schemes (High-resolution and traditional linear schemes) were implemented within our numerical code. All solutions here were obtained using a version of Stone's strongly-implicit (SIP) algorithm [255]. The implementation was carried out with the aid of a deferred-correction approach [238]. To validate the effectiveness and compare the performance of HR schemes, two test problems were considered: advection of a step profile and the Smith and Hutton problem [256]. The model problem is the linear, scalar convection equation:

$$\nabla \cdot \left(\vec{U} \cdot \phi\right) = 0 \qquad (3\text{-}52)$$

where ϕ is a scalar variable being convected by a velocity field $\vec{U}(x, y)$.

Problem 1 Advection of a step profile

Figure 3-15(left) shows the well known benchmark test problem consisting of a pure advection of a transverse step profile imposed at the inflow boundaries of a square computational domain. The background velocity field is $\vec{U}(x, y) = 1\vec{i} + 1\vec{j}$. Several different grid sizes were used, starting from a 20×20 coarse grid and ending with a 240×240 fine grid, to estimate the order of accuracy. However, only the results with 80×80 meshes were illustrated in Fig.3-15 (right).

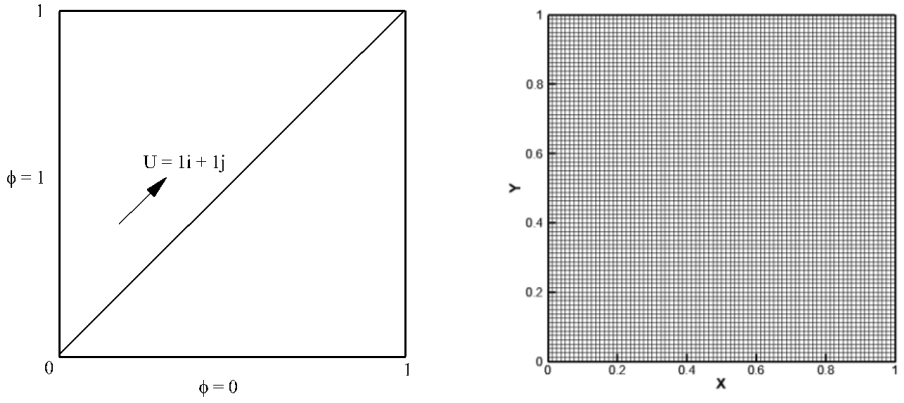

Figure 3-15. (left) physical problem (right) uniform 80×80 mesh system

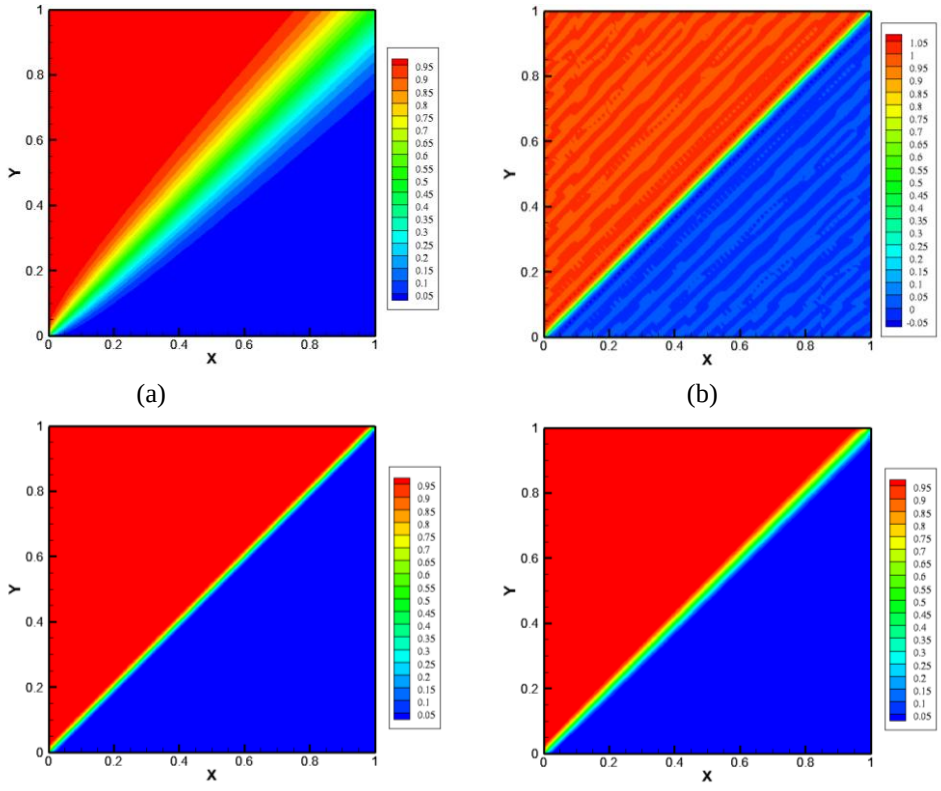

Figure 3-16. Comparison of scalar variable of different schemes (a) FUD (b) CD (c) SUPERBEE and (d) SMART

The computed values of ϕ using FUD, CD, SUPERBEE and SMART schemes are shown in Figure 3-16. It is immediately noticed that the solution from the FUD scheme is extremely inaccurate. The CD scheme produces results with strong oscillations. On the other hand, the two TVD-type HR schemes, namely SUPERBEE and SMART, dramatically improved the results compared to the result of FUD. Clearly, the SUPERBEE yields to the best results because of its highly compressive property. Through with this simple example, we verify that the HR schemes can lead to high accurate and bounded solutions. It should be noted that, under-relaxation technique is a must for some schemes, like SMART in this case. The need of under-relaxation for some HR schemes comes from two aspects: (1) the difference between CBC and TVD criteria [257][258]; (2) the possible non-smooth transitions in NVD [71].

Problem 2 Smith and Huttom problem

In the second test problem, shown schematically in Fig.3-17, a step discontinuity at $x=-0.5$ is convected clockwise from the inlet plane $(x<0, y=0)$ to the outlet plane $(x>0, y=0)$ by a rotational velocity field

$$\vec{U}(x,y)=\begin{Bmatrix}u\\v\end{Bmatrix}=\begin{Bmatrix}2y(1-x^2)\\-2x(1-y^2)\end{Bmatrix} \tag{3-53}$$

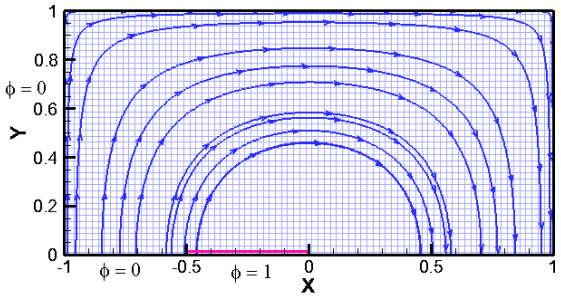

Figure 3-17. Physical domain and grid system for the Smith-Hutton problem

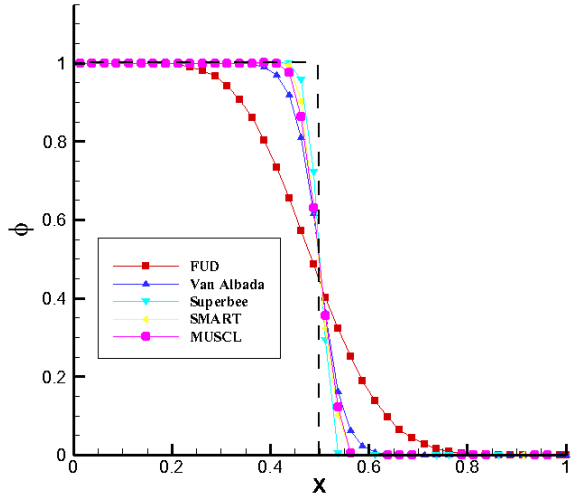

Figure 3-18. Scalar variable profile at exit from the domain, $y=0$

Results are displayed in Fig.3-18. The numerical results obtained with the HR schemes are better than those achieved with FUD. The SUPERBEE, the SMART and the MUSCL scheme profiles are nearly similar. The result with Van Albada scheme is a bit diffusive, but as much as FUD.

Problem 3 Advection of a cubic in a constant flow

In [259], we compare the effectiveness, accuracy and computational cost of more than 20 high-resolutions schemes (the limiter function can be found in Appendix A) when applying to the unsteady pure convection. All the schemes were tested by three one-dimensional problems: (1) sin-profile (2) step-profile (3) semi-ellipse, and four two-dimensional problems: (4) smooth initial data test (5) advection of a square shaped scalar field (6) solid body rotation (7) swirling

deformation flow test and two three-dimensional problems: (8) advection of a cubic in a constant flow (9) advection of a sphere in a turning roller flow. We found that all these high-resolution schemes can avoid the traditional high-order schemes' oscillation problem and can largely improve the accuracy of the results in different dimensions and under different background flow fields. Moreover, there are significant differences of accuracy and computational cost among different schemes. To summarize all the test results, the MUSCL, SMART and UMIST schemes are recommended. Besides, it is also observed that there are two serious limitations of the extension method: (i) low CFL number (ii) lack of cross-terms' approximation. Both limitations get more obvious along with the dimension of the problem which will seriously affect the effectiveness and accuracy of the extension method. An example is given below to highlight the necessary of HR schemes in 3D flow problems. The problem considered here is the unsteady linear equation. The background flow is constant in time and space,

$$u = 1, \quad v = 1 \quad \text{and} \quad w = 1. \tag{3-53}$$

And the initial data is,

$$q(x, y, z, 0) = \begin{cases} 1 & |x - 0.2| < 0.05, |y - 0.2| < 0.05, |z - 0.2| < 0.05 \\ 0 & otherwise \end{cases} \tag{3-54}$$

The spatial domain is $1 \times 1 \times 1$. The time step is $\Delta t = 5 \times 10^{-4}$ and we compute up to time $t = 0.5$. The small time step has been taken here to reduce the temporal discretization error. The cell size is 0.0125 (80 cells). Figure 3-19 shows the initial condition and the final solutions for the FUD and SMART schemes. The maximum values of SMART and FUD are 0.329 and 1.0, and the minimum values are 0.0. It is noticed that the shape of the variable distribution is well kept by the SMART scheme.

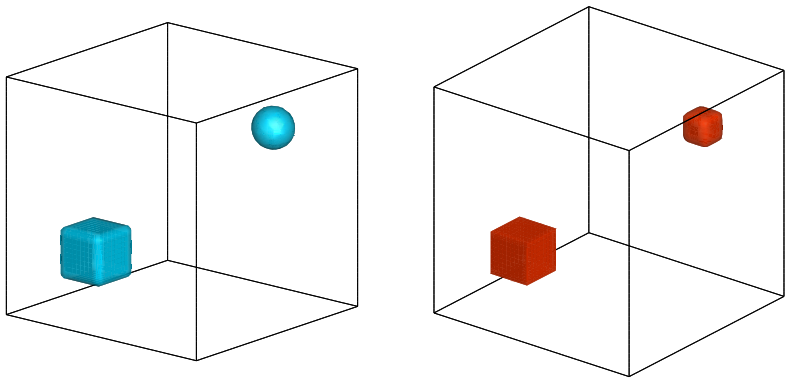

Figure 3-19. Numerical results with the advection of a cubic in a constant flow test (left) FUD, iso-value = 0.25 (b) SMART, iso-value = 0.9

3.5.2 Comparison of temporal schemes combined with HR schemes

The two-dimensional pure advection problems are considered for the comparison,

$$\frac{\partial \phi}{\partial t}+\frac{\partial (u\phi)}{\partial x}+\frac{\partial (v\phi)}{\partial y}=0 \qquad (3\text{-}54)$$

where ϕ is the scalar, and u and v are the two velocity components. This is an ideal problem for examining the performance of both convection schemes and temporal discretisation methods.

For space discretisation, the unified approach for TVD-type high-resolution is considered. All the discretization considered will be "dimensionally split", that is 2D and 3D implementations will consist of one-dimensional schemes applied separately along each of the grid directions.

It should be pointed out that this extension method for high-resolution schemes will not introduce the possibility of oscillation in the final solution. Detailed derivation can be found in [79] and [87]. With respect to this rule, the only possible resource for oscillation is the time scheme.

For implicit schemes, the DFC technology is used and the stopping criterion is set as $\left\| \frac{\phi^{n+1}-\phi^{n}}{\phi^{n}} \right\| \le \varepsilon = 1.0\times 10^{-7}$. The classic SIP solver is used as the linear system solver. Three classical test cases are considered. All the following test cases could provide the true solution no matter the flow structure, which lower the difficulties of accuracy evaluation.

Case I: Advection of a square-shaped scalar field

This is a classical test case for convection scheme test as it presents an increased number of discontinuities. In this case, a scalar square field is advected by a constant velocity field, directed at a $45°$ angle respect to the mesh directions. The domain is 1×1 units, while the size of the square field is 0.25 × 0.25 units. The maximum and minimum values of the field are $\phi_{\max}=10.0$ and $\phi_{\min}=0.0$, respectively. The field is advected for a length equal to 0.5 units from its initial location to the opposite corner of the domain. The u and v velocities are both equal to 1 unit.

Case II: Rotation of a cone-shaped scalar field

In this case, an initial distribution of scalar (consists of smooth hump, cone and slotted cylinder) is advected around by a stationary (in time) velocity field. The size of the domain is 1 unit by 1. The computational domain and the initial distribution can be seen in Figure 3-20.

Hump: $q(x,y,0)=\frac{1}{4}(1+\cos(\pi\cdot\min(r(x,y),1)))$, Cone: $q(x,y,0)=1-r(x,y)$

Slotted cylinder: $q(x,y,0)=\begin{cases}1 \ if & |x-x_0|<0.25 \ or \ |x-x_0|<0.25\\ 0 & otherwise,\end{cases}$

where $r(x,y)=\frac{1}{r_0}\sqrt{(x-x_0)^2+(y-y_0)^2}$.

The center of hump, cone and cylinder is (0.25, 0.5), (0.5, 0.25) , (0.5, 0.75) respectively. The background flow is constant, with a fixed angular velocity $\omega=2.0$ units,

$$u = -(y - 1/2), \quad v = (x - 1/2)$$

Case III: Swirling deformation flow [60]

As the performance of different schemes could depend on the structure of the velocity field, a swirling deformation flow problem is considered here,

$$u = \sin^2(\pi x)\sin(2\pi y)g(t) \quad v = -\sin^2(\pi y)\sin(2\pi x)g(t)$$

This flow satisfies $u = v = 0$ on the boundaries of the unit square. The function $g(t)$ is used to introduce time dependence in the flow field. Here we use, $g(t) = \cos(\pi t / T)$.

on the time interval $0 \le t \le T$. The flow slows down and reverses direction in such a way that the initial data could be recovered at time T: $\phi(x, y, T) = q(x, y, 0)$.

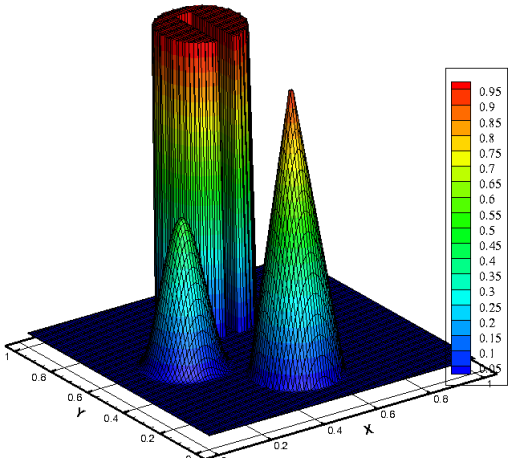

Figure 3-20. Initial condition for solid body rotation and flow swirling tests

The need of SSP method

In [246], an illustrative example with the Burgers equation (nonlinear equation) was presented to show the possible oscillations when non-TVD Runge-Kutta method are coupled with TVD spatial discretization. The objective of the following test example is to show that the same possible oscillation may appear for 2D linear advection equation.

The limiter function is MUSCL scheme. The advection of a square-shaped scalar field is used. Two grid sizes are considered, 40×40 and 80×80. The maximum and minimum values are recorded. A desired scheme should not allow final solution bigger or smaller than initial largest and smallest values. In addition, the RMS errorreflects the overall performance of each scheme and is defined as follow:

$$RMS = \frac{\sqrt{\sum_{ij} \left(\phi_{i,j\,\text{predicted}} - \phi_{i,j\,\text{exact}}\right)^2}}{\text{number of nodes}}$$

The non-TVD scheme we use is borrowed from [246],

$$\phi^{(1)} = \phi^n - 20\Delta t L\left(\phi^n\right)$$

$$\phi^{n+1} = \frac{1}{2}\phi^n + \frac{41}{40}\Delta t L\left(\phi^{n)}\right) - \frac{1}{40}\Delta t L\left(\phi^{(1)}\right),$$

From Table 3-4, we can clearly see that the non-TVD and I3L results are oscillatory (presence of undershoot). On the other hand, the TVD Runge-Kutta method guarantees that the final solution is oscillation-free. This numerical test further supports the opinion 'It is much safer to use a SSP Runge-Kutta method', even for linear PDE problem.

Table 3-4. Performance of TVD and non-TVD time schemes

	40×40 grid			80×80 grid		
	Max.	**Min.**	**RMS error**	**Max.**	**Min.**	**RMS error**
TVD 2nd RK	10.000	0.000	2.165×10^{-2}	10.000	0.000	9.750×10^{-3}
Non-TVD 2nd RK	9.993	**-1.153×10^{-4}**	2.452×10^{-2}	10.000	**-3.392×10^{-4}**	9.609×10^{-3}
Three Time Level	10.000	**-7.993×10^{-3}**	2.139×10^{-2}	**10.176**	**-0.4864**	9.557×10^{-3}

The necessity of high-order time method

The objective of the following test example is to show the preliminary influence of different forms of time marching schemes on the final solution. The first test case is with MUSCL scheme as the spatial scheme and a 100×100 grid is used. The total time steps are 100.

The performances of the schemes are quite different. The solution from the IE scheme is extremely inaccurate, considering the diffusion and shape-changing. The other four schemes (I3L, CN, SSSPK2 and SSSPK3), produce similar results. It is observed that the solution with I3L contains few undershoots, $\phi_{\min} = -0.010$.

Interestingly, the best results are obtained with the Euler Explicit method if we consider the RMS parameter only, which is of the first order in time and takes the least computational effort. Similar results have been reported in Ref. [261], for 1D case. Apparently, the order of accuracy and the absolute error are different concepts. However, the shape of the solution with EE is quite strange, and it is observed that the distortion direction is opposite to IE. This should be the result of negative numerical diffusion [68, page 138].

Considering the computational cost, CN and I3L are implicit schemes and solving linear system solver is needed for each time step. Sometimes several times may be needed considering the application of DFC technology. Thus, both of them are not good choices for the test problem.

To further compare the performance of SSPRK2 and SSPRK3, the rotation of a cone-shaped scalar field and swirling deformation flow tests are performed. Two limiter functions are considered, SMART and MUSCL. The RMS error and computational time is recorded.

In the solid-body rotation test, all the computations lasted for one revolution. For 100×100 grid system, the time steps are 0.001 and 0.0001, which correspond to $Co = 0.1$ and $Co = 0.01$ separately.

In the swirling deformation test, the total simulation time is set to $T = 1.5$. The same grid as in previous case is used. Useful conclusions can be drawn by simultaneously examining Table 3-5 and Table 3-6 and solution figures which are not listed here. Firstly, both SSPRK2 and SSPRK3 can lead to oscillation-free solutions. It is also noticed that the solution from SSPRK2 and SSPRK3 are almost the same for the same test case with the same high-resolution schemes. The required computational cost associated with SSPRK3 is much more than SSPRK2, about 1.3~1.4 times.

Tab.3-5. Performance of SSPRK2 and SSPRK3 time scheme in the solid-body rotation test

		$Co = 0.1$		$Co = 0.01$	
		RMS	**CPU TIME**	**RMS**	**CPU TIME**
MUSCL	**RK2**	9.812×10^{-4}	18.50s	9.811×10^{-4}	2m59.2s
	RK3	9.811×10^{-4}	25.43s	9.811×10^{-4}	4m9.7s
SMART	**RK2**	9.244×10^{-4}	18.27s	9.245×10^{-4}	2m59.0s
	RK3	9.245×10^{-4}	25.36s	9.245×10^{-4}	4m9.7s

Table 3-6. Performance of SSPRK2 and SSPRK3 time scheme in the swirling deformation test

		$Co = 0.1$		$Co = 0.01$	
		RMS	**CPU TIME**	**RMS**	**CPU TIME**
MUSCL	**RK2**	1.02×10^{-3}	4.60s	1.01×10^{-3}	43.89s
	RK3	1.01×10^{-3}	6.25s	1.01×10^{-3}	1m0.8s
SMART	**RK2**	9.614×10^{-4}	4.62s	9.62×10^{-4}	44.02s
	RK3	9.616×10^{-4}	6.22s	9.62×10^{-4}	1m0.7s

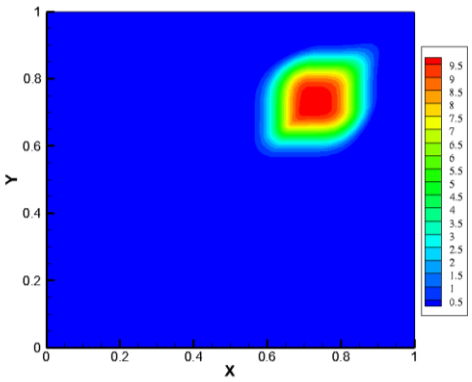

(a) Euler Implicit

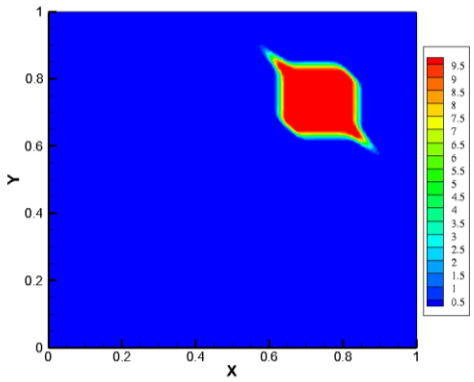

(b) Euler Explicit

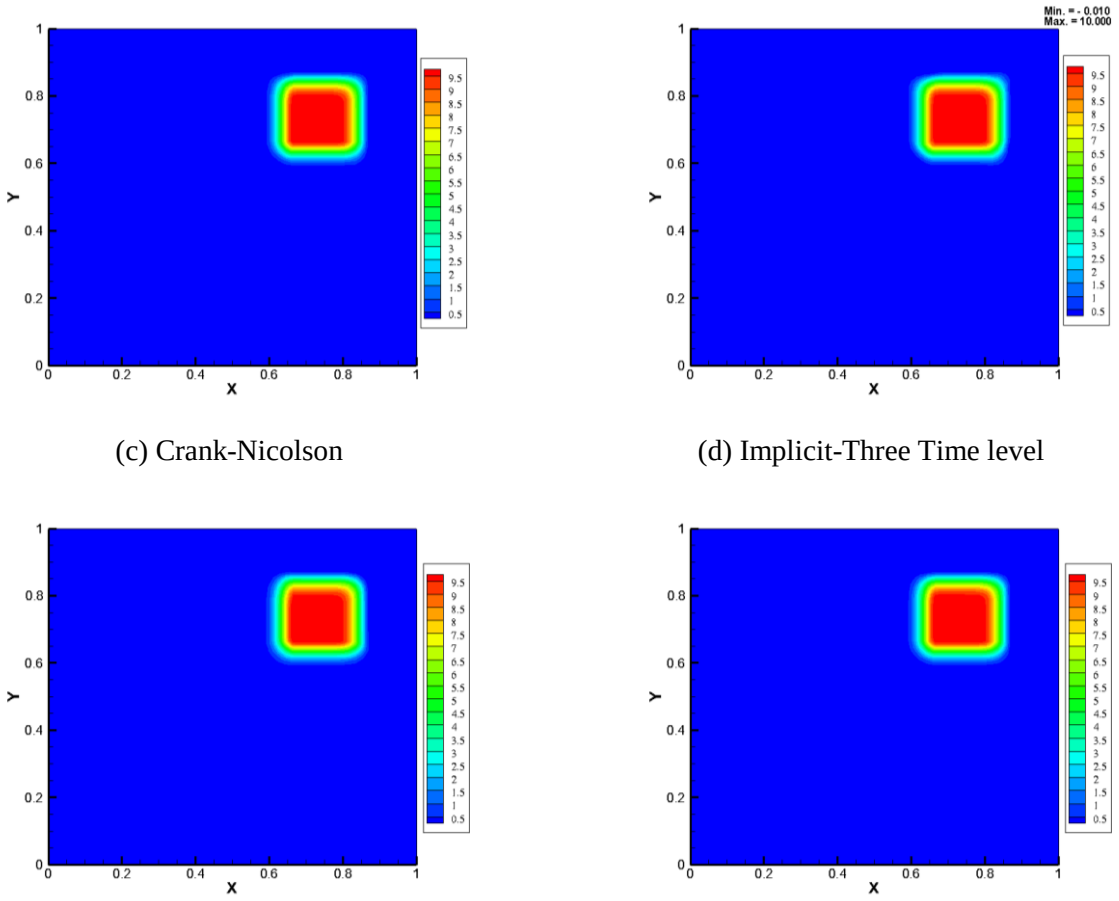

(c) Crank-Nicolson (d) Implicit-Three Time level

(e) SSPRK2 (f) SSPRK3

Figure 3-21. Plots of the scalar fields in the advection of a square shaped scalar test

By comparing the results of different *Co* number, i.e., different time steps, the accuracy does not improve as the further decrease of time step, which means that the condition $Co = 0.1$ is sufficient to satisfy the accuracy requirement.

In conclusion, several temporal discretisation schemes have been evaluated with three time-dependent, linear problems with pure convection. While the ultimate selection of a particular scheme should be based on the nature of a given problem, this work has produced the following guidelines for the selection process:

(i) The Euler Explicit, Euler Implicit, Crank-Nicolson can produce oscillation-free results. However, the implicit three time level scheme introduces oscillations.

(ii) It is necessary to choose the high-order time scheme which holds the property of strong stability preserving. Non-TVD Runge-Kutta scheme could introduce oscillations, while SSP Runge-Kutta can ensure oscillation-free solutions under certain CFL limitation conditions.

(iii) Implicit schemes are not suitable for unsteady pure convection problems because of its computational cost, especially when the deferred correction technique is applied.

(iv) From the accuracy point of view, first Euler Explicit scheme introduces negative diffusion and is inaccurate. There is slight difference between the RMS error of SSPRK2 and SSPRK3 in all test cases, which is a surprising finding.

(v) Considering the computation cost, SSPRK2 performs much better than SSPRK3.

To synthesize the above analysis, the SSPRK scheme is recommended as the temporal discretisation method for the charge density equation.

3.5.3 On the gradient evaluation method for surface decomposition scheme

In this section, the effects of different gradient computation methods are compared. Solving the Poisson equation with homogeneous Dirichlet or Neumann boundary conditions in a domain (Ω) which are expressed in Eqn.(3-55a) and Eqn.(3-55b) provides a good test of the accuracy and computational cost of IDC scheme and its improvement approaches.

$$\Delta\phi = f \quad \text{in } (\Omega) \tag{3-55a}$$

$$\phi = g \quad \text{or} \quad \frac{\partial\phi}{\partial n} = g \text{ on } (\partial\Omega) \tag{3-55b}$$

Integrating (3-55a) over a quadrilateral mesh and using Gauss's formula

$$\sum_{k=n,e,w,s} S_K^P (\nabla\phi)_K^P \cdot \vec{n}_K^P = (f)_P \cdot V_P \tag{3-56}$$

Here, as the structured quadrilateral meshes are used, the globally accepted finite volume notation is adopted. Applying the IDC, a generic equation is obtained,

$$A_P\phi_P + \sum\nolimits_{K=NEWS} A_K\phi_K = (RHS)_P^n \tag{3-57}$$

where the coefficients and some terms are [105]:

$$A_K = \frac{S_K}{\cos\theta_K \cdot |PK|}; \quad A_P = -\sum_{K=NEWS} A_K;$$

$$(RHS)_P = (f)_P \cdot V_P - \sum_{K=NEWS} S_K (\nabla\phi)_K^n \cdot (\vec{n} - \vec{n}_1) \tag{3-58}$$

By applying Eqn.(3-58) for every control volume defining the computational domain, we get a linear system $A\vec{x} = b$. The linear system will be solved with the SIP-solver or the Bi-Conjugate Gradient Stabilized (Bi-CGSTAB) of Van der Vorst [262] with a Modified Incomplete LU factorization preconditioner according to Gustafsson [263]. The reason of the application of two linear system solvers is that we found the performance of different methods with Neumann boundary condition closely linked to linear system solvers. For more implementation details, please refer to [105] and [106]. The whole solving process contains two major iterative loops: the first loop is the deferred correction iterative loop, while the second loop is the iterative nature of

the linear system solver. Two different stopping criteria are defined. For the deferred correction loop, $\frac{\left|\phi_P^m - \phi_P^{m-1}\right|}{\left|\phi_P^{m-1}\right|} < \varepsilon_{sweep}$ is used, while the classical stopping criteria based on the residual which should be less than a given tolerance ε_{solver} is used for linear system solver. In the present study, the values for ε_{sweep} is 1.0×10^{-7}. Considering the discretized system described above includes some explicit terms, which depend on the displacement from the previous iteration, it would be therefore unnecessary to converge the solution of linear system to a so tight tolerance ε_{solver}, since the new solution will only be used to update the explicit terms. In all tests, ε_{solver} is set to be 1.0×10^{-2}. As for one-step and two-step Gauss formula implementation, the extra gradient iteration is controlled by setting the iteration times.

A randomly distorted mesh and an extremely distorted mesh [264] are used, which is depicted in Figure 3-22. The characters of the two meshes are there is obvious skewness and non-uniformity in the inner domain while the nonorthogonality is not serious on boundaries, which will reduce the influence of boundary condition treatment.

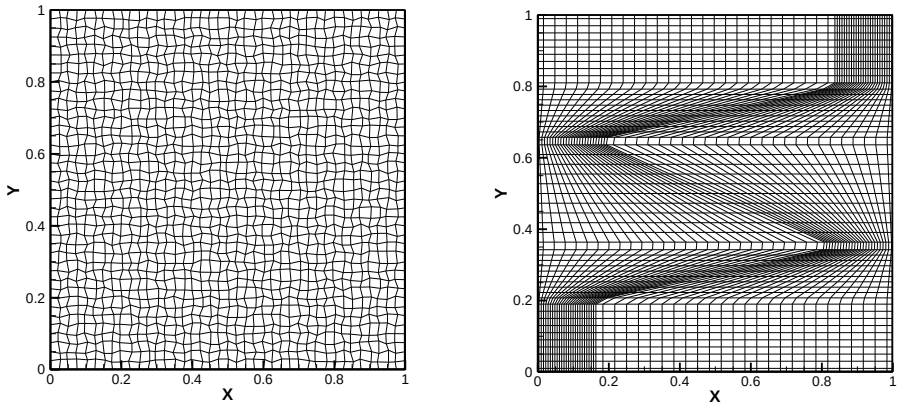

Figure 3-22. (left) Randomly distorted, Mesh II and (right) extremely distorted meshes, Mesh IV

Test Case I

A two-dimensional Poisson problem,

$$\Delta\phi = 6x + 2 \quad \text{in} \quad (\Omega) \tag{3-59a}$$

$$\phi = x^3 + y^2 + xy \qquad \text{on} \ (\partial\Omega) \tag{3-59b}$$

The analytical solution is given by $\phi(x, y) = x^3 + y^2 + xy$.

In Table 3-7, the values of the L_2 error versus different methods have been reported for chosen grid. For both irregular non-orthogonal grids, the solution from simple Gauss formula is extremely inaccurate, especially for particularly skewed mesh. On the other hand, the other four methods, namely two-step Gauss Formula, one-step Gauss Formula, the simple and improved Least-square approaches, dramatically improve the results compared to the simple Gauss formula. For the

random mesh, the simple and improved Least-squares approach and the two-step Gauss formula are the most accurate methods with similar L_2 norm for this test problem. For the extremely distorted mesh, the improved LS approach is the most accurate method. Next in the ranking is two-step Gauss formula followed by the simple LS approach.

Table 3-7. Performance of the various methods with two distorted mesh _case I

	Randomly distorted mesh (40×40)			**Extremely distorted mesh (40×40)**		
	INs	**Sweeps**	**L2 norm ($\times 10^{-3}$)**	**INs**	**Sweeps**	**L2 norm ($\times 10^{-3}$)**
Simple GT	37	22	2.404	302	194	18.199
1 step GT (1)	52	36	1.915	348	227	9.230
1 step GT (5)	60	41	1.206	481	352	4.402
2 step GT	47	31	0.244	341	222	2.459
Simple LS	42	31	0.245	352	228	8.624
Improved LS	41	26	0.253	344	218	2.043

INs: inner iterations

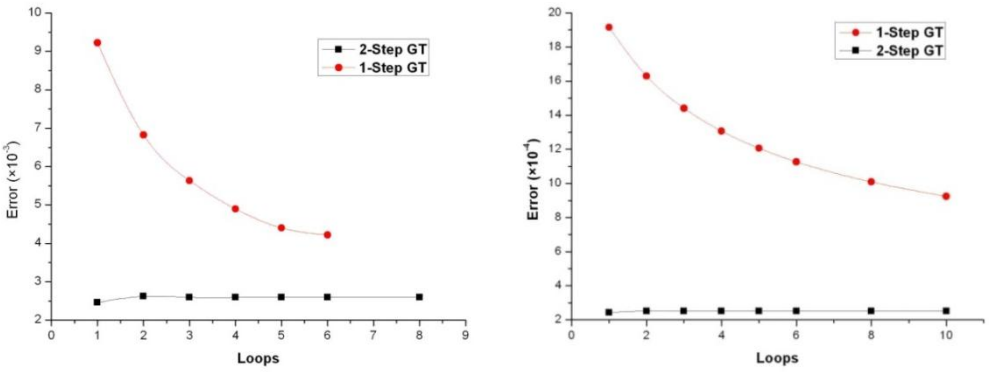

Figure 3-23. L2 Norm Error of 1-step and 2-step GT versus the number of iterations on randomly (left) and extremely (right) distorted meshes

It is noticed that the accuracy of one-step Gauss formula is closely linked with the number of iterations. In Figure 3-23, we have plotted the L_2 norm error of both one-step and two-step Gauss formula versus the number of iterations. For the one-step Gauss formula, the results show that the L_2 error reduces quickly for the first few iteration times and then the reduction speed slows down. For this specific test case, when we increase the times of extra loop to 6, the solution diverged. The reason may be the stability property of the one-step 2nd Gauss method [265]. However, for the two-step Gauss method, the extra loop avoids the stability problem but brings little improvement of the accuracy. From the similar L_2 norm error with two-step Gauss method and improved LS approach, we believe that the error of gradient evaluation induced by skeweness and non-uniformity has been greatly eliminated.

Besides computational accuracy, the computational cost is another significant factor that needs to be addressed. Considering the close relationship between the CPU time consumption and the number of iterations, the number of sweeps and the total number of iterations for different methods with different grid are also listed in Table 3-7. Apart from accuracy considerations, the numbers of iterations clearly prohibit the one-step Gauss' formula use since it requires more iteration times

than other methods. Even worse, the total iteration number of iterations increases greatly with N (the number of iterations for gradient computation). Simple Gauss method holds some but limited advantages in computational cost comparing with other methods. For both meshes, the two Least-squares approach and the two-step Gauss method require roughly the same iteration times.

By summarizing all the results listed above, the Least-squares approach is preferred in this benchmark problem. As for methods of Gauss formula, the two-step Gauss formula could also provide acceptable results.

As the performances of different gradient evaluation methods may link with the distribution of gradient, a test with smooth gradient values has also been done.

Test case II

$$\Delta\phi = 2\pi^2(\cos^2(\pi x) - \sin^2(\pi x)) + 2\pi^2(\cos^2(\pi y) - \sin^2(\pi y)) \qquad \text{in } (\Omega) \qquad (3\text{-}60a)$$

$$\phi = \sin^2(\pi x) + \cos^2(\pi y) \qquad \text{on } (\partial\Omega) \qquad (3\text{-}60b)$$

The computational domain is restricted to a square domain [1×1]. Exact solution is given by $\phi = \sin^2(\pi x) + \cos^2(\pi y)$.

The computational results are listed in Table 3-8.

Table 3-8. Performance of the various methods with two distorted mesh _case II

	Randomly distorted mesh (40×40)			**Extremely distorted mesh (40×40)**		
	INs	**Sweeps**	**L2 norm (×10^{-3})**	**INs**	**Sweeps**	**L2 norm (×10^{-3})**
Simple GT	39	27	7.787	323	188	6.748
1 step GT (1)	45	32	6.506	388	228	3.287
1 step GT (5)	56	41	4.525	486	316	1.711
2 step GT	37	25	1.262	376	208	1.785
Simple LS	36	25	1.207	382	214	2.831
Improved LS	38	25	1.248	369	208	1.887

INs: inner iterations

Considering the accuracy aspect, most results are consistent with the previous test. For extremely distorted mesh, the two-step Gauss method becomes the most accurate method and the difference between simple and the improved LS approach is not as large as previous test. It seems that the accuracy of the two-step Gauss and the improved LS approach is of the same order. As for computational cost, the only advantage of simple Gauss method disappears.

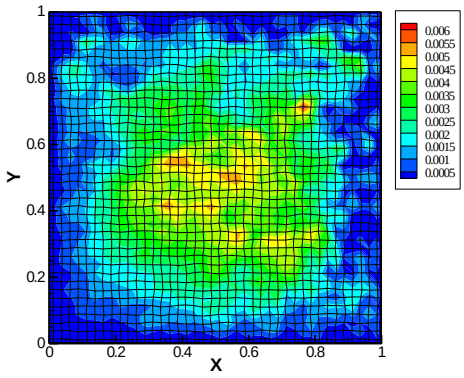

(a) Simple GT

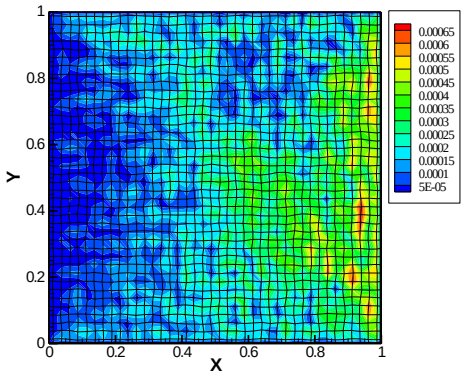

(b) 2-Step GT

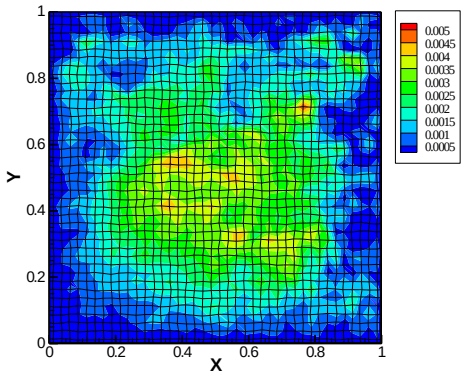

(c) 1-step GT, iteration = 1

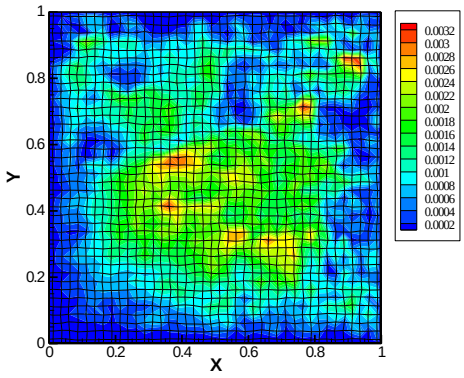

(d) 1-step GT, iteration = 5

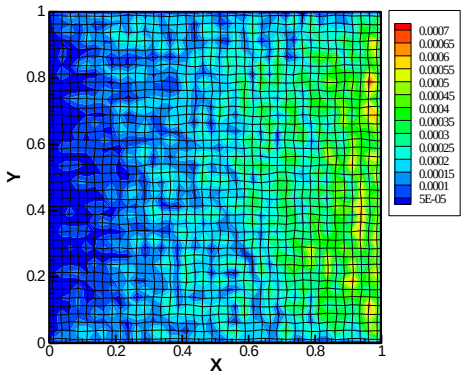

(e) Simple LS

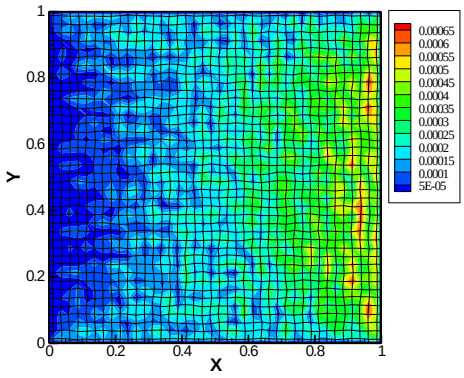

(f) Improved LS

Figure 3-24. Iso-contours of the absolute error with randomly distorted meshes with test II

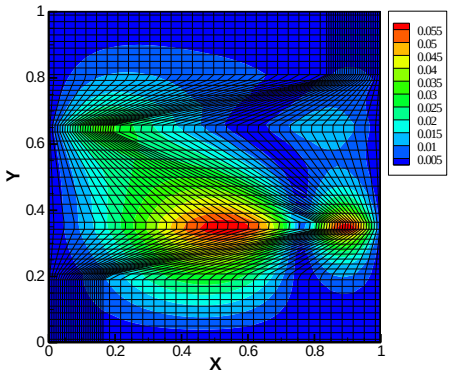

(a) Simple GT

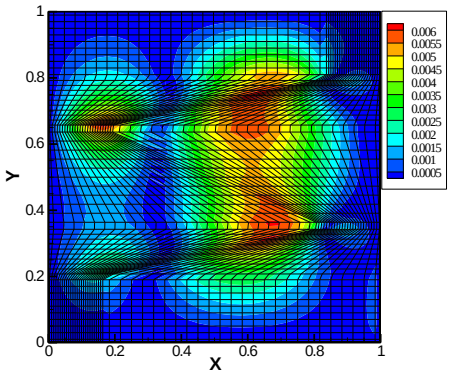

(b) 2-Step GT

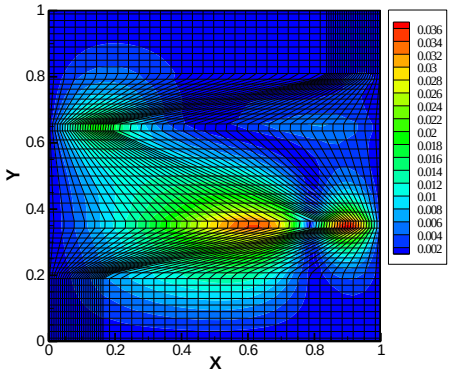

(c) 1-step GT, iteration = 1

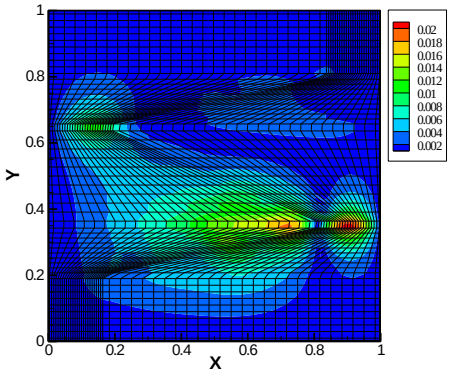

(d) 1-step GT, iteration = 5

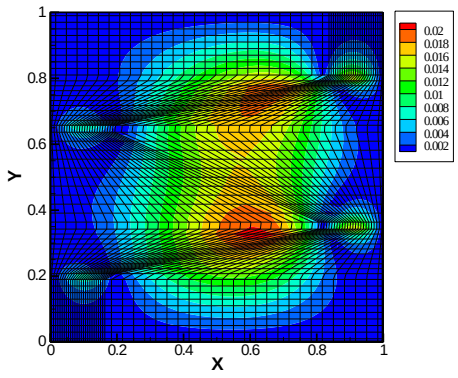

(e) Simple LS

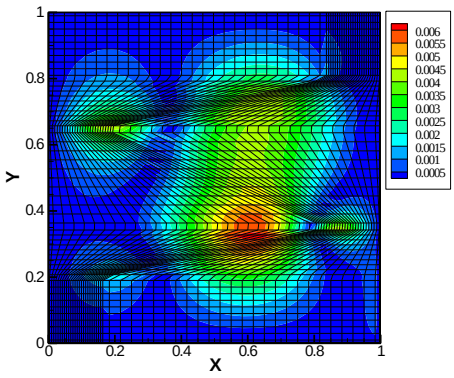

(f) Improved LS

Figure 3-25. Iso-contours of the absolute error with randomly distorted meshes with test II

In Figure 3-24 and Figure 3-25, the absolute errors made by different approaches on 40×40 randomly and extremely distorted meshes are presented. It is immediately noticed that results of two-step Gauss formula and the two LS approach are much better than the other two.

To summarize, the two-step Gauss method and the improved Least-squares approach are recommended for gradient evaluation, with general meshes and test cases.

3.5.4 Numerical verification of connection among CTM, IDC and DGEM

In this section, numerical dedicated tests have been performed to highlight the link between the three methods revealed in the section 3.3.2.3.

According to the test purpose, four different meshes are chosen. The first one is a uniform warped mesh, with an angle θ_K increasing from 0^o to 89.9^o, see Figure 3-26(a). For this one, there is no skewness and the non-orthogonalilty can be only controlled by θ_K. The second one is the randomly distorted grid, see Figure 3-22. The third one is a slightly skewed grid; see Figure 3-26(b). The last one is the particularly skewed Kershaw grid, see Figure 3-22. For the last three meshes the skewness is important and gradually increases from the second to the last one. Another interesting feature of the last mesh is its anisotropically distortion, which is another very severe test for diffusion schemes.

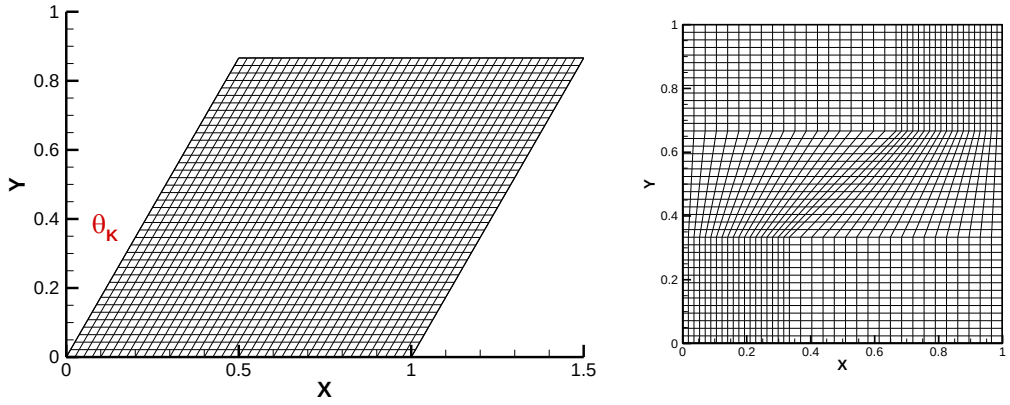

(a) Mesh I (b) Mesh III

Figure 3-26. (a) Uniform skewed meshes (b) slightly skew mesh

Previously we have highlighted the importance of the gradient computation method for IDC scheme and MDGEM. For uniform skew mesh (Figure 3-26a) in absence of skewness, the simple Gauss formula will be used. For the other three meshes, skewness arises and the two-step Gauss formula and the Least-squares approach will also be utilized. For more details about these three gradient evaluation methods, please refer to Appendix B. For CTM, the simple interpolation method with $W_i = 1/r_i$ (where r_i denotes the distance from the centroid of the ith cell to the nodal point) will be used to interpolate the values at nodal points. In this context, we have also tried $W_i = V_i$ where V_i is the volume of the ith cell, without significant gain.

To compare the accuracy as well as efficiency, three parameters are checked and reported: (i) L2 norm (ii) the number of sweeps for deferred correction loop and (iii) the total number of iterations of the linear system solver.

For the first test we consider the computational domain and meshes depicted in Figure 3-26(a) with 'Test Case I' (Eqn. 3-59). Along with the angle θ increasing from 10^o to 89.9^o, the meshes become extremely skewed. First of all, we noticed that all three methods worked well even on the case of $\theta = 89.9^o$. It is indicated that the convergence abilities of three methods are consistent with each

other. Table 3-9 presents the values of the L2 norm versus angle θ for each method. In Table 3-10 and Table 3-11, we have reported the number of sweeps required in the deferred correction process and the number of total number of iterations versus angle θ for the three methods.

Table 3-9. L2 norm versus angle θ for a 40×40 grid ($\times 10^{-6}$)

θ	**10°**	**30°**	**40°**	**50°**	**60°**	**70°**	**80°**	**89.9°**
$L2_{CT}$	6.407	8.336	9.444	10.566	11.587	12.369	12.767	---
$L2_{IDC}$	5.365	2.176	1.277	4.416	7.755	10.561	12.334	12.753
$L2_{DGE}$	5.365	2.176	1.277	4.416	7.755	10.561	12.334	12.753

Table 3-10. Number of sweeps versus θ for a 40×40 grid

θ	**10°**	**20°**	**30°**	**40°**	**50°**	**60°**	**70°**	**80°**	**89.9°**
CT	12	16	21	27	38	55	89	159	---
IDC	11	17	22	28	38	55	83	121	143
DGE	11	17	22	28	38	55	83	121	143

Table 3-11. Total number of iterations versus θ for a 40×40 grid

θ	**10°**	**20°**	**30°**	**40°**	**50°**	**60°**	**70°**	**80°**	**89.9°**
CT	54	77	103	143	206	296	436	629	---
IDC	50	72	100	141	201	293	436	635	751
DGE	50	72	100	141	201	293	436	635	751

It is found that all calculation results of Improved Deferred Correction (IDC) method and Direct Gradient Evaluation (DGE) method of Ferziger and Peric are exactly the same. The numbers of sweep times and total iteration times of coordinate transformation method and the other two methods are about the same, while there is some difference in L2 norm. As discussed in Section3, the main error for coordinate transformation method comes from the approach for the calculation of nodal points' values, and the gradient evaluation method is the main error source for IDC method and DGE method, as there is no skewness in this test case. Apparently, both the gradient evaluation method and interpolation method are affected by the skew angle θ. But the specific influence rule is not clear. In Figure 3-27, we have presented the absolute error made on the $\theta = 30^o$ mesh. In this case, the accuracy of IDC method is slightly better than coordinate transformation method. It is noticed that the error distributions of the two methods are not the same; this is because error came from different error sources.

As for computational cost, coordinate transformation method is cheaper in a single iteration, as it avoids the calculation of gradients of control volume nodes and gradients of the middle points of every faces.

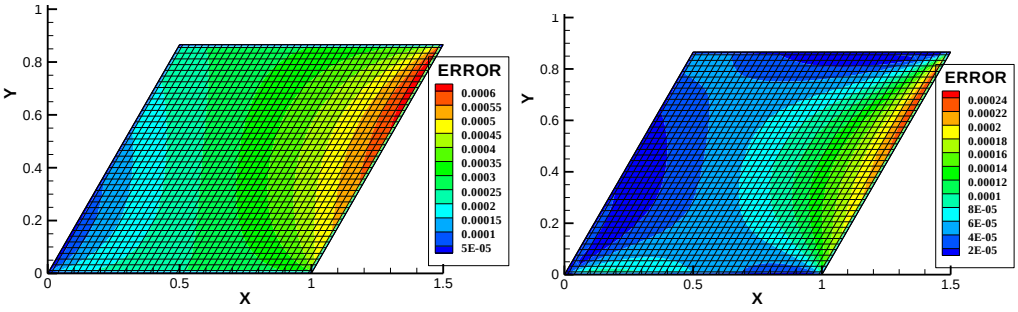

(a) (b)

Figure 3-27. Iso-contours of the absolute error, $\theta = 30^o$ (a) Coordinate Transformation Method (b) Improved Deferred Correction of Surface Decomposition method

Now we focus on the performance of the three different methods when skewness arises in the computational domain. We solve 'Test Case II' (Eqn. 3-60) on randomly distorted (Figure 3-22 left), slightly distorted (Figure 3-26b) and extremely distorted meshes (Figure 3-22 right).

Because of the presence of skewness in the grid, and in accordance with what has been previously stated in previous section, the classical Gauss theorem implementation becomes irrelevant and one has to use the two-step Gauss formula is used for CV node gradient evaluation.

The computational results are listed in Table 3-12, Table 3-13 and Table 3-14. It is immediately noticed that the solution from CTM is much more inaccurate comparing with the two other methods for all meshes. On the other hand, the number of sweeps as well as the total number of iterations are almost the same for all methods on all meshes.

Table 3-12. L2 Norm of error for the three test grids

	Mesh II		**Mesh III**	**Mesh IV**
	20×20	40×40	38×42	51×51
CTM	5.734 e^{-4}	2.455 e^{-4}	3.246 e^{-5}	9.971 e^{-4}
IDC	2.350 e^{-4}	3.022 e^{-5}	2.965 e^{-5}	3.754 e^{-4}
DGEM	2.380 e^{-4}	2.957 e^{-5}	3.062 e^{-5}	3.923 e^{-4}

Table 3-13. Sweeps times for the three test grids

	Mesh II		**Mesh III**	**Mesh IV**
	20×20	40×40	38×42	51×51
CTM	9	14	30	115
IDC	10	14	30	123
DGEM	10	12	30	126

Table 3-14. Total number of iteration of the linear solver for the three test grids,

	Mesh II		**Mesh III**	**Mesh IV**
	20×20	40×40	38×42	51×51
CTM	32	63	146	831
IDC	34	61	148	916
DGEM	36	61	147	917

In Figure 3-28, we have depicted the iso-contours of the solution obtained with the three methods on a 40×40 randomly distorted mesh. The error distributions of IDC scheme and MDGEM are similar, but quite different compared to CTM. For CTM the error is concentrated in the middle area of the domain, where the magnitude of the variable is higher. For IDC and MDGEM the error is mainly distributed where the gradient of the variable is higher.

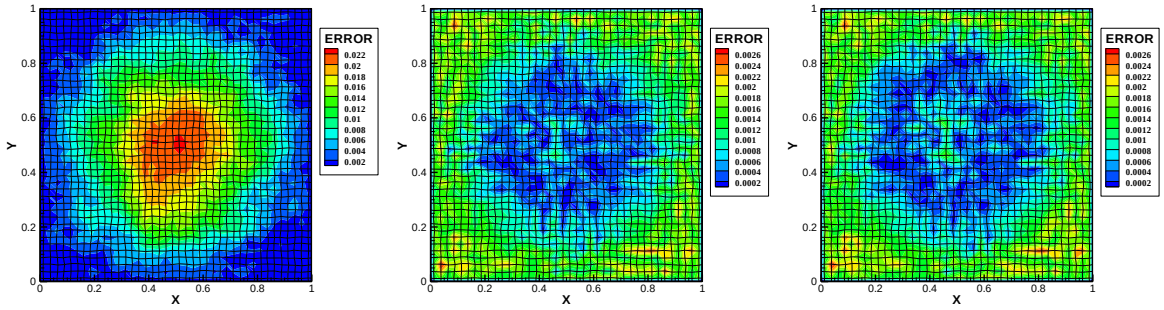

(a) (b) (c)

Figure 3-28. Iso-contours of the absolute error on a 40×40 randomly distorted mesh with (a) CTM (b) IDC with two-step Gauss formula (c) MDGEM with two-step Gauss formula

To further confirm and highlight that the gradient evaluation methods are the key error sources in such computations, we also perform the same numerical test on a randomly distorted grid, but with the simple Gauss formula and the Least-square approach. The computational results are listed in Table 3-15 and iso-contours of the errors are plotted in Figure 3-29 and Figure 3-30. The comparisons among Figure 3-29, Figure 3-30 and Figure 3-28(b), show directly that the IDC and MDGEM combined with simple Gauss formula fall to the level of CTM accuracy. It is also interesting to see that these error distributions are therefore and logically very similar for the three methods.

Table 3-15. L2 norm and total number of iterations and sweeps for the three tested grids for IDC scheme and DGEM combined with different gradient evaluation methods

	Mesh II 51×51			**Mesh III 38×42**			**Mesh IV 51×51**		
	L2	S	T	L2	S	T	L2	S	T
Improved Deferred Correction									
Simple Gauss Formula	1.531	17	72	0.389	30	146	11.89	108	779
Two-step Gauss Formula	0.152	18	75	0.297	30	148	3.754	123	916
The Least-squares Approach	0.228	16	77	0.309	30	147	5.169	123	935
Direct Gradient Evaluation									
Simple Gauss Formula	1.511	15	73	0.419	30	146	12.08	108	793
Two-step Gauss Formula	0.150	16	75	0.306	30	147	3.923	126	917
The Least-squares Approach	0.146	15	76	0.329	30	146	5.356	122	955

L2 : $\times 10^{-4}$; S: Number of Sweep; T: Total number of iterations.

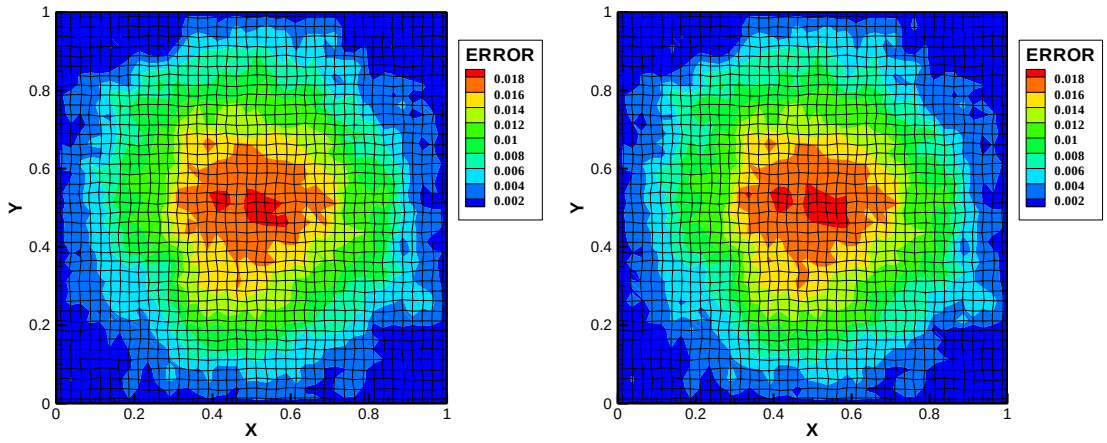

(a) (b)

Figure 3-29. Iso-contours of the absolute error on a 40×40 randomly distorted mesh with (a) IDC with simple Gauss formula (b) DGEM with simple Gauss formula

Still focused on cell gradient evaluation, we shall now perform some tests with IDC scheme and MDGEM combined with (i) simple Gauss formula, (ii) two-step Gauss formula and (iii) the Least-squares approach. Mesh II, III and IV will be as well employed. The results are summarized in Table 3-15. As expected, for the same gradient computation approach, the accuracy and computational cost of IDC and MDGEM are always very close to each other. The two-step Gauss method and the Least-squares approach are much more accurate than the simple Gauss formula whatever the kind of grid considered. Still in terms of accuracy comparison between Least-squares approach and the two-step Gauss formula does not show a clear predominance. The slight differences seem to be more attached to the type of mesh.

For the randomly distorted grid (Mesh II) the Least-squares approach is slightly more accurate than two-step Gauss formula when applied to MDGEM but it is the contrary when applied to IDC scheme. For Mesh III the accuracy is almost the same for the two gradient evaluation methods as well as for the two schemes. For the very critical Kershaw's mesh (Mesh IV) the results of two-step Gauss formula are a bit more accurate. So it is quite difficult to conclude on this point.

The emphasis is now laid on the performances in term of accuracy for the three methods on the most critical mesh i.e. Kershaw grids. As shown in Figure 3-30, although IDC and DGEM are more accurate than CTM, the error distribution is similar. The errors are magnified in regions where there is strong skewness. According to us, in this case, strong skewness introduced serious error both for interpolation accuracy of vertex point values and cell gradient computation. These results emphasize the importance of the mesh quality in the grid design process for practical simulation.

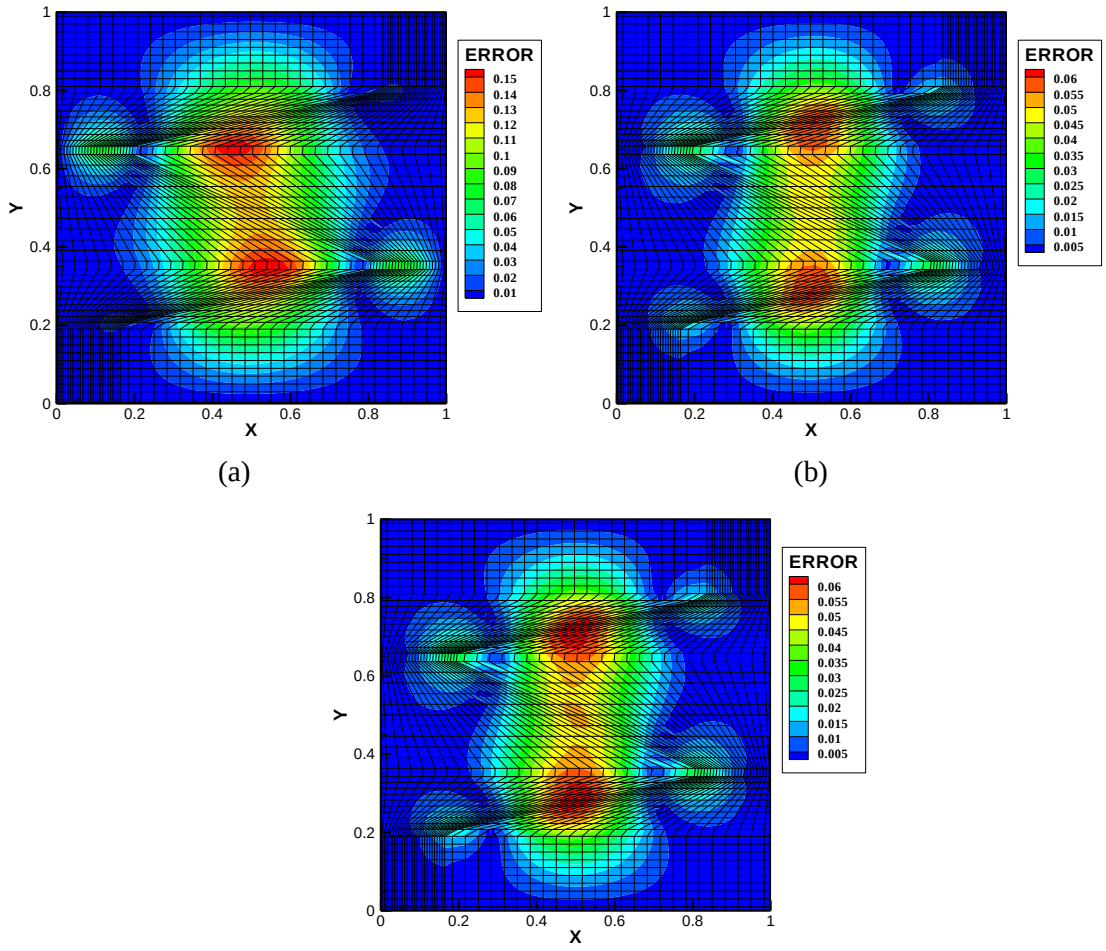

Figure 3-30. Iso-contours of the absolute error on a 51×51 extremely distorted mesh with (a) CTM (b) IDC with two-step Gauss formula (c) DGEM with two-step Gauss formula

Another very important factor in such computations is the CPU time consumption. The emphases were laid on the performances of the three gradient evaluation methods. To evaluate the computational cost we choose the Kershaw grids as the most drastic test. From table 3-15 we can notice than in every case simple Gauss is cheaper than the two others. Two step Gauss and Least Square methods produce a number of sweeps and iterations very comparable with a slight advantage for Least Square method.

3.5.5 Efficient boundary condition treatment for IDC scheme

In this section, numerical test will be performed to investigate the effectiveness of the methods introduced in previous sections.

3.5.5.1 Dirichlet Boundary Condition

For the first test we consider 'Test case I' (Eqn.(3-59)) and uniform skew mesh (Mesh I) in which the non-orthogonalilty on boundaries can be controlled by θ_K.

Table 3-16 presents the values of the L2 norm versus angle θ for the simple method (Eqn.(3-25)) and the improved methods (Eqn.(3-26) and Eqn.(3-27)). In Table 3-17 and Table 3-18, we have reported the number of sweeps required in the deferred correction process and the number of total number of iterations versus angle θ for the two methods. It is found that the computational cost of two improved methods is almost the same. The simple scheme produces convergence results but is very inaccurate, especially in situations involving serious non-orthogonality on boundaries. In Figure 3-31, we have presented the absolute error made on a 40×40 mesh. By comparison, the error distribution of the improved scheme is more reasonable.

Table 3-16. L2 norm versus angle θ for a 40×40 grid ($\times 10^{-3}$)

θ	**10 °**	**20°**	**30 °**	**40 °**	**60 °**	**80 °**
Simple	3.178	8.298	15.254	23.680	41.540	52.916
First	0.256	0.293	0.333	0.377	0.460	0.503
Second	0.215	0.169	0.087	0.051	0.310	0.493

Table 3-17. Number of sweeps versus θ for a 40×40 grid

θ	**10 °**	**20°**	**30 °**	**40 °**	**60 °**	**80 °**
Simple	27	40	53	65	102	215
First	28	50	50	64	98	207
Second	24	45	47	60	92	182

Table 3-18. **N**umber of inner iterations versus θ for a 40×40 grid

θ	**10 °**	**20°**	**30 °**	**40 °**	**60 °**	**80 °**
Simple	38	54	71	89	143	281
First	38	38	66	84	133	261
Second	35	33	63	80	127	236

A test case using the same Poisson problem but with randomly distorted mesh is performed to highlight the performance of the three methods with slight non-orthogonality on boundaries. The numerical results are listed in Table 3-19.

Table 3-19. Performance of the various methods with randomly distorted mesh

	40×40 grid			80×80 grid		
	Inner iterations	**Sweeps**	**L2 norm(**$\times 10^{-4}$)	**Inner iterations**	**Sweeps**	**L2 norm(**$\times 10^{-4}$)
Simple	49	35	6.194	92	66	3.402
First	47	**31**	2.555	91	**63**	0.638
Second	41	**26**	2.526	**91**	**63**	0.640

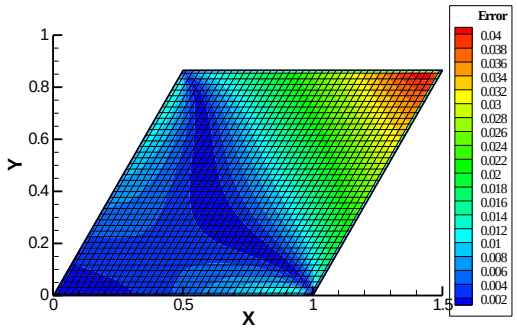

(a) Simple

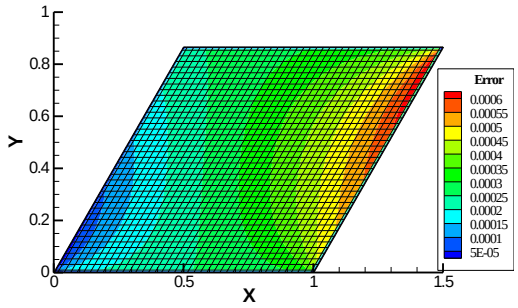

(b) First improvement

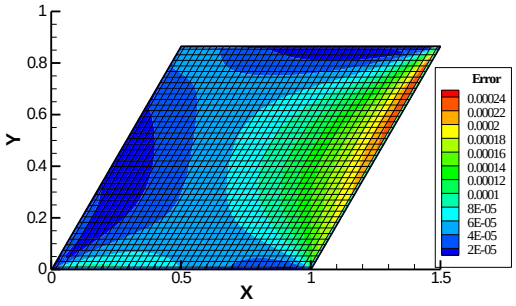

(c) Second improvement

Figure 3-31. Iso-contours of the absolute error, $\theta = 30°$

Even when the non-orthogonality on boundaries is not serious, the accuracy with the simple method is still much worse than the one of other two, especially with the finer meshes. As for the other two methods, the difference in computational cost and accuracy is not obvious in this case. However, the second method is always slightly better.

In conclusion, the new method developed in the present study, i.e., the second one, is recommended to treat the Dirichlet boundary condition with surface decomposition method.

3.5.5.2 Neumann Boundary Condition

To compare the performance of different methods for updating boundary values, we solve the following Poisson problem,

$$\Delta\phi = -2(2y^3 - 3y^2 + 1) + 6(1 - x^2)(2y - 1) \quad \text{in} \quad 0 \le x \le 1 \quad \text{and} \quad 0 \le y \le 1 \tag{3-61a}$$

Dirichlet B.C.:

$$x = 0, \quad \phi = 2y^3 - 3y^2 + 1 \tag{3-61b}$$

$$x = 1, \quad \phi = 0 \tag{3-61c}$$

Neumann B.C.:

$$y=0 \qquad \frac{\partial \phi}{\partial y}=0$$

$$y=1 \qquad \frac{\partial \phi}{\partial y}=0 \tag{3-61d}$$

The computational domain is always restricted in a square domain [1×1]. Analytical solution is given by $\phi=(1-\boldsymbol{x}^2)(2\boldsymbol{y}^3-3\boldsymbol{y}^2+1)$. A specially designed grid is used. The grid is a randomly distorted grid following the procedure of Shashkov and Steinberg [264], except the meshes of the fist and the last line in y-direction. The meshes on these two special lines are parallelograms, with a controllable angle θ, see Figure 3-31.

The performance of various methods may depend on the distribution of scalar variable, i.e., problem-dependent. Another case with smother distribution is considered,

$$\Delta\phi=-2\sin(x)\sin(y) \quad \text{in} \quad 0\le \boldsymbol{x}\le 1 \quad \text{and} \quad 0\le \boldsymbol{y}\le 1 \tag{3-62a}$$

Dirichlet B.C.:

$$\boldsymbol{x}=0, \quad \phi=0$$

$$\boldsymbol{x}=1, \quad \phi=\sin 1\cdot\sin y \tag{3-62b}$$

Neumann B.C.:

$$y=0, \quad \frac{\partial \phi}{\partial y}=\sin x$$

$$y=1, \quad \frac{\partial \phi}{\partial y}=\cos 1\cdot\sin x \tag{3-62c}$$

The exact solution with this case is $\phi=\sin x\cdot\sin y$

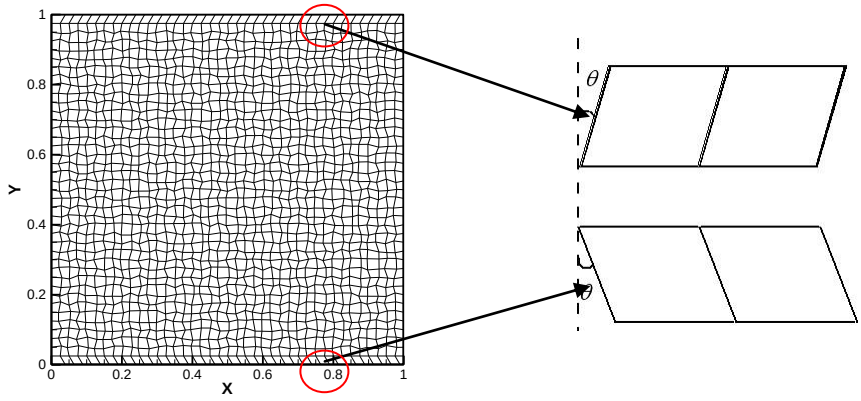

Figure 3-31. Computational domain and grid for Neumann boundary condition tests

The numerical results with the first case are summarized in Tab.3-13 ~ Tab. 3-18. The first three tables were obtained with BICGSTAB solver and the left were achieved using SIP solver. It is found that the performance of different methods depends on linear system solvers. These findings are surprising to us and the reason is unknown at present. In Tab.3-19, we present the test results of the second problem with randomly distorted meshes.

By careful investigation of the results, some conclusions can be reached.

1. With BICGSTAB linear system solver, the simple method performs better than the other two considering computational cost. However, its accuracy is not desirable, especially with serious non-orthogonality on boundaries. The other two methods do not show clear rules for computational cost. However, the accuracy of the second method (Eqn.(3-33)) is better than the first improvement method (Eqn.(3-32)). The iso-contours of the absolute error made on a 40×40 grid and with $\theta = 30°$ are presented in Figure 3-32. More importantly, the results with the second method are not significantly affected by non-orthogonality on boundaries.

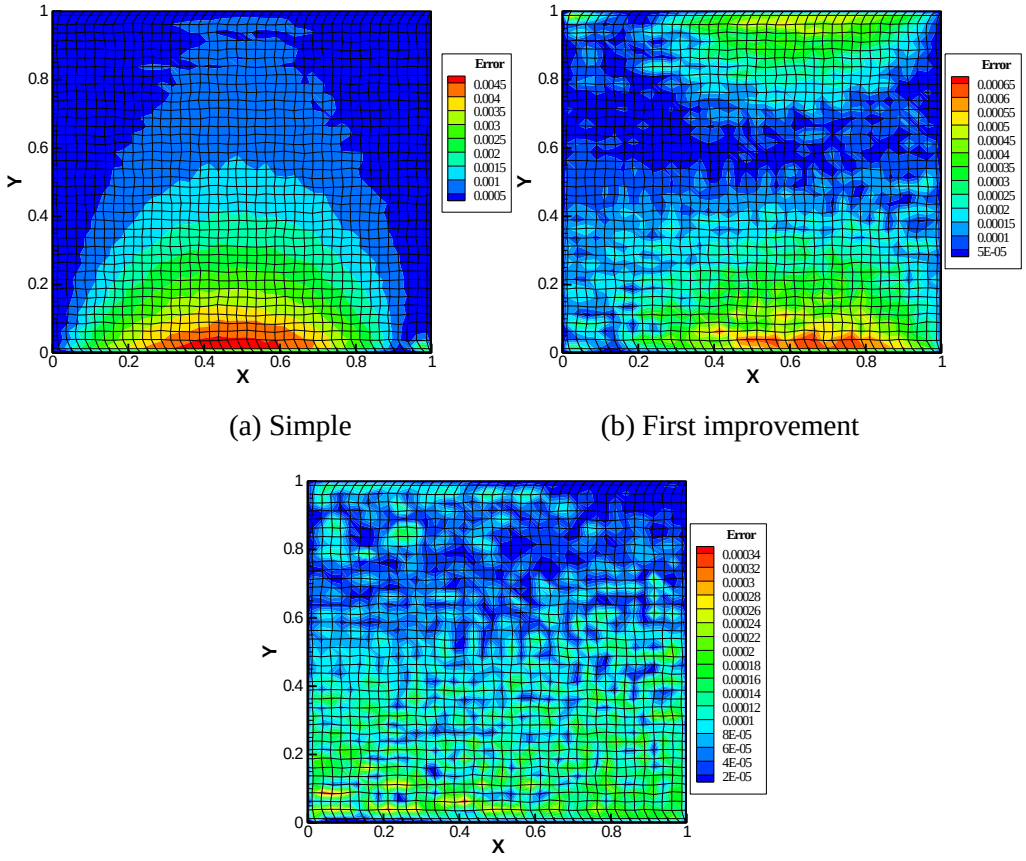

(a) Simple (b) First improvement

(c) Second Improvement

Figure 3-32. Iso-contours of the absolute error made on a 40×40 grid and with $\theta = 30°$, Test case 1.

2. With SIP linear system solver, the above conclusion with accuracy is the same. There are new changes of the computational cost. Both the number of sweeps and inner iterations with the second improvement method are close to those obtained with the simple method. The both are much better than the first improvement method.

3. When the non-orthonality on the boundaries is not severe (randomly distorted mesh in case 2 and the $\theta = 10°$ in case 1), the simple method performs better in terms of computational cost and accuracy.

Table 3-20. L2 norm versus angle θ for a 40×40 grid ($\times 10^{-4}$) with BICGSTAB solver

θ	**10 °**	**20°**	**30 °**	**40 °**
Simple	0.750	2.754	7.380	15.360
First	1.289	1.585	1.964	2.334
Second	1.070	1.070	1.123	1.090

Table 3-21. Number of sweeps versus θ for a 40×40 grid with BICGSTAB solver

θ	**10 °**	**20°**	**30 °**	**40 °**
Simple	54	64	84	119
First	87	72	86	126
Second	56	62	97	139

Table 3-22. Number of inner iterations versus θ for a 40×40 grid with BICGSTAB solver

θ	**10 °**	**20°**	**30 °**	**40 °**
Simple	69	79	100	136
First	72	87	102	143
Second	71	78	114	157

Table 3-23. L2 norm versus angle θ for a 40×40 grid ($\times 10^{-4}$) with SIP solver

θ	**10 °**	**20°**	**30 °**	**40 °**
Simple	0.750	2.754	7.380	15.360
First	1.289	1.585	1.964	2.334
Second	1.070	1.070	1.123	1.090

Table 3-24. Number of sweeps versus θ for a 40×40 grid with SIP solver

θ	**10 °**	**20°**	**30 °**	**40 °**
Simple	15	16	18	20
First	36	34	35	37
Second	15	16	19	27

Table 3-25. Number of inner iterations versus θ for a 40×40 grid with SIP solver

θ	**10 °**	**20°**	**30 °**	**40 °**
Simple	520	552	628	698
First	1639	1354	1293	1073

Second	522	560	640	754

Table 3-19. Performance of the various methods with randomly distorted mesh, test case 2

	40×40 grid			80×80 grid		
	INs	**Sweeps**	**L2 norm(**$\times 10^{-3}$**)**	**INs**	**Sweeps**	**L2 norm(**$\times 10^{-4}$**)**
BICGSTAB						
Simple	61	44	1.154	133	104	3.037
First	62	**45**	1.173	139	**110**	2.772
Second	59	**42**	1.123	**127**	**98**	2.810
SIP						
Simple	459	13	1.154	1716	17	3.037
First	536	**23**	1.173	2184	**24**	2.772
Second	460	**13**	1.123	**1716**	**17**	2.810

INs: inner iterations

In conclusion, we recommend our newly developed method, i.e., the second improvement method, for the treatment of Neumann boundary condition when non-orthogonality on boundaries is severe. If the boundary is almost orthogonal, the simple method is enough.

3.5.6 Three-dimensional extensional implementation of the IDC scheme

To test the accuracy and efficiency of IDC scheme for solving 3D Poisson Equation, we choose the following test problem.

$$\phi_{xx} + \phi_{yy} + \phi_{zz} = f(x, y, z), \quad (x, y, z) \in \Omega \tag{3-63a}$$

$$\phi(x, y, z) = g(x, y, z), \quad (x, y, z) \in \partial\Omega \tag{3-63b}$$

For the first test case, Ω is limited to $[0,1]\times[0,1]\times[0,1]$. If

$$f(x, y, z) = -3\pi^2 \sin(\pi x)\sin(\pi y)\sin(\pi z)$$

and

$$g(x, y, z) = 0$$

the analytical solution of the problem is

$$\phi(x, y, z) = -3\pi^2 \sin(\pi x)\sin(\pi y)\sin(\pi z)$$

Four different grids are considered: uniform orthogonal mesh (Figure 3-33a.), randomly distorted mesh (Figure 3-33b), extremely distorted mesh (Figure 3-33c) and a Double Kershaw mesh (Figure 3-33d) [244].

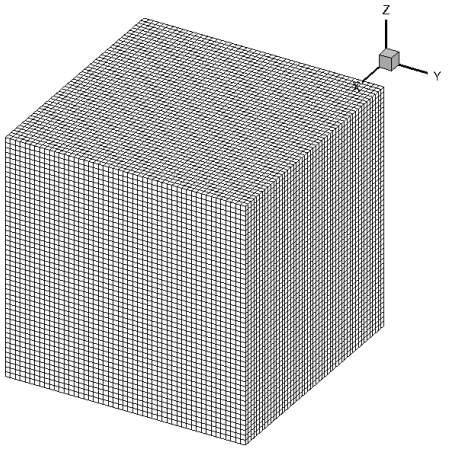

(a) Uniform orthogonal mesh

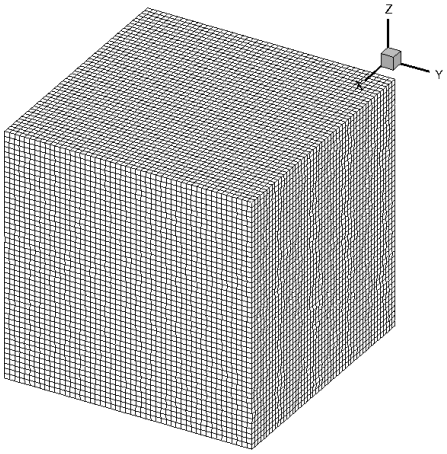

(b) Randomly distorted mesh

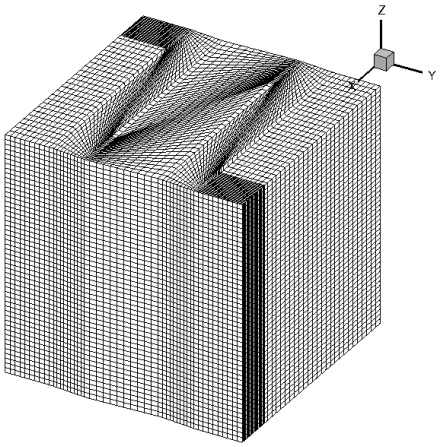

(c) Extremely distorted mesh

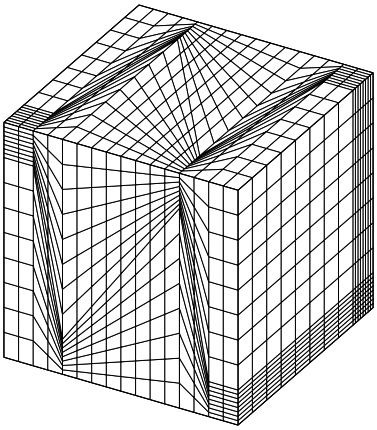

(d) a Double Kershaw mesh

Figure 3-33. Computational meshes for 3D test

The method for gradient evaluation is the 2nd order Gauss Theorem Method. The computational results are listed in Table 3-20 and plotted on Figure 3-34. Table 3-20 presents the different indicators that we choose to evaluate the performance of various methods.

Table 3-20**.** Total number of iterations, sweeps and errors for the three test grids

	Grid 1 50×50×50	**Grid 2 50×50×50**	**Grid 3 51×51×51**
L2 norm（$\times 10^{-5}$）	0.033	0.048	1.206
Total number of sweeps	2	8	84
Total number of iterations	1362	2267	30511
CPU time	12.201s	19.925s	4m14.7s
Max Error	3.290e-4	8.412e-4	2.260e-2

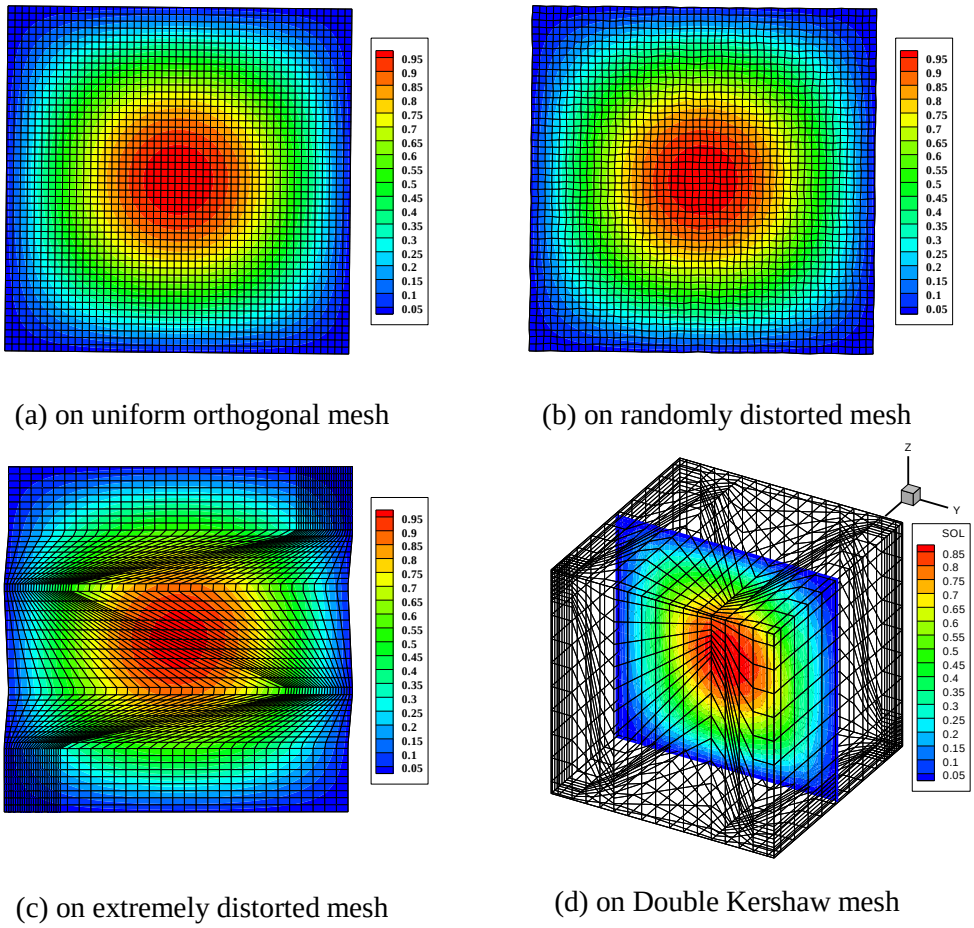

(a) on uniform orthogonal mesh

(b) on randomly distorted mesh

(c) on extremely distorted mesh

(d) on Double Kershaw mesh

Figure 3-34. Iso-countours of the computational solution at z = 0.5. (a) with uniform orthogonal mesh Grid 1 (50×50×50) ; (b) with randomly distorted mesh Grid 2 (50×50×50); (c) with extremely distorted mesh Grid 3(51×51×51); (d) with a double Kershaw mesh (16×16×16)

In Table 3-21, the results of convergence rate for 2D and 3D test problems are summarized. It is well-known that the efficiency of linear system solver has a great impact on the whole computational time. From Table 3-20, we firstly noticed that the CPU time spent in solving the linear systems is more than 68% of the total CPU time of the computation for all tests. In our computational tests we used an extended version [267] of the Stone's SIP solver. It is worth noting that both the stopping criteria for the linear system solver and the outer iteration loop (sweeps) would seriously affect the computational cost. Here they have been set to 10^{-2} and 10^{-7} respectively. Even though the test problem and grid non-orthogonality are not fully similar for both 2D and 3D cases, the same degree of distortion, $\alpha = 0.2$, have been used [268]).

Comparing the CPU time per cell for 2D and 3D case for the same mesh size in each coordinate direction, we can notice a larger increase for the 3D case. This should be attributed to the following differences between the 2D and 3D cases: (1) the computational task for every single cell, (2) the computational cost for each SIP loop and (3) the computational cost for each sweep loop. There are four surfaces for a single 2D quadrilateral mesh, while there are six surfaces for a 3D hexahedron mesh, which means that the computational task to account the nonorthogonal contribution to the diffusive fluxes computation in 3D is 1.5 times more than in 2D. This point can be verified by

comparing the total iterations times per surface of 2D and 3D cases, which are always similar for the same mesh size in each coordinate direction. For every single sweep loop, the increase time in 3D is mainly due to: the 2nd-order Gauss Formula for gradient evaluation and the Low and Upper Decomposition of SIP solver.

Table 3-21. Comparison of CPU time per cell for the randomly distorted mesh in 2D and 3D

	Two-Dimension		**Three-Dimension**	
Number of cells	40×40	80×80	40×40×40	80×80×80
Number of sweeps	4	4	3	3
Number of SIP loops	418	1505	3	3
CPU time for SIP	---	0.190s	3.420s	57.650s
Total CPU time	0.024s	0.248s	5.028s	84.313s
CPU Time per Cell	1.500 e-5s	3.860e-5s	7.86e-5s	1.648e-4s

---: Lack of data; Computations are performed on a 3 MHz Pentium workstation.

We also test the problem with the Double Kershaw mesh. The grid is known as one of most stringent test cases, as all six components faces are seriously non-orthogonal. Through the success of the application of IDC scheme to the mesh, we expect the IDC scheme combined with our extension method can be applied to arbitrary 3D meshes.

3.6 Conclusions

All governing equations in Navier-Stokes, Electro-hydrodynamics (EHD) and Electro-Thermo-Hydrodynamics (ETHD) system are rewritten into a general transport equation. A finite volume discretisation technique has been described.

The discretisations of the temporal and spatial terms (convection and diffusion) have been outlined in Section 3.3. The proposed discretisation treatment is second-order accurate in space and time, even on non-orthogonal meshes for complex geometries.

For convective schemes, we systemically described the so-called high-resolution (TVD-type and NVD-type) schemes, including their basic idea and expressions. High-resolution schemes can guarantee bounded solutions and preserve the second-order accuracy at least. Some practical details for the implementation (e.g., extension to multi-dimensional, boundary condition treatment and potential problems for unstructured meshes) are discussed.

For temporal schemes, several traditional schemes (e.g., Euler Implicit, Euler Explicit, Crank-Nicholson and Implit Three Time Level) and so-called strong-stability preserving (SSP) high order time schemes have been examined.

For diffusive schemes, we focused on a newly proposed scheme for the non-orthogonality treatment. The scheme is based on the normal decomposition method. We successfully build its connection with other widely used methods (i.e., direct gradient evaluation method and coordinate transformation method) for the calculation of diffusive flux. In addition, the ways for its optimal

boundary condition (both Dirichlet and Neumann types) and extension to three-dimensional problems are also presented.

In Section 3.4, a discretisation procedure for coupled systems of equations has been presented. The SIMPLE algorithm is used to treat the pressure-velocity coupling system for both steady and transient flows. The Rhie-Chow interpolation is used to prevent the generation of checker-boarding pressure field for collocated variable arrangement.

In the numerical test section, we compared the performances of various high-resolution differencing schemes. The behavior of different temporal discretisation schemes combining with high-resolution schemes is also given. For diffusion scheme, the importance of gradient evaluation method for the performance of normal decomposition schemes is highlighted.

Chapter 4 Program procedure and validation

4.1 Introduction

The numerical algorithm and various discretisation schemes described in the previous chapter have been used to develop the computer programs which can be applied to Electro-hydrodynamics (EHD) and Electro-Thermal-Hydro-Dynamics (ETHD) problems.

One version uses the general quadrilateral mesh, which can be applied to both simple and complex geometry two-dimensional problems. Another version uses multi-block hexahedral elements for three-dimensional problems. Both versions are mainly detailed in [248] for some practical implementation.

Before applying the numerical solver to complete EHD and ETHD problems, some validation tests need to be performed. Some problems, for which either analytic solutions or well established experimental or numerical results exist, are selected as the test cases.

In Section 4.2, the solution sequence for the Navier-Stokes system with additional coupled equations (e.g. energy equation, charge density and electric potential equations) is explained in details. The update of boundary conditions and physical parameters are also included.

In Section 4.3, the validity of the space charge – electric field couple module is tested with two problems. The first one is the hydrostatic solutions between two parallel planar electrodes. The other one is a steady state corona discharge using a non-orthogonal grid. The purpose of the latter case is to highlight the applicability of our solvers to problems with complex geometry.

In Section 4.4, the classical two-dimensional lid-driven skew cavity and Rayleigh-Bénard convection (RBC) are used to validate the Navier-Stokes and energy modules. For lid-driven skewed cavity problem, we highlight the effectiveness with the IDC scheme for the pressure correction equation. For RBC problem, the numerical validation is based on the comparison between the numerical value of linear stability criterion, Ra_C, with the theoretical value, i.e., 1708.

Finally, some closing remarks are given in Section 4.5

4.2 The calculation procedure for EHD and ETHD system

The first step with the numerical simulation is to generate the mesh for the computational domain. Here, some in-house programs were developed for simple geometry problems. For two-dimensional and three-dimensional problems, the pre-processor software GridgenV15 has been used for this purpose.

The Poisson and charge density transport equations with two unknown variables: electric potential ϕ and space charge density q, are the two governing equations describing the unipolar injection model. The Poisson equation is solved with the proposed FVM-IDC scheme. With orthogonal meshes, the IDC scheme becomes the 2nd central differencing. The charge density equation is solved with the FVM-TVD algorithm. Various temporal schemes (IE, I3L, EE, 2nd TVD-RK and 3rd TVD-RK) were implemented in our solvers.

For transient computations, the whole algorithm to obtain the electrical, velocity, pressure and temperature characteristics inside the physical domain consists of two loops: one inner loop and one outer loop. The inner loop solves the Navier-Stokes equations within the SIMPLE algorithm. To sum up, the complete procedure includes the following steps:

1. Set up the initial conditions. The complete zero-field and hydrostatic equilibrium solutions are the two most common options.
2. Start the calculation of a new-time step with the computation of Poisson equation.
3. The electrical field is computed with the Gauss formula or the Least-squares approach.
4. Solve the charge density equation with the FVM-TVD algorithm. The discretization of the temporal and convective terms is separated based on the method of line approach. Both implicit and explicit time schemes are incorporated into our solvers.
5. Solve the Navier-Stokes equations with the SIMPLE algorithm. An inner iteration loop is required. The blended scheme with FUD and CD schemes is implemented to solve the mass and momentum conservation equations. The Euler implicit (IE) scheme and implicit three levels time (I3L) scheme are used for the time marching purpose. The electric field and space charge density are used for computing the electric body force $\vec{f} = q\vec{E}$. The temperature field is used to compute the buoyancy force. To judge the convergence of the inner loop, the stopping criteria based on reduction of the residual is used [70].
6. Solve the energy equation. The energy equation can be solved after the SIMPLE loop for velocity and pressure or may be included into the inner loop of SIMPLE algorithm. The choice depends on the coupling degree between the velocity and temperature fields.
7. For non-autonomous injection, we need to update the boundary condition for charge density equation at the end of the time loop. For temperature-dependent physical properties, we need to update the values of ε and K with the latest temperature field.
8. If the final time is not reached, return to step 2.

The full algorithm of the numerical solver for both EHD and ETHD problems is illustrated in Figure 4-1.

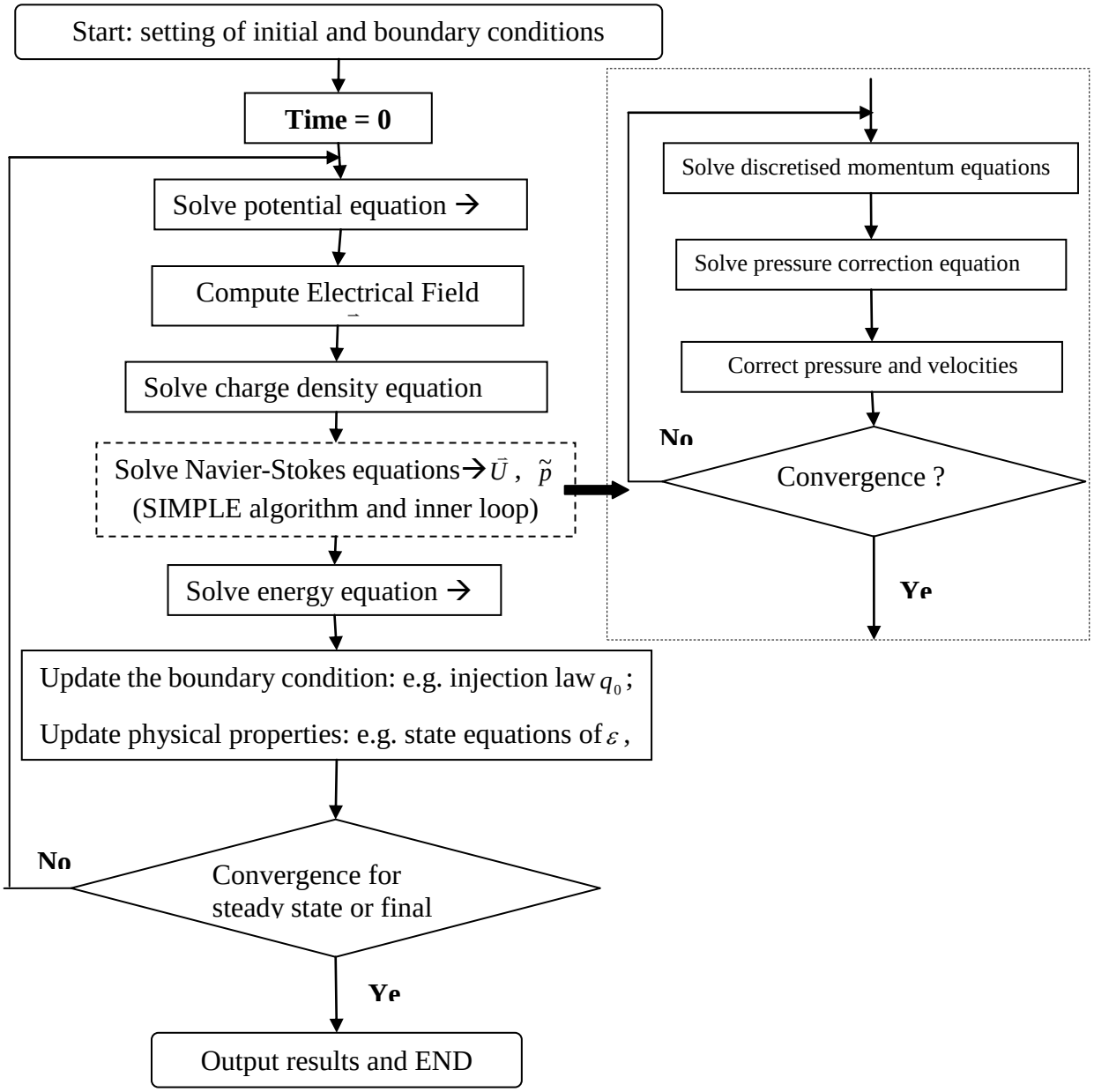

Figure 4-1. Computational cycle of the simulation process. The figure in the left dash box is the inner loop of SIMPLE algorithm

4.3 Electric field-space charge coupled module

Accurately predict the distributions of space charge density and electric field in EHD problem is the most important motivation of the present study. In this section, we selected two test cases to show the effectiveness of the proposed techniques for the charge density equation.

4.3.1 Steady hydrostatic solution between two planar electrodes

Considering the problem of unipolar injection between two parallel planar electrodes, the system admits a steady hydrostatic solution which means the velocity field keeps zero and the charge density is transferred with drift velocity only. Assuming the injection is from the lower electrode, the analytical solutions for the charge density is

$$q(y) = \frac{a}{2}\frac{1}{\sqrt{y+b}} \tag{4-1}$$

which decreases from the injector and the electric field,

$$\phi = -\frac{2}{3}a(y+b)^{3/2} + c \tag{4-2-1}$$

$$E(y) = a\sqrt{y+b} \tag{4-2-2}$$

modified by the space charge distribution.

The constants *a* and *b* in Eqns. (4-1) and (4-2) depend on the injection strength *C* (see below).

$$\frac{2}{3}a\left[(1+b)^{\frac{3}{2}} - b^{\frac{3}{2}}\right] = 1 \quad , \quad b = \frac{a^2}{4C^2} \quad \text{and} \quad c = 1 + \frac{2}{3}ab^{3/2} \tag{4-3}$$

Several typical values of the *C* parameter, which stands for different injection strength, will be used in the present study. The corresponding *a* and *b* are provided in Table 4-1.

Table 4-1. Various injection strengths and their corresponding *a* and *b* constants

C	***a***	***b***
0.1	0.4363	4.7590
0.25	0.6651	1.7696
1.0	1.1256	0.3167
10	1.4882	5.539×10^{-3}
100	1.4999	5.62×10^{-5}

For autonomous and homogeneous injection from the bottom electrode, the hydrostatic solution is essentially one-dimensional. However, in order to demonstrate the ability and accuracy of the FVM-TVD algorithm for multi-dimensional problems, both two- and three-dimensional cases are solved. Since there is no difference between two- and three-dimensional solutions, we only listed the 2D results below. Both weak $(C = 0.1)$ and strong $(C = 10)$ injection cases are considered. From the analytical expressions, it is noticed that the hydrostatic charge density and electric field distributions show slower variation in the vertical direction in the weak injection regime than in the strong injection regime. This difference indicates the grid size for strong injection simulations should be smaller than the one for weak injection, at least in the vertical direction. In Figure 4-2 and 4-3, we take 50 and 100 cells in vertical direction for weak and strong injection separately. The

validity and accuracy of the TVD algorithm is highlighted by above numerical results which are in very good agreement with the analytical hydrostatic solutions.

Weak Injection $(C = 0.1)$

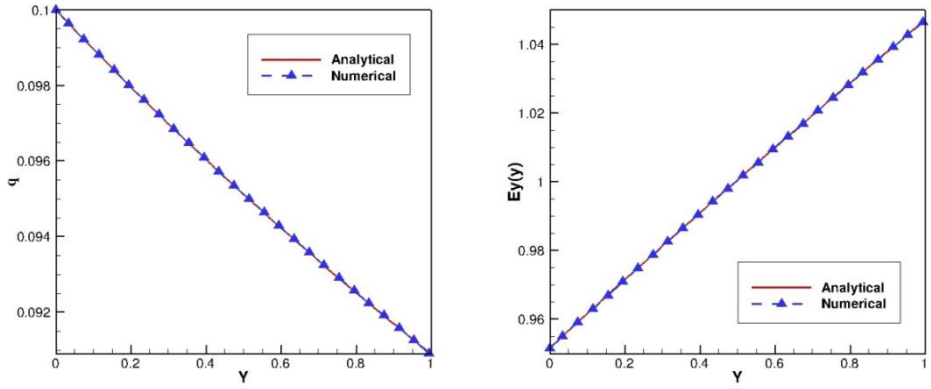

Figure 4-2. Charge density (left) and electrical field (right) in weak injection regime, $\Delta t = 10^{-3}$

Strong Injection $(C = 10.0)$

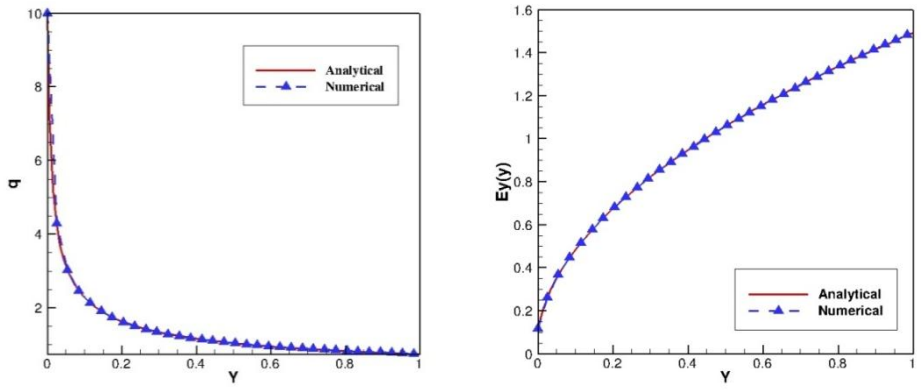

Figure 4-3. Charge density (left) and electrical field (right) in strong injection regime, $\Delta t = 10^{-3}$

4.3.2 Hydrostatic solution in a two coaxial cylinders configuration

4.3.3 A simple gas discharge problem

The second problem is a steady simple gas discharge problem in point-plate geometry. The geometry of the problem is shown in Figure 4-4. A constant voltage is applied to a hyperbolical electrode, having a tip curvature radius of R and a length of *L*. The electrode is perpendicular to an infinitely large ground plate at a gap *d*. The discontinuous electron injection is also applied to the hyperbolical electrode.

As the problem is symmetric only half of the domain is considered. The boundary conditions are indicated on figure 4-5. The injecting surface on the blade is limited from the edge of the blade until the point referred by s_0= (-1.095E-5, 4.517E-5) and q_0=0.01C.

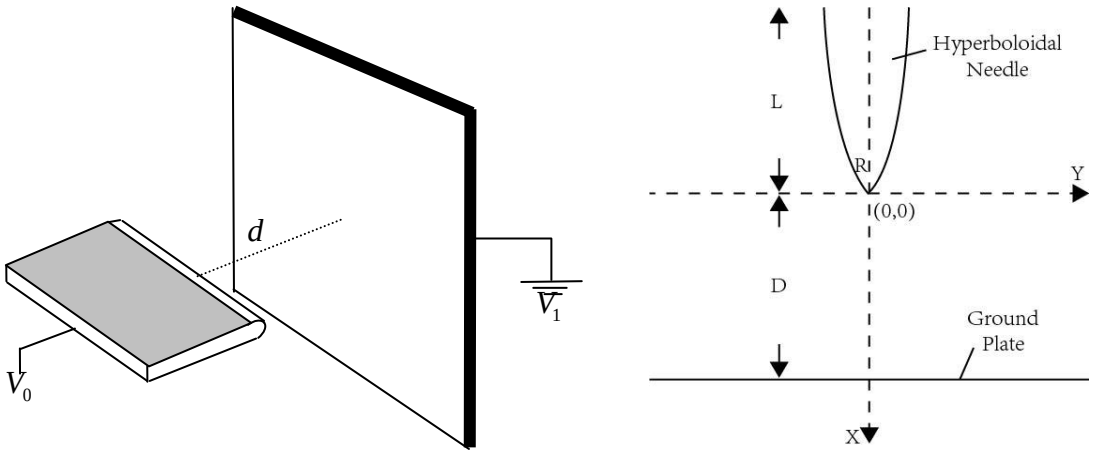

Figure 4-4. Sketch of the blade-plane configuration.

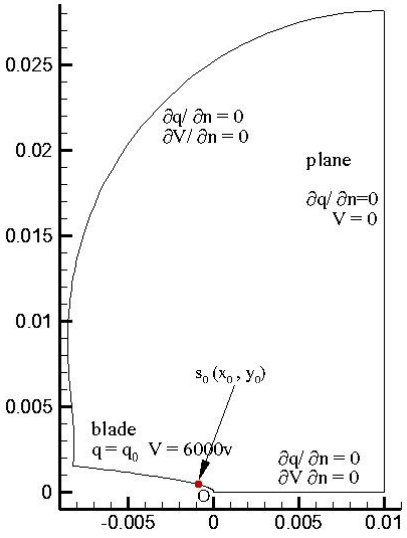

Figure 4-5. Sketch of the computational domain with boundary conditions.

The governing equations describing the space-charge effects arising from electrical corona are the steady Poisson equation and the current continuity equation,

$$\nabla^2\phi = -\frac{q}{\varepsilon_0} \tag{4-4}$$

$$\nabla\left(K_0 q\cdot\nabla\phi\right) = 0 \tag{4-5}$$

where ε_0 is the gas permittivity, $\varepsilon_0 = 8.85\times10^{-12} F/m$; K_0 is the mobility of charge carrier, $K_0 = 2.0\times10^{-4}\,\mathrm{m}^2/\mathrm{V}\cdot\mathrm{s}$.

To obtain the steady solutions for above coupled equations, the segregated iterative algorithm [54] or a simple time marching approach can be used. The time marching approach means we convert the steady charge density equation to be time dependent. Then the two equations are solved in a segregated manner in each time step. After long enough time, a steady state will be reached. Here, the emphasis is the spatial scheme. Thus, a fist Euler Explicit scheme is used for time marching.

The grid shown in Figure 4-6 is generated from the equipotential and electric field lines of the space-charge free solution [269] [270]. The grid of Figure 4-6 consists of 100×100 = 10000 cells. As the grid size is rather small, the time step should also be small enough to satisfy the CFL constraint. In the present study, Δt is set to be 10^{-8}. To judge the steady state, we compared the solutions of charge density and electric potential of present time step with the ones at previous time step. When $\frac{|\varphi - \varphi_0|}{\varphi_0} \le 10^{-7}$, where φ stands for the charge density or electric potential, we stop the computation and believe the solutions reach a steady state. The whole computation lasted for 13071 time steps.

For the computation of the Poisson equation, the IDC scheme and the improved Least-Squares approach are used. The SMART scheme is chosen as the limiter function for the TVD approach.

The numerical solution obtained by Adamiak with the Finite-Element Method combined with the Method Of Characteristics (MOC) is very close to Figure 4-7 (a) and (b). It is noticed that solutions of the charge density with both methods are bounded in the range [0, 0.01].

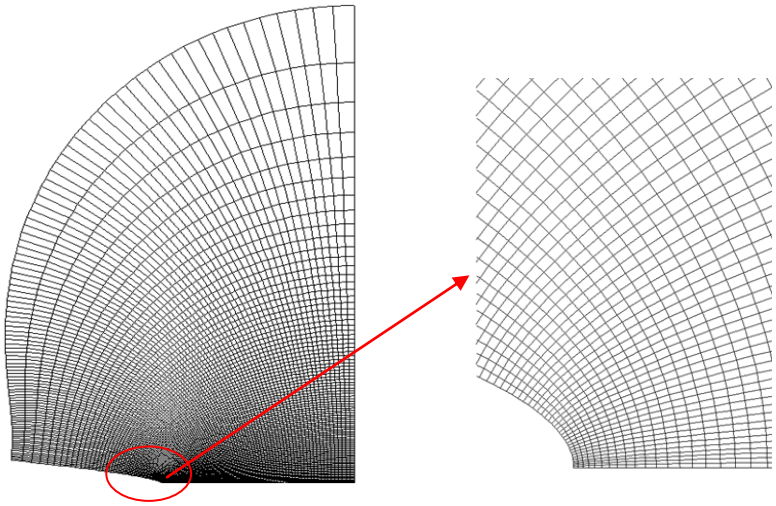

Figure 4-6. Computational grid constructed from equi-potentials and field lines [269]

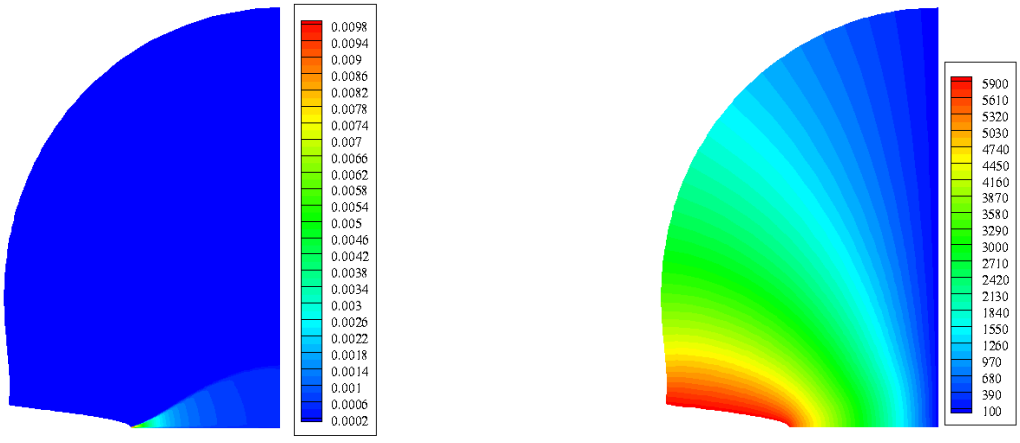

(a) Charge density distribution (b) Electric potential distribution

Figure 4-7. Numerical solution of the simple gas discharge problem with the FVM-TVD-IDC approach

To make a quantitative comparison of the solutions obtained with FEM-MOL technique, we presented the charge density profile in the radial direction and in the y direction along the vertical plate in Figure 4-8. The results were compatible with the solutions obtained with the FEM-MOL method, which testifies the effectiveness of our FVM-TVD-IDC numerical algorithm. The main advantage of our method compared with FEM-MOC is a significant decrease of computational cost. Indeed the methods based on MOC require a re-meshing of the computational domain with additional interpolations at each time step which are not necessary in our case since the same mesh for electric potential and charge density is used.

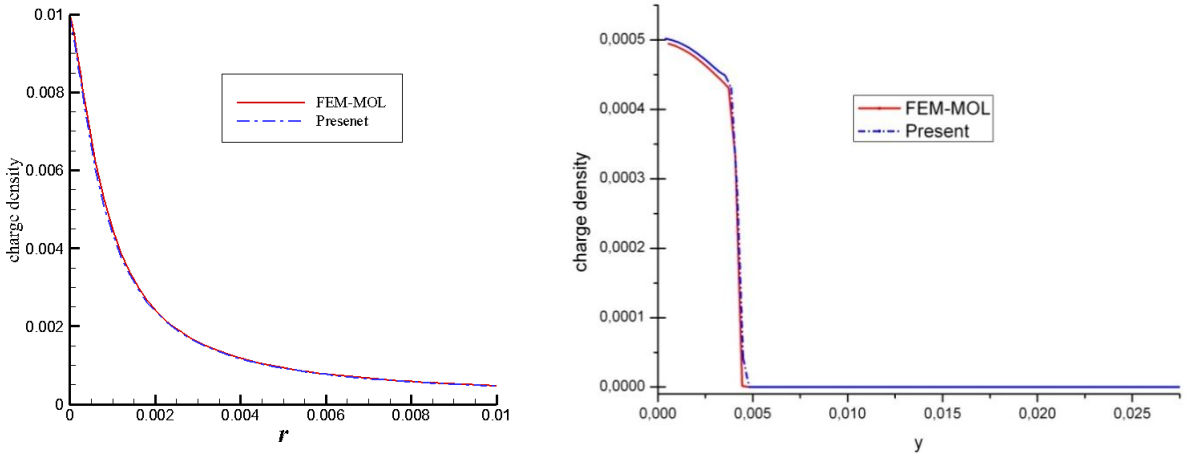

(a) (b)

Figure 4-8. Comparison of charge density distribution along the horizontal symmetric line versus *r* (a) and on the plane electrode versus *y* (b).

Another numerical test with the computation of hydrostatic solutions in a two coaxial cylindrical configutration is done and details results can be found in [260].

4.4 Navier-Stokes and energy modules

The first test case chosen below is to highlight the application of IDC scheme to pressure correction equation. The second one is to verify the energy module.

4.4.1 Lid-driven skewed cavity

Laminar Lid-driven cavity flow has long served as a standard test case for both orthogonal and non-orthgonal grids. The problem is depicted in Figure 4-9 (a). The top wall is moving from the left to the right at a constant speed, U_{lid}. The aim of the problem is to demonstrate the capability of our solver for complex geometry problems and to show the effectiveness of the IDC scheme in a full Navier-Stokes computation framework.

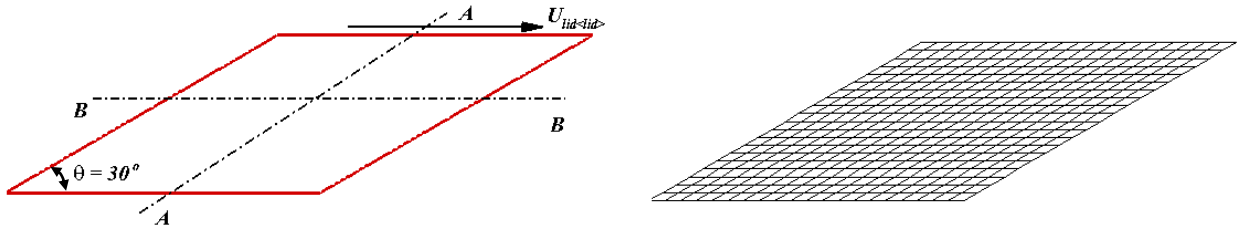

(a) (b)

Figure 4-9. (a) Lid-driven skew cavity flow (b) uniform skewed non-orthogonal meshes

Demirdzic *et al.* [271] have investigated this problem with a body fitted algorithm and obtained the benchmark solutions by using a 320 × 320 quadrilateral grid. The case with inclined angle θ = 30° was studied. Calculations were carried out for two Reynolds numbers, 100 and 1000. A uniform skewed grid with 100×100 cells was generated for this study as depicted in Figure 4-9(b). Note only 20×20 cells are depicted here on figure 4-9b. The streamlines are presented in Figure 4-10. These flow patterns agree well with those obtained by Demirdzic et al. [271]. Centerline velocity profiles for *u* (A-A direction) and *v* (B-B direction) velocity components are shown in Figure 4-11 and 4-12.

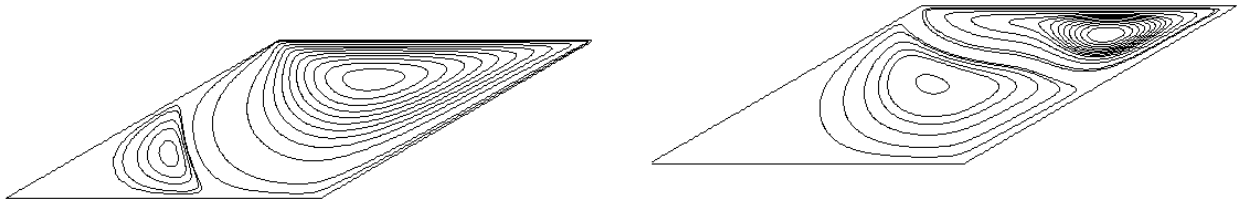

(a) Re = 100 (b) Re = 1000

Figure 4-10. Calculated stream functions contour for skewed lid-driven skewed cavity flow

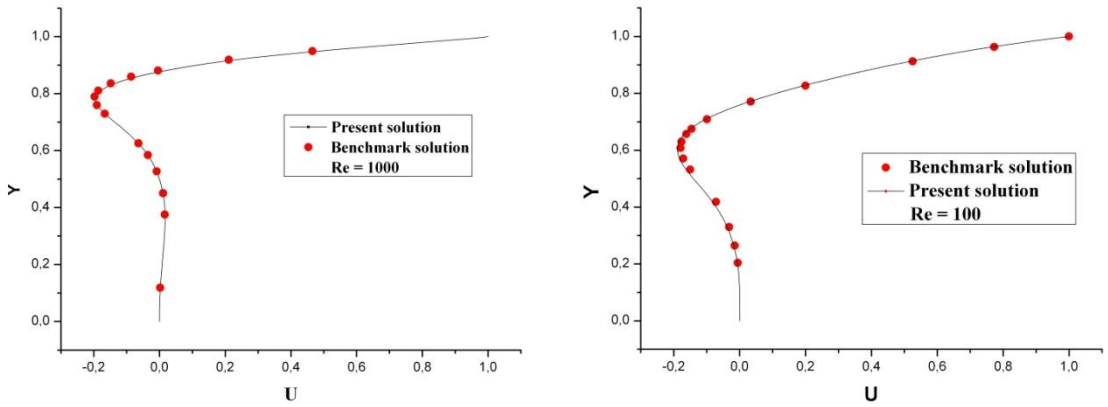

Figure 4-11. Comparison of the computed velocity at the centerline with the benchmark solution: velocity component u along A-A line

From above comparisons, we see that our numerical results match the benchmark solutions fairly well.

In [128], Peric stated that the SIMPLE algorithm with the simplified one-step pressure correction equation became inefficient when the angle between grid lines approaches 45^{o}, and it usually failed

to converge for angles below 30. It should be noted that the SDC scheme is used by Peric to solve the unique pressure correction equation. When applying the IDC scheme for solving the pressure correction equation, we can obtain convergent solutions even for an angle of 20. However, the problem has not been solved completely, as we failed to obtain convergent solution at angle of 10. Some more studies are required for this point.

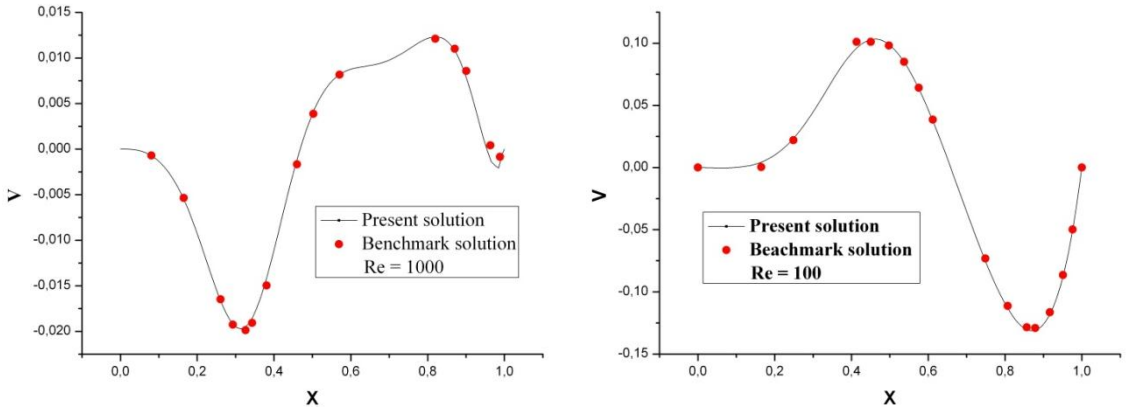

Figure 4-12. Comparison of the computed velocity at the centerline with the benchmark solution: velocity component v along B-B line

4.4.2 Two dimensional Rayleigh-Bénard convection

The classic Rayleigh-Bénard convection problem is used as test case to validate the energy module within our numerical solver. Considering a planar horizontal fluid layer $0 \le x \le L$ and assume the temperatures at the undeformable top and bottom surfaces of the layer to be fixed.

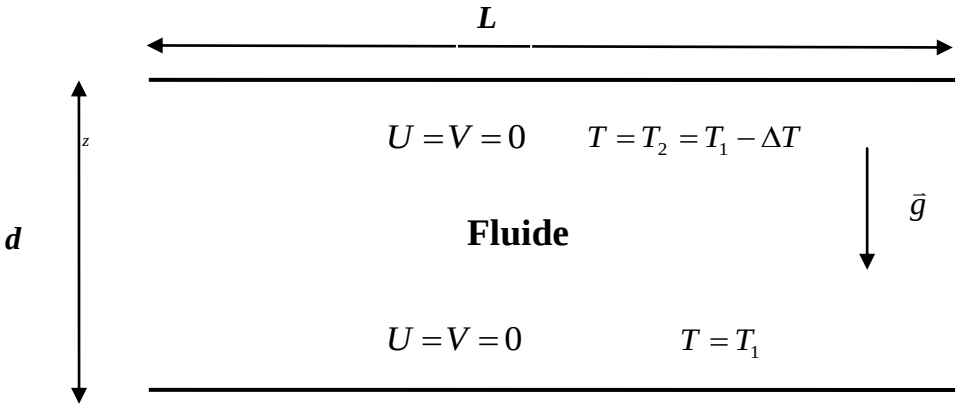

Figure 4-18. Geometry and boundary condition for Rayleigh-Bénard convection

The sketch of the computational domain with boundary conditions is presented in Figure 4-18.

$T = T_1$ at $y = 0$,

$T = T_2 = T_1 - \Delta T$ at $y = d$,

where $\Delta T = \beta h$. In the case of $\beta > 0$, the system is potentially unstable. It is well-known that the main parameter that drives the physical phenomenon is the Rayleigh number (Ra). In fact, when Ra is lower than a first critical value, the flow stay at rest and heat transmission is only due to conduction. Above a critical value, the fluid is put into motion exhibiting convective rolls. The critical value of Ra has been determined both analytically [272] and experimentally [273], being independent of the Prandtl number (Pr). For the case of both top and bottom surfaces of the layer are rigid, the critical Rayleigh number and its corresponding critical wave-number:

$$Ra_C = 1707.762 \quad , \qquad k_c = 3.117$$

We numerically solved the equations of Navier-Stokes with energy equation to provide a numerical prediction of the linear stability criterion. Close to the instability threshold, the perturbations of every physical quantity f grow according to the exponential law $f = f_0 e^{\sigma t}$. The growth rate σ is positive above the instability threshold and negative below it. The linear criterion is characterized by $\sigma = 0$. If we let the system evolve from rest, the tiny numerical fluctuations will provide suffice to induce the motion. After an initial period of still state, an interval of exponential growth of the velocity is observed, to see Figure 4-19. For a given set of *L*, *Ra* and *Pr* number, we calculated $\sigma_m = \max \sigma(L, Ra, \Pr)$ and represented σ_m as a function of *Ra* for given *Pr*, see Figure 4-20. For the case *Pr=10*, $\sigma_m = \sigma_m(Ra)$ is straight line segments, cutting the Ra-axis at,

$$Ra_C(numerical) = 1706.6$$

a value very close to the one provided by stability analysis. Generally, the difference between the numerical and the analytical ones decreases with finer grid size. It should be noted that the expression $\sigma_m = \sigma_m(Ra)$ is linear function only in the range *Ra* is close to R_C. However, the perturbation amplitude is proportional to $(R - R_C)^{1/2}$ at small values of the expansion parameter. Thus we cannot use Ra values which are too close to Ra_C, otherwise the system needs very long time before the convection starts. During the computation, *L=1* is chosen to keep consistent with half of the critical wave length, $\lambda_C = \pi / k_C \approx 1.0$. The symmetric boundary condition is applied to vertical sides to simulate the convection in an infinite layer. We fixed *Pr* as 10 and picked *Ra* = 1750, 1800 and 1850 to determine the relation $\sigma_m = \sigma_m(Ra)$. The maximum value of the vertical velocity V_{max} in the computational domain is used as the representative quantity and its time evolution is plotted on Figure 4-19.

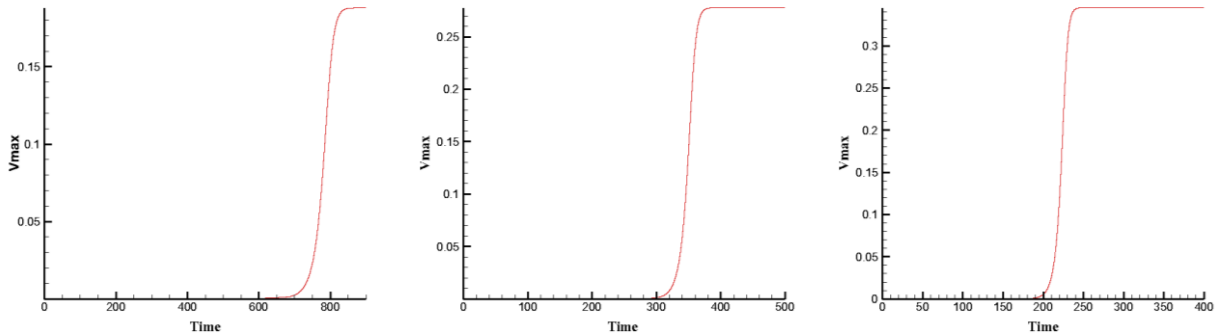

(a) Ra = 1750 (b) Ra = 1800 (c) Ra = 1850

Figure 4-19. The evolution of Vmax in the domain, *Pr*=10, *L*=1, 100×100 uniform grid;

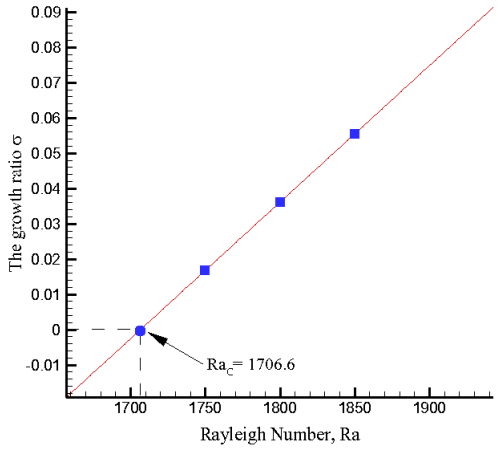

Figure 4-20. Growth ratio σ versus Ra for $L = 1$ and $Pr = 10$

Besides the critical criterion, it is also interesting to have a look of the Nu – Ra curve, which has been widely used to express the experimental results. The mean Nusselt number is defined as

$$\overline{Nu} = Q / Q_C$$

where Q is the actual heat flux across the cavity and Q_C is heat flux that would result from pure conduction. The heat flux Q may be calculated by summing the convection and diffusion fluxes through CV faces at any grid line of x = constant. Owing to the inherent conservativeness of finite volume method, it is equal to the wall heat flux, which is determined by the difference in the wall and at the centers of the near-wall CVs. Both the hot and cold wall heat fluxes were recorded in Table 4-2 and shown in Figure 4-21. It is expected that there is always little difference between ***Nu_hot*** and ***Nu_cold***. It is also noticed that the bifurcation of RBC is supercritical as there is no velocity jump at R_C and hysteresis loop.

It is noticed that there is a decrease of Nu number at *Ra*=7000 and 8000, which should be due to the change of the flow structures. Up to *Ra*=7000, the flow is steady with one convective cell, while at Ra = 8000, the flow adopts a two-cell structure, to see Figure 4-22. This kind of flow structure bifurcation will also be observed for unipolar injection problem, in the next chapter.

Table 4-2. Numerical results on the heat transfer between two parallel plates

Ra	**1700**	**1750**	**1800**	**1850**	**1900**	**2000**	**2100**	**2200**	**2300**	**2400**	**2600**
Nu_hot	1.0	1.035	1.074	1.112	1.147	1.213	1.274	1.330	1.328	1.431	1.518
Nu_cold	1.0	1.035	1.074	1.112	1.147	1.213	1.274	1.330	1.328	1.431	1.518
Ra	**2700**	**2800**	**2900**	**3000**	**4000**	**5000**	**6000**	**7000**	**8000**	**9000**	**10000**
Nu_hot	1.557	1.595	1.630	1.663	1.924	2.104	2.243	2.356	2.011	2.153	2.280
Nu_cold	1.557	1.595	1.630	1.663	1.924	2.104	2.243	2.356	2.011	2.153	2.280

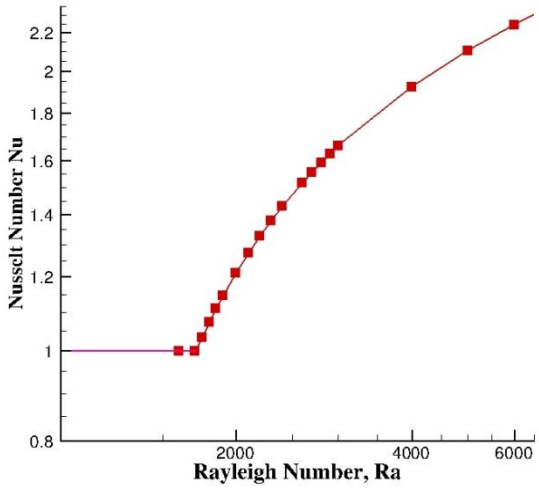

Figure 4-21. Numerical results on the heat transfer of Rayleigh-Bénard flow problem. The Nusselt number is plotted against the Rayleigh number. Pr = 10, L = 1. Symmetrical boundary conditions have been applied to the lateral walls.

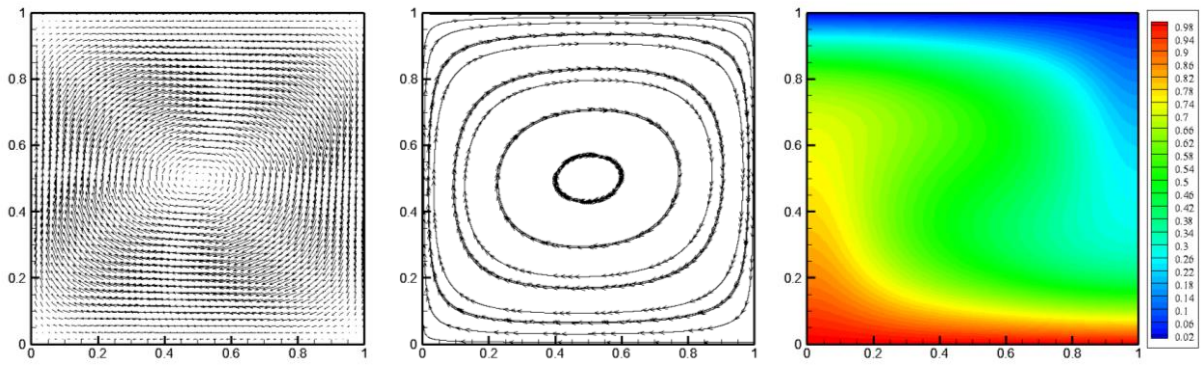

(a) Ra = 7000, one convective cell

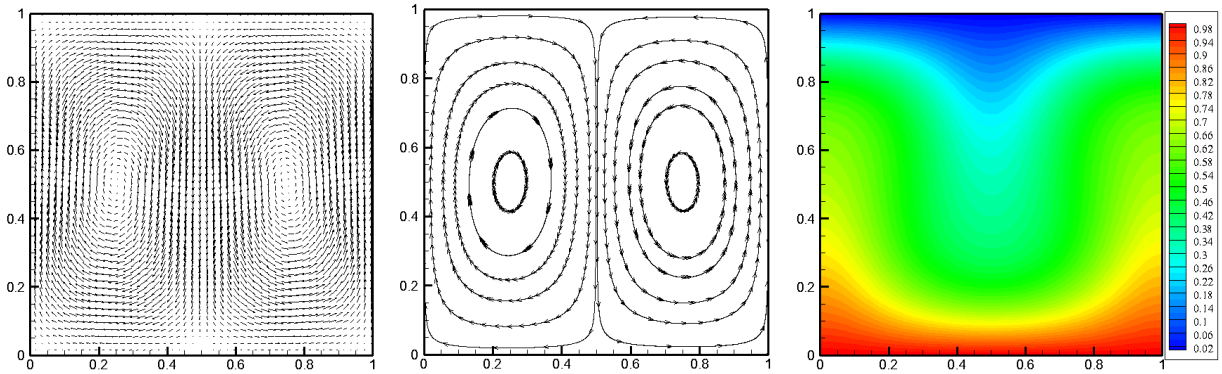

(b) Ra = 8000, two convective cells

Figure 4-22. Velocity field, stream function contour and temperature field distribution for (a) Ra = 7000 and (b) Ra = 8000, Pr = 10, L = 1

4.5 Closure

In this chapter, the solution procedure for the EHD and ETHD problems was explained in detailed. The electric field-space charge couple module, Navier-Stokes and energy module were validated with various meaningful test cases. Very good agreements with known results are obtained.

Chapter 5 Numerical simulation of electro-convection in insulating liquids induced by unipolar injection: finite amplitude convection

5.1 Introduction

Unipolar injection from an electrode into a perfectly insulating liquid is a fundamental problem in the field of electrohydrodynamics. The question of hydrodynamic instability appears when the geometries of electrodes are highly symmetrical. Three typical cases are: parallel planar plates, co-axial cylinders and concentric spheres. In the present study, only the first case will be investigated. Considering the condition that the charge is uniformly injected into the liquid, the motionless state with zero velocity fields ($\vec{U}=0$) is a solution of the whole system. The motionless state is also named hydrostatic solution. The linear stability problem is to decide the critical condition under which the motionless solution destabilizes.

For linear instability phenomena, the unipolar injection shares analogy to the Rayleigh-Bénard (RB) problem (a horizontal fluid layer heated from below). In RB problem, the motion starts only when the adverse temperature gradient (characterized by Rayleigh number, Ra) exceeds a critical value [275, page 10]. In addition, the motion ensuing from the surpassing the critical temperature gradient has a stationary cellular character (neutral stability) [275]. In pure unipolar injection, the qualitative conclusions are more or less the same: (1) there is a critical voltage which is associated with the onset of the motion; (2) the motion is in the form of cellular convection near the critical voltage. However, the detailed linear stability mechanisms are slightly different from each other.The instability study of the problem was done by Atten and Moreau [144]. Their study well explained the linear instability mechanism and defined a non-dimensional number as the attractor of the pure unipolar injection problem.

The analogy to the RB problem is no longer valid for the liquid in motion due to the conduction mechanism of the scalar quantity in motionless state: drift with a finite velocity $K\vec{E}$ for charge carrier, diffusion for heat [276]. Considering the behavior of the system for T close to T_C, there is a discontinuity at T_c for the steady amplitude of the convective velocity and the steady current, while the steady amplitude of the convective velocity and average Nusselt number varies in a continuous way with Ra in RB problem, to see Figure 4-15. In addition, the unipolar injection problem is also characterized by a sub-critical bifurcation. In the interval $[T_f, T_C]$, there exist one stable and one unstable finite amplitude solutions. This is related with a hysteresis loop, which can be shown with the velocity amplitude and the electric current. Both the linear and nonlinear stability phenomena have been verified with experimental of the space-charge limited (SCL). Some representative results are presented in Figure 5-1 to show the two stability criteria. In Figure 5-1a, Ne is the

electric Nusselt number and is defined as $Ne = I / I_0$, the ratio of measured steady current I and current I_0 without liquid motion. It is noticed that the discontinuities at nonlinear (51V) and linear (56 V) instability voltages. In Figure 5-1b, the non linear criterion is $T / T_c C = 0.933$ and the critical amplitude of velocity field is $A = 1.6$.

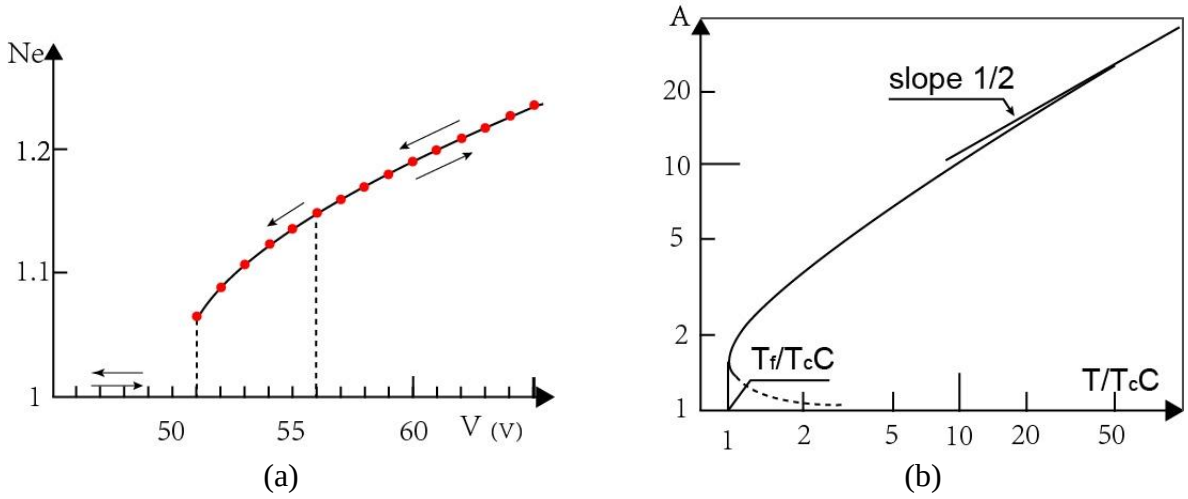

Figure 5-1. (a) Variations of *Ne* as a function of applied voltage [276] when SCL injection into a mildly polar liquid, Pyralene 1460TM between plane parallel electrodes. (b) Velocity amplitude for steady electro-convection as a function of $T / T_c C$ $(C = 0.1)$ [153].

Increasing the voltage, the electric current is steady and there is no motion in liquids. At a certain voltage V_C, corresponding to the linear criterion, the fluid is set in motion and the current jumps to a higher value and then continues to increase with voltage. If the voltage is decreased, the fluid keeps its motion and current do not reach its original value for $V < V_C$, but until a value $V_f < V_C$ is reached, where V_f is the nonlinear criterion.

The linear and nonlinear phenomenon can also be characterized by a sub-critical (backward) bifurcation from a mathematical viewpoint. In the interval $[V_f, V_C]$, there exist two finite amplitude solutions, one stable and the other one unstable [276]. This is related with a hysteresis loop and jumps of the steady values of both the velocity amplitude and the current at the linear V_C and nonlinear criteria V_f [148].

Linear instability mechanism

Theoretically, the main object of the instability study is to determine the critical conditions for which at least one perturbation begins to grow exponentially by examining the time evolution of the perturbations.

A simple argument can help to qualitatively understand the linear stability. At stationary state, the charge density distribution decreases from the injector into the fluid due to Coulomb repulsion while the electric field is increasing. If we consider the virtual displacement of a fluid 'parcel' which conserves its charge towards the collector, we see that it is then subject to a greater Coulomb

force than the fluid immediate to it. It will thus have a tendency to continue its displacement towards the collector. The coupling between charge and velocity perturbations is then positive [276]. This positive coupling indicates the stationary charge distribution is unstable. When the electric force is strong enough to overcome viscous damping, small velocity perturbation will amplify. A more accurate explanation which takes into account the change of charge density during the displacement of blob was given in [276].

In the case of weak injection limit ($C<<1$), the linear stability is characterized by the criterion $T_c C^2 = 220.7$, while in the other asymptotic case of space charge limited ($C \to \infty$), $T_c \to 161$. For arbitrary injection strength, the critical values can be found in [144] and Figure 5-2 which is plotted with the data provided in [144] to highlight the tendency of T_c varying with the injection strength. In addition, the critical non-dimensional wave number k_c takes values close to 5 and only slightly depends on C, see Figure 5-3. The shape of the curve is analogous to the one of RB problem, to see Figure 2 in [275, page 15].

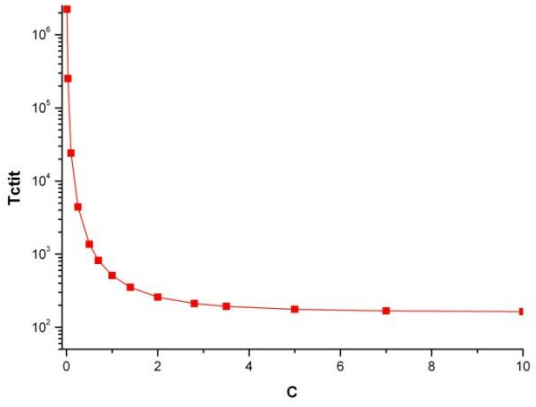

Figure 5-2. Linear stability criterion T_c for various injection strength C

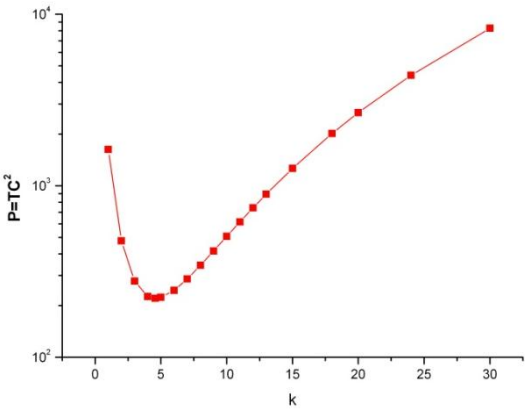

Fig.5-3 Numerical values of parameter $P=TC^2$ characterizing the marginal perturbations of wave-number k in the case of weak injection

The experimental studies have been carried out for the SCL injection into viscous mildly polar liquid in planar geometry. Both the linear stability and nonlinear phenomena have been observed successfully with the help of the measured electric current. However there are clear discrepancy between the experiments and theoretical analysis, when comparing the experimental value of $[T_c]_{\exp} \approx 100$ [175] and the theoretical value $[T_c]_{the} = 161$. The difference remains yet unexplained [59]. Some attention should be paid to the assumption made in [144]: infinite space; the fluid is non-autodissociable; homogeneous and autonomous unipolar injection; the neglect of diffusion transport of charge. The difference between $[T_c]_{\exp}$ and $[T_c]_{the}$ may come from these simple hypotheses. For example, when taking into account the diffusion mechanism for charge transport, the difference will decrease [277]; when the physical domain is limited, the vertical wall boundary conditions will stabilize the flow (a higher $[T_c]_{the}$), especially for the case of finite size [56]; the assumption of autonomous injection would also lead to lower bounds for the critical linear criteria [276].

Only the critical conditions can be derived with the tool of standard linear stability analysis. As for the flow configuration, the non-linear analysis is required.

Nonlinear instability

The great features of the nonlinear instability mechanism have been derived by Félici who used a simple hydraulic model in the case of weak injection between two parallel plates [147]. Atten and Lavroix [148] extended the foregoing simplified model to the case of hexagonal cell and studied the nonlinear stability problem with a Galerkin method. They successfully predicted the existence of a nonlinear stability criterion as well as a hysteresis loop associated with the discontinuities in current and liquid velocities.

When the motion sets in, it always takes place with a maximum liquid velocity greater than the ion drift velocity, and there is a region of the convection cells where ions could not enter into the region and the region would therefore remain avoid of charges.

Due to this charge void region, the electric torque increases with velocity more than linearly and thus more rapidly than viscous resistance. In other words, a smaller electrical potential (or a smaller *T*) is needed to compensate the drag.

With this hydraulic model, the nonlinear criterion and the amplitude of velocity field (*A*) follows the following rules:

$$T_f = T_c C \qquad \text{and} \qquad A(1+A) = 2\frac{T}{T_c C} \;\rightarrow\; A \approx \left(\frac{2T}{T_c C}\right)^{\frac{1}{2}} \quad \text{with} \quad \left(T >> T_f\right)$$

Atten and Lacroix [146] improved the model by assuming the motion was in the form of steady hexagonal cells. With a Galerkin method, these authors [148] also proved the existence of a nonlinear stability (T_f) which is smaller than the linear one, i.e., $T_f < T_c$. Along with the nonlinear phenomenon, a hysteresis loop is associated with the discontinuities in current and liquid velocities at both criteria. The value of the nonlinear stability obtained by Atten and Lacroix [146] is $[T_f]_{the} \approx 110$, which is not far from the experimental one $[T_f]_{\exp} = 90$ [19]. In the present study, we choose three typical injection strengths $C = 0.1,\ 1.0$ and 10.0 to represent the weak, moderate and strong injection. The linear and nonlinear stability criterion of theoretical predictions are summarized in Table 5-2 with the original data are from [144] and [148].

The nonlinear behavior of electro-convection is completely new compared with the thermal-convection with the Rayleigh-Bénard problem. The difference is due to the physical difference in the transport of the scalar quantity (charge density versus temperature): heat is transferred by diffusion alone whereas the charge carriers migrate under the action of the electric field. In general, the effects of diffusion transfer for charge density can be neglected.

Therefore the liquid flow can entrain charge carriers against the force exerted by the electric field on them and prevent the injected charges from entering directly the return columns. In these columns the charge density takes values lower than the average ones.

The general structures and features of electro-convection are quite different for weak and strong injection. A brief introduction is made below,

Convective motion for weak injection $(C << 1)$

The weak injection case is characterized by $C << 1$ and, therefore by a weak effect of the Columbic repulsion between charge carriers. The charge density can be considered as remaining constant along the charge carriers trajectories. The weak space charge only slightly alters the uniform field distribution. When the liquid starts to move, the field on the injector and the current density only slightly increase. Considering the small value of the charge density at the injecting electrode, the electric current can be viewed constant and independent of the state of motion.

Some particular approximate solutions have been obtained by imposing some further assumptions, like the flow is a steady two-dimensional convective roll structure and with small Reynolds number [144]. The details of the analysis can be found in [144] and [148]. The main conclusions are summarized below:

1. The non-linear criterion takes the value $T_f = 0.933 T_C C$ corresponding to a non-dimensional amplitude of the convective roll: $A \approx 1.6$.
2. The asymptotic behavior for large T values is such that $A \propto (TC)^{1/2}$.
3. Two regimes (viscous dominated and inertial effects dominated) can be defined. In each regime, the typical velocity follows different laws.
4. The transition between the two regimes should occur for a particular value of the critical Reynolds number, which should be on the order of 10. However, such a transition will not be always observed because a convective regime where the viscous effects are dominant can always exist. In some cases, we may find that the system passes from the no-motion state to fully chaotic.

It should be pointed out that with metallic electrode, weak injection is more physically realistic, as the amount of charge created at the metal/liquid interface is limited by the electrode process. However, experimental with weak injection has not been carried out yet.

Convection under space charge limited injection $(C \to \infty)$

Comparing to weak injection, electro-convection induced by SCL injection is better documented and has been verified experimentally. With the help of the experimental Schlieren observations using transparent electrodes, four typical flow structures can be preliminarily distinguished.

1. When the applied voltage is smaller than the linear stability criterion, there is no motion.
2. Near the onset of motion, the flow is in the form of stable hexagonal cells. However, it must be emphasized that the flow state is always time dependent once the liquid is in motion. There are fluctuations imposing on a well-defined average values.
3. When the voltage further increases, the hexagonal cells turn to unstable filaments.
4. Finally, the flow becomes turbulent at higher voltage.

There are also two asymptotic states of electro-convection with SCL injection: viscosity dominated and inertial dominated regimes. In each state, another two or three spatial regions can be

distinguished. Some theoretical predictions are obtained with the approximate equations that hold in different regions. These predictions are also verified with experimental data.

Viscosity dominated regime: $I / I_0 \propto T^{1/2}$

Inertial dominated regime: $I / I_0 \propto (T / R)^{1/4} = M^{1/2}$

where I and I_0 are respectively the measured electric current and the current (depending on C) which would exist without liquid motion. The current density ratio (I / I_0) is named as the electric Nusselt number. Since M number is some kind of fluid property-dependent parameter, the electric Nusselt number saturates in the inertial dominated regime. The transition between the two convective states in the case of SCL electro-convection, which means that the viscous and inertial effects are of similar importance, is associated with a transition number $(MR)_T \approx 30$, which is an electric Reynolds number related to an ordinary Reynolds number: $\mathrm{Re}_{tr} \approx 10$.

Generally, the applied voltage is gradually increased and then decreased with a small margin to measure the steady current during the execution of physical experiments. This typical operation process offers the idea for accurate numerical determination of linear and nonlinear stability criterion.

Besides the theoretical and experimental studies, the numerical approach has been also applied to the problem, most of which concerning two-dimensional problems. The main difficulty of numerical studies comes from two aspects: (1) strong nonlinear coupling between the distribution of electric field and charge density (2) the diffusion of charge being negligible. Since at the electrodes the velocity goes to zero, and that the continuity of the current requires that the bulk convective transport is matched by drift transport, the boundary regions must be characterized by strong gradients. The hydrostatic solution in the previous chapter can help to understand the strong gradients of charge density. In addition, the existence of charge void region is another major problem because of serious variation of charge density near the "separatrix" between the void and charge covering regions.

Table 5-1. Summarization of published numerical simulation work with unipolar injection problems

Author(s) and References	**Numerical methods**	**Notes**
Castellanos & Atten, 1987 [151] weak injection	1. The whole system is solved; The Navier-Stokes equations are solved with SIMPLER algorithm; 2. Finite difference method with first order upwind scheme;	The predicted linear stability criterion is $T_C = 22075$; [*] There is no zone void of charge due to the numerical diffusion; One cell structure was found for T = 3000, C=0.1 M = 60;
	1. The velocity field is imposed with a 2D self -similar	A better estimation for the hysteresis loop is obtained, but the method failed to sustain the

	function; 2. The particle-type method is applied to the charge density equation;	"vacillation" of the velocity;
Castellanos & Atten, 1987 [58] weak injection	1. Finite difference method with second upwind differencing scheme 2. The whole system is solved;	The predicted linear stability criterion is $T_C = 23710$; [*] $T_f\big\|_{M=\infty} = 10400$ $T_f\big\|_{M=60} = 10100$
	1. The velocity field is imposed with a 2D self-similar function; 2. The particle-type method is applied to the charge density equation;	The predicted value $T_C C^2 = 194.6$ is in good agreement with the asymptotic theoretical value, 220.75. There is a long transient regime with large amplitude oscillations around slowly increasing average; At the end of long transient regime, the oscillation dies out;
Chicon et. al., 1997 [34] Strong injection Weak injection	1. The velocity field is imposed with a 2D self-similar function; 2. The improved particle-type method is applied to the charge density equation;	Strong injection ($C = 10$): $T_C = 171$, $T_f = 126.5$ Weak injection ($C = 0.1$): $T_C = 23450$, $T_f \approx 2040.2$ The convective state obtained is always time-dependent for both strong and weak regimes, and the power spectra behaves in a similar way to those obtained experimentally; The fluctuations never die out;
P A Vazquez, et. al., 2006 [66] Strong injection Weak injection	1. The velocity field is imposed with a 2D self- similar function; 2. The improved particle-type method (PIC) and the Flux corrected transport (FCT) method [**] are applied to the charge density equation;	Both methods (PIC and FCT) lead to steady state solution and satisfactory results for both weak and strong injections; Only with PIC method, small oscillations of velocity and electric current are observed; and they may be a function of the mesh size;
P A Vazquez, et. al., 2008 [67] Strong injection	1. The whole system is solved; 2. The Navier-Stokes equations are solved with Finite Element Method;	Strong injection ($C = 10$): $T_C \approx 163$ [*] (without the convective term) Two roll structure is observed for $T \geq 400$ Weak injection ($C = 0.1$) Two-roll structure is observed for $T = 30000$

Weak injection	3. The improved particle- type method and the Flux corrected transport method are applied to the charge density equation;	For the first time, the range of T, which is a bit far away from the linear stability value, is investigated.
Ph. Traoré & A. T. Pérez, 2012 [56] Strong injection	1. The whole system is solved; 2. The Navier-Stokes equations are solved with Finite Volume Method with Augmented Lagrangian method [188] as velocity -pressure coupling algorithm. 3. The TVD scheme is applied to the charge density equation;	Strong injection ($C = 10$): $T_C \approx 155.64$ [*] Two roll structure is observed for $T = 300$ Flow structures for a wide range of *T* were investigated; At sufficiently high *T* value, electro-plumes were observed for the first time;

[*] It should be noted that the comparison among these linear stability values are of little meaning as these values can be improved with finer grid (for FD and FCT) or more particles (for PIC).

[**] The components of FCT method are: two-step Lax-Wendroff method as high order scheme, First order upwind as low order, oscillation-free scheme and Zalesak limiting procedure [64].

Some concluding remarks can be made from the above summary.

1. The method for charge density equation lies in an essential position for the complete algorithm. The drawback of PIC method is its computational cost [66], while FCT method is quite complicated. In addition, PIC method cannot be applied to convection-diffusion problems.
2. For velocity field, the method of imposing a 2D self-similar function is quite popular. Though the method can be applied to both strong and weak injection, its applicability is limited to the range which is slightly below or above both linear and nonlinear criterion.
3. Considering the numerical results, all algorithms can successfully predict the linear stability criterion. However, accurate determination of the nonlinear stability criterion puts forward higher requirement for numerical method.

The present study is dedicated to the following aspects of electro-convetion in a dielectric liquid layer subjected to unipolar injection with numerical tools:

1. To build an efficient numerical tool which can be applied to electro-convection of dielectric liquid inducing by unipolar injection of arbitrary injection strength; a new algorithm for the charge density equation is an important component of the numerical tool.
2. To accurately determine the linear and nonlinear criterion and to show the flow structure of the system in the finite amplitude region;
3. To investigate the effect of charge density diffusion for the whole system; the method we developed for charge density equation can easily take into account diffusion transport mechanism.

4. As the velocity and pressure field are solved directly instead of imposing, our numerical solver can be used for $\boldsymbol{T}$ of wide range. The successive instabilities of the electro-convection and the route to chaos have been identified for strong injection.
5. Our numerical tool bas been successfully extended to the three-dimensional cases. However, as the code has not been parallelized, the computational time is an important limiting factor.

5.2 Finite amplitude convection

In the present study, we will solve numerically the whole set of coupled equations associated with the electro-convection in a dielectric liquid subjected to unipolar injection. The typical problem we consider is the homogeneous and autonomous unipolar injection between two rigid parallel electrodes which has been widely studied theoretically, experimentally and numerically. It should be noted that only the experiments with space-charge limited (S.C.L.) injections have been carried out.

Problem description

A perfect dielectric fluid is immersed between two plane electrodes of length *L* and a distance *d* apart. The system is considered to extend infinitely along the transversal direction so that the flow can be taken as two dimensional. An electric potential is applied between the plates so that injection charge occurs. The electric field forces the charges away from the injector and in this way a space charge appears in the bulk of the liquid. The physical problem is schematically described in Figure 2-2. The fluid is assumed be incompressible, isothermal and insulating with constant mass density, dynamic viscosity and permittivity. The dimensional governing equations are

$$\nabla \cdot \vec{U} = 0 \tag{5-1}$$

$$\rho_0 \left(\frac{\partial \vec{U}}{\partial t} + \vec{U} \cdot \nabla \vec{U} \right) = -\nabla p + \rho_0 \nu \nabla^2 \vec{U} + q\vec{E} \tag{5-2}$$

$$\nabla \cdot \left(\varepsilon \vec{E} \right) = q \qquad \vec{E} = -\nabla \phi \tag{5-3}$$

$$\frac{\partial q}{\partial t} + \nabla \cdot \left(q\left(K\vec{E} + \vec{U} \right) \right) = 0 \tag{5-4}$$

noting that the non-dimensional diffusion coefficient in charge density equation is set to zero to keep consistent with the theoretical analysis [144] and [148]. The potential effect for this problem will be discussed in details in Section 5. 4. It is more convenient to work with non-dimensional style. Taking d, ϕ_0, $\varepsilon\phi_0 / d^2$ and $K\phi_0 / d$ as the scales for distance, potential, charge density and velocity respectively, the governing equation of EHD problem can be written as,

$$\nabla \cdot \vec{U} = 0 \tag{5-5}$$

$$\frac{\partial \vec{U}}{\partial t} + \left(\vec{U} \cdot \nabla\right)\vec{U} + \nabla \tilde{p} = \frac{M^2}{T}\Delta \vec{U} + M^2 q\vec{E} \tag{5-6}$$

$$\Delta \phi = -q \quad \vec{E} = -\nabla \phi \tag{5-7}$$

$$\frac{\partial q}{\partial t} + \nabla \cdot \left(q\left(\vec{E} + \vec{U}\right)\right) = 0 \tag{5-8}$$

Three non-dimensional parameters appear in the above equations,

$$T = \frac{\varepsilon \phi_0}{\eta K}, \qquad C = \frac{q_0 d^2}{\varepsilon \phi_0} \qquad M = \frac{1}{K}\left(\frac{\varepsilon}{\rho}\right)^{1/2}$$

The physical meanings of these parameters are well explained in Table 2-1. Symmetric conditions are imposed on the velocity at the lateral walls to represent the infinite horizontal layer of fluid and electrodes. Figure 5-4 shows the non-dimensional computational domain and boundary condition for the problem.

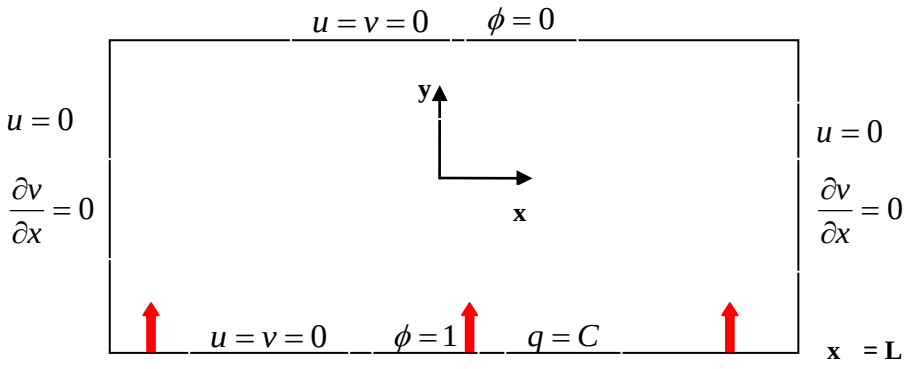

Figure 5-4. Non-dimensional physical domain and boundary conditions for the homogeneous and autonomous unipolar injection problem between two parallel plates

As for the non-dimensional length in horizontal direction, we choose $L = 0.614$ and $L = 0.687$ respectively for strong $(C = 10)$ and weak injection $(C = 0.1)$, both lengths being the critical half wavelengths of a convective cell. For moderate injection we set $L = 0.650$ which is different from the critical wavelength. The effect of this choice to the linear and nonlinear stability criterion will be discussed later.

The numerical method has been explained in details in chapter 4. Considering that one main topic of this thesis is to develop an efficient numerical method for electro-convection problem, various options are incorporated into the numerical solver for charge density equation.

1. Time marching method: Euler Explicit, Euler Implicit, 2nd TVD Runge-Kutta and Implicit three time level;
2. TVD scheme: more than 20 limiter functions;

The performance of different options will be compared to determine the optimal schemes for electro-convection problem.

5.2.1 Numerical determination of linear and nonlinear stability criteria

A first trivial test of the numerical algorithm was carried out by using $T < T_C$ and comparing the results with the hydrostatic solution, to see Chapter 4. The second test was based on the comparison of the linear stability criteria with those determined with the linear stability analysis approach. In addition, the nonlinear criterion has also been computed with our numerical tools and compared with those determined with the Galerkin method. The results are summarized in Table5-2. Linear stability analysis shows that the threshold value (T_C) depends on C but not on M which has also been verified with our numerical results.

Table 5-2. Comparison of numerical and analytical linear and nonlinear criterion for weak, moderate and strong injection regimes

	C	M	T_C (present)	T_C (analytical)	T_f (present)	T_f (analytical)
Weak injection	0.1	50	24022.5	24147.57	[6000,6500]	~ 2400
Moderate injection	1.0	50	520.0	510.993	[230, 240]	244
Strong injection	10.0	10	163.2	164.1	[109,110]	111.7

Note: For solving charge density equation, the implicit three time level and SMART scheme are adopted; the grid system owns 50 and 100 cells of equal size in X and Y direction;

5.2.1.1 Numerical method for the determination of linear stability criterion

For a fixed unipolar injection system with given *L, C* and *M,* the simplest idea to determine the linear stability value is to select two *T* values, with one slightly above and the other one slightly below the theoretical one, and then run the computation to see whether there is motion in the domain or not. A potential problem is that it needs an extremely long time for the system to set into motion when *T* is very close to the linear stability value. The closer *T* gets to T_C, the longer time will be needed. Thus this simple method is not efficient to determine the linear criterion, an indirect search is necessary. The idea is similar to the one used in Chapter 4 to calculate the Ra_c for RB problem. We have used the maximum value of the vertical velocity in the domain of computation as a representative physical quantity. Interestingly, the value also happens to be the amplitude $A = \max\left(\sqrt{V_x^{\,2} + V_y^{\,2}}\right)$ of the velocity field. It is expected that, in the very first stage of growth, the velocity follows the law $v_{\max} = v_0 \exp(\sigma t)$. Having fixed *L, T* and *M,* we calculate σ_T from the first interval of exponential growth, and represented σ_m as a function of *T.* By a linear extrapolation, the linear stability value, which corresponds to $\sigma = 0$, can be determined.

The original data of Vmax evolving with time, and the growth rates with T and the extrapolation step are presented in Figure 5-5.

Some important aspects should be noted for accurate and efficient calculation of the linear stability criterion.

1. Generally we need only two sets of values of (σ, T) to extrapolate to obtain the linear threshold T_C. For better accuracy, the selection of T should be close to the analytical T_C, as the time evolution of perturbations strictly follows the exponential law in this limited range. If we use some T which are far away from the analytical T_C, a lower value would be obtained. An example with strong injection case can be found in Figure 5-6.

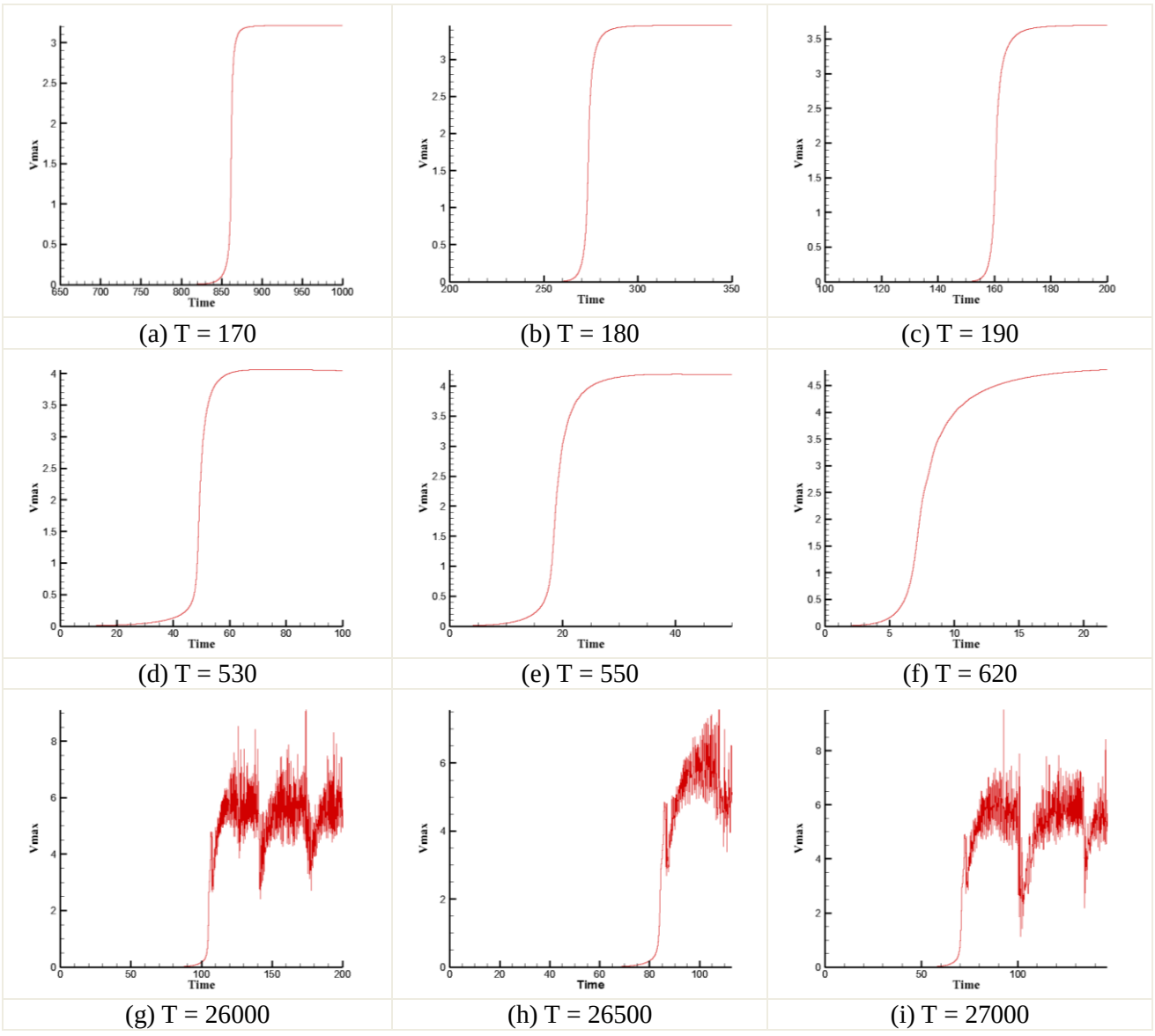

(a) T = 170 (b) T = 180 (c) T = 190

(d) T = 530 (e) T = 550 (f) T = 620

(g) T = 26000 (h) T = 26500 (i) T = 27000

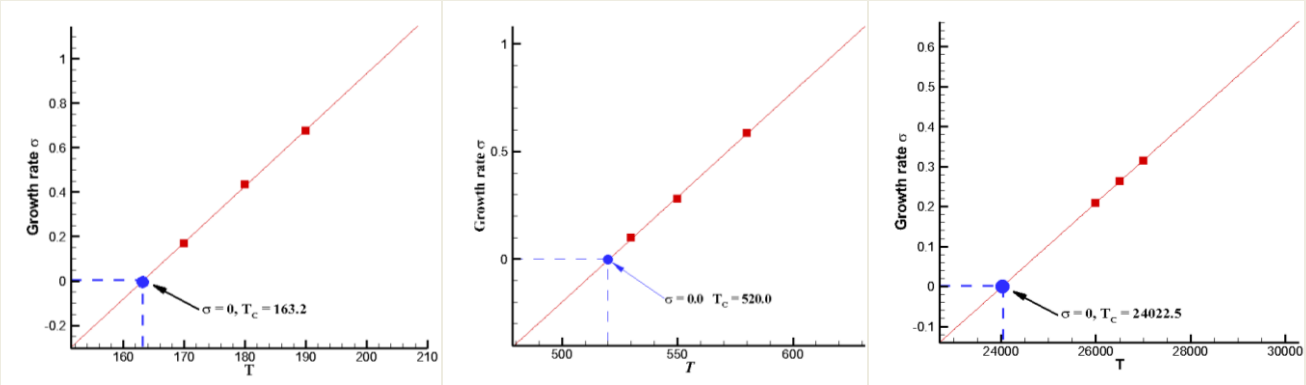

(j) Strong injection C = 10.0 (k) Moderate injection C = 1.0 (l) weak injection C = 0.1

Figure 5-5. The evolution of the maximum velocity in the domain and growth rate versus *T*, (a-c) strong injection; (d-f) moderate injection; (g-i) weak injection;

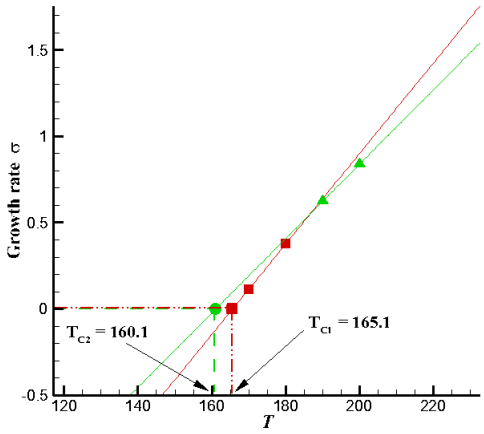

Figure 5-6. On the importance of appropriate selection of T value for more accurate T_C estimation

2. Technically, the linear stability value obtained above is the value for a fixed grid system. The final critical value should be computed with the grid system of indefinitely small size. Normally, the finer the grid the smaller the difference between the predicted T_C and the analytical value, see an example in Appendix D. With T_C evaluated with several sets of grids, another extrapolation may help to obtain a final value. However, this technique is not very practical for several reasons. Firstly, the computational cost increases a lot. Secondly, we observe that the T_C predicted with a single moderately fine grid is very close to the analytical one. Thirdly, there is some artificial error induced by computation of the growth rate, which may offset the improvement by the extrapolation approach. Thus, in the present study, we did not use the extrapolation with several grids for linear stability determination. Instead, we always used a single grid to compute the linear stability value and the error is believed to be small.

3. It is found that the grid size and time step is relevant to the time of the onset of the motion from numerical results. The general law is: the smaller the grid size or bigger time step the longer non-dimensional time is required for the system to set into motion. An example is presented in Figure 5-7. Three sets of uniform grid are used. The control cells in horizontal

direction are fixed as 100. For the first set grid, only 65 units of non-dimensional time is required for the system to reach the final steady state, while 100 and 150 units of time are needed for the second and third cases.

The essential reason for this phenomenon has not been investigated yet. We think it may be linked to the amplitude of the numerical perturbation. Assuming the system evolves from a rest state, the motion starts only when the numerical fluctuations have reached a certain level. The numerical fluctuations may be proportional to the grid size and time step, which means that the coarser the grid or the bigger the time step the numerical fluctuations more easily meet the requirement level.

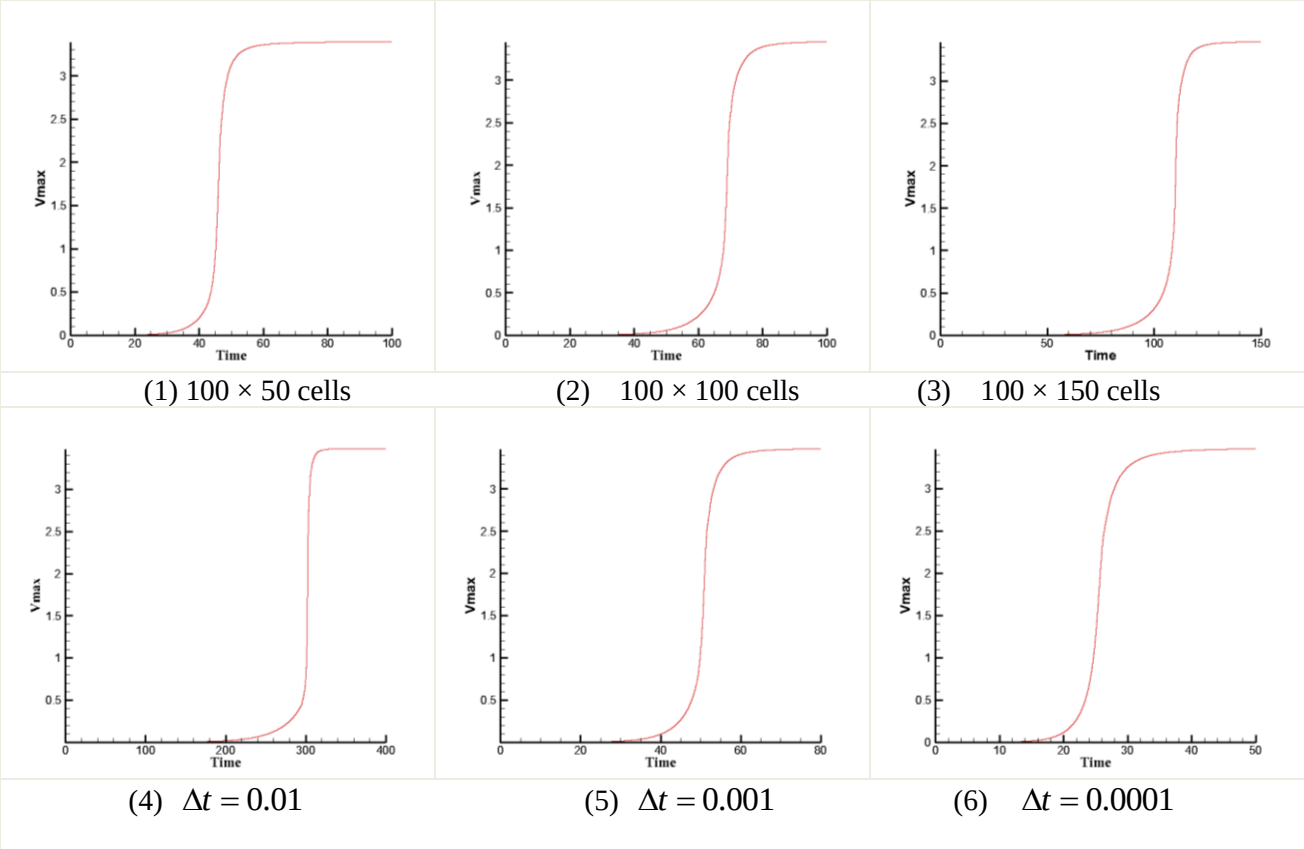

Figure 5-7. An example to show the transition period is relevant to grid size (1-3) and time step (4-6); strong injection case (C=10, M=10, T=180); the I3L method is used for charge density equation; (4-6) are computed with the 100 × 50 cells grid system;

4. Generally, two types of initial fields can be used: complete zero-field and hydrostatic solution field. In fact, the two initial fields correspond to two typical physical operations with the unipolar injection system. For zero-field, it means we actually solve a unipolar injection with a sudden step voltage. For hydro-static solution field, it requires starting from applying a small voltage and then increase step by step. For strong and moderate injection, there is no big difference between the solutions with different initial fields. However, the difference is significant with weak injection case. In Figure 5-8, we provide the solution of a weak injection system $(C = 0.1,\ M = 50,\ T = 30000)$ starting from the complete-zero field, which is obviously different from Figure 5-5 which is computed with the hydrostatic solution. The motion starts from the beginning. There is no transition period with the

hydrostatic solution. In fact, the hydrostatic solution never forms; see Figure 5-8 (middle). The solution is unsteady with drastic oscillations. In addition, there is no charge free region in the domain.

5. In Table 5-2, it is observed that there is a certain gap between the computed *Tc* and analytical one with moderate injection. The difference should be due to the inconsistence between the non-dimensional size of physical domain and the most unstable wavelength. Theoretically, for a sufficiently large domain, the system would automatically organize itself with the most unstable wavelength, which corresponds to the lowest T_C, see Figure 5-3 and Figure 5-9 (left). However, with a limited region, there exist some selection mechanisms. In [56], the authors provided a curve which shows the variation of T_C with the horizontal length of the computational domain, see Figure 5-9 (right).

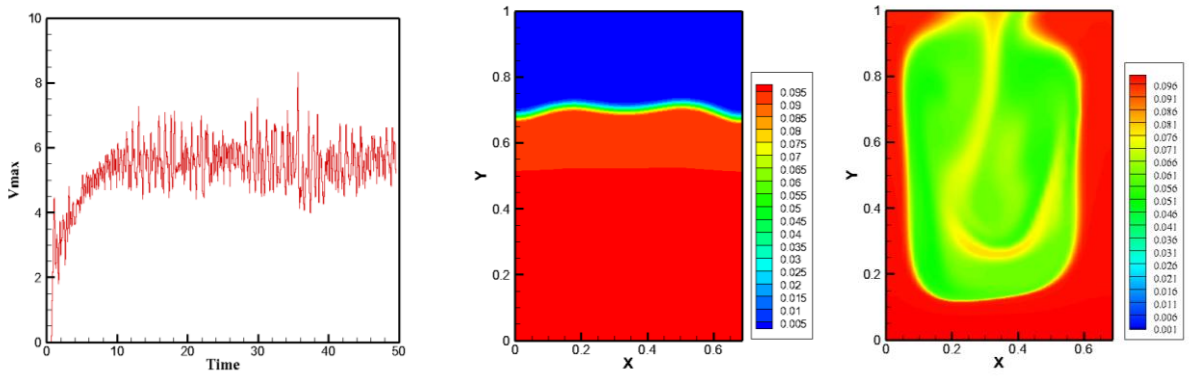

Figure 5-8 Time evolution of the maximum velocity in the domain from complete-zero field (left), the contour map of the charge density of a very early step (middle) and the final time step (right); $(C = 0.1, M = 50, T = 30000)$; $\Delta t = 1\times10^{-4}$, 200×50 uniform grid system.

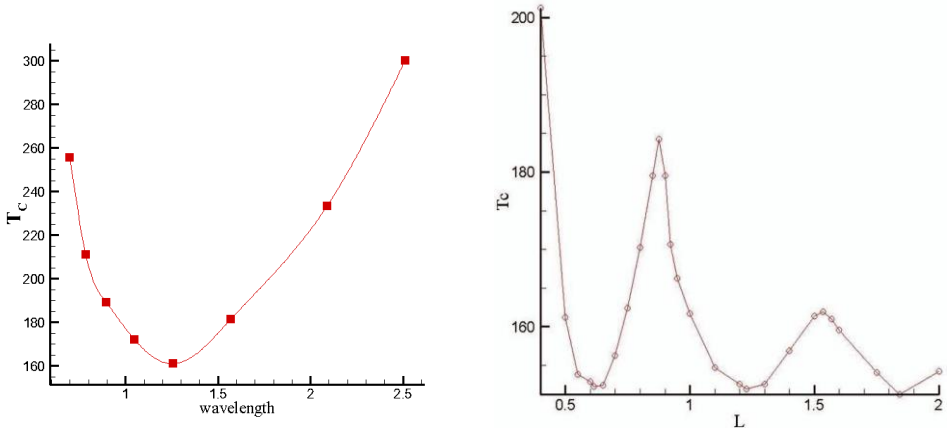

Figure 5-9 The marginal perturbations of wavelength λ in the case of Space charge-Limited Injection (left) [144] and T_C versus L for a strong injection system (C = 10.0 and M = 10) [56]

In [56], the authors firstly pointed out that all minima correspond to the same value of T and occur at one or more times half of the most unstable wave-length $\lambda/2 = 0.614$. Here, we would like to build the relationship between Figure 5-9 (left) and Figure 5-9 (right). Considering the range $L \in [0.4, 0.9]$ of Figure5-9(right), where only one convective cell is possible, T_C value should be consistent with the region $\lambda/2 \in [0.8, 1.8]$ of Figure 5-9(left). This argument can be understood in

a reverse way. Generally, we will define the size of the domain with the most unstable wavelength, and then we can obtain the T_C for this wavelength, which is also the linear stability threshold. By contrast, we now firstly define the domain with a size which may deviate slightly from the most unstable wavelength. The size of the domain would correspond to a wavelength. During the simulation process, this wavelength will be the final selection of the system to organize its convective cell. In other words, we computed the linear stability value which corresponds to the wave-number $k = 5.23$ for the moderate injection case.

5.2.1.2 Numerical procedure for the determination of nonlinear stability criterion

It is more difficult to obtain a precise determination of parameter *T* for non-linear criterion than for the linear one, theoretically and numerically. An important premise for the accurate prediction of the nonlinear criterion is that the charge free region is computed precisely.

To decide the nonlinear criterion, T_f, it is necessary to start from an initial state of stationary convection if there is. In the physical experiments, this is achieved by first applying a voltage higher than the linear criterion and then by slowly decreasing it to a target value U_t.

The same thought can be carried out with the numerical practice. We start from a steady or quasi-steady solution obtained with a *T* higher than T_C, and then we decrease *T* value step by step to see whether Vmax tends to zero or not.

Case I: If $T > T_f$, the final stationary state is reached through a transition characterized by an exponential decrease of Vmax, see Figure 5-10 (b) and (c).

Case II: If $T < T_f$, the velocity decrease is more important and Vmax also decreases following an exponential law within a certain range, see Figure 5-10 (a).

As the total transition process does not require much time, the simple 'try' method can be used for the determination of nonlinear stability criterion. In [148], Atten proposed a technique which is similar to the one for the linear stability criterion, and that could be used to determine the nonlinear stability criterion. His idea bases on the assumption that the growth rate in the above mentioned case II varies linearly with *T* in a certain range below T_f. Then a linear extrapolation can be used to obtain T_f which corresponds to the zero growth rate. Though the assumption was verified with our numerical results (see Figure 5-10-d), T_f obtained in this way is far from the analytical one.

The results are summarized in Table 5-2. For strong and moderate injection cases, the results are in good agreement with the theoretical values, which proves the high accuracy of our numerical solver. However, there is a considerable discrepancy in the weak injection case.

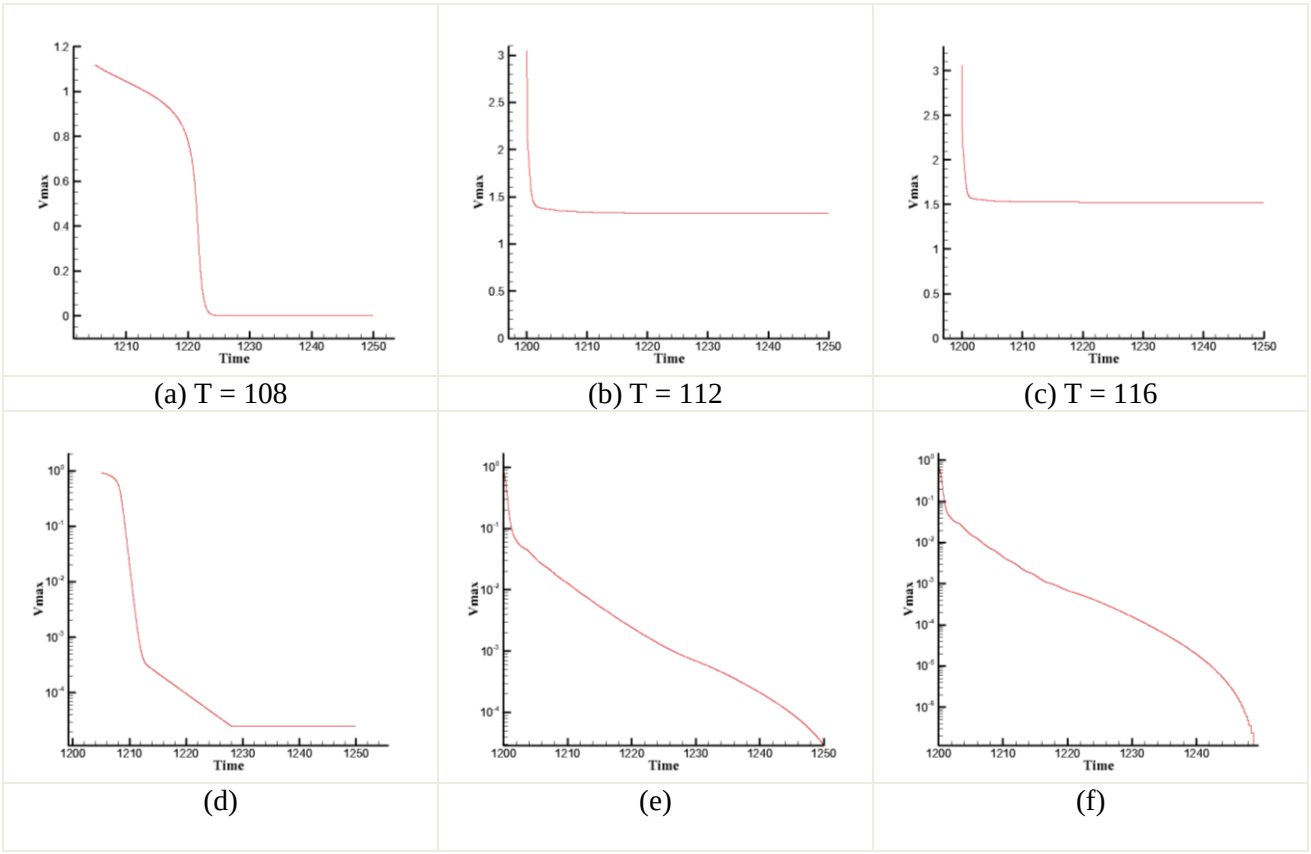

Figure 5-10 Strong injection (C=10.0 M = 10.0), time variation of Vmax after T parameter has been suddenly decreased from T=170 to T=108 (a), 112 (b) and 116(c); (d-f) are the semi-log plot of (a-c) to highlight the existence of exponential ranges

To analyze the reason for this discrepancy, we firstly recomputed the solutions by decreasing from $T = 26000$. The conclusion is more or less the same. We attribute the discrepancy to the drastic oscillation in the charge density and velocity field. For strong and moderate injection, the velocity field is steady, and we observe a sharp line (named "separatrix") separating charged and uncharged adjacent regions. In the weak injection case, the velocity is changing in time, and the frontier of the "separatrix" may be very complex. Due to the oscillations, part of the charge near the "separatrix" will be dragged into the region initially free of charge, thus causing a decrease in the driving torque after a certain time delay. This in turn will decrease the velocity giving rise to a bigger delayed electric torque and so on. This mechanism could explain why the system becomes static even when T is still far away from T_f.

5.2.2 Flow structure with finite amplitude convection

In this section, we investigate the flow structure of the finite amplitude convection of unipolar injection system. Finite amplitude convection means the flow structure with T slight above T_C and or in the range of $[T_f, T_C]$.

5.2.2.1 Flow structure of finite amplitude convection with strong unipolar injection

Firstly, the simulation was run with *C=10*, *M=10* and *T=200*, which is slightly above the threshold value. Thus, we expected to get instability and that a roll would develop. Figure 5-13 shows the main calculating results with this set of parameters. These results exhibit good agreement with other published results, either with FCT or PIC method, imposing velocity or solving the whole coupled system.

The evolution of the amplitude of the velocity roll is shown in Figure 5-11. The computation started from a complete-zero field. In the early stage, the amplitude reaches a zero value after a transient regime (see the inset figure in Figure 5-11). In the beginning, we thought this was due to the grid size or time step. However, even with an extremely fine grid system and small time step, the phenomenon never vanished. Our explanation is: when some charge carriers suddenly enter into an originally stationary field, they will induce some local velocity disturbance which needing time to damp out by the viscosity of the system. Thus, we believe that this phenomenon has its own physical sources. Some further work needs to be done to quantitatively understand the phenomenon.

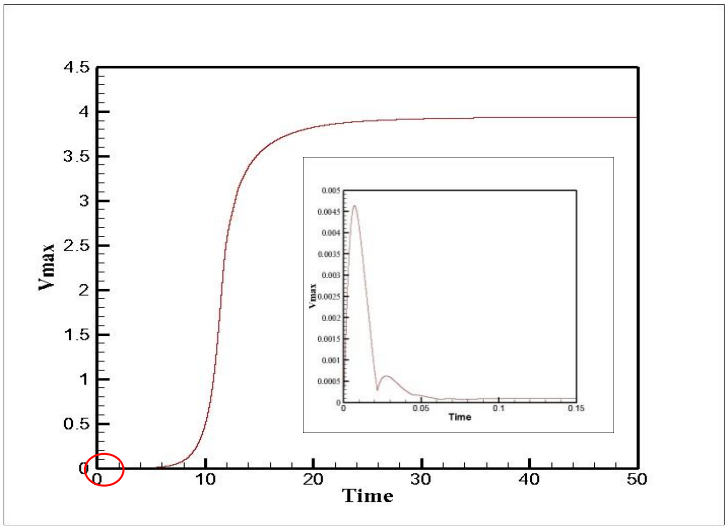

Figure 5-11. Evolution of the amplitude of the velocity roll for T = 200, C = 10, M = 10 with a 101 × 201 uniform grid system and 10^{-4} time step

After the above mentioned transition range, the system is at a quasi-stationary state before a slow increase of the velocity takes place. Then the convective motion starts, following an exponential law, which is consistent with the evolution of perturbations predicted by Landau [279]. Finally, a steady state is reached.

Figure 5-12 (a-d) show the distribution of electric charge for different time points, aiming at the evolution process of the system. The system sets into motion at a specific time (here t=6.0) because of the numerical perturbation. A one-side hump appears in the charge density distribution figure; see Figure 5-12(b). The randomness of numerical perturbation means which half side owns higher average charge density is unpredictable. The most important characteristic of the solution has three aspects: (1) there is a central region with no electric charge and there is a sharp frontier between

this void region and the charge covered region; we confirm again that the success of capture of this void region is the precondition for nonlinear criterion prediction; (2) the curve which separates the two regions is named ‘separatrix’ and we observed that it is connected with the upper electrode, which provides a path for the charge carriers in the void region to escape; this is an important proof of the fact that the Coulomb repulsion was included in our solver [152]; (3) only one cell structure forms at the final state, see Figure 5-12(e) and (f).

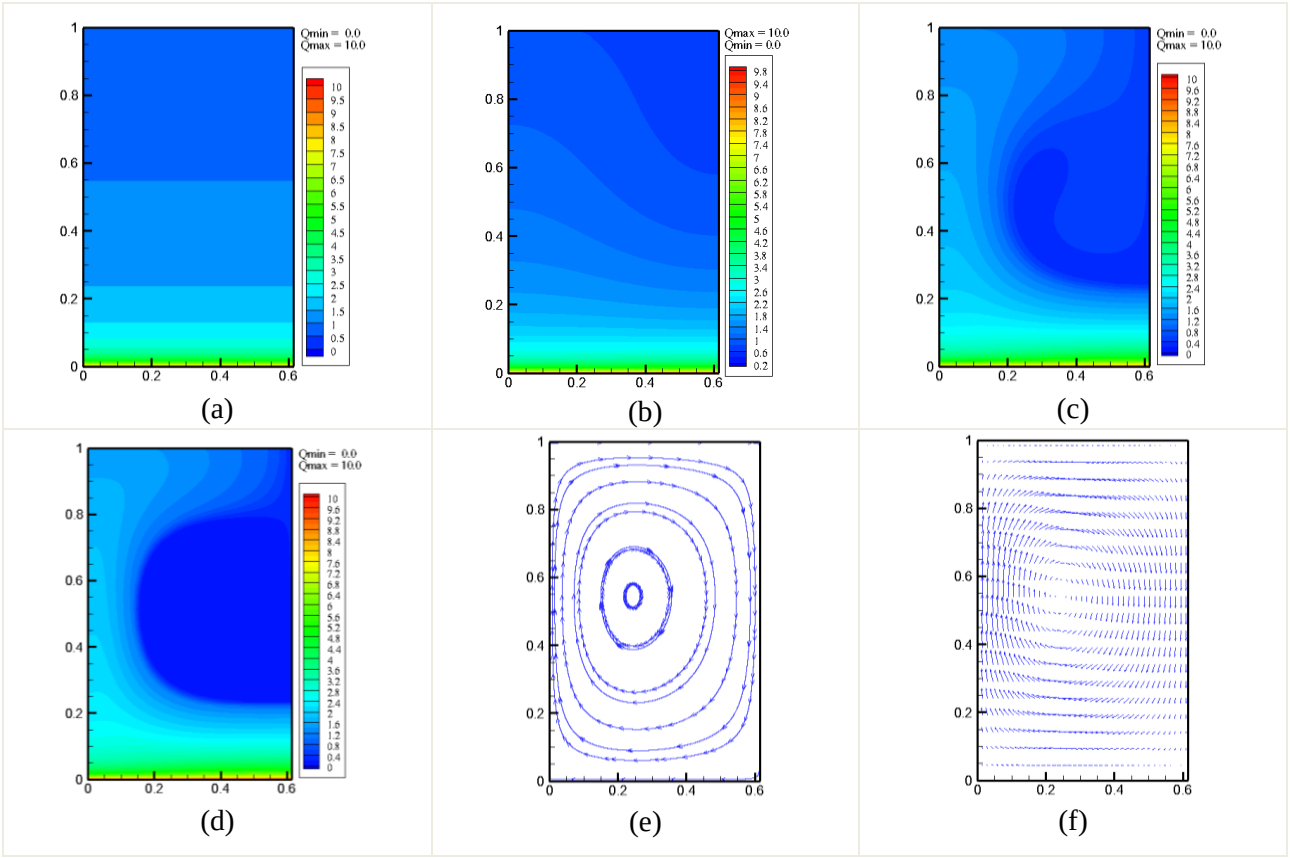

Figure 5-12. Numerical results with a strong injection system (a-d) charge density distribution: (a) hydrostatic solution (b) t = 10.0 (c) t = 12.0 (d) t = 50.0; (e) streamline at steady state (f) velocity vector at steady state; Parameters: T = 200 C = 10 M = 10;

As mentioned before, the core issue of the numerical simulation of electro-convection under unipolar injection is the method for charge density equation rather than the Navier-Stokes equations themselves. Thus we can also incorporate our numerical solver of the charge density equation and Poisson equation with the imposing velocity field. The details of this combination method and the expression for the self-similar background velocity field can be found in [34]. An example is given below.

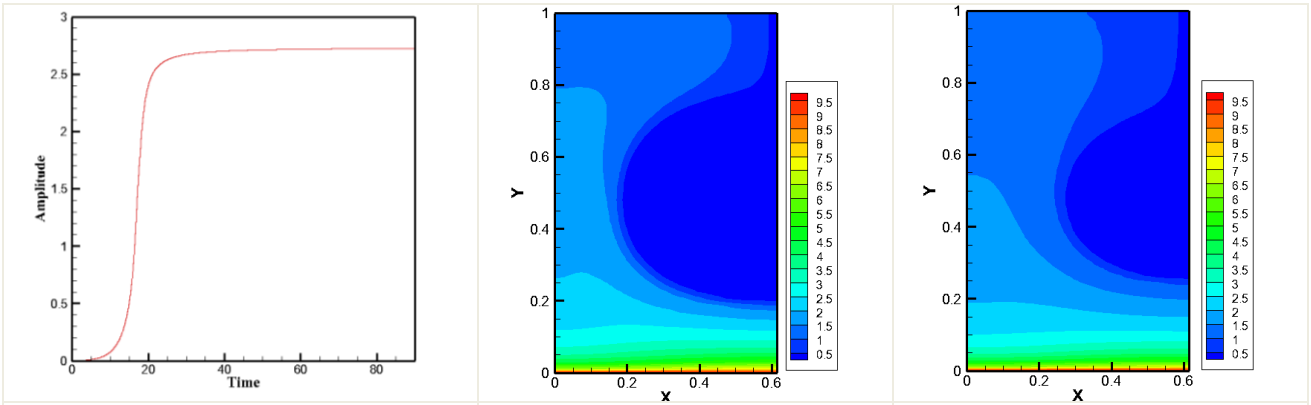

(a) (b) (c)

Figure 5-13. Numerical results with a strong injection system by imposing velocity field method; (a) time evolution of the velocity amplitude; (b) charge density distribution of the steady state (T=178, C=10.0, M=10.0) (c) charge density distribution of the steady state (T = 130, C = 10.0, M = 10.0), backward decreasing from T=178 case;

Through the comparison of the above results with the one obtained by solving the complete system, we firstly prove that this combination technique with imposing velocity field works well for strong injection case.

Another motivation of this computation is to state our understanding of the chaotic motion in finite amplitude convection range. The starting point is the phenomenon observed by physical experiments. It is observed that the motion is time-dependent even in a domain just above the linear critical voltage U_c. The fluctuations of the electrical current and velocity have a well-defined average value [20]. With the standard discrete fast Fourier transform technique, the power spectral of the measured signal (the total current) has been studied and found that the spectral has a well-defined main peak at some frequency f_1 and decay exponentially following a law $\exp(-f/f_c)$. In [66] the PIC method was applied to the problem of finite-amplitude electro-convection, both in strong and weak injection regimes. The solutions of velocity amplitude and electrical current are always time-dependent. By the spectral analysis, the authors believe that they successfully reproduced the physical time-dependent convective state with numerical tools. However, we are not confident with their conclusion.

Firstly, we used both imposing velocity method and solving Navier-Stokes equations method, and we did not obtain oscillatory solutions for any M value when T is slightly higher than T_C, which means the oscillations should not be due to the solving velocity field, but to the charge density equation treatment.

Secondly and most importantly, P. A. Vazquez, et.al, [66] mentioned that the oscillations observed with PIC method are related to the mesh size. It is observed that along with the increasing of the mesh resolution, the amplitude of the frequency components reduces. The solutions without grid-independent test are not acceptable from numerical simulation point of view. It is possible that these oscillatory behaviors have their numerical origins.

When applying our numerical method to the strong injection problem, we successfully capture the main characteristics of the flow structure but we did not notice any oscillatory behavior of velocity

or charge density field. However, no agreement has been reached about the causes for the chaotic behavior of electroconvection [58][59][280][281]. It is important to note that this question has decisive significance with the evaluation of numerical method for unipolar injection. On the one hand, if the chaotic current oscillations are in correlation with the turbulization of liquid convective motion, we need not to improve our numerical method. On the other hand, if the chaotic behavior is due to the nonuniform injecting properties of the electrode surface [281], attention should be paid to the more realistic injection law rather than our numerical algorithm. Further discussion with this point is beyond the scope of the present study and more theoretical work is required.

Next, the simulation was run with *C=10* and different *M* and *T*. The critical values T_C and T_f of the linear and nonlinear criterion and the corresponding hysteresis loop for the velocity are shown in Figure 5-14, which is in good agreement with the theoretical analysis. In the subcritical region, i.e., $T \in [T_f, T_C]$ the velocity amplitude follows a $(T_C - T)^{1/2}$ law when *T* is close to T_C.

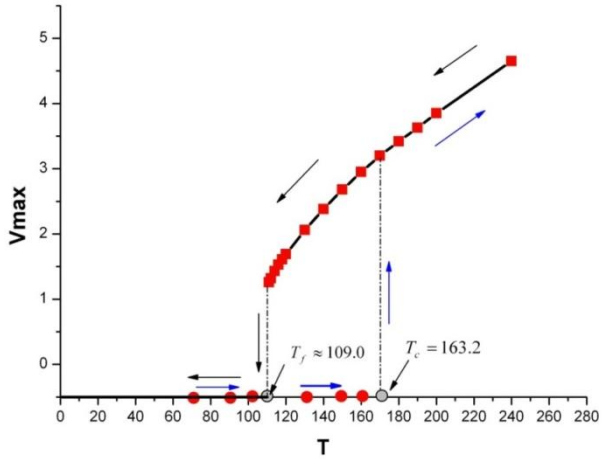

Figure 5-14. Vmax versus T with the strong injection case; Parameters: C = 10 and M = 10

With the systematic summarization of the numerical results, we can define some universal laws of the flow structure of strong injection in the finite amplitude convection range.

1. A steady state with one cell structure can always be reached; The roll develops faster for greater *T*; The area of charge-free region is increasing with *T*;

2. The existence of a narrow channel connecting the charge-free region with the receiving electrode; It seems the width of the channel is constant for different *T* and *M* values;

3. Though the linear stability criterion does not depend on M parameter, the transition time required to reach the steady state is related to it, see Figure 5-15. In addition, the final velocity value depends on *M*, when *M* is small, here, $M \leq 20$, which is inconsistent with the conclusion commonly assumed [34].

5.2.2.2 Flow structure of finite amplitude convection with weak unipolar injection

The difference between the weak and strong injection case is reflected in two aspects:

(a) The weak effect of the Coulombic repulsion between charge carriers. In this case, the charge density can be considered as remaining constant along the trajectories of charge carriers.

(b) The weak space charge only slightly alters the uniform potential (or electric) field distribution; see Figure 5-16 as an example. Considering the electric current through the emitter electrode, it has little to do with the state of motion and almost keeps constant. This point is the reason why physical experiments have not been taken, as it is hard to distinguish the electric current due to residual conductivity or due to ion injection.

From numerical calculation point of view, there is no difference between strong and weak injection simulation. However, there is notable difference between the solutions. Firstly, we compute a case with a *T* number slightly above the threshold value. The main results are summarized in Figure 5-18. We have also tried other *T* numbers, like 25000 and 30000. The main characteristics of the solutions are the same and can be summarized as follows:

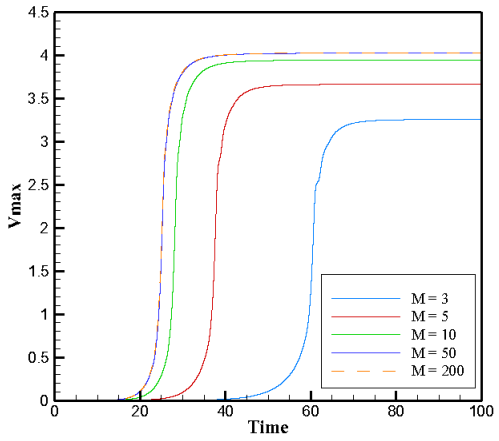

Figure 5-15. Vmax versus Time with different M values; Parameters: C= 10 and T =200

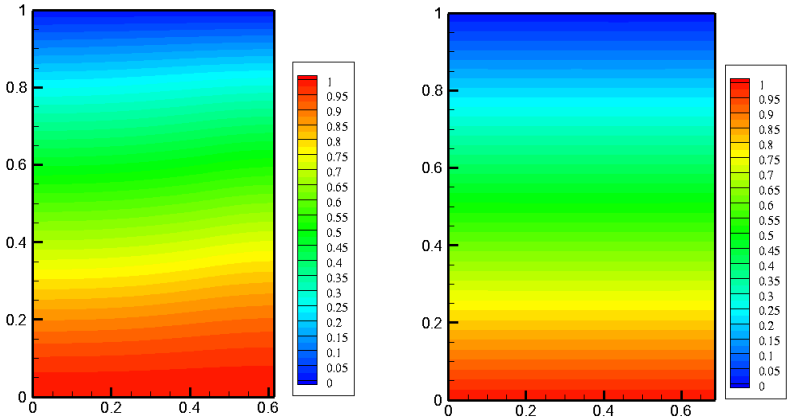

Figure 5-16 Comparison of electric potential field between a strong and weak injection (left) C=10, T=200, M=10, the final steady state (right) C=0.1, T=30000, M=50, t=100s;

1. The final solution is chaotic with serious oscillation reflected in the Vmax - time and electric current - time curves; see Figure 5-17 (d) and (e).

2. The final state is a two-roll structure; see Figure 5-17 (c). One-roll structure has also been observed at time $t \approx 48.5$, see Figure 5-17(b). The transition between one-cell and two-cell has also been observed by P. A. Vazquez et al, with FCT and PIC method [67]. It should be pointed out that the transition time is very short, no more than 5s in this case.

3. Even with serious oscillations, the time aveage value of electric current is just slightly above the stationary current, to see Figure 5-18 (i). This is in agreement with the above analysis and indicates that we can not use the electric Nusselt number to describe the flow regimes in weak injection case.

The expression of the non-dimensional electrical current depends on nondimensional expression, with Eqn. (5-7) and (5-8), it can be expressed as

$$\int_{y=costant}\left[q\left(V+E_y\right)+\frac{\partial E_y}{\partial t}\right]dx \qquad (5\text{-}9)$$

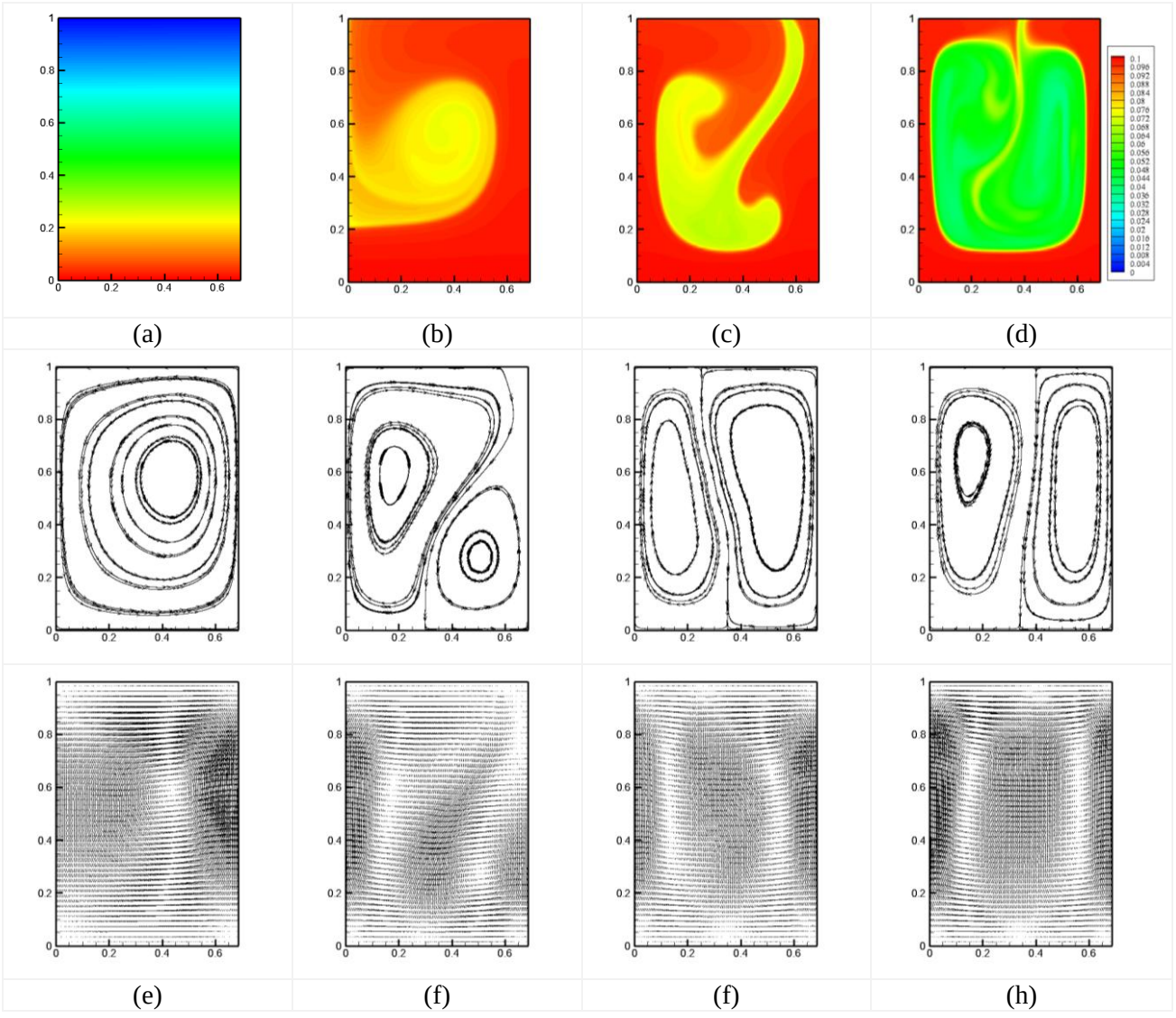

(a) (b) (c) (d)

(e) (f) (f) (h)

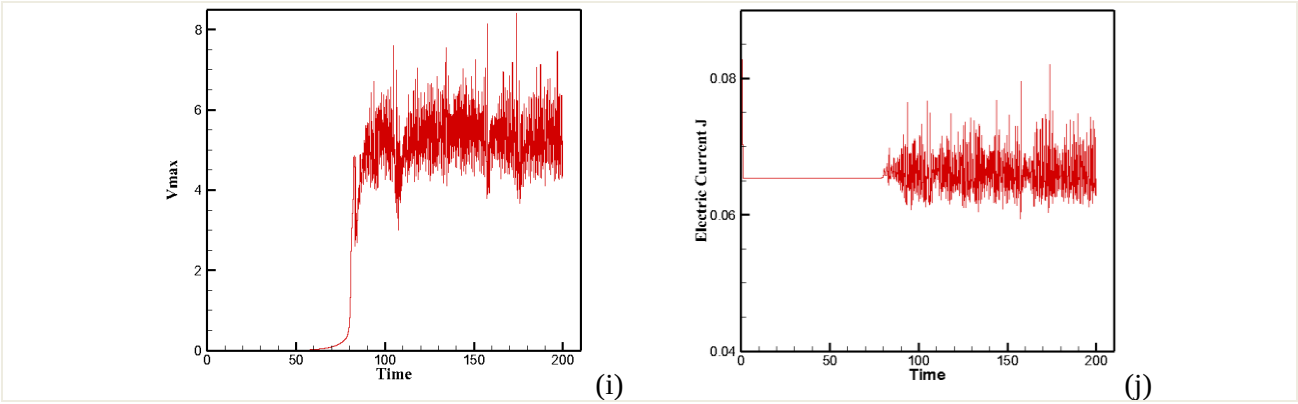

Figure 5-17. Numerical results with weak injection; charge density with (a) hydrostatic solution (b) t=83.5 (c) t =85.0 (d) t=200; streamline and velocity vector at (e) t=83.5 (f) t=85.5 (g) t=87.5 (h) t=89.5 (i) Vamx versus time (j) electric current versus time; Parameters: T=28000 C=0.1 M=50;

The last term in the square brackets corresponding to the displacement current is an important contribution to the actual time fluctuation of the current. Only including this term, the current at any y-plane can strictly follow the Ampère's law at any time moment.

To highlight the evolution of one-roll and two-roll structures, we computed the angular momentum of the domain with the following formula and plotted it in Figure 5-18.

$$AM = \int_{cell} (\vec{r} - \vec{r}_0) \times \vec{U} dS \qquad (5\text{-}10)$$

where $\vec{r}_0$ is the position vector of the centre and *S* represents the area of the control volume in 2D. In addition to using the center point, we also computed the angular momentum of both left and right half domains.

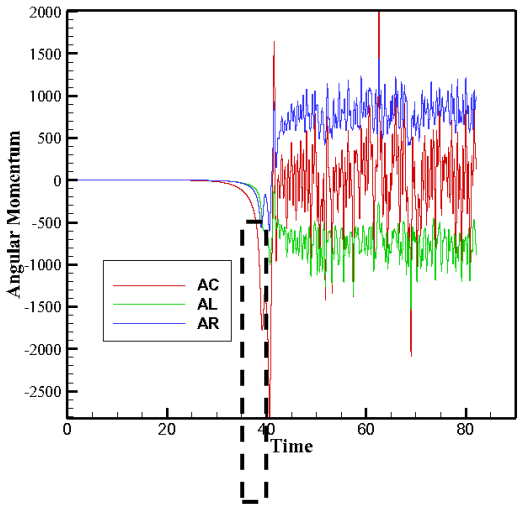

Figure 5-18. Evolution of the angular momentum for T = 28000 C = 0.1 M = 50; the dash box is the transition regime between one-cell and two-cell structures; AC, AL and AR stands for angular momentum with center point of the whole domain, the left half and the right half domain

The flow starts from a stationary state (AC = 0), then one-cell structure is formed along with strong oscillations (AC increased to a peak value). In a short time, the average value of AC tends to zero,

but AL and AR help showing the two-cell structure as both of them are osillating with non-zero average.

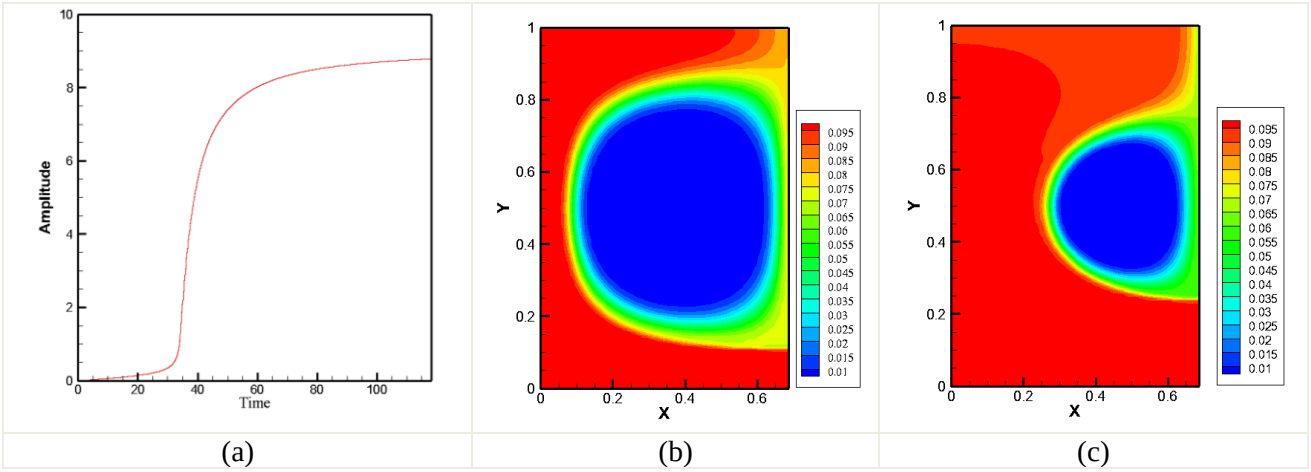

(a) (b) (c)

Figure 5-19. Numerical results with a weak injection system by imposing velocity field method; (a) time evolution of the velocity amplitude; (b) charge density distribution of the steady state (T=24000, C=0.1, M=50.0) (c) charge density distribution of the steady state (T=3000, C=0.1, M=50.0), backward decreasing from T =24000 case;

The above flow strucuture is quite different from other published results. Considering most of these results are based on velocity imposing method, we recompute a similar case but without solving Navier-Stokes equations. Instead, we use the same velocity imposing method to highlight that the difference is not from Navier-Stokes solver. The results are presented in Figure 5-19.

These results are in good agreement with solutions computed with the PIC method [34] [66] and FCT method [66]. In fact, these results are similar to the solution in the strong injection case. A fully developed and steady roll structure is formed.

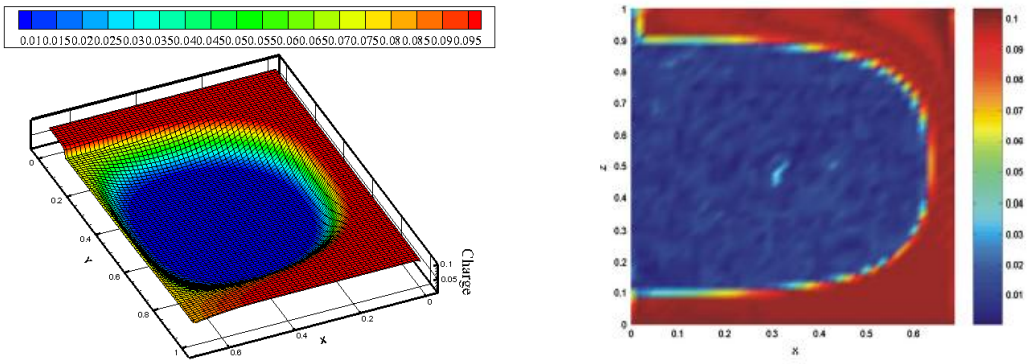

(a) (b)

Figure 5-20. (a) Three dimensional plot of the charge density distribution corresponding to Figure 5-20; (b) charge density distribution with C=0.1, M=50, T=30000 using PIC method, a copy of Fig.8 of [66]

An internal charge-free region was well captured. An interesting finding is that our numerical results show a non-zero electric charge, along the right side, which is about 70% of *C* value. This non-zero field is also observed in [66] with FCT method, which is easy to understand because of the similarity between FCT method and our TVD algorithm. However, with the PIC method, the

density is essentially zero along the right side, see Figure 8 in [66] (reproduced in Figure 5-20(right)) and the authors attribute the deviation mainly to the symmetric boundary condition treatment. The PIC method imposes no boundary condition for the charge density there, while FCT method (also TVD algorithm) uses $\partial q/\partial \vec{n} = 0$ where $\vec{n}$ the unit vector normal to the boundary. Then the question is 'which solution is closer to the real physical solution'. We will analyze this problem in the next chapter.

The emphasis of this section is to understand the reason why two methods (imposing field method and solving Navier-Stokes equations) lead to completely different solutions.

First of all, we observed the similarity of the flow structures between a strong injection case (T=1300, C = 10, M = 10) and the weak injection case (T=30000, C = 0.1, M =50). Both of them evolve from a hydrostatic solution. After a transition phase following an exponential law, a one-cell structure state is reached. Then in a short time, the motion changes to a two-cell structure and oscillates around some main frequencies all the time, see Figure 5-21.

Then a natural thought is: the way to the chaotic regime for strong and weak injection may be the same and we just need to select a *T* value slightly above the *Tc* in the weak injection simulation. If we reduce *T* number to a value which is slightly above T_C, we should obtain a steady solution just as in the strong injection case. However, with numerical results shown in Figure 5-22, this thought is proved to be incorrect. Even with *T*=24160 (*M*=100), which is only 0.06% above T_c, the final state is still very chaotic, noting that this test takes a long time, the system set into motion at t=9.0033×10^6. To summarize, for the weak injection system *(C=0.1, M=50)*, the system passes from no-motion state to a fully chaotic state in 2D.

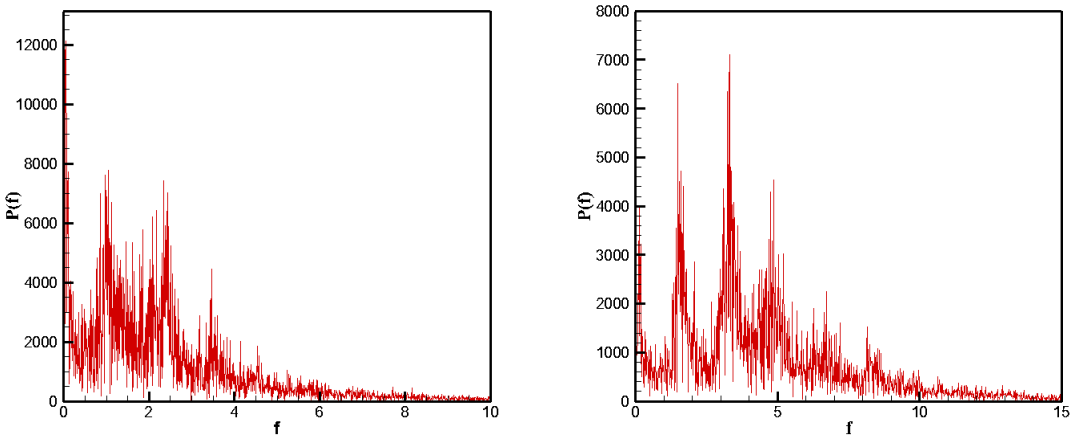

Figure 5-21. Power spectral for (left) a strong injection L=0.614, C=10.0, M=10, T=1300; (right) a weak injection L=0.687, C=0.1, M=50, T=30000

Secondly, we made a preliminary estimation of the time average value of *Vmax*, see the results in Figure 5-23 and evaluation curves in Figure 5-24. The sudden reduction of *Vmax_average* between 5500 and 6000 is due to the appearance of electro-plumes. It is well-known that plumes only appear for high values of the Reynolds number. In addition, it is observed that *Vmax* increases as $T^{1/2}$ in [27000, 45000] range, which is consistent with the law in the inertial effect dominating

regime [276]. From above analysis, we can conclude that the system (C = 0.1, M = 50 or 100) passed from the no-motion state to fully developed chaotic state. Is this possible?

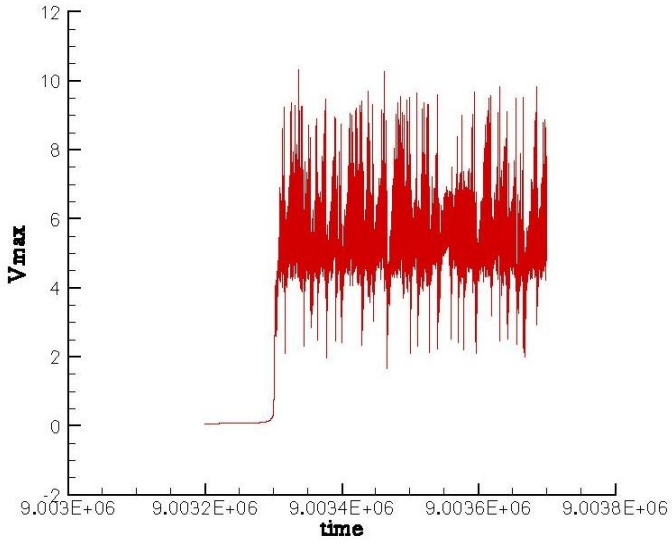

Figure 5-22. Time evolution of Vmax with a T very close T_C, T = 24160, M= 100, C= 0.1.

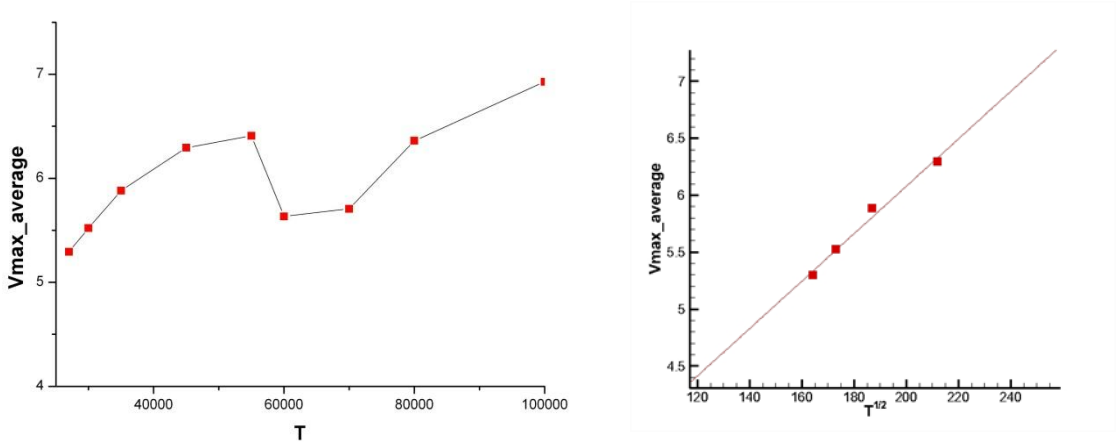

Figure 5-23. Time average of Vmax values in a weak injection system, C = 0.1 and M = 50; (left) vs. T (right) V vs. $T^{1/2}$

In [283], P. Atten mentioned the possibility that the viscous effect dominated regime may not exist in weak injection case, which is an obviously different phenomenon from the strong injection case. To judge which regime the electroconvection locates, it is useful to define the Reynolds number $R = \rho KV/\eta$. For convection under space charge limited (SCL) injection, the transition Reynolds number is on the order of 10 [19]. The same argument also makes sense for the weak injection case [283]. An important difference between strong and weak injection is the linear stability criterion T_C. Considering the large T_C for small C value, there is a wide varying range for R_C, as $R_C = T_C / M^2$. Then, it is possible that with some sets of systems (T, M, C), the inequality $\mathrm{Re} > Rc > \mathrm{Re}_{\mathrm{transition}}$ holds. Once $Rc > \mathrm{Re}_{\mathrm{transition}}$, it means the system is in the inertial dominated regime at T_C and the Vmax–time curve should behave very chaotically, just as Figure 5-22 shows.

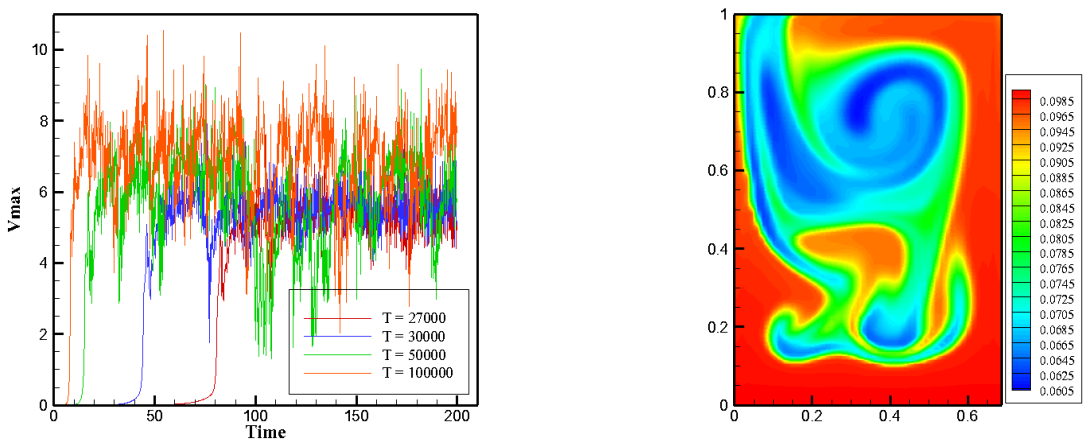

(a) (b)

Figure 5- 24 (a) Evolution of the maximum vertical velocity for weak injection with C = 0.1 and M = 50; (b) A snapshot of the thermal plume appearing in T = 70000 case; these simulations have been carried out with a 51× 151 uniform grid system.

With our numerical results with weak injection case, we successfully validated Atten's prediction about the appearance of special transition procedure in weak injection with numerical tools.

In addition, we highlighted an important drawback of the imposing velocity field method in weak injection simulation. The imposing velocity field has been widely used for electro-convection under both weak and strong injection. However, as we have showed that the system (C=0.1 and M=50) does not own the viscous-dominated regime, not to mentioned the self-similar rolls structure for fluid motion. Therefore the validity of applying the imposing velocity field method to the system must be questioned.

Lastly, these findings reminded us of a thought, unlike strong injection case, M parameter may play an important role in the type of flow structures in weak injection case.

In the rest of this section, we firstly list some numerical results of a weak injection system (C=0.1, M=5) which shows quite different solutions with M=50. Like Prandlt number, M parameter is related to physical properties of the system. For dielectric liquid, its range can be limited to $[3,500]$, see Table 2-2.

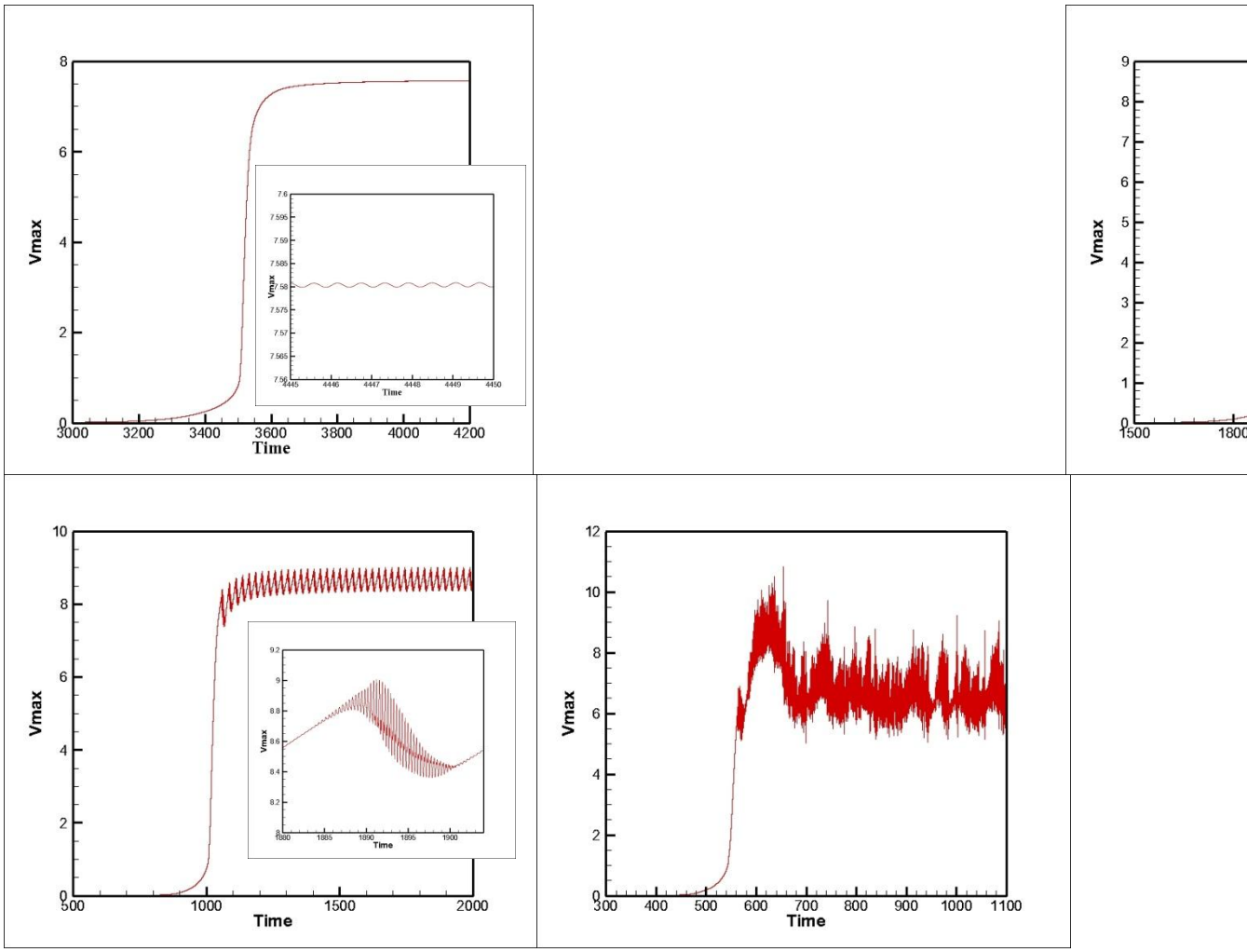

Figure 5- 25 Evolution of the maximum vertical velocity for weak injection with C = 0.1 and M = 5; (top left) T = 27000 (top right) T = 30000 (down left) T = 40000 (down right) T = 100000

At T=27000, the evolution of the velocity amplitude is similar to what we observed in the strong injection case. However, after the exponential growth period, the amplitude value does not tend to be steady. Instead, there exist very slight oscillations, see Figure 5-25 (top left). These small oscillations have been verified with finer grid systems and smaller time step. We name this kind of state as 'quasi-steady'. The corresponding charge density distribution and velocity field are presented in Figure 5-26. It is easy to find the cell-structure and the developing process is also quite similar to the strong injection case. In addition, the final charge density distribution is identical to the solution obtained with the velocity imposing method; see Figure 5-20 (b).

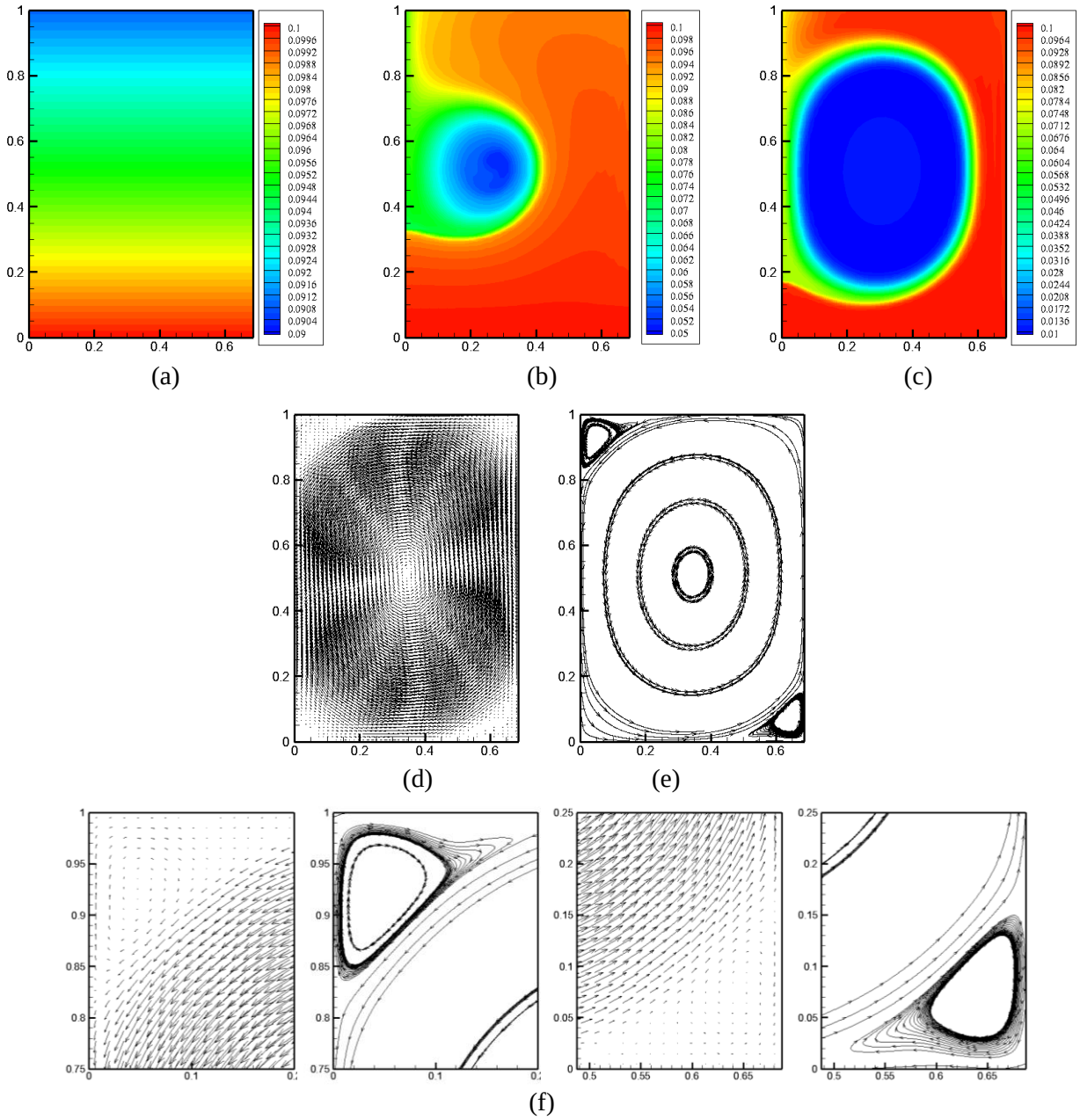

Figure 5-26. Numerical results with a weak injection system by solving Navier-Stokes equation numerically; charge density distribution of (a) hydrostatic solution (b) time=3500 (c) time=4000; (d) velocity field (e) stream functions (f) drawing of partial enlargement of (d) and (e); (c) - (f) are at final quasi-steady state; Parameters: C=0.1, M=5, T=27000; 51 × 101 uniform grid and $\Delta t = 10^{-3}$

Surprisingly, we observed two small vortes at corners; see Figure 5-26 (f). This finding has been verified with a larger domain (1.374×1) computation. We think these vortexes are concomitant phenomena of the quasi-steady state. The numerical linear stability value, $T_{C,}$ nonlinear stability value, T_f, and the associated hysteresis loop of the same weak injection system are plotted in Figure 5-27. The obtained T_C is very close to the analytical value. Though the obtained T_f value ($T_f\big|_{M=5} \in [3250,3500]$) is still a bit far from the analytical one ($T_f = 0.933 T_C C = 2252.97$), it is much better than the one obtained in M=50 system, $T_f\big|_{M=50} \in [6000,6500]$.

It is interesting to find the corresponding amplitude value of T=3250 is 1.66, which is quite close to the analytical value 1.6. In addition, Vmax curve in the range [3250, 24000] follows a nonlinear law as $T^{1/2}$, which is also inconsistent with the analytical prediction. We attribute the discrepancy to the comprehensive effect of numerical diffusion and the slight oscillations.

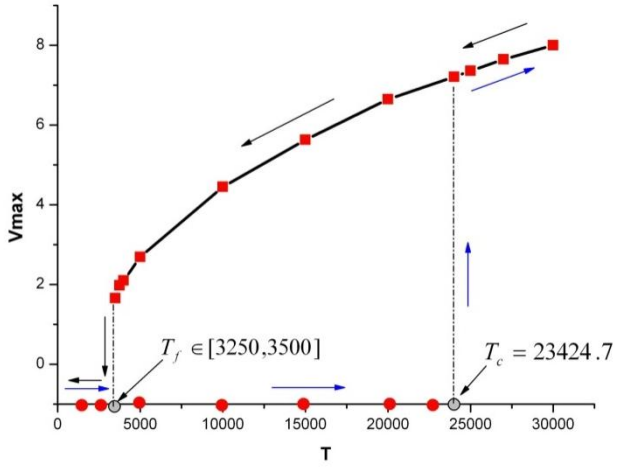

Figure 5-27. Evaluation of Vmax versus *T* with the weak injection case; Parameters: *C*= 0.1 and *M* = 5

At *T*=30000, the flow structure is the same as at *T*=27000. The only difference is that the amplitude and frequency of the oscillation increase with *T* value; see Figure 5-24 (top right). As *T* further increases to 40000, the flow entered a new state, see Figure 5-24 (down left). The flow is generally periodic with one-cell structure. However, the amplitude of the velocity field varies dramatically in each cycle. At *T*=100000, the flow is fully chaotic, see Figure 5-24 (down right). It should be stressed here that the flow keeps the one-cell structure at the chaotic state, which is different with the two-cell structure of strong injection at final chaotic state.

From above solutions of weak injection case, we notice that the flow structure highly depends on *M* value. Thus, it is a natural thought to have a look what will happen if we continually change *M*. In figure 5-27, we present some results for the same *C* and *T* with different *M*. Some other computations with *M*=5, 6 and 7 have also been done to help summarizing the general change in the law of the flow structure.

In discussing the obtained results, we follow a descriptive approach to delineate the overall physical picture of the phenomena. Considering the much more complex flow structures than strong injection case, these descriptions reflect my personal understanding of the physical problem, and some more rigorous, quantitative analyses should be done to verify some of our assumptions in the coming future.

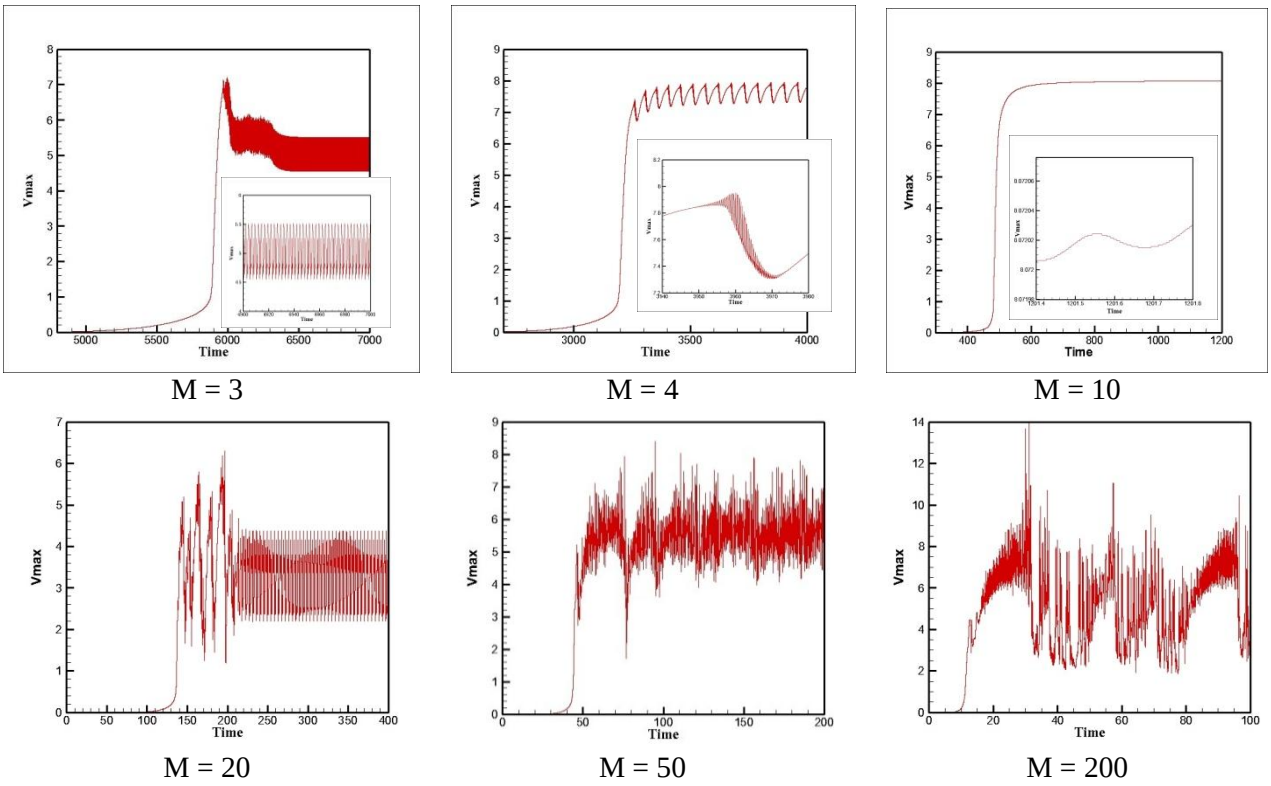

Figure 5- 28. Evolution of the maximum vertical velocity for weak injection with C=0.1 and T=30000

Firstly, we summarize what we observed with Figure 5-28 and some other results not listed.

1. The flow structures of *M*=5, 6, 7 and 10 are of the same type. A final quasi-steady state is reached after the exponential growth of the velocity field. The flow contains only one primary cell. There exist small oscillations on the quasi-steady velocity field. In addition, the amplitude and frequency of the oscillation increase when M decreases.
2. The flow structure of *M*=4 is quite similar to the one obtained with *T*=40000 and *M*=5. And for *M*=3, the flow structure is consistent with the one obtained with *T*=50000 and *M* =5. Though these solutions are unsteady, the one-cell structure is kept.
3. The flow structure of *M*=20, 50 and 200 are relatively more complicated, since there were serious oscillations appearing in the charge density distribution and velocity field. For *M*=20 and *T*=30000, the final solution is of one-cell structure, but the direction of the cell varies periodically, see Figure 5-29.
4. For *M*=50 and *T*=30000, the solution is of unsteady two-cell structure. The evolution process and final state is close to what we observed with the strong injection case (*C*=10, *M*=10, *T*=1300).
5. For *M*=200 and *T*=30000, some electro-plumes were observed, see Figure 5-30. It should be pointed out that these plumes were developed after the formation of two-cell structures; see Figure 5-28 (a). The evolution process and final state is close to what we observed with the strong injection case (*C*=10, *M*=10, *T*=4000).

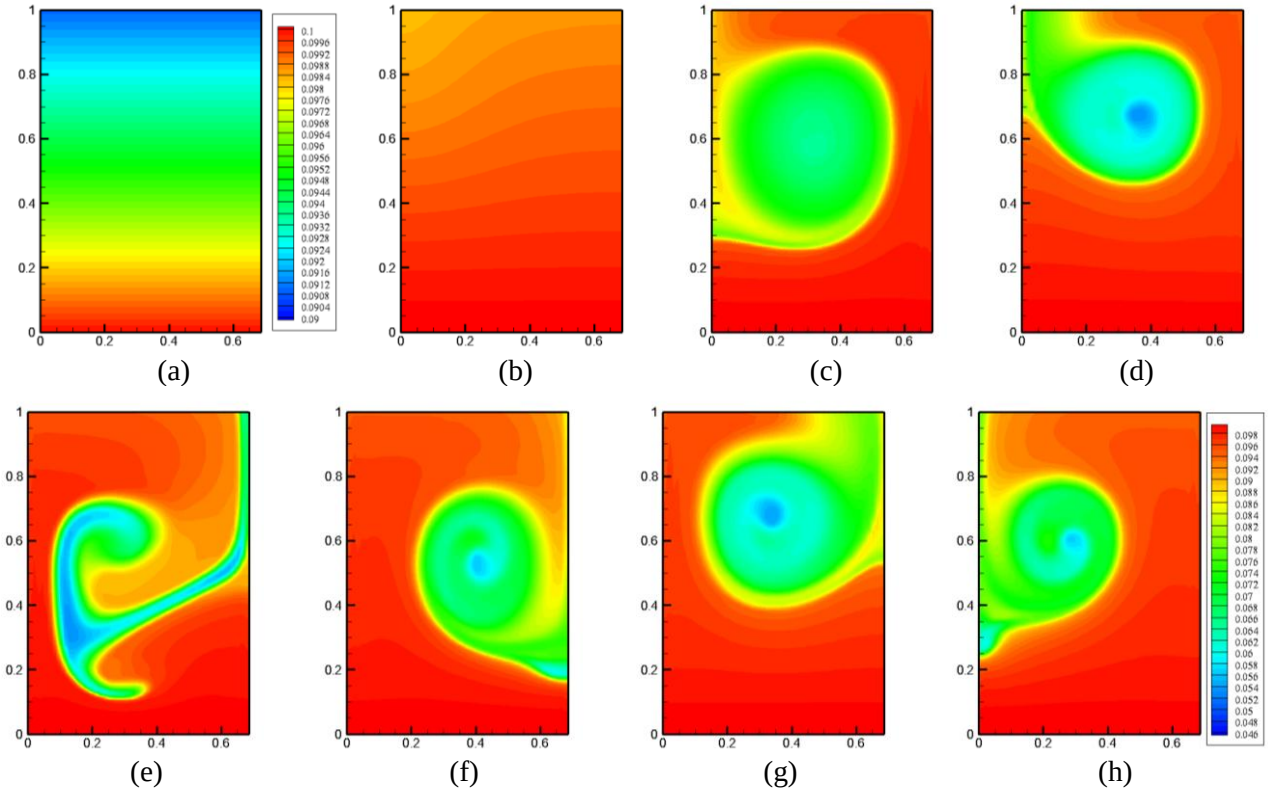

Figure 5-29 Numerical results with weak injection; charge density with (a) hydrostatic solution (b) t=110.5 (c) t=140.0; (d)-(h) a complete cycle to show the change of void region direction; Parameters: T= 30000, C=0.1, M=20;

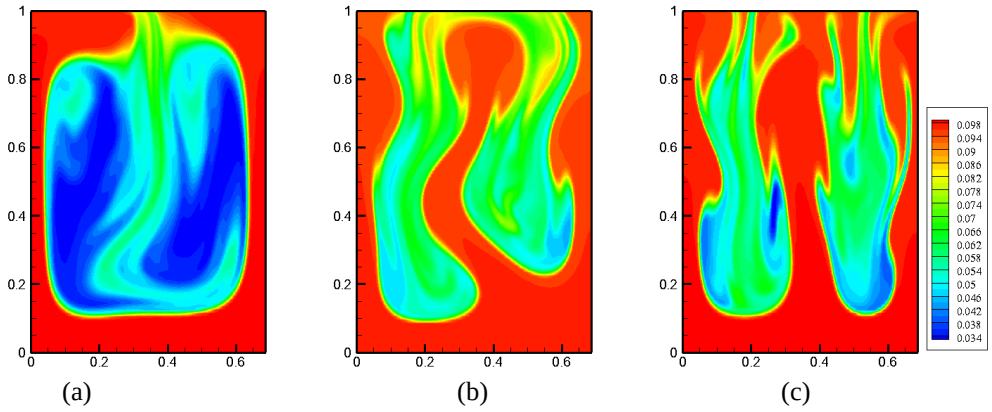

Figure 5-30 Charge density distribution of a weak injection (C= 0.1, M=200, T=30000); (a) Two cell structure (b) electro convective plumes (c) a moment corresponding to four-cell structure;

In the next paragraph, we will illustrate our understanding of the complex phenomenon in weak unipolar injection case.

1. It is well-known that whether the viscous or inertial effects are dominant the electro-convective regime depends on the non-dimensional electric Reynolds number $R = T / M^2$. It has been determined experimentally that the transition R number (R_T) is 10 for strong injection case. The transition R number for weak injection case has been estimated to be on the order of 10. However, an exact value has never been provided.

2. For strong injection, as the linear stability criterion is on the order of 100, $R_C = T_C / M^2$ may always be smaller than R_T. In other words, the strong injection system may always starts from the no-motion state to a viscous effects dominating state. However, considering the linear stability criterion for weak injection (taking C=0.1 as the example) is of the order of 10000, it is possible that $R_C > R_T$ for some relatively small *M* value. Under this condition, the system would pass from the no-motion state to the state where inertial effects dominate or viscous and inertial effects are of the same order. This is exactly what happens in the range $M \in [3,10]$.
3. For $M \le 10$, R increases along with the decrease of M. The inertial effects become more and more important. For inertial effects dominating regime, we assume that the convection follows a routine to final chaotic state: quasi-steady (R_1) →quasi-periodic (R_2) → aperiodic (R_3) → chaotic (R_4). For a specific small M, it is possible that $R_C = T_C / M^2$ appears in any region among R_1, R_2, R_3 and R_4. From the solutions showed in Figure 5-25, we obtain,

   $R_T \in [R_1, R_2], \qquad 5 \le M \le 10$

   $R_T \in [R_2, R_3], \qquad M = 4$

   $R_T \in [R_3, R_4], \qquad M = 3$

   These findings are consistent with the results listed in Figure 5-24, which is obtained with a fixed *M* (M=5) and various *T* values. With the increase of *T* till its value greater than 30000, it is possible to reach the same state of at *T*=30000 with *M*=4 or *M*=3.

4. For $M \ge 10$, the viscous effects are dominant with both strong and weak injection cases. Then a natural thought is that the weak injection system in this range may follow the same way to chaotic state as the one in strong injection system. However, the solutions showed in Figure 5-27 do not support this viewpoint. It has been found that both the velocity and charge density (electric current) fluctuate in time even when *T* is slightly greater than T_C in weak injection system, which is in contrast to the strong injection case. These oscillations should belong to the essential nature of the flow. The source for these regions may be the weak Coulomb repulsion between ions and the existence of a small amount of charge inside the hole in the cell. With the oscillatory convection, *M* may dramatically change the bifurcation behavior of the flow. For $M \ge 50$, it is observed that the average value of the velocity is independent of *M* for the same *T* and the amplitude of the velocity fluctuations strongly depends on *M* value. The fluctuations increase with *M*. This typical law can be qualitatively understood from a physical point of view, since large values of *M* correspond to lower ionic mobility, which means that ions are more strongly dragged by the liquid and can therefore be more easily trapped in the 'separatrix' between the free region and the charge occupied areas. To summarize, the electro-convection due to weak injection is in the viscous dominating regime when $M \ge 10$. However, the flow is unsteady even at *T* slightly greater than T_C and the M significantly affects the flow regime. The basic law is that the flow is more volatile with the higher values of *M*.

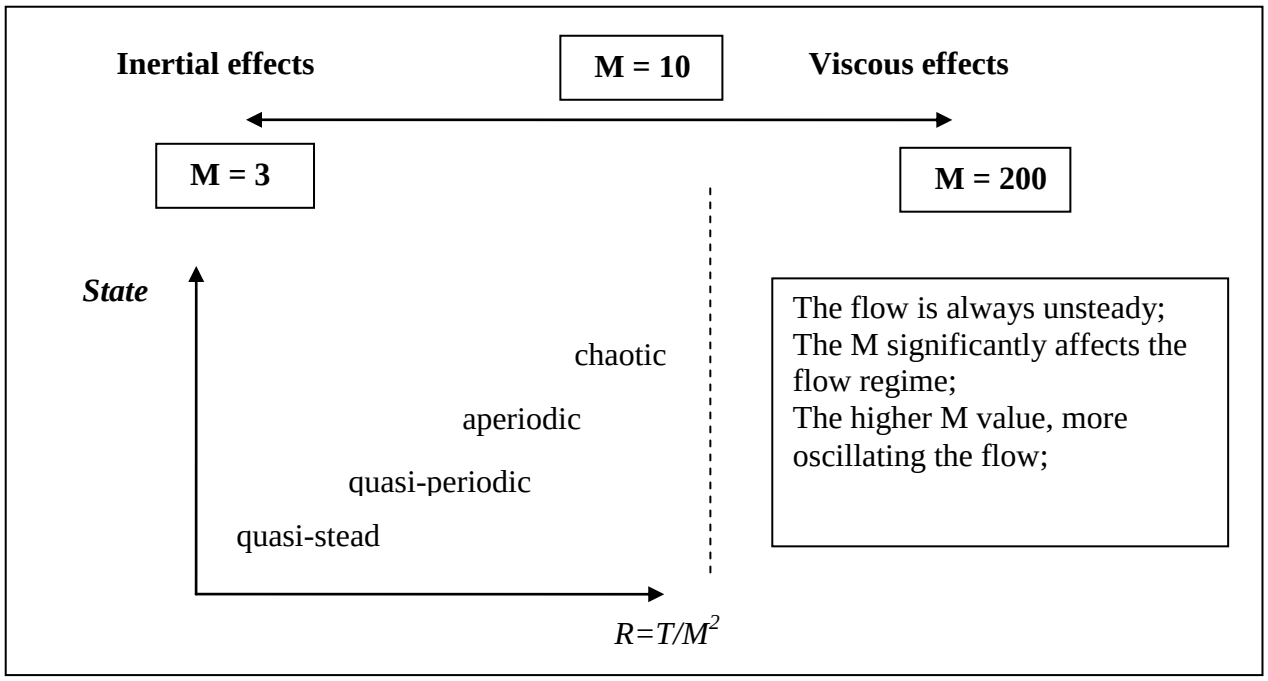

Figure 5-31. A summarization of the relationship between M and flow regimes in weak injection system

As the physical experiments with weak injection have never been done, the above findings may help to understand outcomes of future experiments. In addition, it seems that the quasi-steady flow can only be found in a narrow region $M \in [5,10]$. Thus it is important to select appropriate material when designing some experiments to highlight the possible flow structure (like hexagonal and quasi-cellular motion in strong injection case) and the hysteresis loop associated with the linear and nonlinear stability criterion.

5.3 Conclusions

In this chapter, the problem of electro-convection due to unipolar injection between two parallel electrodes has been tackled with a novel numerical algorithm based on finite volume method. One key component of the whole algorithm is the application of TVD scheme to the charge density equation.

When the electric potential between two parallel electrodes immersed in a dielectric liquid is high enough the development of a subcritical electro-convective instability occurs in the bulk. A linear and non linear critical value of the electric potential give rise to a hysteresis loop when a representative quantity is plotted versus the potential. Transient evolution of electro-convection in a dielectric liquid between two parallel plates is analysed numerically. Both strong and weak injection cases are considered.

The linear and non linear stability parameter noted respectively T_c and T_f that we obtained numerically are very close from the ones predicted by the stability analysis. The very good agreement indicates that the simulation is able to capture the important features of

electro-convective flows both in strong and weak injection. It completely validates our numerical tool for such simulations.

In addition, the flow structure of electro-convection in the finite amplitude regime has been discussed in details. Particularly, we observed that the flow structure at T slightly above T_C highly depends on M parameter with the weak injection case. The reason for such a relationship has been analyzed thoroughly. In weak injection, the discrepancy, for the non-linear criterion T_f, between the predicted value of the hydraulic model and our result is also explained by the inertially dominated regime that the simple model of Felici cannot undertake.

Chapter 6 Numerical simulation of electroconvection in insulating liquids induced by unipolar injection: numerical aspects

Some numerical details and skills will be introduced and discussed in this chapter. Some are for a better approximation of physical problems, some for reducing computational cost. As the method for solving Navier-Stokes equations belongs to the standard techniques in CFD fields, we will only discuss about solving details of the charge density equation and Poisson equation.

6.1 On solving the charge density equation

In Chapter 3, we use some pure advection problems to test the performance of different time schemes and TVD schemes. Here, we extend the comparison with the strong injection problem. Before further discussion, it is important to demonstrate how to correctly treat the boundary conditions.

6.1.1 On symmetric boundary condition

In Figure 6-1, we notice the difference of the charge density distribution near symmetric boundaries between our TVD algorithm and PIC method.

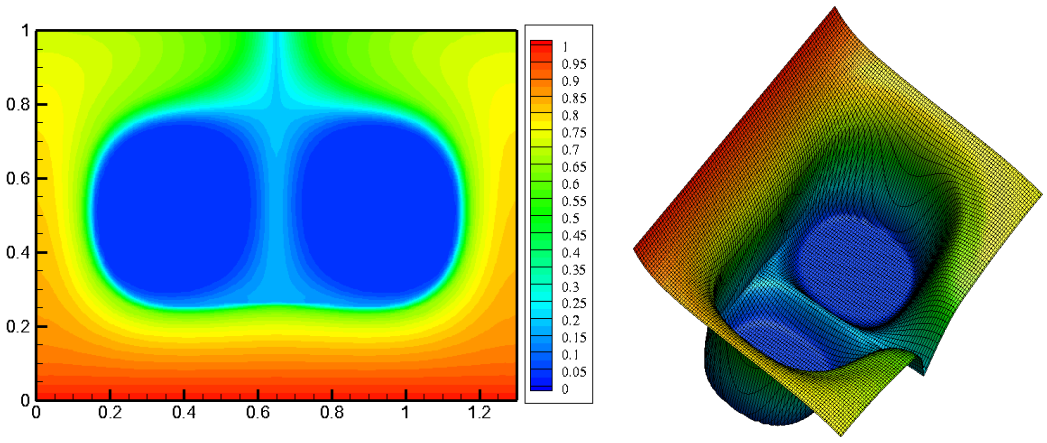

Figure 6-1. Charge density distribution at steady state of a moderate injection case;
Parameters: C = 1.0 M = 50, T = 550

Here we will prove that our results are more accurate through a simple example. The idea is simple: since there are some potential questions about the symmetric boundary condition treatment we just enlarge the domain to twice larger, which means the symmetric boundaries disappear, and recomputed the same condition. The results in Figure 6-1 clearly show that there are some non-zero charges in the central region. With the PIC method, if the symmetric boundary conditions are simply treated with the same method for outlet boundary condition (i.e., imposing no boundary

constraint), some important physical phenomenon may not be caught. The observed non-zero field region of charge density should be due to the weak or moderate injection cases, which is easy to understand.

6.1.2 On injecting and collecting electrodes

For electro-convection between two parallel plates, the injecting and collecting electrodes represent two kinds of boundary conditions for charge density equations. In chapter 2, we have explained the physical boundary conditions requirement for the charge density equation. For emitter electrode, the charge density should be provided following the injection law. For collecting electrode, the physical boundary condition is of no need if we neglect the diffusion term. Taking into account the diffusion term, an extra boundary condition is necessary to complete the system. Various choices are possible: the zero-slope method or the extrapolated method. Here, we firstly discuss the case of neglecting diffusion term.

$$\frac{\partial q}{\partial t} + \nabla \cdot \left(q\left(\vec{E} + \vec{U} \right) \right) = 0 \tag{6-1}$$

We define $\overline{U^*} = \vec{E} + \vec{U}$ as the background field for charge density variable. It should be noted that this background field is not divergence-free, i.e., $\nabla \overline{U^*} \neq 0$.

Injecting electrode

At the injecting electrode, the velocity field is always zero due to non-slip boundary condition, while $\vec{E}y$, the vertical componential of electric field, is always positive. Thus, the condition $\overrightarrow{U^*} = \vec{E} + \vec{U} > 0$ is always guaranteed during the whole computation process. That means we actually treat the classic "inflow boundary condition" for the charge density equation at the emitter electrode.

Let us consider the boundary condition (also the injection law)

$$q(x = 0, t) = g_0(t) \tag{6-2}$$

where $g_0(t)$ is a given function. With the finite volume method, the conservation law of the charge density equation at the first inner control volume can be expressed in the form,

$$Q_2^{n+1} = Q_2^n - \frac{\Delta t}{\Delta x}\left[F_{3/2}^n - F_{1/2}^n \right] \tag{6-3}$$

where $F_{1/2}^n$ and $F_{3/2}^n$ are some approximation to the average flux along $x = 0$ and $x = \Delta x$. Generally, we can compute the exact flux $F_{1/2}^n$ by integrating along the boundary,

$$F_{1/2}^n \approx \frac{1}{\Delta t}\int_{t_n}^{t_{n+1}} Q_1 \cdot \overrightarrow{U^*} dt = \frac{\overrightarrow{U^*}}{\Delta t}\int_{t_n}^{t_{n+1}} g_0(t) dt \tag{6-4}$$

The essential problem is to express $Q_{5/2}$ and $F_{3/2}^n$, see Figure 6-2. As our TVD algorithm is a five-point method, a special formula is needed to express $Q_{5/2}$ with Q_1, Q_2 and Q_3, which is not an easy task because of their non-uniform distribution. With the FUD scheme, a three-point method, the problem will not appear. Thus one possibility is to apply the FUD scheme at the first cell, together with the high-resolution TVD schemes at other cells. Rather than explicitly switching to a different formula at the inlet boundaries, we prefer to use the ghost-cell method for its generality and simplicity. The motivation for the method is that we apply the same formula for all the inner cells. We then define a ghost cell, Q_0, with the same size of the first inner cell. We want to express $Q_{5/2}$ with Q_1, Q_2 and Q_3 with the same formula for other interior cells. The problem is now how to set the value of the ghost-cell.

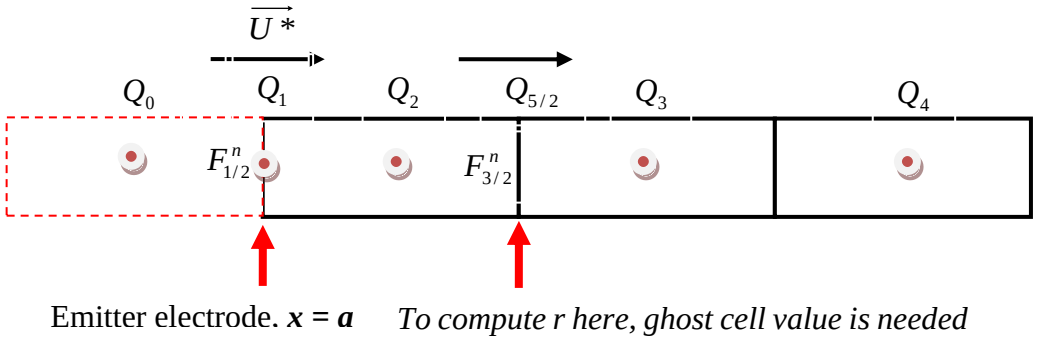

Figure 6-2. The computational domain near the emitter electrode, the domain is extend to one ghost cell for specifying boundary conditions

For convection-diffusion equations, a simple and widely used method is the linear extrapolation [47, page 159][284],

$$Q_0^n = 2Q_1^n - Q_2^n \tag{6-5}$$

For the advection equation we can easily compute sensible values using our knowledge of the exact solution. We would like to set

$$Q_0^n = \frac{1}{\Delta x}\int_{a-\Delta x}^{a} q(x,t_n)dx \tag{6-6}$$

Of course the true solution isn't even defined for $x < a$, but we can easily extend the solution past the boundary using our knowledge of characteristics, setting

$$q(x,t_n) = q\left(a, t_n + \frac{a-x}{\bar{U}}\right) = g_0\left(t_n + \frac{a-x}{\bar{U}}\right) \tag{6-7}$$

Then

$$Q_0^n = \frac{1}{\Delta x}\int_{a-\Delta x}^{a} g_0\left(t_n + \frac{a-x}{\bar{U}}\right)dx = \frac{\bar{U}}{\Delta x}\int_{t_n}^{t_n+\Delta x/\bar{U}} g_0(\tau)dx \tag{6-8}$$

Again, we could approximate this integral by the second-order approximation, obtaining

$$Q_0^n = g_0\left(t_n + \frac{\Delta x}{2\bar{U}}\right) \tag{6-9}$$

For autonomous injection, we simply set

$$Q_0^n = Q_1^n = C \tag{6-10}$$

The difference of the two setting methods can be highlighted with the computation results of electric currents. For computation of buoyancy-driven convection problem, it is important to check the conservation of heat flux. Here we follow the same idea to check the conservation of electric current. It is well-known from the Ampère's law that the electric current through any horizontal plane should be consistent with the one through the injection electrode.

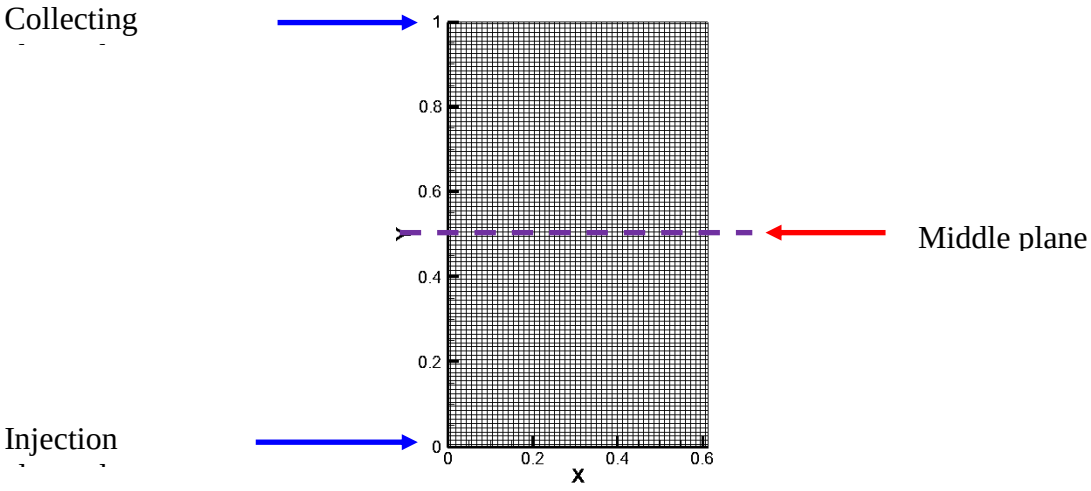

Figure 6-3. The computational domain and grid system with the strong injection to show the importance of proper boundary condition treatment.

Taking a strong injection system (C=10, M=10 and T=240) as the example, we output the electric current though the injection, middle plane and collecting planes, see Figure 6-3. The numerical results with different extrapolation methods for setting values of ghost-cells are present in Figure 6-5. Only with the second extrapolation method, the Ampère's law is fully respected.

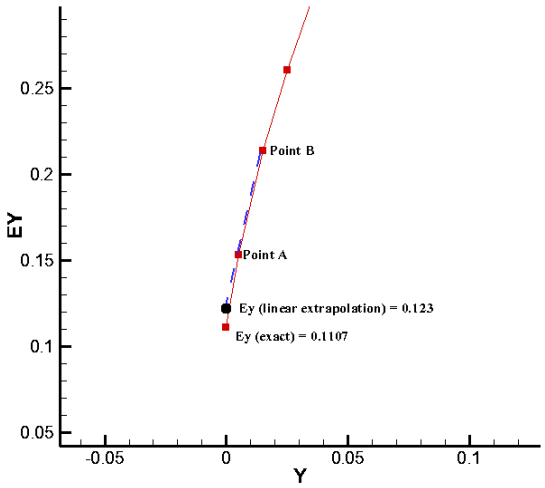

Figure 6-4. Values of electric field at bottom plate: analytical vs. linear extrapolation

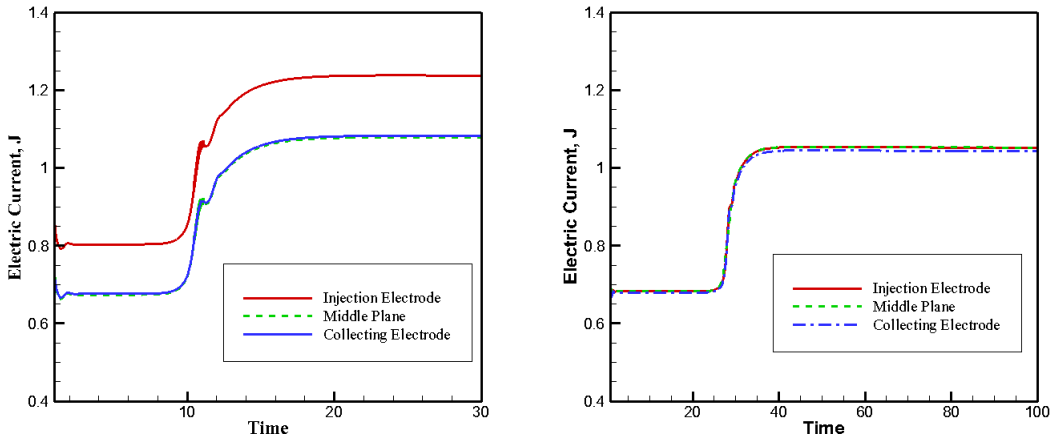

Figure 6-5. Evolution of electric current of different planes with time (left) linear extrapolation (right) setting with knowledge of characteristics; Parameters: C = 10, T = 240, M = 10; 51×101 uniform grid;

It is also observed that in Figure 6-4, there is also some slight difference among the injecting and collecting electrodes. The difference may come from inaccurate extrapolation method when computing the electric field on bottom plates. During the calculation process, we first solve the Poisson equation for potential, and then evaluate the electric field in the inner domain with some gradient evaluation methods (like Gauss formula or Least–squares approach). Some extrapolations are needed to decide the electric field on the boundary nodes. A linear extrapolation is used to obtain the results in Figure 6-5. However, the linear extrapolation method is not that accurate. For simplicity, the hydrostatic solution can be used to demonstrate the problem. The difference between the exact hydrostatic value and the value obtained by linear extrapolation (with point A and B in Figure 6-4) is about 11%, while the current difference is about 15%.

Collecting electrode

At the collecting electrode, the velocity field is also always zero due to non-slip boundary condition, while $\vec{E}y$ is always positive. Thus, $\overrightarrow{U^*} = \vec{E} + \vec{U} > 0$ and we actually treat the outflow boundary condition for the charge density equation at the emitter electrode.

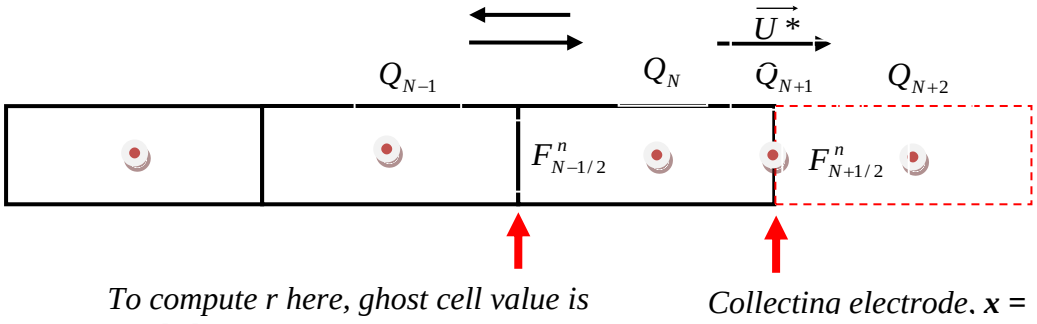

Figure 6-6. The computational domain near the collecting electrode, the domain is extend to one ghost cell for specifying boundary conditions

There are two types of 'ghost-cell method'. The first type is the one introduced above. With this method, we need not to develop special formula for a use near the boundaries, e.g. $F^n_{3/2}$ and we have to extend the computational domain to include only one additional cell. However, some special treatment is necessary to determine the fluxes at the physical boundaries, e.g., $F^n_{1/2}$. We name this type of method as 'half ghost-cell method'. The other type is the 'full ghost-cell method'. This method follows the idea that all physical boundaries as the interior interfaces are treated with the same formula for the original interior faces. If the five-point convection schemes are used, two additional cells are required for each boundary. The values of these ghost cells are set at the beginning of each time step in some manner that depends on the boundary conditions and perhaps the interior solution [72]. With this method, a variety of boundary conditions can be treated with a unified approach, which greatly simplifies the practical implementation.

Eqn. (6-1) is of hyperbolic type, and then we should not specify any physical condition at the outlet boundary in principle. However, some numerical boundary conditions may be needed, which depends on numerical schemes and numerical treatment approaches.

Half ghost-cell method

Two steps are needed for this method. Firstly, we need a formula to express Q_{N+1} with other inner cells, like Q_N and Q_{N-1}. It is in this step that some numerical condition should be specified. If we set

$$Q_{N+2} = Q_N$$

a Neumann condition $\frac{\partial q}{\partial n} = 0$ is used.

Secondly, a ghost cell is needed to compute the $r = (Q_{N+2} - Q_N)/(Q_N - Q_{N-1})$ value which is necessary for $F^n_{N-1/2}$ if the velocity directs from right to left. Both zero-order and first-order (or linear) extrapolations can be used.

Zero-order extrapolation

$$Q^n_{N+1} = Q^n_N \tag{6-11}$$

First-order extrapolation

$$Q^n_{N+2} = 2Q^n_N - Q^n_{N-1} \tag{6-12}$$

Full ghost-cell method

With this method to treat outlet boundary condition, we compute $F^n_{N+1/2}$ with the same formula as the one for other interior interfaces. Theoretically, if we use a one-sided scheme such as FUD, then we do not need any numerical boundary condition. If we use ghost cells, then we can assign arbitrary values to the ghost cells on the right with no effect on the interior solution, since these values will never be used. If we use the five-point method (like TVD schemes) that does use values to the right, then some numerical boundary conditions must be specified. In general, we must take some care in how we specify these conditions to obtain a stable and accurate method. Since there is no physical boundary, we should guarantee that the information to compute values of cells near the boundaries only from left even if some values of right appear in the expression.

Besides the method of switching to FUD for cells near the outlet boundaries, we can also achieve the goal by carefully setting the values of ghost cells. With zero-order extrapolation,

$$r_{N+1/2} = \frac{Q_{N+2} - Q_N}{Q_N - Q_{N-1}} = 0 \qquad \text{and} \qquad F^n_{N+1/2} = \overrightarrow{U^*} \cdot Q_N \tag{6-13}$$

since $\left(\overrightarrow{U^*} > 0\right)$. The method becomes some kind of FUD method. With linear extrapolation, there is a possibility that noise generated at the right boundary will propagate back into the domain and contaminate the solution elsewhere and perhaps even cause instability. Generally, the TVD schemes are highly dissipative for this left-going waves and so this will not cause serious problems and the method can be proved to be stable [72].

In the present study, we use the 'half ghost-cell method' and first extrapolation for the treatment of collecting electrode. It should be noted that the charge-diffusive boundary layer at the electrode will not affect the mainstream solution of our problem.

6.2 Comparison of the time marching algorithm

In this part, we extend the comparison of different time marching methods with the complete unipolar injection problem. The purpose of this and of the next section is to provide some

guidelines for the selection of time and TVD schemes in calculation of unipolar injection problems.

Four different time schemes including Explicit Euler (EE), Implicit Euler (IE), Implicit Three Time Level (I3L) and the optimal second-order TVD Runge-Kutta method (RK2TVD) will be considered. A strong injection system (C=10.0, M=10.0) will be used as the test case. With different T parameters, the final solution will be steady or unsteady. Two typical T values are selected: one ($\underline{T}$=240) representing the steady case and the other one for unsteady (periodic) case. The SMART scheme will be used in all the test cases. The physical domain is [0, 0.614] × [0, 1].

Case I. T = 240.0 M = 10.0 C = 10.0

In this case, a 50 × 100 grid system has been used. The results for two time steps of 10^{-3} and 10^{-4} are presented in Table 6-1. It is immediately noticed that all the solutions of *Vmax* are almost the same, which proves that all time schemes work well for the test cases. The required computational effort associated with each scheme is also shown in the same Table. Though explicit schemes require less computing time than implicit schemes, the difference is tight. The CPU results may prohibit IE's use since its computational cost is high.

Table 6-1. Performance of the various time schemes in the steady unipolar injection test

		Implicit Euler	**Explicit Euler**	**RK2TVD**	**Implicit 3 Levels**
Time step = 10^{-3}	CPU time	10min21s	10min14s	9min48s	10min18s
Total time = 30	Vmax	4.650	4.649	4.650	4.650
Time step = 10^{-4}	CPU time	86min43s	79min12s	83min17s	84min36s
Total time = 30	Vmax	4.652	4.652	4.652	4.652

Case II. T = 550.0 M = 10.0 C = 10.0

In this case, a very fine 100 × 200 grid system has been used to reduce the potential effect of the spatial discretization scheme. The time evolution curves with two different time steps are shown in Figure 6-7. The information of the maximum vertical velocity component and CPU cost are summarized in Table 6-2.

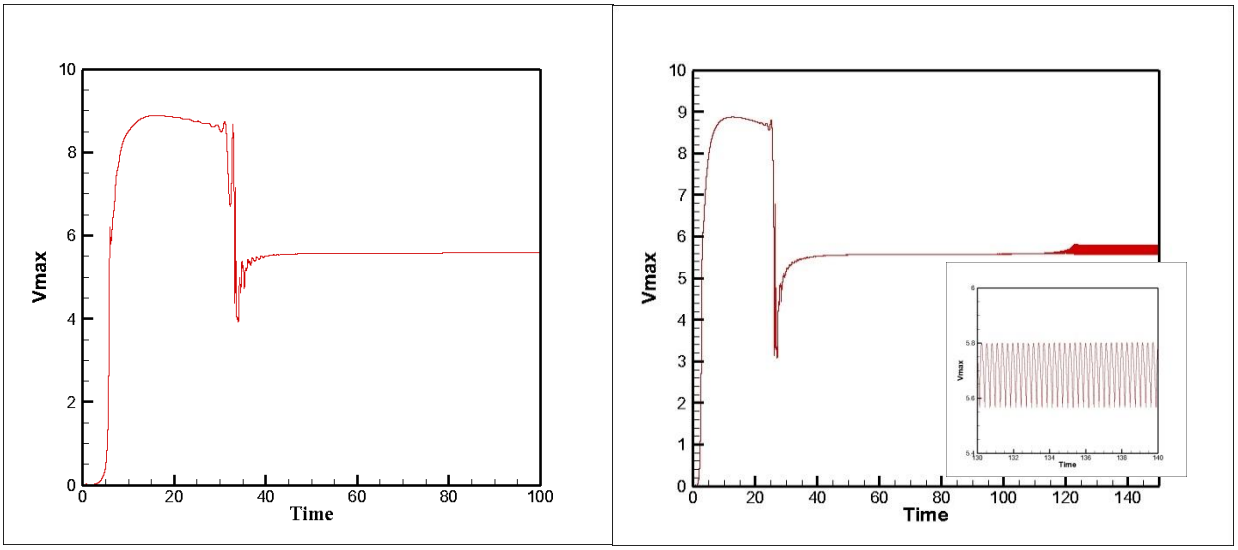

Figure 6-7. Evolution of the maximum vertical velocity for strong injection with C = 10 M = 10 T = 550 (left) Euler Explicit and dt = 10^{-3} (right) Implicit Three Time Level and *dt* = 10^{-4}. These simulations have been carried out with a 101× 201 uniform grid system.

It is a surprise to see that the final solution is steady with $dt = 10^{-3}$ and regular periodic with $dt = 10^{-4}$. The difference should be due to numerical diffusion introduced by temporal discretisation. Further tests with a smaller time step, 5×10^{-4}, were done to verify the solution with $dt = 10^{-4}$ is grid-independent.

As shown in Table 6-2, the computations with EE and RK2TVD scheme failed because of the violation of CFL condition. However, the divergent points for EE and RK2TVD scheme are different. The computation stopped when Vmax is 4.35 with EE scheme and 7.295 with RK2TVD, which means the CFL coefficient is smaller for RK2TVD than EE scheme. It should be noted that if we further increase the time step to 5×10^{-3}, the computation with implicit time schemes will also diverge.

Table 6-2. Performance of the various time schemes in the unsteady unipolar injection test

		Implicit Euler	**Explicit Euler**	**RK2TVD**	**Implicit 3 Levels**
Time step = 10^{-3} Total time = 120	CPU time	456m12s	Divergent	Divergent	317m7s
	Vmax	5.581			5.581
Time step = 10^{-4} Total time =120	CPU time	2222m54s	2089m6s	2129m16s	2186m3s
	Vmax*	5.686	5.685	5.686	5.686
	Amplitude	0.120	0.120	0.120	0.120
	Frequency	21.89	21.89	21.89	21.89

Vmax*: the time average value

From the solutions with *dt = 10^{-4}*, we firstly noticed that the accuracies are the same. Comparing the CPU cost, Implicit Euler again is not efficient at all. EE and RK2TVD scheme require less computer time than I3L, but the difference is very limited. If we optimize the stopping criteria with deferred correction loop and linear system solver for implicit schemes, the difference will be

further reduced. It is interesting to find that I3L method is well suited to simulate unipolar injection problems. In above test cases, the lowest value of the charge density is almost zero (non-zero value is of 10^{-6}). In conclusion, I3L and RK2TVD schemes are recommended.

6.3 Comparison of TVD schemes

In this section, we would like to highlight the importance of the selection of an appropriate TVD scheme. From a practical implementation point of view, various schemes can be easily incorporated into our numerical solver under the unified approach introduced in chapter 3. The only difference is the selection of the flux limiter function.

The strong unipolar injection (C=10, M=10) is selected as the test case. The domain space is 0.614 × 1 units, and a 51× 101 grid is used. The time scheme is I3L method and 10^{-3} is set as the time step. Only the numerical linear and nonlinear criteria with different convection schemes are tabulated in Table 6-3. Special attention should be paid to the numerical nonlinear criterion, as it reflects the overall performance of each scheme.

Table 6-3. Performance of the various discretization schemes in the unipolar injection test

Schemes	**Linear criterion T_C**	**Nonlinear criterion T_f**
FUD	162.2	[117, 118]
CD	164.5*	[108, 109] *
MINMOD	164.5	[112, 113]
SUPERBEE	165.9	[108, 109]
MUSCL	165.2	[110, 111]
SMART	164.6	[109, 110]

*: the values were obtained with the data before the divergence;

Firstly, we observed that there is serious problem with solution obtained with the CD scheme. On the one hand, there are clear non-physical oscillations in the evolution curve of Vmax and significant undershoot with charge density distribution, see Figure 5-38. The amplitude of the oscillation increases along the T value. More seriously, the computation with CD scheme would suddenly stop after long a enough time.

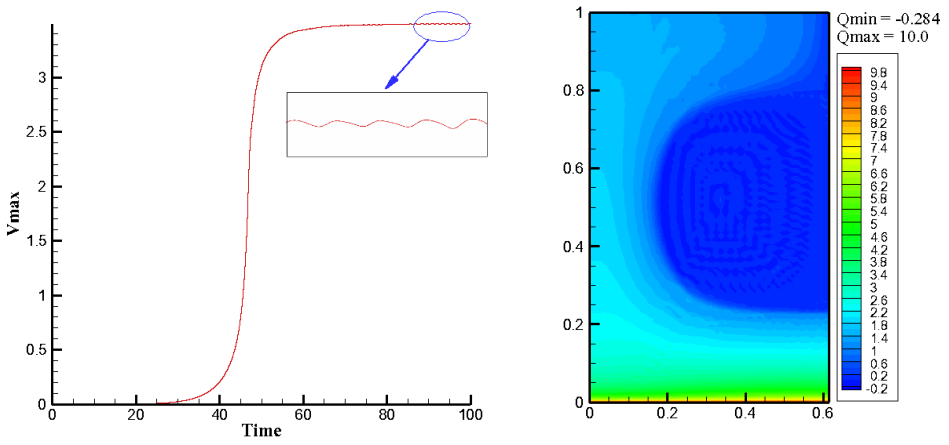

Figure 6-8 Time evolution of the maximum vertical velocity and charge density distribution at time = 100 unit for a C = 10 M = 10 T = 200 system; CD scheme is used to solve charge density equation

From Table 6-3, we firstly noticed that all schemes can successfully lead to an accurate linear stability criterion. However, the numerical prediction of the nonlinear criterion promotes more advanced challenges. As explained before, the subcritical nonlinear phenomenon is closely linked to the area and shape of the free-charge region.

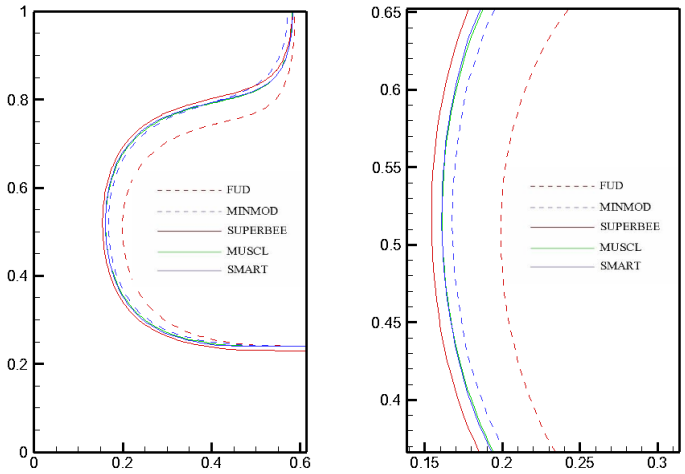

Figure 6-9. Contour lines ($q = 0.5$) with different convection schemes; Parameters: T = 190, C = 10, M = 10; 51×101 grid;

In Figure 6-9, we plotted the contour lines ($q = 0.5$, representing the free-charge region) of the solutions with different convection schemes. It is noticed that all the schemes can lead to oscillation-free solutions. However, the solution from the FUD scheme is extremely inaccurate. The other monotonic scheme, produce more accurate results. By enlarging the figure, we can distinguish the difference: MINMOD is more diffusive than the other three. The same conclusion can be reached by checking the minimum value of the solutions: FUD (0.1186), MINMOD (0.0302), SUPERBEE (0.0143) and SMART (0.0142). Though SUPERBEE scheme can lead to the largest area of free-charge region, its prediction of nonlinear critical value is not the best one. The reason may be that the 'over-compressive' behavior in smooth region of the scheme [285] and the shape of the void region is not well-preserved. Only with MUSCL and SMART schemes, both

linear and nonlinear criteria can be well predicted. Thus, the two schemes are recommended for unipolar injection simulation.

6.4 On Non-uniform meshes

From the above numerical solutions of strong and weak injection, we noticed that the charge density distributions are quite different. Taking the hydrostatic solution as an example, the charge density distribution and electric field show a very slow variation with the vertical direction in the weak injection case, see Figure 5-16. In contrast, both charge density and electric field show drastic variations near the injecting electrode in strong injection cases. Since the numerical error (here it means the truncation error) depends on the derivative of the variable and the grid spacing, it is a natural thought to apply the non-uniform grid for the calculation of strong injection case. The same technique has been strongly recommended in [34] when dealing with PIC method.

Generally, there are two types of non-uniform grids. For the first type the grid size increases or decreases with a constant expansion ratio. In the other type one cuts the whole domain into several sub-domains and the nodes are evenly distributed in each sub-domain. As mentioned in chapter 3, our TVD algorithm can be directly applied to non-uniform grid system without any modification. Although the derivation of TVD schemes is based on uniform grid, the final expression doesn't show its clear dependence on the uniformity of the grid system.

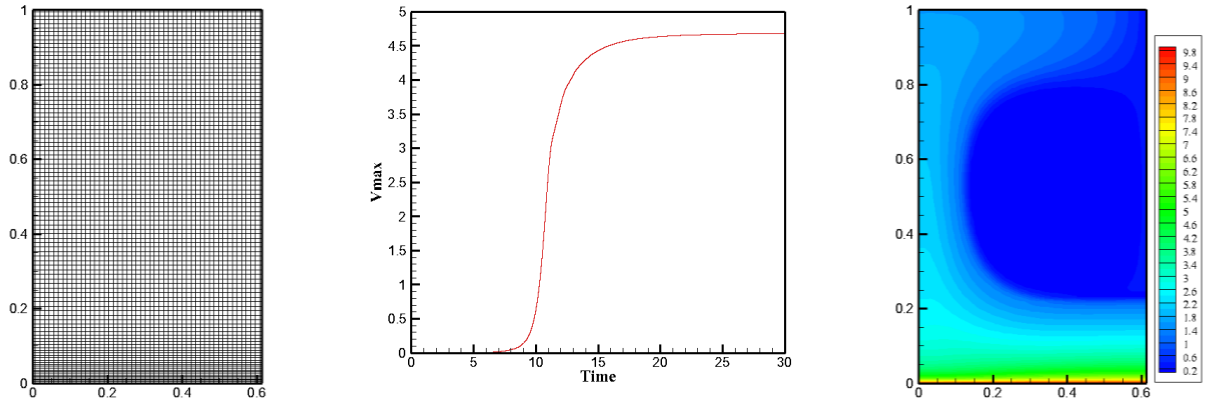

Figure 6-10 (left) a specially designed 51 × 101 non-uniform grid (middle) time evolution of Vmax (right) charge density distribution at steady state for a C = 10 M = 10 T = 240 system;

To apply our TVD algorithm to the first type of non-uniform grid, we need to design some specific formula for boundary condition treatment. With the second type, we need to be sure that the expansion ratio with the grid sizes between sub-domains is less than 0.5, otherwise there is no guarantee of the boundedness property [231]. Here we give a simple example to prove the effectiveness of our numerical solver with non-uniform grids. The physical domain is [0, 0.614] × [0, 1] and the non-uniform grid system contains 100 cells in y-direction and 50 uniform distribution cells in x-direction. The 100 cells in vertical direction are separated into two parts: the size of the first 20 (near the injection electrode) increases with a constant expansion factor, 1.05, and the spacing is uniform with the left 80 cells. The grid system, the charge density distribution at final steady state and the time evolution curve of *Vmax* are plotted in Figure 6-10. By checking the

final Vmax value, the solution of this dedicated grid is roughly equivalent to a 51 × 151 uniform grid system.

6.5 On solving the electric potential equation

There have been various discussions about solving a single Poisson equation. Here, we place some emphasis on two skills of solving Poisson equation in the whole unipolar injection system.

On starting fields

For solving a single Poisson equation with iterative method, it is convenient to start from a zero-field guess of the solution variable. However, for our time marching numerical method for unipolar injection, this choice is not economical from the viewpoint of CPU time saving. Instead, we strongly recommend setting the solution of previous time step as the starting field of present time step. Though this approach requires some more storage for two time levels of electric potential, the computational cost reduces markedly.

For weak injection case, we can even always start from the hydrostatic solution. It is well known that the final solution of a Poisson equation depends on both source term and boundary conditions. In unipolar injection system, the relatively small value and variation of source term limits their effects on the final solution.

On solving times

The second skill follows the idea that there is no necessity to solve Poisson equation in each time step since the electric field is not very sensitive to the charge variation. We introduce a control parameter to define the frequency of solving Poisson equation in the whole system. Two simple cases were tested with strong injection cases (C = 10, M = 10). One case (T = 240) stands for steady solution, while the other one represents (T =600) the unsteady case. We solve the Poisson equation every ζ (= 2, 4, 6, 8) time step and compare the solutions and CPU costs. There is a clear reduction of CPU time along the increase of ζ. At the same time, the numerical solutions of both steady and unsteady cases need exactly the same time.

However, it is not easy to define the limit value of this parameter. For chaotic regime, there is some risk to apply this technique as there could be dramatic changes of charge density in short time period.

6.6 Three-dimensional electro-convection: a simple example

The previous studies of electro-convection between two parallel plates are limited to two dimensions. Two very recent publications [155][289] tried to investigate the problem in three-dimensions. In [155], the PIC method is extended to 3D and is used to compute the charge density equation. A cylinder configuration was used and only weak injection case was considered. The velocity field is not obtained by solving the Navier-Stokes equations but imposing a self-similar field. The linear stability criterion which is the same with 2D solutions has been

successfully reproduced. An obvious drawback of this method is its computational cost. In [289], the authors examined the 3D flow structure qualitatively and quantitatively in a box configuration. The commercial software FLUENT is used as the simulation tool. A key problem considered in [289] is the EHD turbulence. It is interesting to note that the numerical method used in [289] is very novel though not many details were revealed. In this paper, the whole algorithm is based on finite volume method and a special boundary condition implementation incorporating with classic QUICK scheme is used to solve the charge density equation. The Navier-Stokes equations were solved directly to get the velocity and pressure fields. The strong injection case was run. It is found that the flow structure of 3D electro-convections is more chaotic than 2D case. In addition, a new distribution of length scales which has not been observed in 2D has been successfully shown in 3D results.

A simple example is provided here to show our numerical algorithm can be easily extended to three-dimensional problems. The same box configuration as [289] is considered, to see Figure 2-5 in Chapter 2. Instead of chaotic regime, we are concerned with the steady regime which means the driving parameter T is close to the linear stability criterion T_C. It has been shown through experiments that the flow structure is of hexagonal cells which are similar to the well-known thermal cells in RB convections.

With finite volume discretization and the dimension splitting idea, the extension of our numerical algorithm to 3D is straightforward. Comparing with the PIC method, the superiority of our TVD algorithm in the computational cost in 3D is even more obvious. In the following, the geometry of the configuration and the complete numerical method are described. Then, two sets of numerical solutions are presented to show the flow structure.

Two parallel square electrodes are separated by a distance d. The electrode is normal to the y-axis and the length of each side is L. The charge carriers are injected from the bottom side and the injection strength is set as strong. The aspect ratio L/d is used to control the physical domain. For the bottom injection electrode, the value of the charge density and electric potential is maintained at a fixed value. The up electrode is grounded which means the electric potential always keeps zero. We assume the zero-gradient condition for the charge density at this electrode. For all the vertical sides, we apply the symmetric boundary conditions for all variables including charge density, electric potential and velocity fields.

Two aspect ratio, 1.2 and 4 are selected. The large one is to ensure that the physical domain is larger than the theoretical wavelength. The uniform 50×100×50 (G1) and 200×100×200 (G2) grid systems are used to discretize the small and big physical domains.

Our numerical solver was firstly verified by computing the hydrostatic solution with G1 grid. Taking the charge density and electric potential indexes, the maximum difference between the numerical solutions and the analytical solutions are less than 5%.

The second test is to determine the linear stability criterion. The method to compute T_C is the same with 2D cases. With the G1 grid, three T values (180, 190 and 200) are used to extract the exponential ratios from the Vmax-time figure, see Figure 6-11(a). Similar to what we observed in 2D case, the velocity keeps zero at the beginning until a time where the growth ratio becomes

exponential, then a steady convective state is reached. The obtained T_C value is 165.6 which is very close to the theoretical one, i.e. 164.1. The flow structure with T=200 is presented in Figure 6-12. The charge distribution for *y=0.5* horizontal planes is plotted in Figure 6-12(a). It is observed that the charge is confined in a narrow region; see Figure 6-12(b). The whole region was separated into two regions: charge-covered and charge-free region. The convective cells are of three-dimensional structure rather than quasi-two-dimensional straight rolls. In Figure 6-12(c) we plotted the velocity field. The direction of the velocity vector follows the distribution of charge density. The up-direction vectors appear at the charge-covered region.

However, due to the small size of the physical domain, we failed to observe the complete structure of a convective cell with L/d=1.2 case. In the second calculation, we extend the aspect ratio L/d to 4.

Figure 6-11(b) shows the evolution in time of the amplitude of the convective cells in the lager domain computation. Compared with Figure6-11(a), there is a non-smooth stage before reaching the final steady state. This adjustment stage may be due to the determination of a critical wavelength.

In Figure 6-13(a), we plotted the two-dimensional section of normalized space charge at y=0.5. This figure can be compared with the results provided in [289], see Figure 6-14. There is a good qualitative agreement. The void region of charge is further highlighted in the iso-surface figure of charge density in Figure 6-13(b). The velocity vectors are shown in Figure 6-13(c). The left part of Figure 6-13(c) is the enlarged drawing which corresponds to the central region of Figure 6-13(c) right part. The up-direction and down-direction vectors follow the same rules shown through the small domain case. It is easy to see the three-dimensional irregularly shaped rolls.

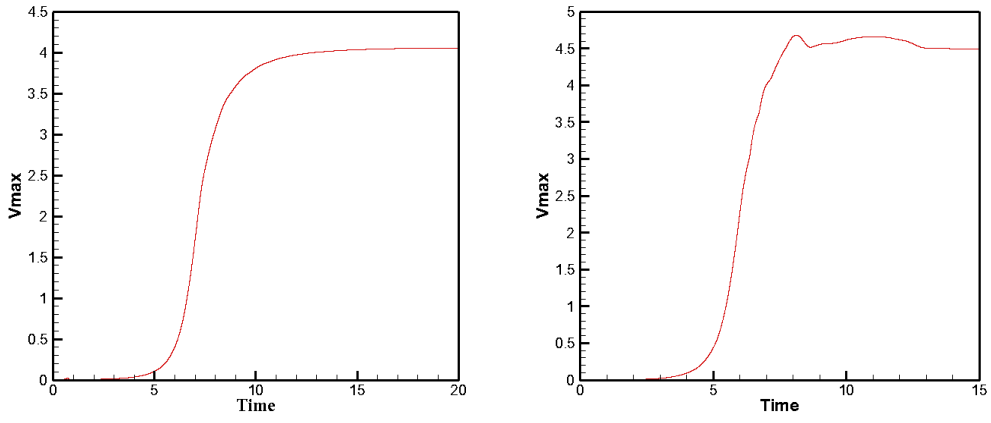

(a) *L/d* = 1.2, T=200, M=10, C=10 (b) *L/d* = 4, T=240, M=10, C=10

Figure 6-11. The time history in dimensionless unit of the maximal vertical velocity in 3D cases

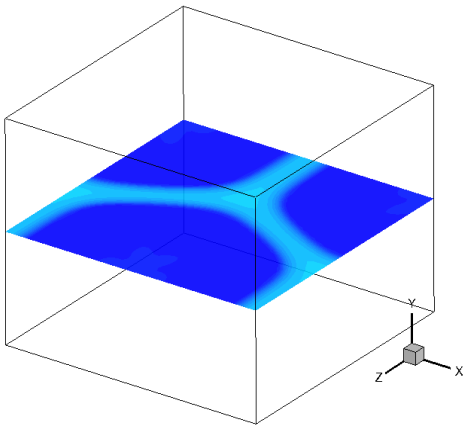

(a) charge density distribution at *y=0.5* plane

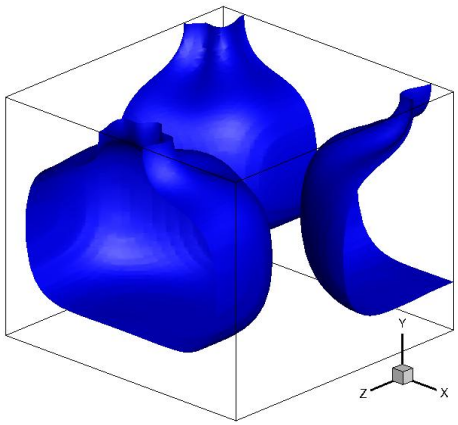

(b) iso-surface of charge density *q=1.0*

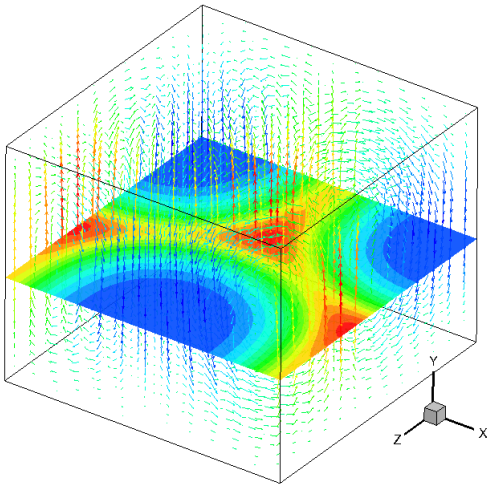

(c) velocity vector of convection cells in the inner domain

Figure 6-12. Numerical solution with *L/d* = 1.2, T=200, M=10, C=10

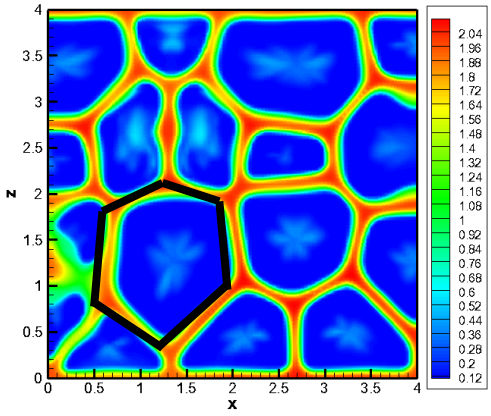

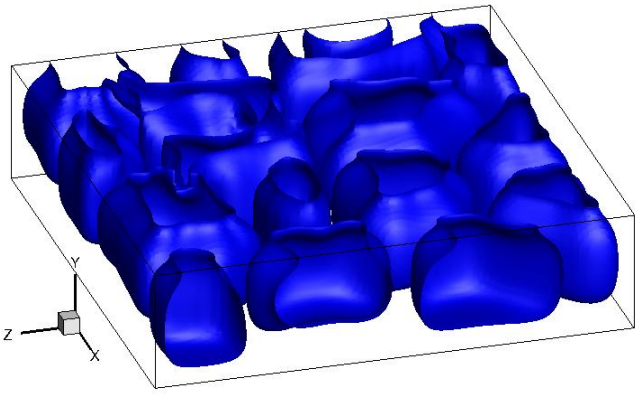

(a) charge density distribution at *y=0.5* plane

(b) iso-surface of charge density *q=1.0*

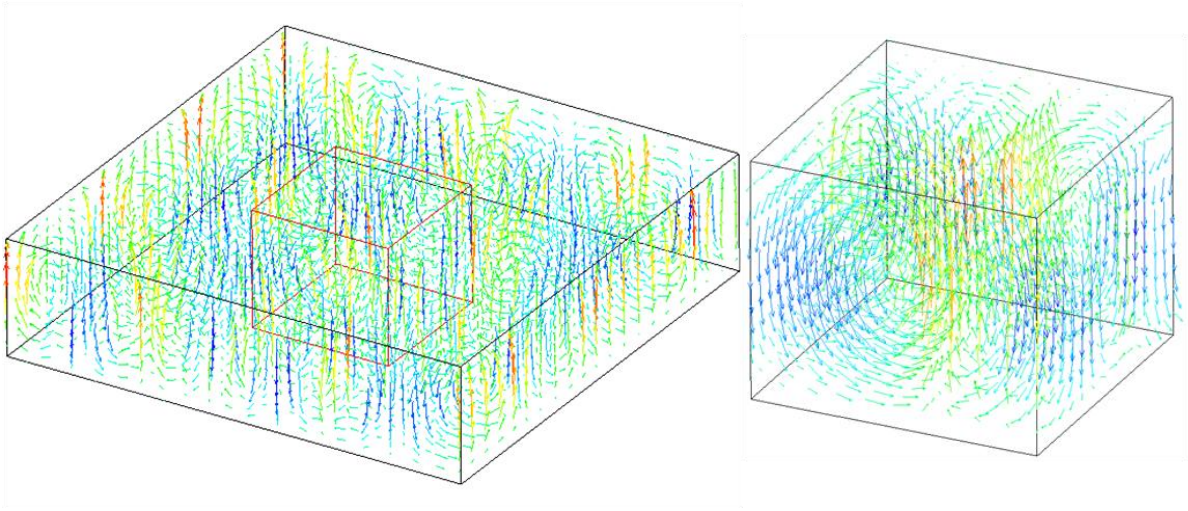

(c) velocity vector of convection cells in the inner domain

Figure 6-13. Numerical solution with L/d = 4, T=240, M=10, C=10

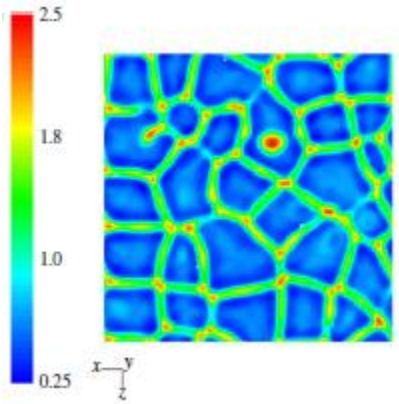

Figure 6-14. Normalized space charge at $y=0.5d$; Parameters: L/d = 6, C=10 and T=500 [289, Figure 5(a)]

However, we failed to observe the regular hexagonal structure. In the center region, we find an irregular hexagonal cell.

It has been stated in [287] that three-dimensional results own a larger range of roll structure size which is opposed to the two-dimensional simulations. The reason is three-dimensional mixing encourages the formation of smaller-scale eddies. In our results, rolls of different sizes are also observed.

In order to successfully obtain the regular hexagonal structure, we may need to further enlarge the physical domain to further reducing constraints imposed by the vertical boundaries. Large domain means more cells and computational cost. Further work is needed to obtain more accurate results. The code must be parallelized to be able to use meshes of small grid size in the simulations. For unsteady flow regime because of higher T parameter, time step must also be taken into account.

6.8 Conclusions

In this chapter, we focused on the numerical aspects of our numerical solvers for EHD and ETHD problems. The unipolar injection between two parallel electrodes has been selected as the standard test case.

For the charge density equation, we firstly discussed the boundary condition treatment method at the injection electrode. With the ghost-cell method, the importance of appropriate extrapolation is explained and demonstrated. For the time marching method, the implicit three time level (I3L) and explicit 2^{nd} order Runge-Kutta TVD (RK2TVD) are recommended considering the computational cost and accuracy. For the comparison of various TVD limiter functions, we use the linear and nonlinear criteria as indicators. It is interesting to notice that all convective schemes can lead to good estimations of the linear criterion. However, there is an obvious difference with the prediction results of the nonlinear criterion. The nonlinear stability criterion which reflects the overall performance of each scheme should be used for accuracy comparison. The MUSCL and SMART schemes are recommended for unipolar injection simulation.

Our numerical algorithm can be easily extended to the three-dimensional cases. With two simple examples, the three-dimensional structures of the convection cells are shown. Due to the effects of the physical domain size, we observed irregular cells rather than the regular hexagonal cell.

Chapter 7 Numerical simulation of electroconvection in insulating liquids induced by unipolar injection: flow structure

In chapter 5, we discussed the flow structure of electro-convection in the finite amplitude regime which means T parameter close to the linear and nonlinear stability criteria. In this chapter, we shall maintain our focus on the flow structure of electro-convection between two parallel plates. Emphases will be put on the stabilizing role of the diffusion mechanism for charge transport, the successive instabilities and the way to the chaotic state and flow structure in a 2D box.

7.1 Role of charge diffusion for strong injection

Diffusion is the third transport mechanisms for charge density besides drift and convection. Considering the small coefficient of charge diffusion, it is a common practice to neglect this transport mechanism. The complete conservation equation of charge density can be expressed as,

$$\frac{\partial q}{\partial t} + \nabla \cdot \left(q\left(\vec{E} + \vec{U} \right) \right) = \alpha \nabla^2 q \qquad (2\text{-}17)$$

where α is the nondimensional diffusion coefficient, with a typical value between 10^{-3} and 10^{-4}.

From the theory of partial differential equations, neglecting the diffusion term change Eqn.(2-17) from a second-order elliptic type to a first-order hyperbolic one. To close the system, one more boundary condition is required for the elliptic equation than for the hyperbolic one. For charge density equation, this extra condition specifies how the charge is removed from collecting electrode, i.e., ejection law. Here we use the same zero-slope method,

$$\frac{\partial q}{\partial y} = 0 \quad \text{at} \quad y = d$$

In the numerical simulation, there is some numerical diffusion due to physical and temporal discretization schemes. Even without the physical diffusion term, we actually compute a hyperbolic equation with numerical diffusion. The only difference is the amplitude of the diffusion coefficient.

Let us recall the charge density distribution we obtained in the previous content, see Figure 5-12(d), 5-17(d). There is always a region containing a small amount or no charge. In addition, the transition between the two regions is not smooth but with sharp gradients. The formation of the charge-free region is due to the drift mechanism. As there is no physical diffusion term, the few charge carriers in the void region can only escape from the upper electrode. When taking into account the diffusion mechanism, the boundary between the two regions tend to be smoothed out along with the increase of α. Then it is natural to reach a qualitative conclusion: if the physical

diffusion is neglected completely, all theoretical estimations of the finite-amplitude electro-convection, the nonlinear criterion and hysteresis loop are greatly overestimated.

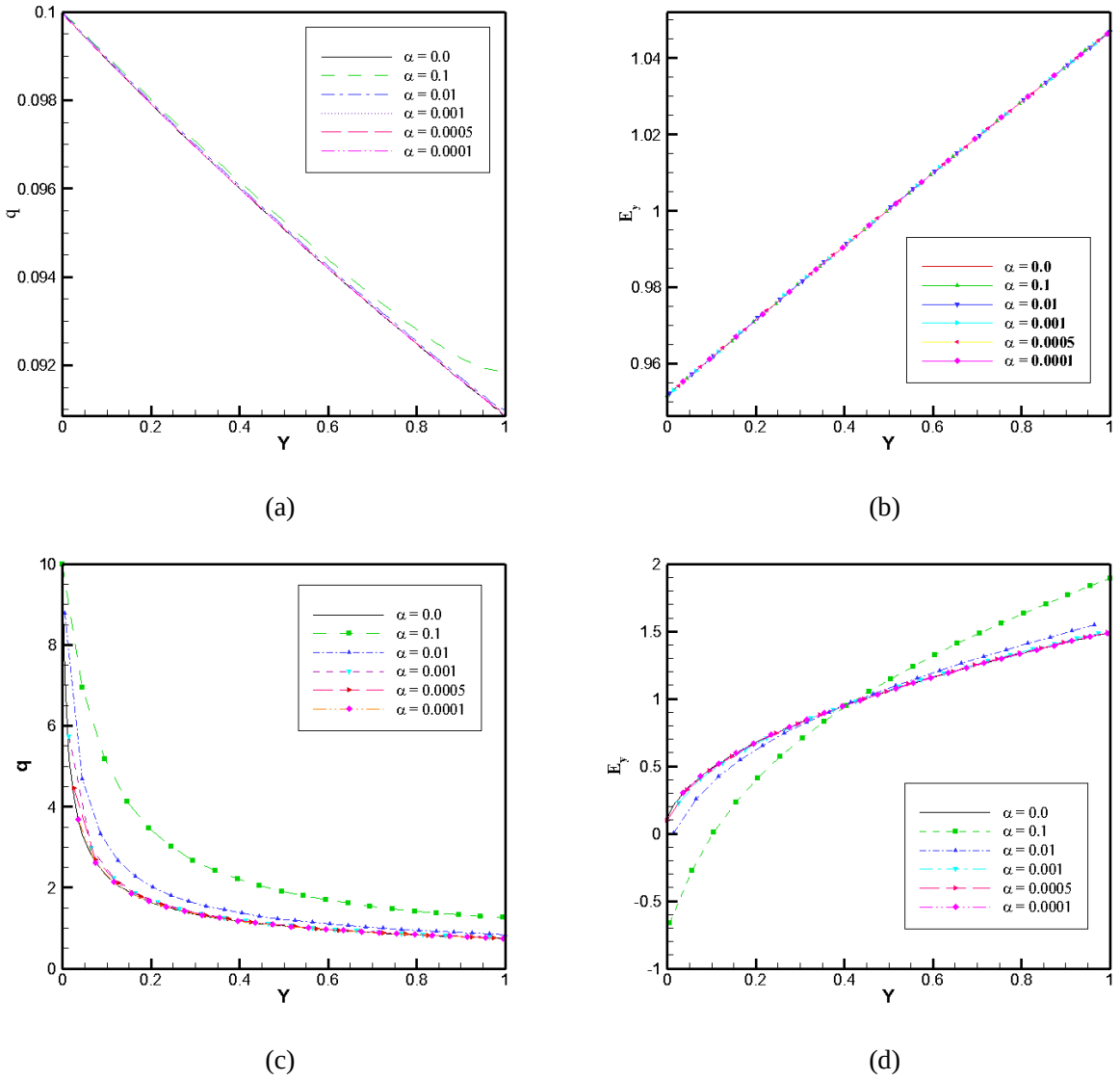

Figure 7-1. Charge density and electric field in the steady hydrostatic state for weak (C=0.1, (a) and (b)) and strong (C = 10.0, (c) and (d)) injection with various diffusion coefficients

In [88][152], Pérez and Castellanos discussed the role of the charge diffusion in finite-amplitude electroconvection of weak injection both analytically and numerically. Some conclusions for the weak injection cases have been made,

1. Diffusion stabilizes the system, increasing substantially the non-linear criterion and reducing the subsequent amplitude of the electro-convection. However, the linear stability criterion is not affected by the appearance of diffusion under weak injection condition.
2. The charge density distribution depends on the balance between Coulomb repulsion and diffusion. A new parameter $C/\alpha^{\frac{1}{2}}$ can be defined to measure the relative importance of both mechanisms. For small value of $C/\alpha^{\frac{1}{2}}$, the diffusion becomes dominant and cannot be neglected.

In the present study, we try to complete the analysis for strong injection case. The first motivation is to verify whether the above conclusions hold for the strong injection case or not. The main part of the numerical algorithm is the same with our solver for the case neglecting the diffusion term. We apply the 2nd order CD scheme to discretize the diffusion term. To limit the numerical diffusion, all results presented in this section are based on a 101×201 uniform grid.

First, we compared the hydrostatic solution of weak and strong injection cases with various diffusion coefficients. The numerical results are summarized in Figure 7-1, showing the charge density and electric field distributions. For the weak injection, a very small change due to the introduction of physical diffusion is observed; see Figure 7-1 (a) and (b). The distinguishable difference can only be seen in the charge density figure with $\alpha = 0.1$. In contrast, the change with strong injection is obvious, even with $\alpha = 0.01$; see Figure 7-1 (c) and (d). From this comparison, we may expect that the diffusion mechanism may play a more prominent role in strong than weak injection. In the next step, the steady solutions with convection are compared.

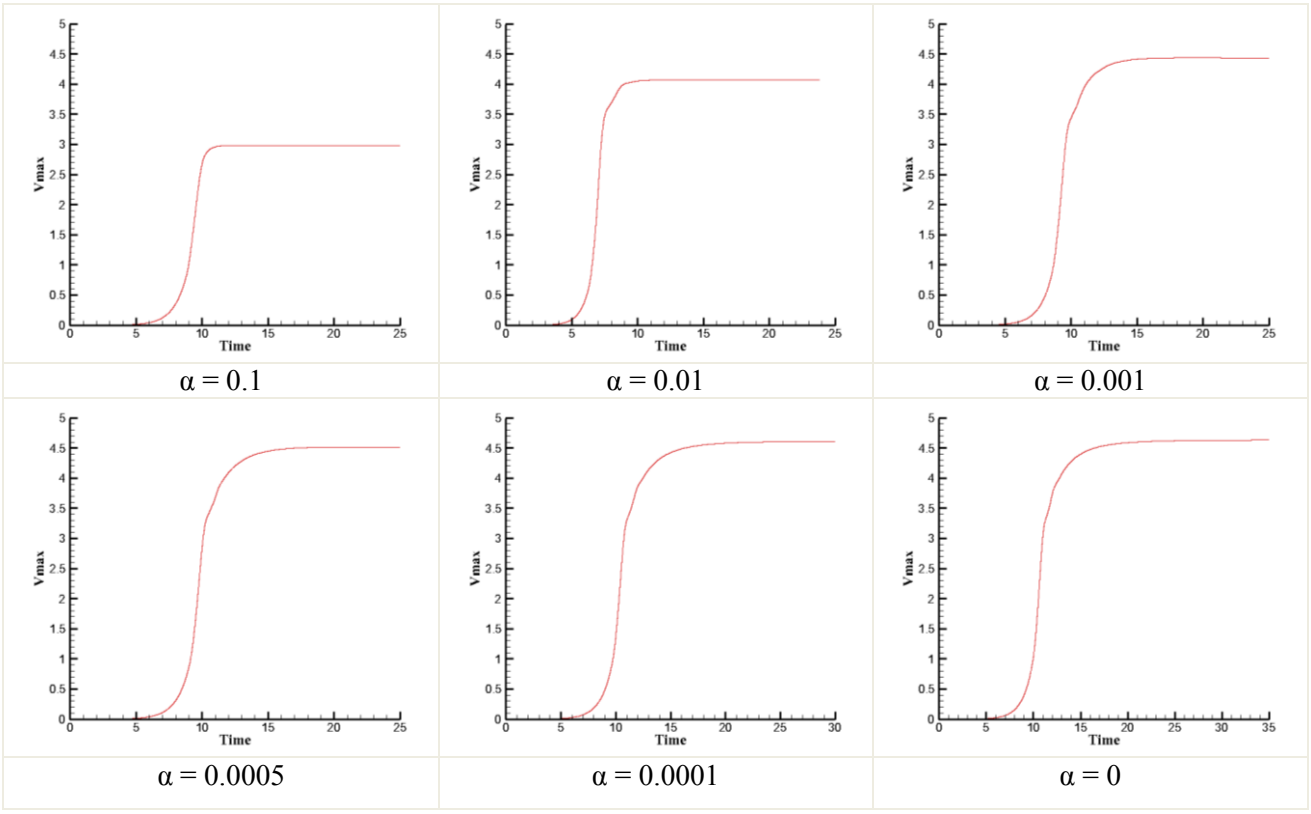

Figure 7-2. Time evolution of the maximum vertical velocity component with different α

Through gradual increase of the diffusion coefficient, we try to figure out the general rules how the system behaves with diffusion coefficient. Five values are selected and the typical value range [10^{-4}, 10^{-3}] is included.

In Figure 7-2, we have plotted the evolution of the amplitude of the velocity field versus the time for different diffusion coefficients. It is clear that all systems follow the same routine to a final steady state, i.e., an exponential evolution after the hydrostatic period. The only difference is the value for the velocity amplitude of final steady state. In Figure 7-3, we listed the maximum vertical velocity component at steady state with different diffusion coefficients. It is found that the amplitude decreases with the increase of the diffusion coefficient, which is consistent with the

conclusion obtained with weak injection case. In addition, when $\alpha \leq 10^{-3}$, the decline becomes fairly small.

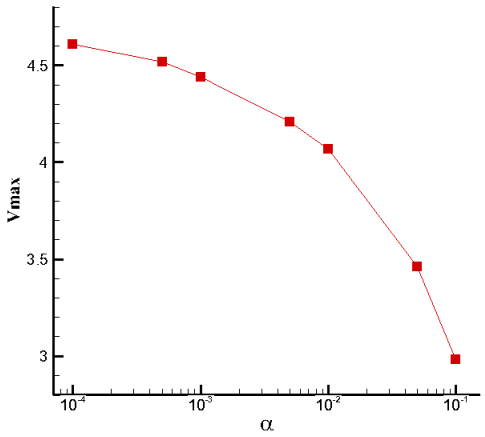

Figure 7-3. The maximum vertical velocity component at steady state with different diffusion coefficients α for a strong injection; Parameters: T = 240, C = 10, M = 10

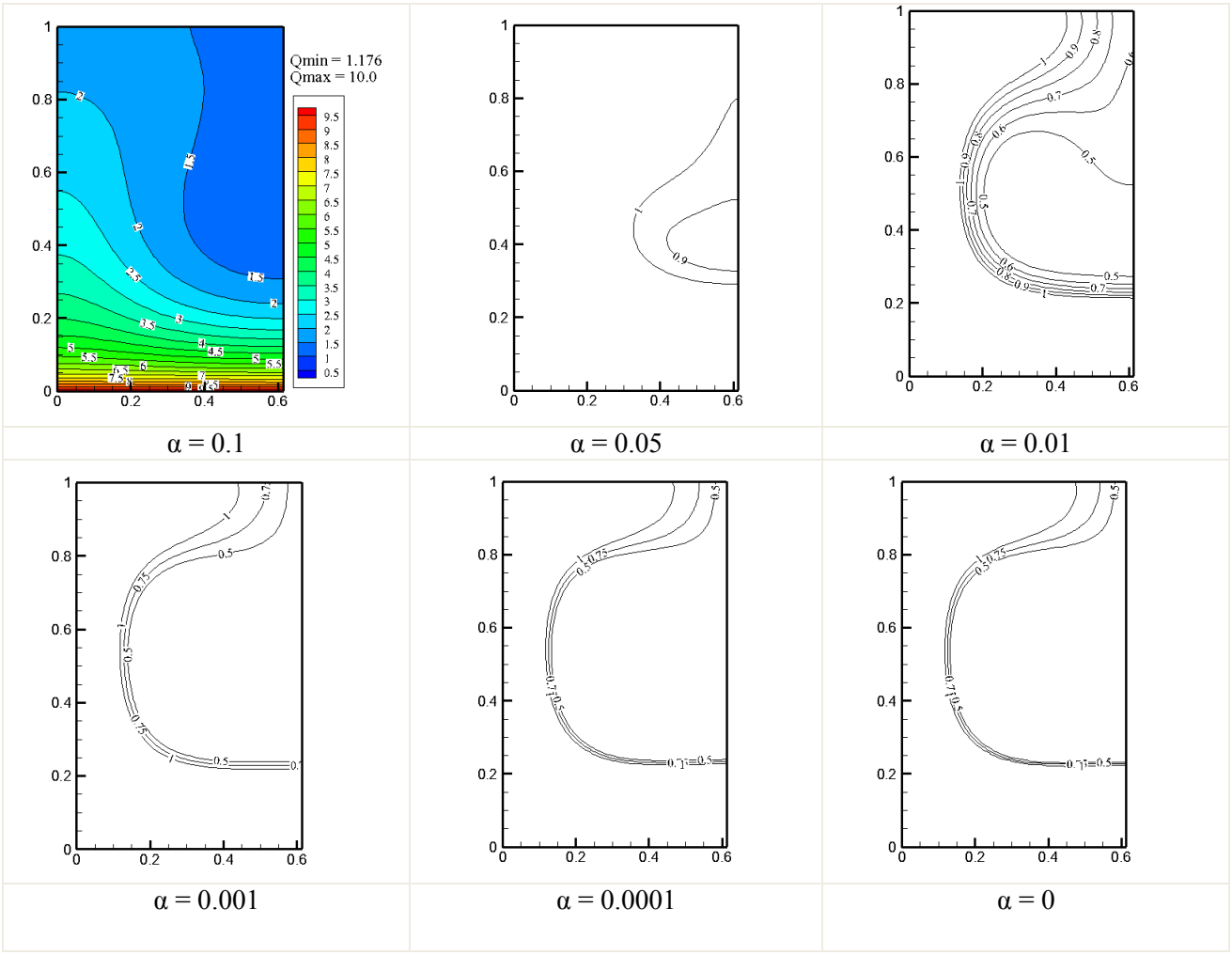

Figure 7-4. Charge density distribution with different non-dimensional parameter α;
Parameters: T = 240, C = 10, M = 10;

In Figure 7-4, we plotted the charge density distribution of various systems at final steady state. Here, we focus on the transition between the void region free of charge and the charge-covered region. Some characteristics and rules can be summarized:

1. Along with the increase of α, the area of charge free region decreases. For $\alpha = 0.1$, the minimum value of the charge density is 1.176, and we can regard that the charge-free region does not exist in this case.
2. By checking the area between iso-lines with value of 0.5 and 1.0, we find that the transition also becomes smoother with the increase of α .
3. The solutions for α = 0, 10^{-3} and 10^{-4} follow the above laws. However, solutions are almost the same with slight difference.

As we have explained that the area and shape of the free-charge region is closely linked with nonlinear stability criterion, we show the non-linear criteria and their associated hysteresis loop obtained for different α in Figure 7-5.

We noticed that the linear stability value depends on α, which is opposite to the conclusion for weak injection case. Then we can reach a conclusion that the critical value T_C depends on the strength of injection C and also on the value of diffusion coefficient for the case of strong injection (see Table 7-1), which can be understood with the high charge gradients present in the stationary solution. This conclusion may help to partly explain the difference between the distinction between the analytical and experimental linear stability values in SCLC regime.

We also see that diffusion stabilizes the system, decreasing the linear stability criterion, increasing the nonlinear stability criterion and reducing the subsequent amplitude of electro-convection. Comparing with weak injection, the effect of diffusion is more important in strong injection case if we consider the decisive parameter, $C/\alpha^{\frac{1}{2}}$.

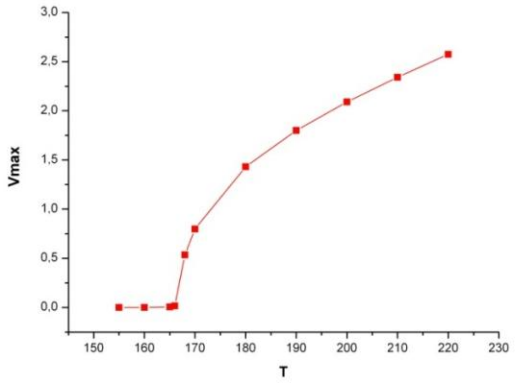

(a) $\alpha = 0.1$

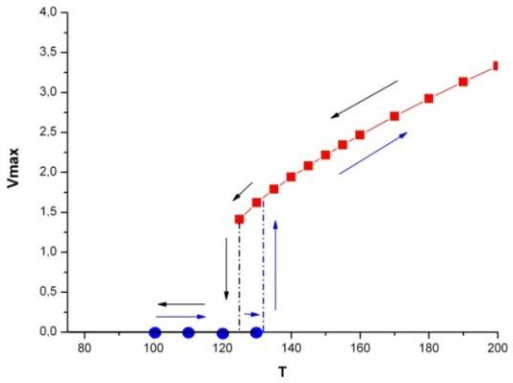

(b) $\alpha = 0.01$

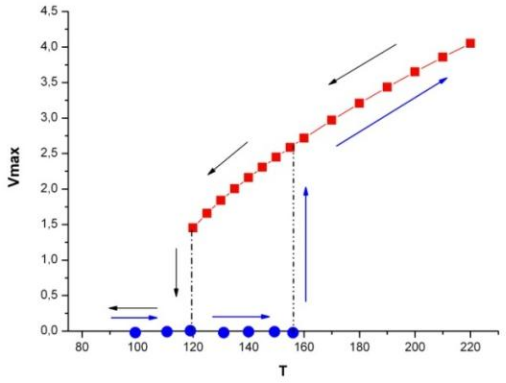

(c) $\alpha = 0.001$

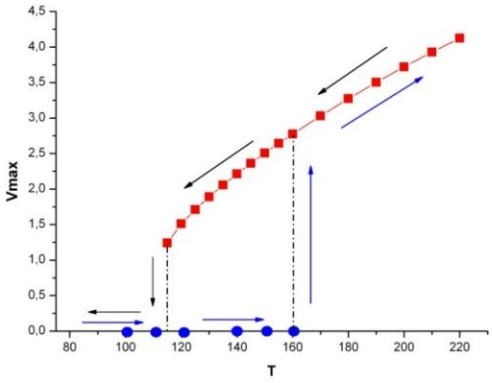

(d) $\alpha = 0.0005$

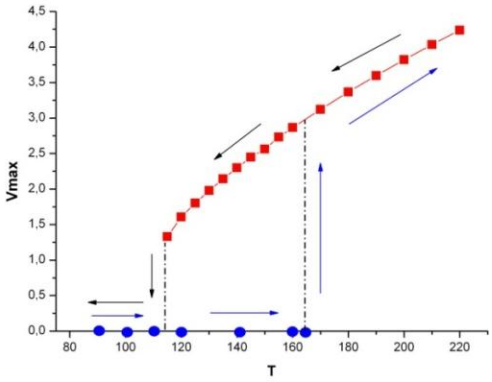

(e) $\alpha = 0.0001$

Figure 7-5. Hysteresis loop for a strong injection system, C=10, M=10. Noted that α=0.1, the hysteresis phenomenon disappeared;

Table 7-1. Linear and nonlinear criterion for strong injection (C=10) system with various diffusion coefficients

α	0	0.01	0.001	0.0005	0.0001
T_C	164.1*	135.8	155.7	159.8	163.8
T_f	111.7	[122, 123]	[117, 118]	[112, 113]	[111, 112]

* is the analytical value; -- means no existence;

7.2 Bifurcation studies for strong injection

The nature of the transition to turbulence is a basic question in fluid mechanics. For two-dimensional problems, it is more correct to use the concept ‘chaotic’ than ‘turbulent’ which is virtually linked with three-dimensional characteristics. Similar to Rayleigh-Bénard flow, the unipolar injection system tends to display an increasing degree of complexity as *T* is increased no matter what kind of boundary condition is applied to vertical sidewalls. In this section, we only consider the case of strong unipolar injection between two infinite horizontal plates, thus symmetric boundary condition will be used.

For simplicity, we are trying to answer the question: ***what will happen to the system if we increase T value?*** This simple question is essentially equivalent to define the transition route towards chaos under supercritical conditions in unipolar injection system. Our objective is to numerically exhibit the cellular development and the rich bifurcation route to chaos with the strong unipolar injection system. The same strong injection system (C=10, M=10) will be used as the representative example.

In [67], Vazquez et al., investigated this problem for the first time with their FE-PIC method. They found that an oscillatory two-roll structure was developed at T=400, T=500. In their numerical results, the solution of T=300 is still a well-developed one-cell structure. In a very recent publication [56], Traoré and Pérez firstly observed the same two-roll but steady structure at T = 300. Some other important observations are summarized below,

1. They noticed that the flow started to oscillate periodically in time and space at T=260 for the first time.
2. Steady two-cell structure are kept till T=500.
3. Above T=500, the two convective cells again start to oscillate and the regime becomes unsteady but still periodic.
4. Above T=1500, the unsteadiness of the flow is more pronounced and a new regime characterized by the appearance of plumes arises.
5. Further increasing T, the flow becomes fully unsteady and electro convective plumes are generated more frequently.

It should be noted that if the flow regime is unsteady, the numerical results normally are very sensitive to the spatial and temporal discretization steps. As the grid and time step information in [56][67] are not clear, it is believed that the numerical diffusion is the reason for the difference between these two references. In the present study, we use a very small grid size and time step to reduce the effects of numerical diffusion. All the numerical calculations are based on a 101 × 201 uniform grid and a 10^{-4} time step. The emphasis of this section is to complete the study of [56] with the quantitative analysis of the amplitude spectra information.

7.2.1 Flow structure for moderate values of T parameter

With the gradual increase of T till 260, the flow keeps the same structure (steady one-cell) as at T=200 (see Figure 7-6). At T=260, we noticed that the flow started to oscillate periodically with a single basic frequency in time and space. The oscillation can be highlighted though the periodical variation of the charge density distribution, see Figure 7-7.

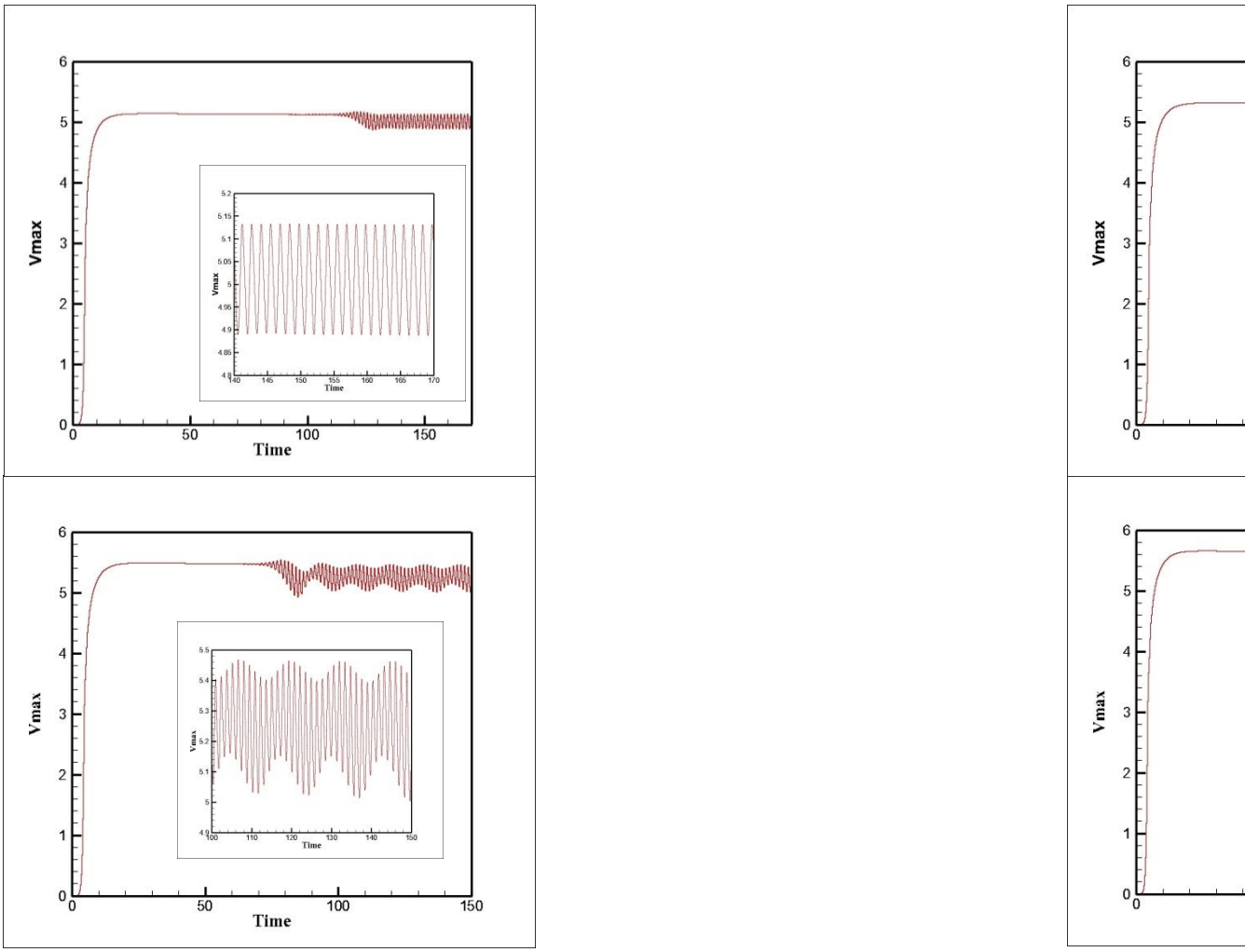

Figure 7-6. Evolution of the maximum vertical velocity for strong injection with C = 10 M = 10 with time (top left) T = 260, (top right) T = 270, (down left) T = 280 and (down right) T =290

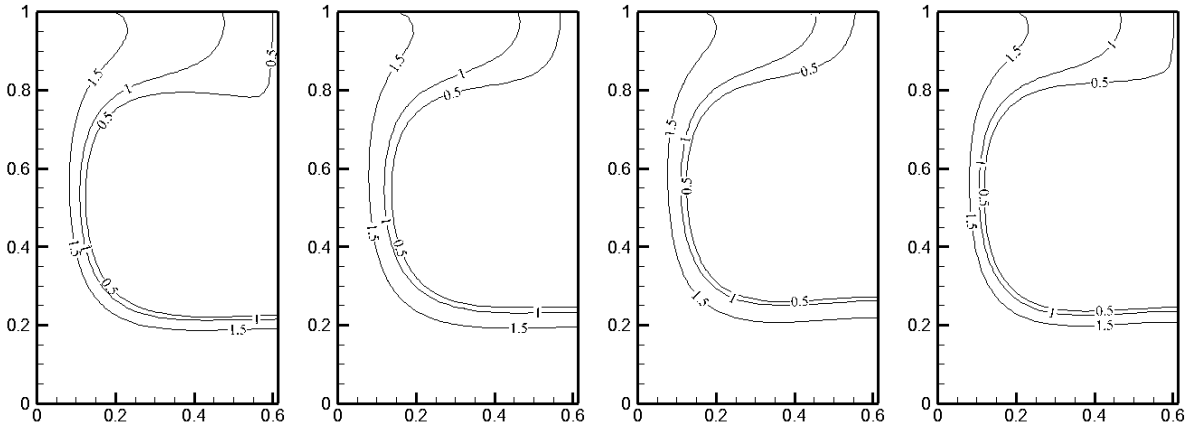

Figure 7-7. Charge density distribution of a periodic cycle of a strong unipolar injection system (*C*=10, *M*=10) with *T*=260. To highlight the difference, only contour lines between [0.5, 1.5] were presented.

Considering the physical domain is only half of the critical wavelength, it is natural to ask if this bifurcation behavior corresponds to the classical symmetry breaking. A computation with the same system and T (260) value on a [0, 1.228] × [0, 1] domain was done to verify this viewpoint. By carefully checking the charge density distribution, the velocity and the potential field, we found that these values at any two points which are symmetric with the line $x = 0.614$ are always the same. The property can also be seen in the evolution of the angular momentum, see Figure 7-9. The constant zero value of AC in Figure 7-9 and the equality between the absolute values of ALa and AR at any time moment mean that the velocity field is highly symmetric with the central line, $x = 0.614$. Thus, this bifurcation does not represent a symmetry breaking behavior.

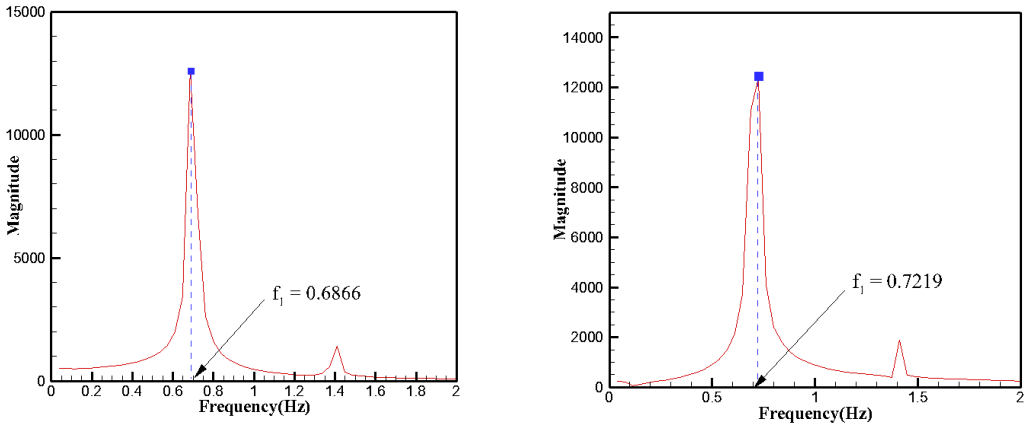

(a) (b)

Figure 7-8. Power spectral for C=10, M=10 (a) T=260 and (b) T=270

At T=270, the flow is still in regularly periodical regime, but with higher basic frequency and amplitude of oscillation, see Figure 7-6 and Figure 7-8. The simultaneous varieties of basic frequency and amplitude bring some difficulties to determine the onset of bifurcation with T number, if we assume that the onset of this bifurcation corresponds to a periodic flow with infinitely small amplitude and infinitely high frequency.

At T=280, the periodicity of the flow has been lost. Instead, a quasi-periodic bifurcation solution with two irrelevant families of frequencies is developed.

At T=290, we surprisingly find that the asymmetric flow returns to a symmetric state. However, the flow is no longer with one cell structure in the final state. The flow starts from the hydrostatic solution. After an exponential increase in the maximum of velocity amplitude, a steady one-cell state is reached, which is the same with a smaller value like T=240. Then this state slowly starts to oscillate before suddenly to switch to a new steady state which corresponds to a two cell structure. It is noticed that the two cells are highly symmetrical. The maximum difference between the absolute values of AL, AR at final steady state (see Figure 7-9b) is no more than 0.5 %. The number 290 is the smallest T value which shows the two- cell strucutre among all published literature. This is again due to the high accuracy of our numerical solver and the small grid size and time step we used.

To summarize, the flow structure of strong unipolar injection presents significant changes in a narrow region. The flow passes through four different regimes: steady one cell, periodic one cell, asperodic one cell and steady two cells.

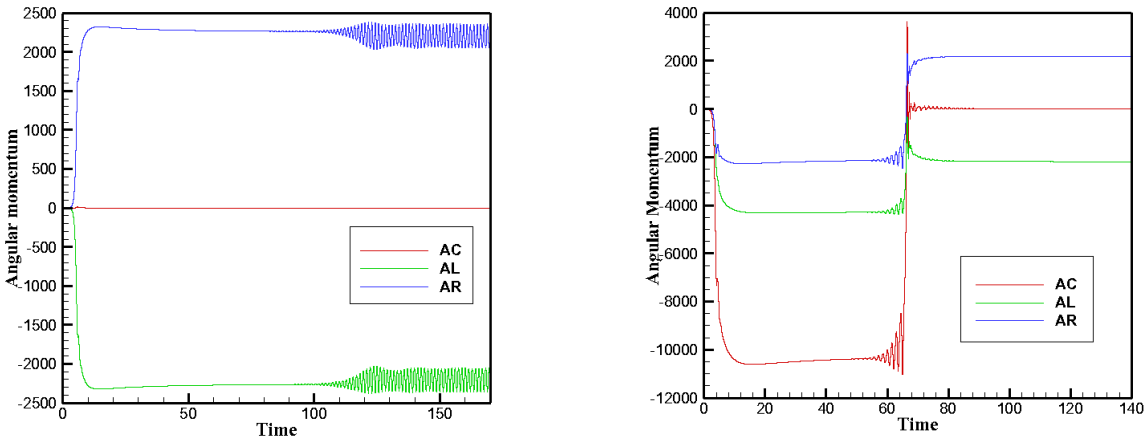

(a) (b)

Figure 7-9. Evolution of the angular momentum for C=10 M=10: (a) T=260, [0, 1.228] × [0, 1] domain; (b) T=300, [0, 0.614] × [0, 1] domain. AC, AL and AR stands for angular momentum with center point of the whole domain, the left half and the right half domain

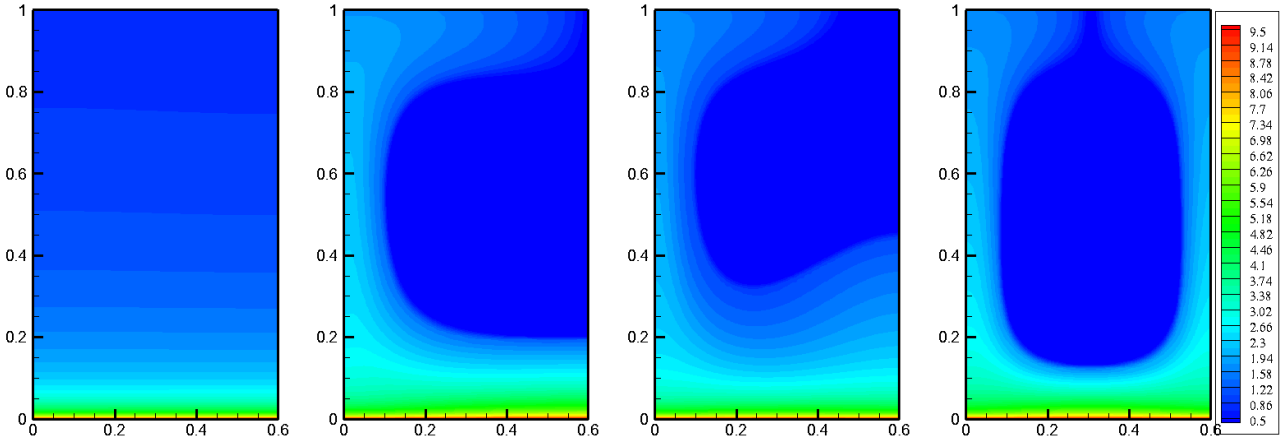

(a) (b) (c) (d)

Figure 7-10. Contour map of the charge density at different time steps to highlight the evolution routine from one cell to two cells (a) t = 1.0 (b) t = 45 (c) t = 70 (d) t = 100. Parameters: C=10, M=10, T=300

7.2.2 Flow structure for high values of T parameter and path for chaotic regime

Above *T*=485 the two convective cells start again to oscillate slowly and the solutions exhibit the periodic nature plotted in Figure 7-11. In the viewpoint of stability theory, the nonlinear system has evolved from the fixed critical point to the periodic attractor.

In Figure 7-11, we also plotted the power spectrum for the solution computed at T=485 and T=540. It was observed that the characteristics of the frequencies were the same. There is a basic frequency and several ultra-harmonic frequencies in each solution. It is interesting to notice that these frequencies strictly obey the following rules:

$$f_2 = 2f_1 \quad f_3 = f_1 + f_2 = 3f_1 \qquad f_4 = f_1 + f_3 = 4f_1 \qquad f_5 = f_1 + f_4 = 5f_1$$

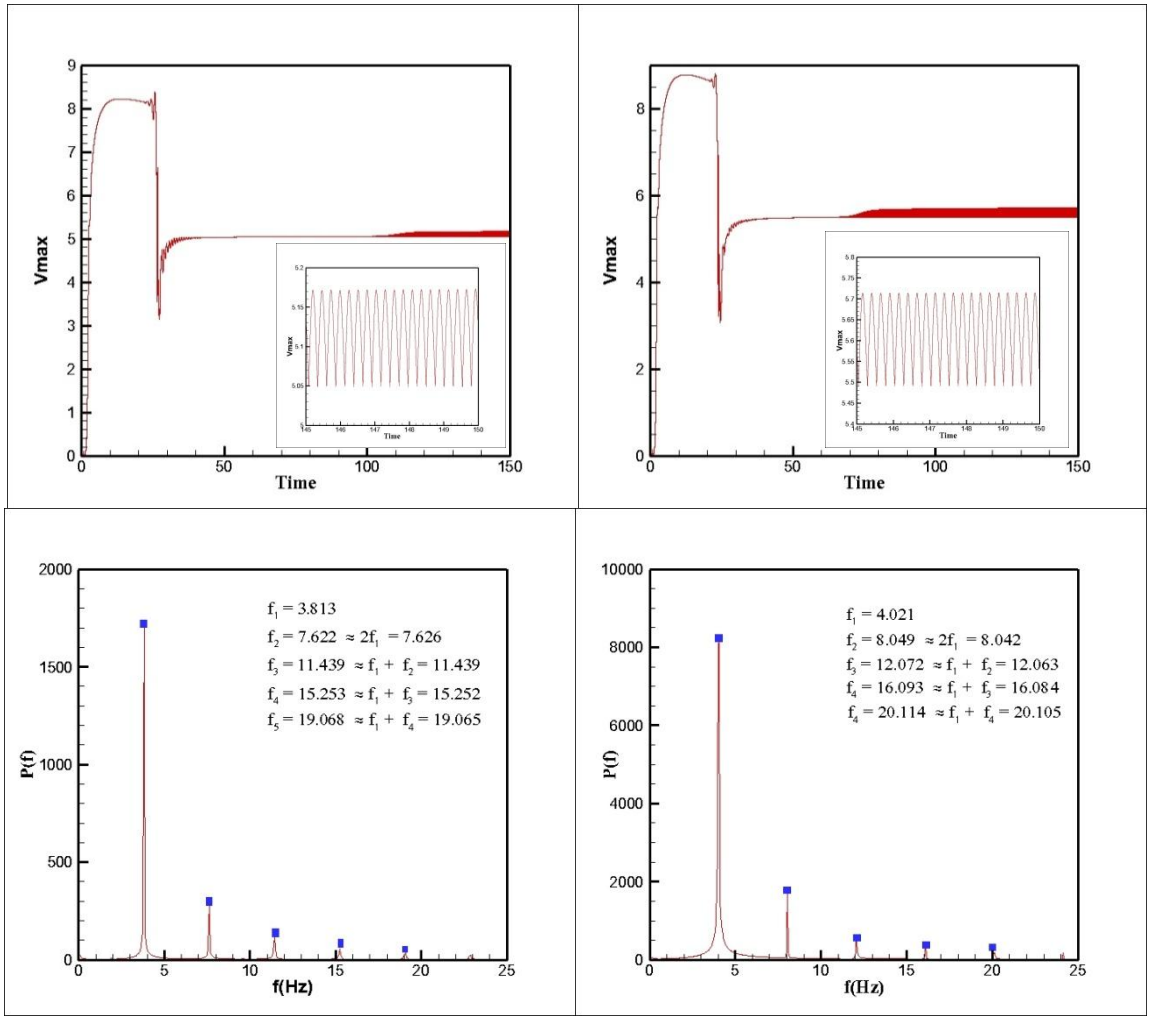

Figure7-11. Illustration of the evolution of the maximum velocity and corresponding power spectrum of T=485 (left) and T=540 (right); Parameters: C=10 M=10; 101 × 201 grid and 10^{-4} time step;

It is noted that the above relationship can be summarized as

$$f_m = f_1 + f_{m-1} = mf_1$$

which is well-known in nonlinear system theory [286].

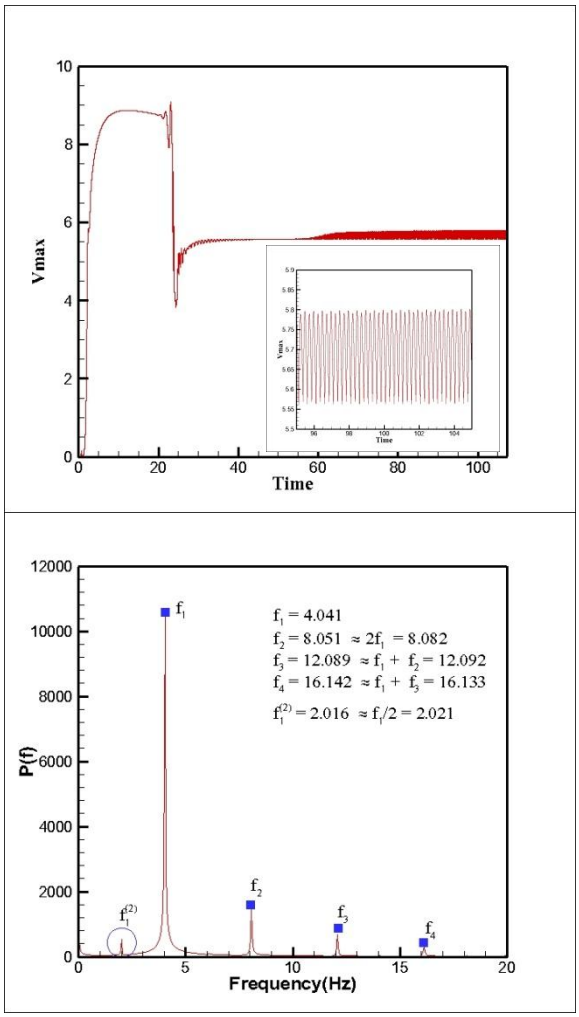

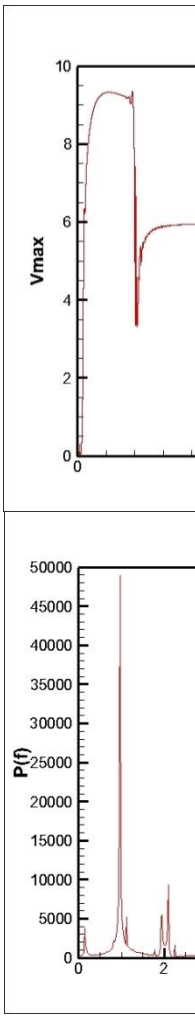

Figure 7-12. Illustration of the evolution of the maximum velocity and corresponding power spectrum of T=550 (left) and T=600 (right); Parameters: C=10 M=10; 101 × 201 grid and 10^{-4} time step;

The differences between the two sets of solutions are the time-average velocity, the basic frequency (f_1) and that the amplitude of the oscillations increases with the T parameter. Till now, we have not found a general law between the basic frequency and T value like linear or quadratic in the range [485, 540]. Thus, it is difficult to determine the onset of this bifurcation behavior.

When the electrical stability parameter is increased to T=550, the periodic nonlinear system is split into the one having two irrelevant familiars of frequencies, see f_1 and $f_1^{(2)}$ in Figure 7-12. For f_1 , it seems to follow the same increasing law as the previously predicted basic frequency between 485 and 540. The other newly born harmonic frequency $f_1^{(2)} = 2.016$ is very close to $f_1/2$. We think this is a sub-harmonic frequency related with the fundamental one. Sub-harmonic frequency denotes the frequency that is below the fundamental frequency of an oscillator and can be expressed as f_1 / m where $m = 1,2,4,8,\cdots$[286].

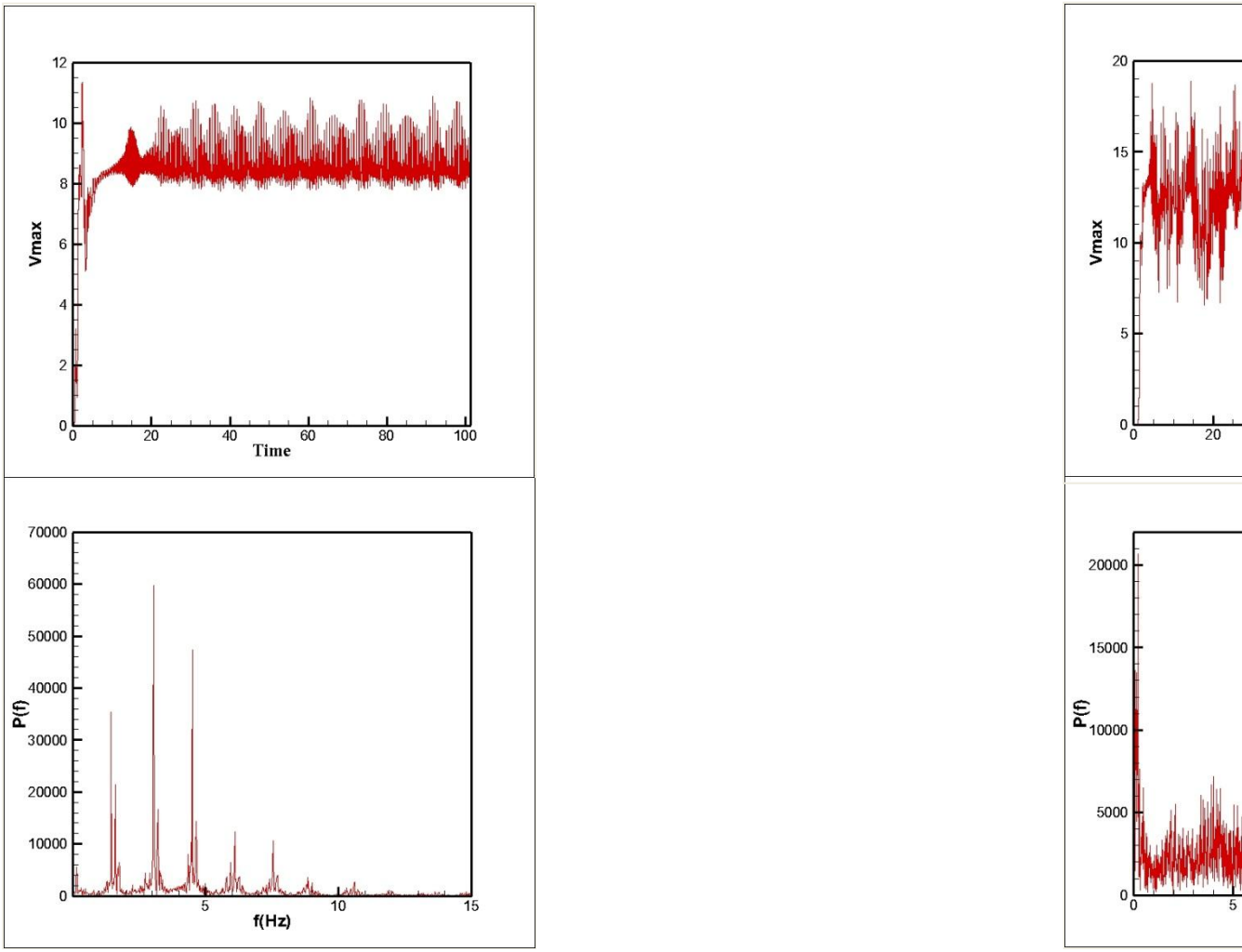

Figure 7-13. Illustration of the evolution of the maximum velocity and corresponding power spectrum of T=1000 (left) and T=2800 (right); Parameters: C=10 M=10; 101 × 201 grid and 10^{-4} time step;

By considering both the appearance of the new peak in the spectrum and the fact that the limit cycle is made of two loops, the system reaches a period-doubling bifurcation.

In the next set of plots with T = 600 and T = 1000 (Figure 7-12 (right) and Figure 7-13(left)), this tendency is even clearer with the appearance of other peaks. The attractor becomes smoother and smoother, although keeping a pseudo-periodic structure.

Finally, the flow will enter into a chaotic regime from the quasi-periodic regime. It is not easy to strictly define the starting value for the chaotic state as the appearance of new peaks (sub-harmonic frequencies) and other related ultra-harmonic frequencies is continuous. Taking solution at T=2800 for example, it is found that the power spectrum does not show any sharp peak, but a smooth bump around $f_1 \approx 4.0\,\mathrm{Hz}$, see Figure 7-13 (right). By converting the power spectrum figure into the semi-log style, it is easy find that the power spectra exhibits a well-defined exponential decay $\exp(-f / f_C)$ in the range between f_1 and the further limit where the power reaches the noise level introduced by the numerical round-off error, see Figure 7-14. The broadband spectra qualitatively agrees with the physical experimental results and can also be viewed as a characteristic when the system is in the chaotic regime.

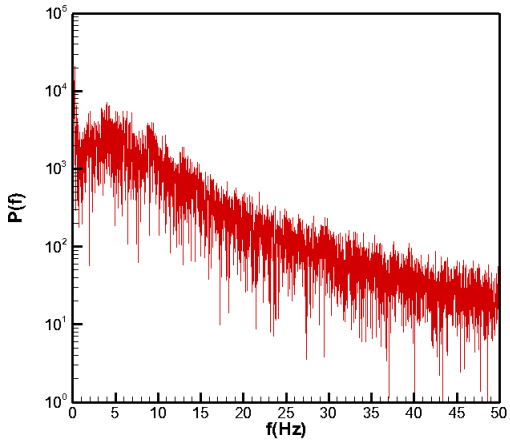

Figure 7-14. Power spectra of velocity fluctuation of solution with a strong injection system (T=2800, C=10, M=10) in semi-log style, the same data with Figure 5-52(right).

Though the physical experiments with strong injection has been done in a wide range of voltage, $[0,200U_C]$, it does not make sense to compare our frequency information obtained with $T < T_t$, where T_t denotes the critical transition value between the quasi-periodic and the chaotic regimes. Experimentally, it has been found that the liquid passed directly from rest to time-dependent (periodic) motion if U overtakes the critical voltage U_C. Then a second frequency and a bi-periodic motion state were found at U slightly above U_C. It should be emphasized that the physical reasons of this periodic and bi-periodic motion have not been well explained yet. The periodic flow after T=485 (C=10, M=10) and the bi-periodic flow after T=550 (C=10, M=10) we found numerically represent the essential property of this nonlinear system. However, it is interesting to find that the obtained numerical solutions in 2D chaotic regime and the physical solutions in 3D turbulent regime share some common features. In [56], the author noticed that the variation of the frequency of the main peak f_0 of the velocity fluctuation with solution at T higher than 3000 is linear with respect to T value, which well agrees with the law extracted from physical experimental results.

Through careful examination of the charge density distribution at the starting period of the solution at T=1500, it is interesting to find some electro-plumes in the domain. These plumes are different from the ones formed with blade-plate or line-source injection structure. Under these configurations, the motion starts at the first beginning after the charge is injected into the system because of the non-symmetry of the physical system. A feature common to these circumstances is the existence of local regions where the charge density distribution is higher than that of the surroundings. The typical problem of EHD plume between a blade injector or a line source and a flat plate has been thoroughly investigated experimentally [150], theoretically [38][39] and numerically [139][287]. Our numerical solver can be easily applied to problems with a point-plate configuration, a simple example is provided in Figure 7-15. In this simulation, the laminar and stationary motion between a single point injection source and a flat plate are presented. One can note that the boundary condition for charge density variable is no longer homogeneous but with a single non-zero value at the central point in the bottom plate.

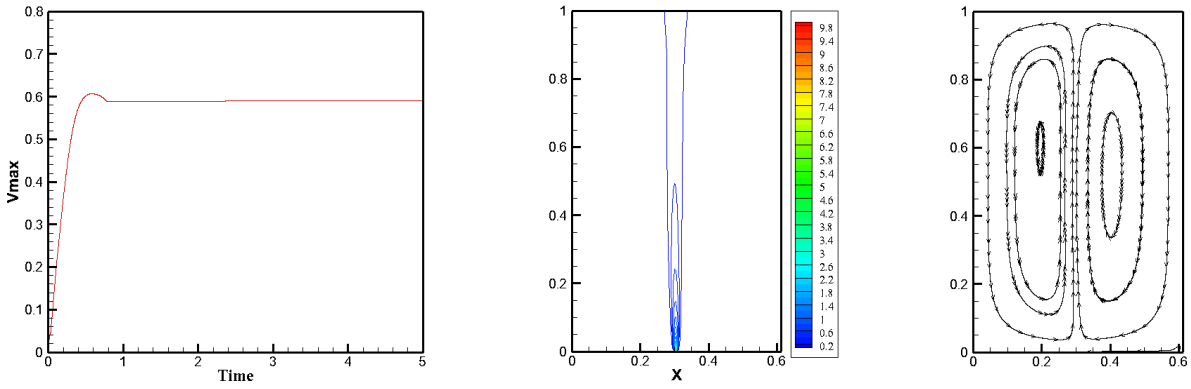

(a) (b) (c)

Figure 7-15. EHD plume between a blade-plate configuration (a) the time history in dimensionless unit of the maximal vertical velocity; (b) charge density distribution (c) streamline function at final steady state; Parameters: C = 10, M=10, T = 2000, $\alpha = 5\times10^{-4}$; [0, 0.614] × [0, 1] with 101×201uniform grid system; wall boundary condition for vertical sides [274];

In the present study, we successfully exhibit the electro-plumes induced by homogeneous boundary condition for charge density. The appearance of the electro-plumes comes as no surprise as the thermal plumes under homogeneous thermal boundary condition are well-known phenomena. A schematic flow example for thermal plume and electro plume are presented in Figure 7-16. It is easy to find the multi thermal plumes are formed at both heating and cooling walls, while electro-plume can only be formed at the injecting plate. This difference was qualitatively analyzed by P. Atten *et al.* in [276], and we highlight it with the numerical simulation. It should be noted that the difference of the number of plumes in the domain in not an essential characteristic. In fact, if we further increase *T* number which corresponds to higher voltage difference, we find more electro-plumes.

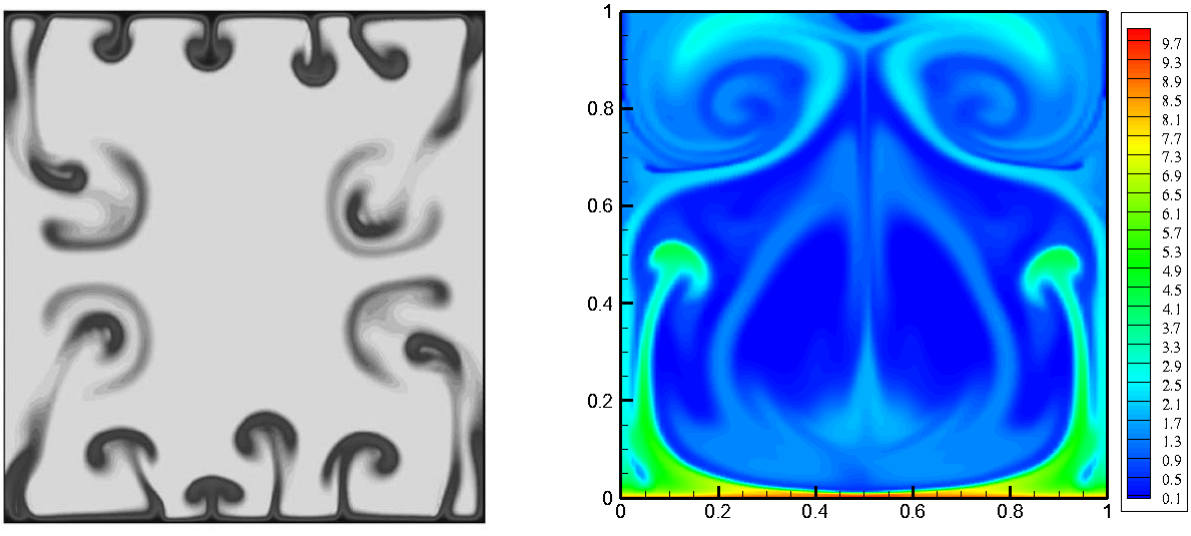

(a) (b)

Figure 7-16. (a) Early stage of Rayleigh-Bénard convection (Pr = 15, A = 1, $Ra = 10^8$) with adiabatic lateral walls [288]; (b) Early stage of electro-convection (C = 10, M = 10, $T=10^4$) with lateral walls;

In the next, we make a simple description of the electro-plumes with the solution at T=4000. The results presented in Figure 7-17 were computed with zero-initial field and symmetric vertical boundary conditions for velocity. An important characteristic is that the hydrostatic solution state has never been reached, which can be verified from the time history curve. It is noticed that the motion quickly started after the injection. At *time = 0.35*, the contact surface between the charge covering and charge free regions is no longer a horizontal line. Then from *time = 0.35* to *time = 0.75*, some plumes were formed and developed at this contact surface. Later, the plumes were formed and detached from the injecting plate intermittently. The appearance of these plumes should be due to the destabilization of the laminar sub-layer near the surface [56].

Similar to thermal plumes in Rayleigh-Bénard convection, the electro-plumes regimes may play a crucial role in real flow structures. On the one hand, the critical T value for the appearance of the electro-plumes is about $12T_C$, which is easily satisfied under experimental condition. On the other hand, the electro-plumes are responsible for much of the charge transport. Thus, some more studies should be done to classify the dynamics of electro-plumes and related regimes of motion.

Till now, for a given strong injection system (C=10, M=10), we successfully defined the way to chaotic state with our numerical tool.

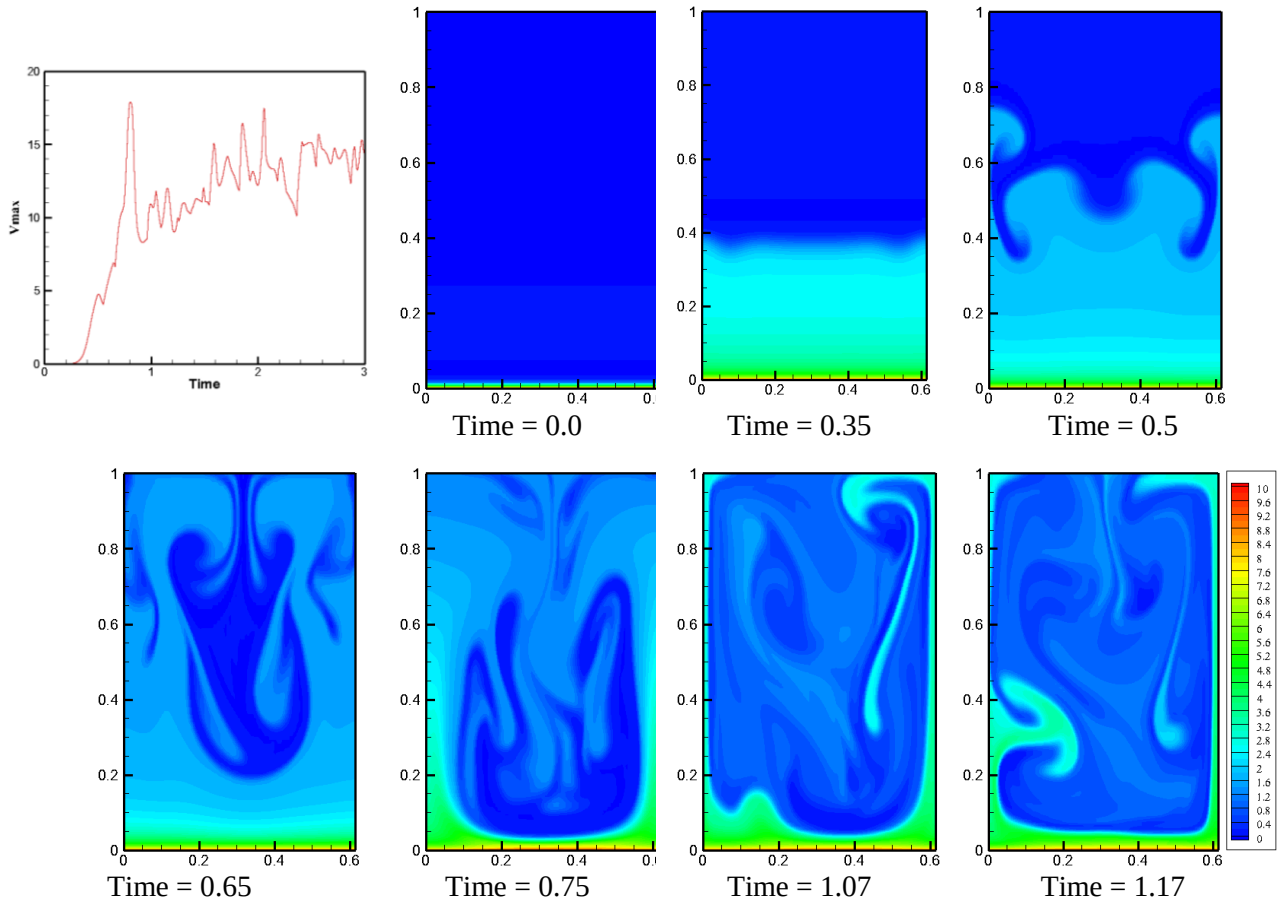

Figure 7-17. Evolution of the electro-plumes for C = 10, M = 10, T = 4000; 101 × 201 uniform grid and the time step is 10^{-5}; the first curve is time history of *Vmax*;

7.2.3 Effects of charge diffusion and M parameter on flow structure

Though the linear and nonlinear stability criteria are not seriously affected by small diffusion coefficients ($\alpha \in [10^{-4}, 10^{-3}]$) and M value in strong injection system, the bifurcation behaviors and their corresponding critical values at higher T ($T > 240$) strongly depend on α and M. In addition, the initial field may also dramatically change the unsteady solutions. Three examples are provided here as a prelude for future research to systematically illustrate the detailed effects.

In the first case, we compute a strong injection case with small diffusion coefficient for charge transport. Solutions are presented in Figure 7-18.

We noticed that the flow is still in steady one-cell structure flow regime. Generally, the charge diffusion tends to stabilize the flow and prevent the appearance of further bifurcation. This is consistent with the fact that the same bifurcation phenomena would happen with a higher T when numerical diffusion increases with the grid size or time step. In the second test, a series of calculations were performed with $M = 50$. Some main results are summarized in Figure 7-19.

Through the comprehensive analysis of solutions of electric and velocity fields, some general features can be summarized:

1. Overall, the system with M=50 follows a similar way to the chaotic state as for M=10: no motion → steady one cell → steady two cells →periodic → pseudo-periodic → chaotic.
2. From the stage of steady one cell to steady two cells, the transition of M = 50 system is different from what we observed with M=10. We did not find the periodic or pseudo-periodic oscillation.
3. The critical values for the transition from one-cell to two-cell structures and from steady two-cell structures to a periodic state are separately in the ranges [330,340] and [600, 650], which is for both higher than the ones we found with M=10 case.
4. However, once the flow becomes unsteady with oscillations, the amplitude of the oscillations are much higher than in M=10 case. The increase of the oscillation amplitude can be explained with the physical meaning of the M parameter.

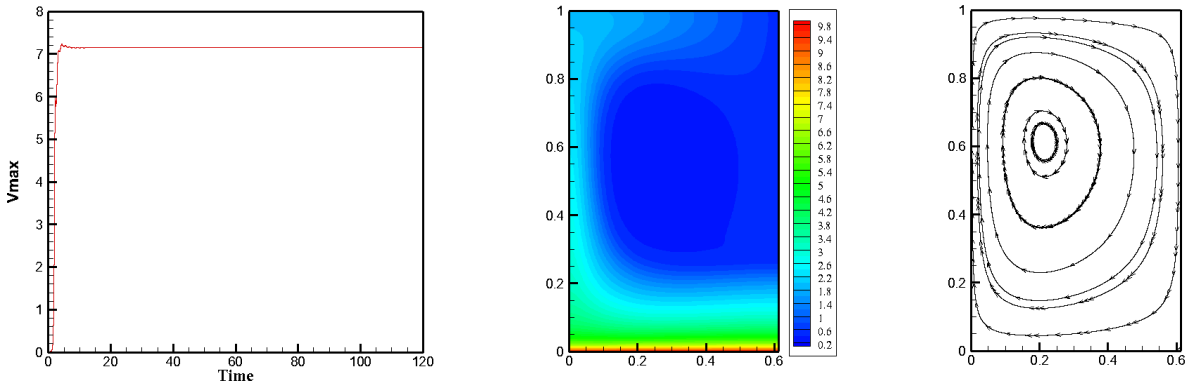

(a) (b) (c)

Figure 7-18. Numerical results with a strong injection system; (a) time evolution of the velocity amplitude; (b) charge density distribution and (c) stream function of the steady state; Parameters: T=500, C=10.0, M=10.0, $\alpha = 5\times10^{-3}$;

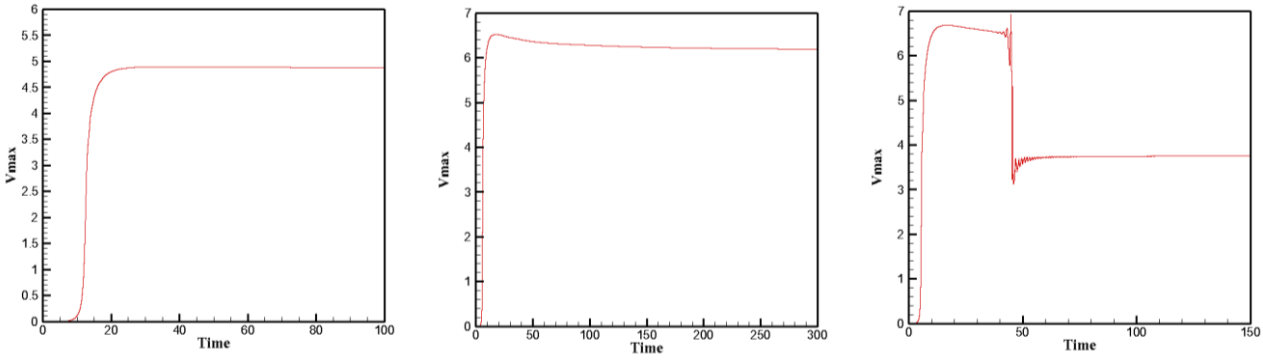

(a) T = 240 (b) T = 330 (c) T = 340

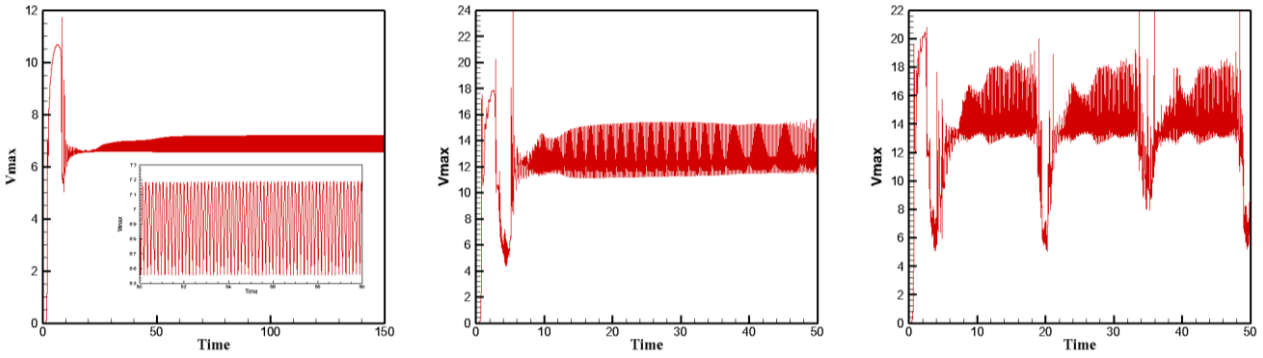

(d) T= 650 (e) T = 1600 (f) T = 2000

Figure 7-19. Evolution of the maximum vertical velocity with time for a strong injection system (C=10 and M=50) with various injection strength; starting from hydrostatic solutions;

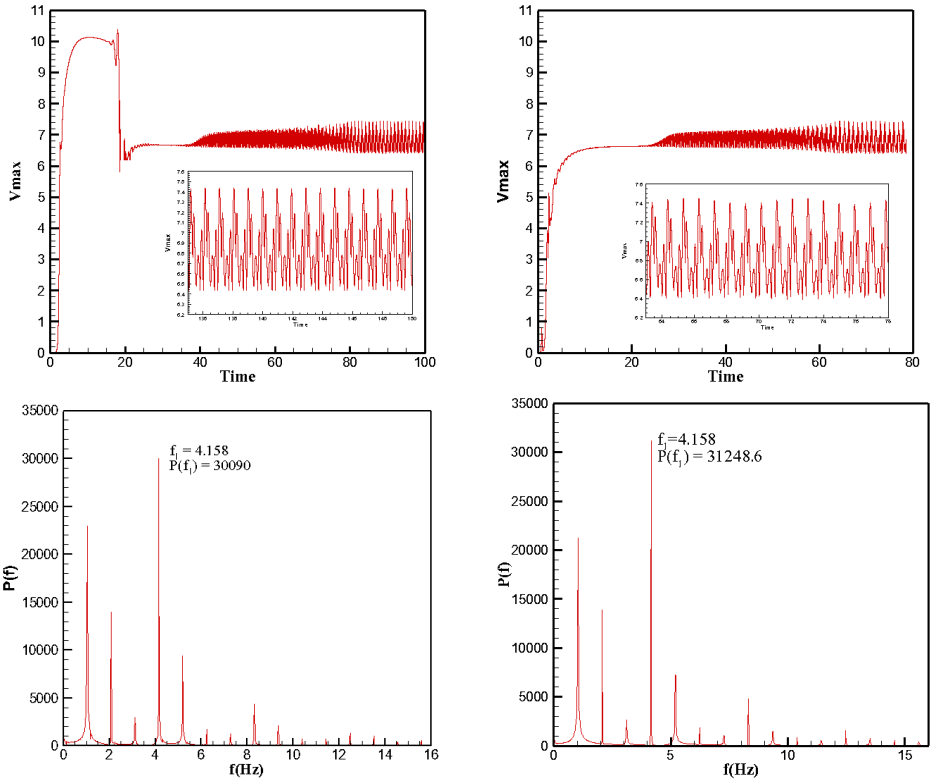

Figure 7-20. Illustration of the evolution of the maximum velocity and corresponding power spectrum of T = 700 (left) start from hydrostatic solution (right) start from zero-initial field; Parameters: C = 10 M =10; 101 × 201 grid and 2×10^{-4} time step.

From above solutions, we highlight the difference of bifurcation behaviors between the cases *M=10* and *M=50* under strong unipolar injection.

As explained before, the zero-initial and hydrostatic field represents different physical problems. It is well known that the final solution does not depend on initial field for steady case, while chaotic solution is very sensitive to changes in the initial conditions. In principle, highly regular oscillations are more or less independently on the initial conditions. Thus we present a case in the pseudo-periodic stage (*C*=10, *M*=10 and *T*=700).

From the above two sets of solutions, we firstly noticed that the ways to final state are different from each other. For the solution with hydrostatic initial field, there is a one-cell structure before *time = 20*. For the solution with zero-field, a two-cell structure is formed at the first beginning of the motion. Secondly, though the average values of *Vmax* at final pseudo-periodic stages of the two cases are more or less the same, there is a discernible difference between the power spectrum figures. Generally, the solution with zero-field is more chaotic than the one computed with hydrostatic solution, which agrees with our expectation. Starting from the zero-field implies a step injection and there exists a local velocity disturbance (see inset figure in Figure 5-12). For small *T*, this disturbance will be damped out completely because of the viscosity of fluid. Then, a hydrostatic state is reached and the fluid continues to evolve to a new motion regime depending on *T* which is introduced by tiny numerical fluctuation. However, for high *T*, this disturbance will not be damped out completely and the fluid motion will occur. As the amplitude of the local velocity disturbance is higher than the one of the numerical fluctuation, a direct consequence is that the time to reach the final state is shorter for the case starting from zero-field. In addition, the more chaotic final state should also be due to this local velocity disturbance.

7.3 Electro-convection in a two-dimensional finite box: strong injection

In physical experiments, the lateral wall boundary conditions are more realistic. In this section, we will have a look at the influence of the lateral walls on the linear and nonlinear stability criterion and the overall structure of the flow pattern that develops when the T number exceeds its critical value.

The effective properties of electro-convection in a container of finite size depend on the related extensions along the different spatial directions (length, height and width). In the present study, only the two-dimensional enclosure will be considered. It is important to define a new non-dimensional geometry parameter

$$A = \frac{L}{d}$$

where L is the length of the horizontal electrode and d is the thickness between the two parallel plates.

In the theory of pattern formation in continuous system, it is known that even distant boundaries may have surprisingly important effects, which is the consequence of the breaking down of the continuous symmetries [288].

In the following, the vital role played by the presence of limiting lateral walls is discussed for the electro-convection due to unipolar strong injection. To run the simulation, the velocities boundary conditions for lateral boundaries are assumed to be of no-slip type. In RB problem, the thermal convection in an enclosure also depends on the type of thermal boundary conditions along the lateral walls, like conducting or adiabatic walls. The same arguments should also make sense for electro-convection problem. However, the reality is a little more complicated for injection problem as specific boundary conditions should be assigned for both charge density and electric potential. In the present study, we consider a case where the boundary conditions for electric potential and charge density are the same as shown in Figure 5-4. The parameters of the injection system are set as C=10 and M=10 or 50.

To systematically analyze the problem, two sets of computations were performed.

1. The ratio number A continuously changed from $A_{min}=0.4$ till $A_{max} = 5.0$. For this set of computations, our main concern was the law of the critical T number (namely T_C) varying with A value. Qualitatively, it is easy to understand that T_C with a small A should be higher than with a big A value since the lateral walls tend to stabilize and place extra constraint on the flow. In addition, we are also very interested in the flow structure for T slightly above T_C as it provides important information about the hysteresis phenomenon at the subcritical region. To maintain the same computational accuracy, the nodes in horizontal direction have been increased with A and the size of the control cell have been kept constant.
2. The ratio number A is fixed at 0.614. We gradually increase T to show the increasing degree of complexity when the extension of the system increases.

7.3.1 Linear and nonlinear stability criterion with A

For unipolar injection in an enclosure, the system possesses the same hydrostatic solution as the case with symmetric boundary conditions. In addition, the system also possesses the property of neutral-stability. In other words, the hydrostatic solution is unstable and the motion starts once $T > T_C$, where $T = T_C$ is the critical (neutral) regime corresponding to the onset of steady-motion with infinitesimal amplitude perturbations and with a unique wavenumber $k = k_C$. Since this neutral-stability problem has not been tackled with the linear stability analysis approach, we try to solve it with our numerical tools.

For the range $A \in [0.4,5.0]$, we observed that:

1. If $T < T_C$, the flow always stays at the motionless state, which means the fluid in the layer is stable with respect to infinitesimal perturbations.

2. When $T > T_C$, the tiny numerical fluctuations would introduce the motion. We especially stressed that the motion may not be steady even if T is only slightly above T_C, which is different from the computation of strong injection with symmetric boundary condition.

All evolution curves start from the hydrostatic solution (V_{max} = *0.0*), then pass an exponential transition range (some examples can be found in Figure 7-23). We can use this exponentially developing process to determine T_C following the same procedure applied to the case of symmetric boundary condition. Our numerical results of the linear criterion T_C versus A are summarized in Table 7-2 and Figure 7-21. Several interesting features can be highlighted:

1. When the aspect ratio A decreases, the critical threshold for the onset of convection increases. The critical T number increases by more than two times when A is reduced from 1 to 0.4.
2. When A is large enough, $A \to \infty$, $T_C \to 164.1$, where 164.1 is the critical value for the corresponding infinite layer. In our simulation, we obtained 164.2 with A = 10.

Table 7-2. Neutral ***T*** number as a function of the enclosure aspect ratio in the case of no-slip sidewalls

A	**0.4**	**0.5**	**0.6**	**0.614**	**0.7**	**0.8**	**0.9**	**1.0**	**1.1**	**1.2**
T_C	616.6	457.3	351.9	340.6	287.3	256.0	236.1	231.9	235.2	216.3
A	**1.3**	**1.4**	**1.5**	**1.6**	**1.7**	**1.8**	**1.9**	**2.0**	**2.1**	**2.2**
T_C	203.2	197.7	193.4	191.1	190.5	189.3	184.6	181.2	178.9	176.9
A	**2.3**	**2.4**	**2.5**	**2.6**	**2.7**	**2.8**	**2.9**	**3.0**	**3.07**	**10**
T_C	176.2	176.3	174.3	172.4	171.8	171.0	170.7	170.7	170.6	164.2

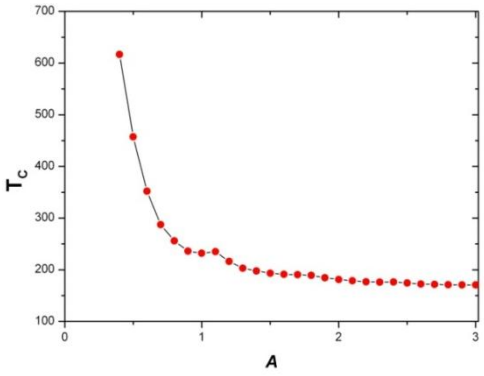

Figure 7-21. T_C versus A for a strong unipolar injection in an enclosure with wall boundary condition for lateral sides; Parameters: C=10 and M=50

The curve is not smooth. For example, there is a hump at T_C with A=1.1, which may be related with the modes of the most dangerous perturbation that replace each other when aspect ratio A is varied. In Figure 7-22, we provide the iso-lines of the charge density at the specific time which corresponds to the initial stage of development. For the case A = 1.0 the convection starts from one side, which is similar to what we observed with symmetric boundary condition; for the case A = 1.2, the convection starts from both sides. In addition, the final solutions at steady state of the two different aspect ratios are also quite different from each other, to see Figure 7-23.

Figure 7-23 shows the computational results of two-dimensional electro-convection in a box with various A values and T parameter slightly above the linear critical criterion.

In summary, the flow structures can be divided into two parts:

(i) $A \leq 1.0$

For this part (see Figure 7-23 (1) and (2)), when T is slightly above T_C, the flow motion will tend to a steady-state. The most important feature is that there is not charge-free region, as the minimum charge densities for A=0.4 and 1.0 are 0.567 and 0.693 respectively. In addition, there is no jump of velocity value at T_C, and the velocity starts from zero value at T_C and continuously increases with T value, which is similar to the situation of Rayleigh-Bénard flow.

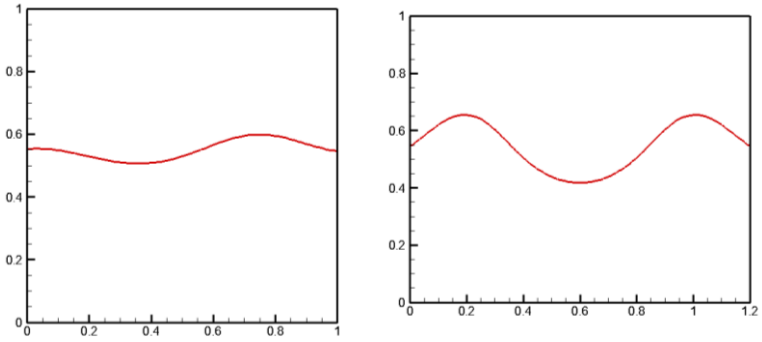

(a) (b)

Figure 7-22. Charge density isolines with value of 1.0 at (a) time = 60.0 with A=1.0 and T=250 (b) time=25.0 with A=1.2 and T=250

(ii) $A \geq 1.1$

At A=1.1, the flow motion also tends to a steady-state, with an evolution process quite similar to what we observed with the case with symmetric boundary condition. There is one charge-free region (q_{min} = *0.0284*), and two-steady main convective cells are formed (to see Figure 7-23(3)). Extra small vortices are founded near corners.

With $A \in [1.2,1.6]$, the flow motion generally keeps the same flow structure as for A=1.1 with one charge-free region and convective cells. The only difference is that the flow is unsteady with oscillation. The oscillation becomes more serious and irregular as A parameter increases.

At A=1.7, the state of the motion is still unsteady. The flow structure undergoes an important change. In this case, the flow no longer keeps one charge-free region and two primary convective cells. Instead, two empty regions and four primary cells can be observed at some moment, see Figure 7-23(6).

Before A reaches 2.0, the flow state is unsteady and the structure varies between two cells and four cells. Interestingly, we found that the time ratio of four cells increased along with A values.

At A = 2.0, 2.1 and 2.5, the flow ends with a steady state of four cells. The difference between the solutions with A = 2.1 or 2.0 and A = 2.5 is that the former case firstly evolves into a two-cell

structure (see the turning point at time ≈ 50 in Figure 7-23 (10-1)) then change to the final four-cell structure, while such transition between two and four cell structure disappears in the latter case. This difference indicates a change of the most dangerous perturbation mode, which is similar to what happened in Figure 7-23.

With $A \in [3.0,3.5]$, the final state of the flow again starts to oscillate. In addition, we notice there is some velocity jump in the *Vmax*-time figure, which corresponds to the change of number of charge-free regions and convective cells. The amplitude of the oscillation is much smaller than in the case of $A \in [1.2,1.6]$.

It is interesting to compare the solution with wall and with symmetric boundary conditions. For symmetric boundary condition, the solution with T slightly above T_C is always stable. No small vortices at corners will be induced by the primary vortices. The number of convective cells in horizontal direction increases by one as A increases by 0.614. For $A \in (n \cdot 0.614, (n+1) \cdot 0.614)$, there exists a specific A value (namely A_T) which corresponds to the change of the number of convective cells from n to n+1. For $A < A_T$ the number of convective cells remains n and the size of cells extends with the increase of A. This extension corresponds to the change of the most dangerous disturbance wave-numbers. For $A > A_T$ the number of convective cells suddenly increases by one. There is no transition solution which simultaneously owns n and (n+1) cells during the developing process.

For wall boundary condition in moderate and large domain ($A \geq 1.1$), the number of convective cells in horizontal direction also increases with A but with 2 as the unit. This is because the solution in the enclosure will not allow the existence of half charge-free cell. More importantly, the final state may not be steady. In addition, the unsteady solution may simultaneously own n and (n+2) cells during the developing process.

The difference is highlighted by the comparison cases with A = 2.0 and A = 5.0, see Figure 7-23 (15), (16) and (17).

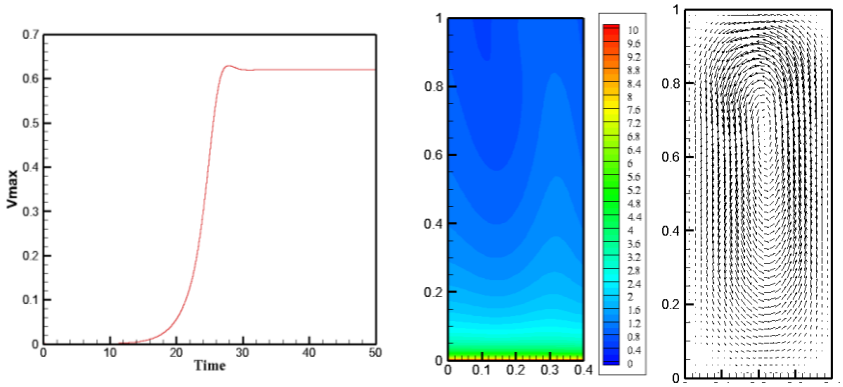

(1) A = 0.4, T = 700, q_{min} = 0.567

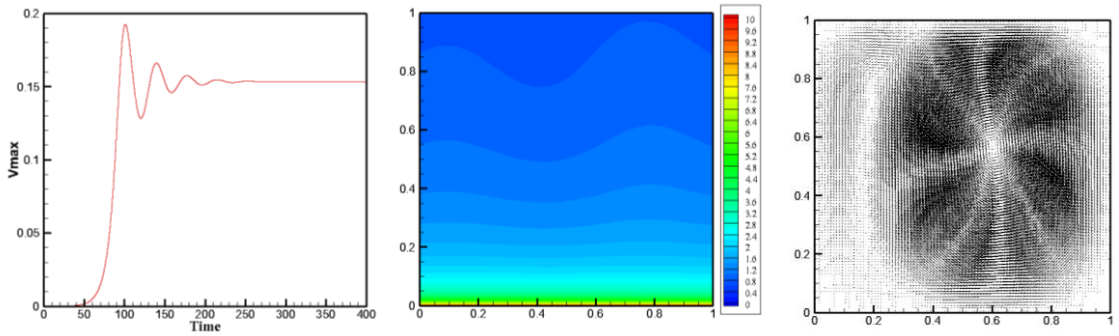

(2) A = 1.0, T = 250, q_{min} = 0.693

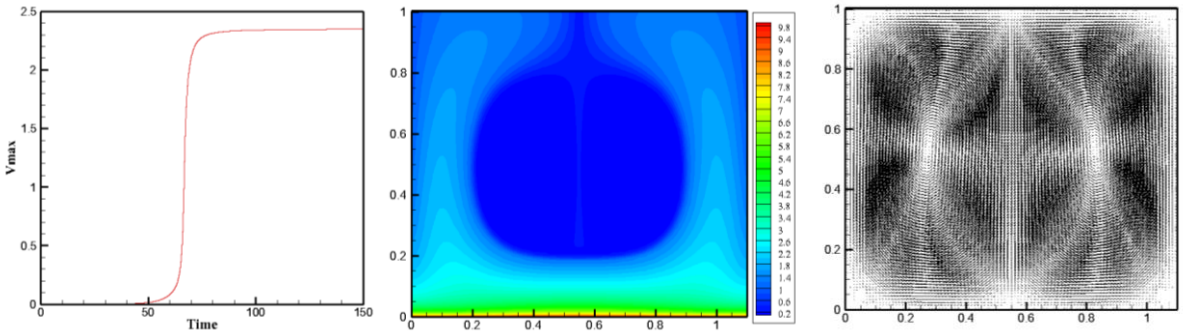

(3) A = 1.1, T = 250, q_{min} = 0.0284

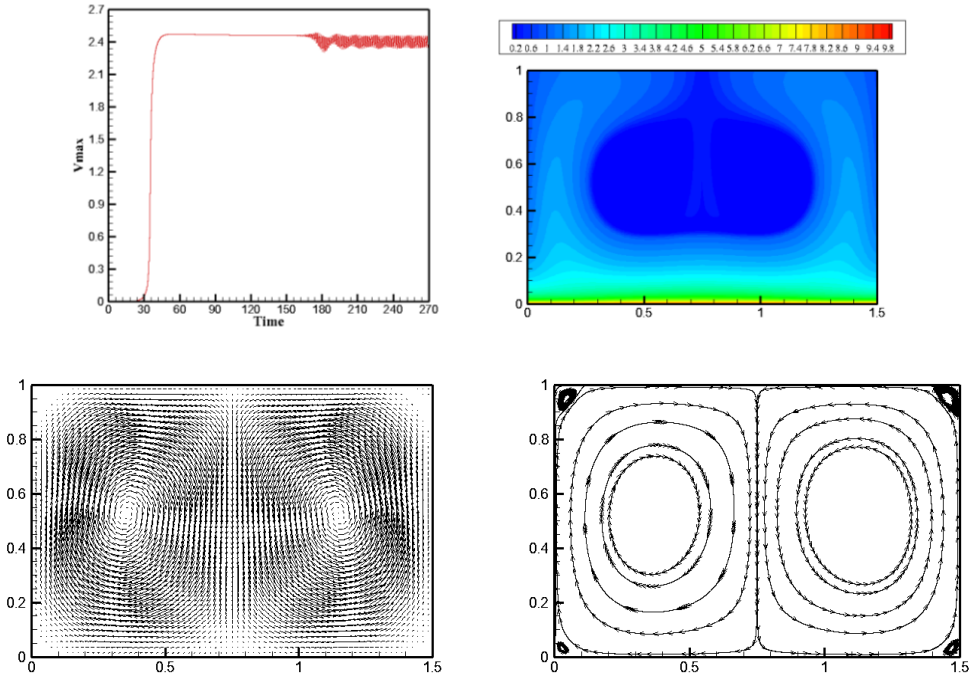

(4) A = 1.5, T = 220

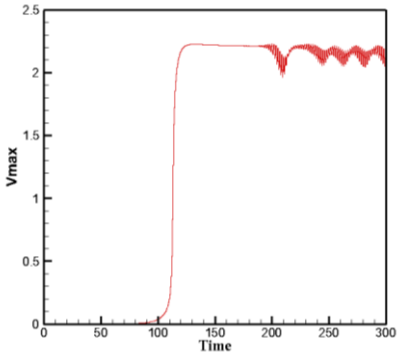

(5) A = 1.6, T = 200

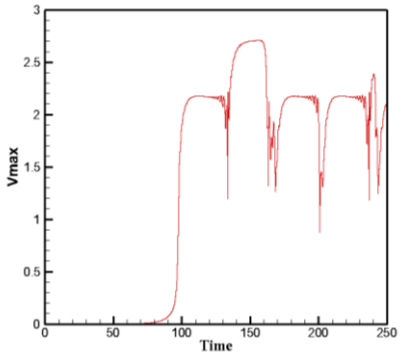

(6-1) A = 1.7, T = 200

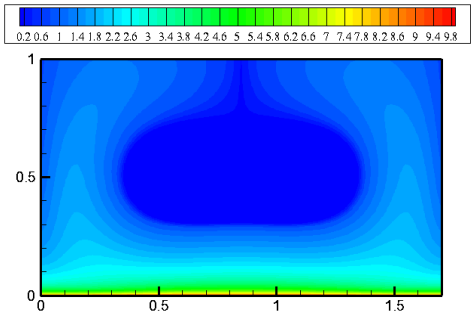

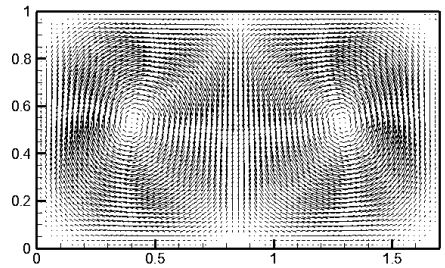

(6-2) A = 1.7, T = 200 at time =120

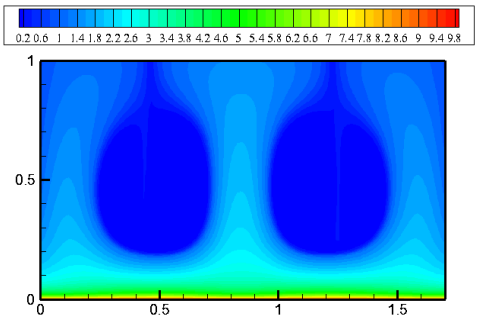

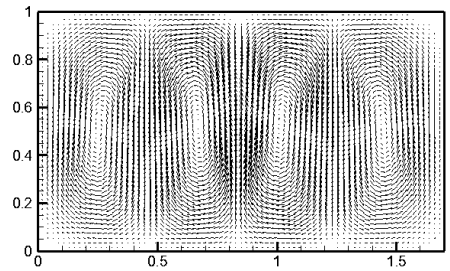

(6-3) A = 1.7, T = 200 at time =140

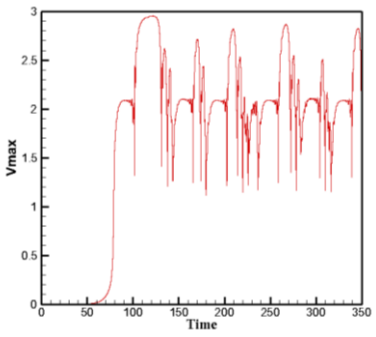

(7) A = 1.8, T = 200

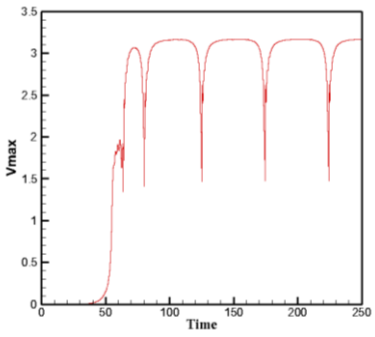

(8) A = 1.9, T = 200

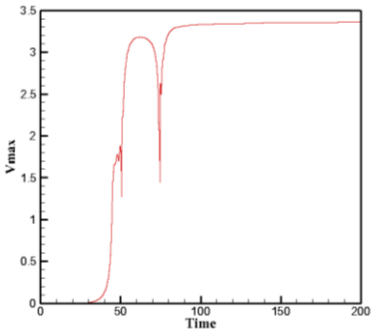

(9) A = 2.0, T = 200

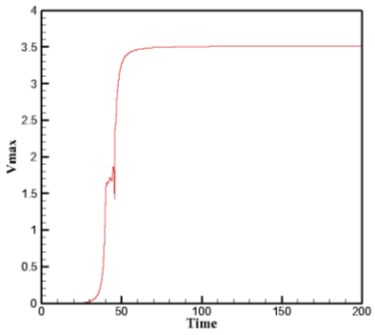

(10 - 1) A = 2.1, T = 200

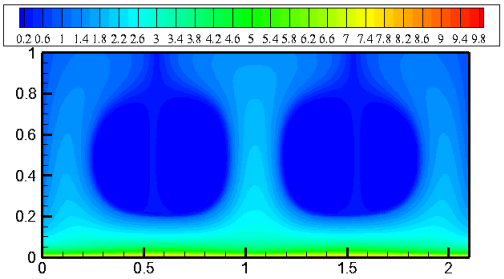

(10-2) A = 2.1, T = 200

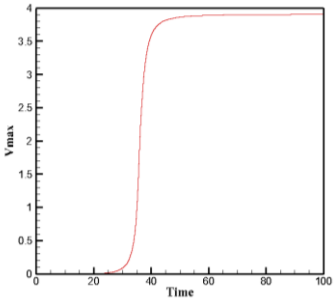

(11 - 1) A = 2.5, T = 200

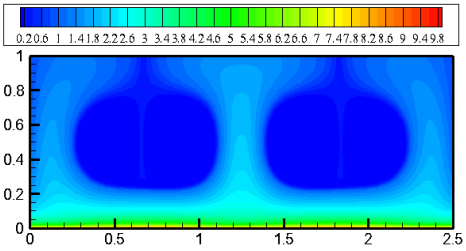

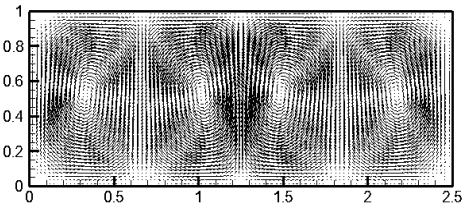

(11-2) A = 2.5, T = 200

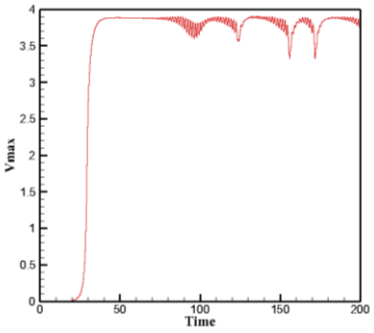

(12) A = 3.0, T = 200

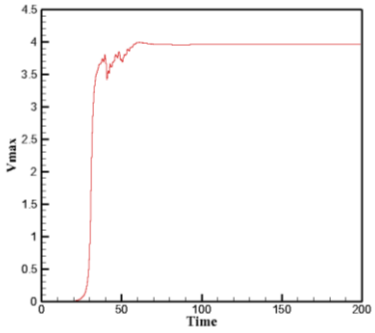

(13) A = 3.7, T = 200

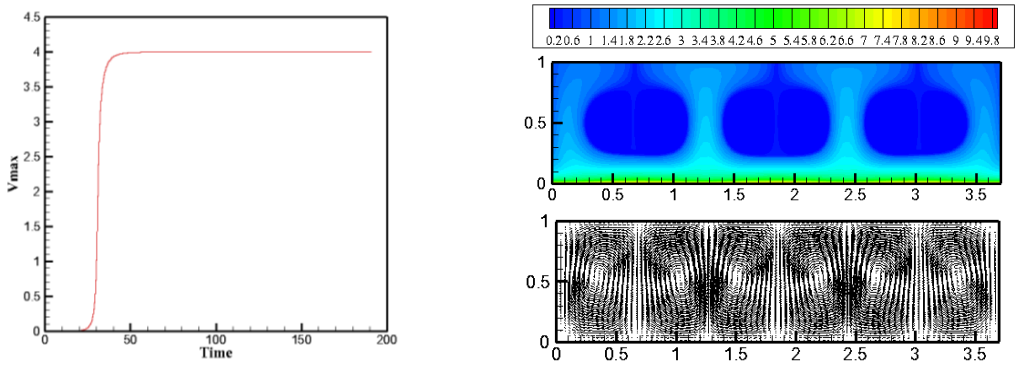

(14) A = 3.9, T = 200

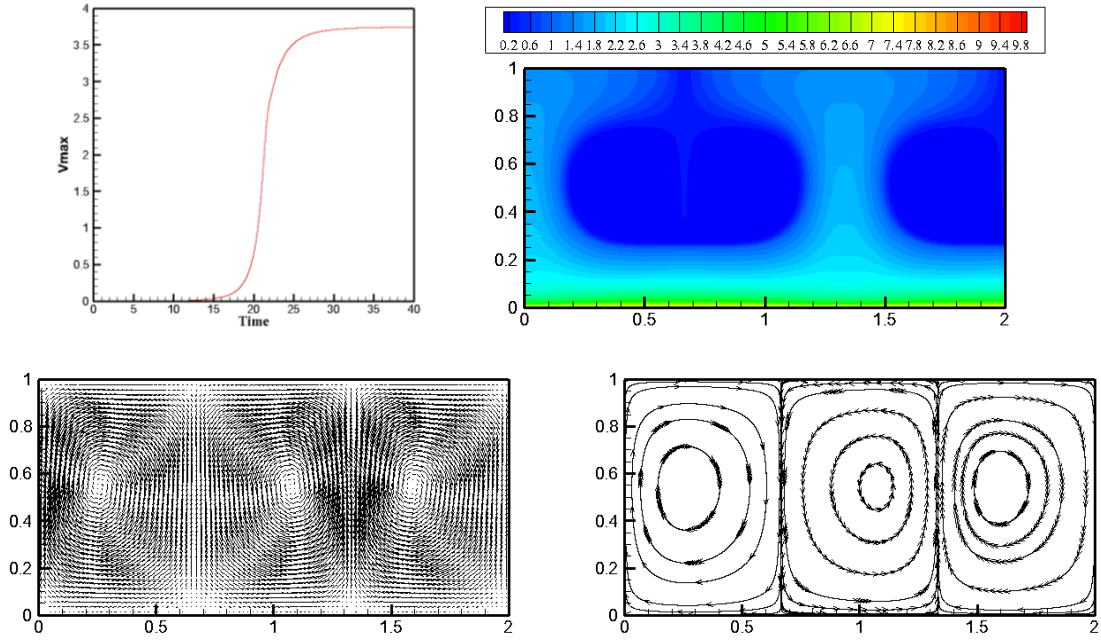

(15) A = 2.0, T = 200, symmetric B.C.

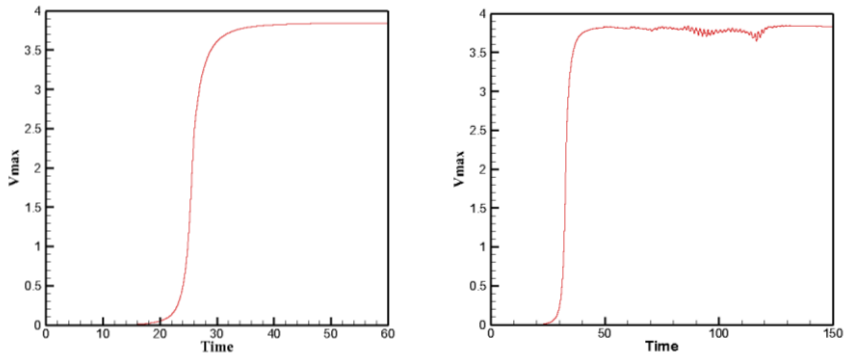

(16-1) A = 6.14, T = 190, sysmetric B.C. (17-1) A = 0.614, T =190, wall B.C.

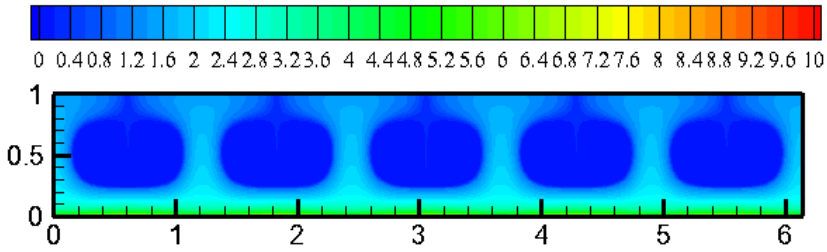

(16-2) A = 6.14, T = 190, sysmetric B.C.

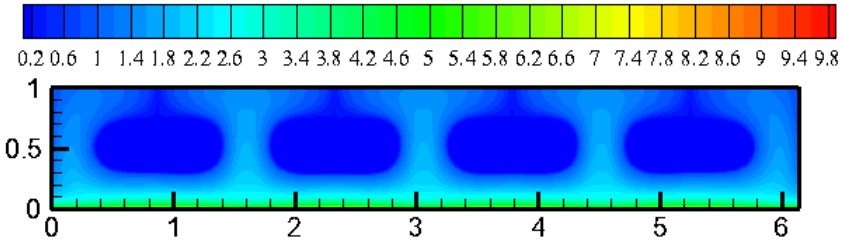

(17-2) A = 6.14, T = 190, wall B.C.

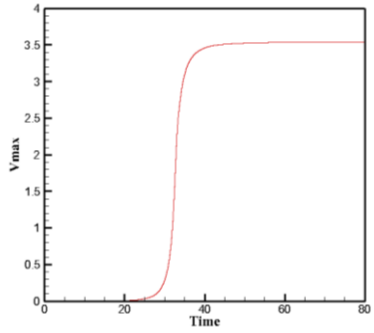

(18-1) A=10, T =190, sysmetric B.C., Vmax_final = 3.539

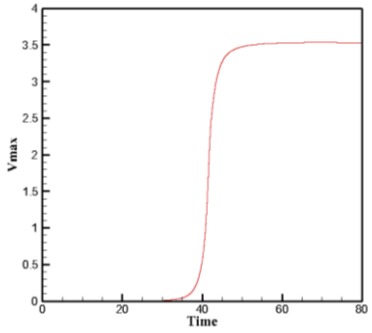

(19-1) A = 10, T = 190, wall B.C. , Vmax_final = 3.531

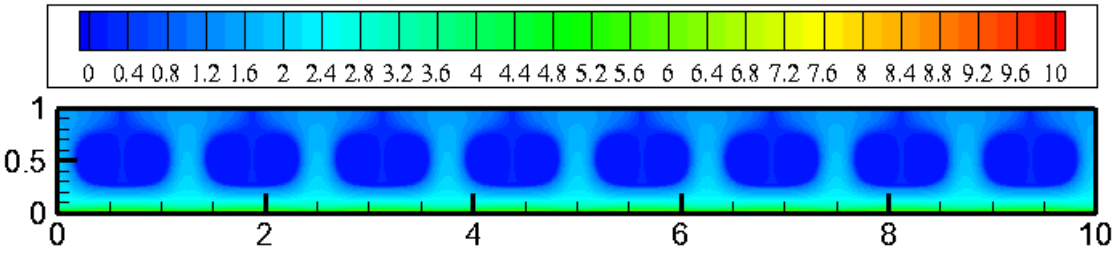

(18-2) A = 10, T = 190, symmetric B.C.

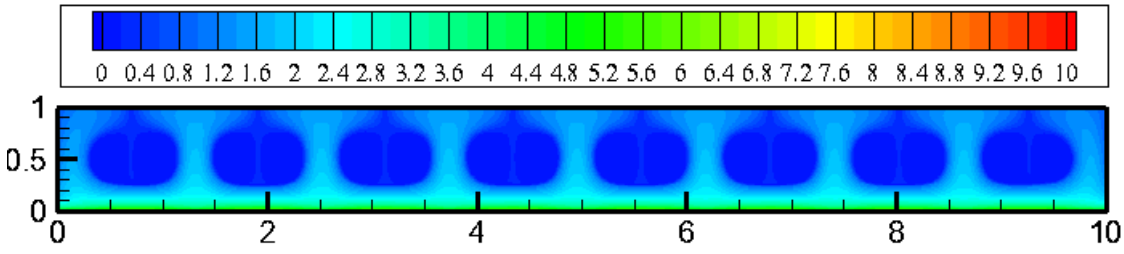

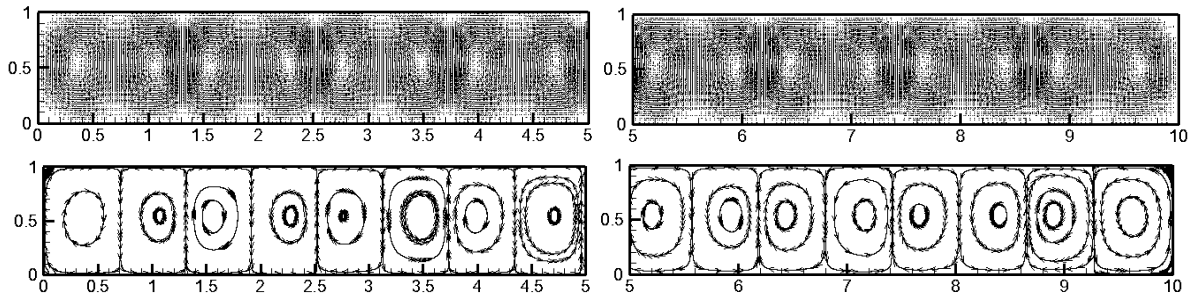

(19-2) A = 10, T = 190, wall B.C.

Figure 7-23. Numerical results of two-dimensional electro-convection induced by strong unipolar injection from below in rectangular containers for various values of aspect ratio

(i) $A = 10.0$

Let us take A = 10.0 as the example to see what will happen to the electro-convective flow in large enclosure. For comparison purpose, the computation with symmetric boundary conditions was also done. The two set of solutions are highly consistent with each other if we compare the evolution history of motion, the Vmax value of final steady state, the number and size of charge-free region and convective cells. In addition, T_C with wall boundary condition at A = 10.0 is 164.2, which is very close to 164.1, the critical value for infinite long parallel plates. We think the effects of wall boundary condition with the case of $A \geq 10$ on flow structure are very weak and the solution is expected to be identical to the case of infinitely long parallel plates.

To summarize, the wall effects of vertical wall boundary condition on electro-convection in the enclosure are strong with small aspect ratio. The effects are mainly reflected in the linear stability criterion and flow structure. The most important characteristic with small A is the high T_C value which indicates the flow is stabilized by the wall. Another interesting feature with the solution obtained with small A at T slightly above T_C is the lack of free-charge region. As the increasing of the aspect ratio, the effect gradually decreases and the solution tends to the one with symmetric boundary condition, i.e., the infinite long case.

In the next part, we will consider the problem of the effects of wall boundary conditions on the nonlinear stability and the associating hysteresis loop. Three typical cases (A=0.614, 1.0 and 1.1) were selected and the results are reported in Figure 7-24. To obtain results with A=0.614 and 1.0, the initial conditions should be carefully chosen.

Case I $A = 1.1$

The obtained hysteresis loop is quite similar to the one with symmetric boundary conditions. The main characteristic of the flow is the development of a subcritical instability featuring the existence of a linear and non-linear criterion and consequently the appearance of a hysteresis loop. When the T values are below the critical one T_c, the fluid viscosity counterbalances the electric force and the liquid stays at rest while the ions move to the counter electrode with the electric drift velocity $K\vec{E}$. Above T_c which features the linear stability criterion the liquid is suddenly put into motion with a characteristic jump. In 2D the flow motion organizes itself in the form of two primary convective

cells of equal width, which is also equal to the half-length of the box, i.e. 0.55, see Figure 7-23(4). If starting with the solution obtained with T=300 recomputed with successively decreasing T values, and if $T > T_f$, we would reach a new steady solution with smaller Vmax and area of charge-free region. For $T < T_f$, the velocity reduces suddenly to zero and the solution goes back to the hydrostatic state. Comparing with Figure 5-14, the solution with wall boundary condition at A=1.1 shows higher T_C and T_f.

Case II $A = 0.614$

In this case, the first simulation has been executed at **T**=300 starting from rest. Successfully, T has been increased in steps of 10, starting from the solution obtained at previous value, up to T=500. Three different flow regimes are observed.

$$340.6 \le T \le 430$$

In this range, the flow motion ends with a steady-state without charge-free region. Vmax at 340.6 (the numerical T_C value) is zero and smoothly increases with T parameter.

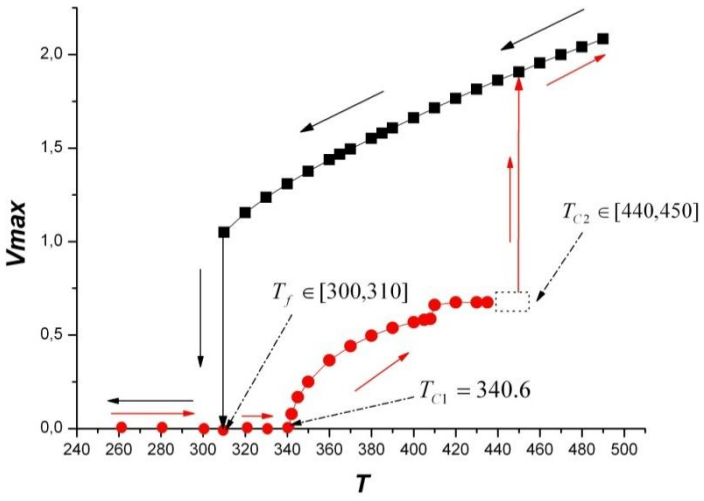

(a) A = 0.614

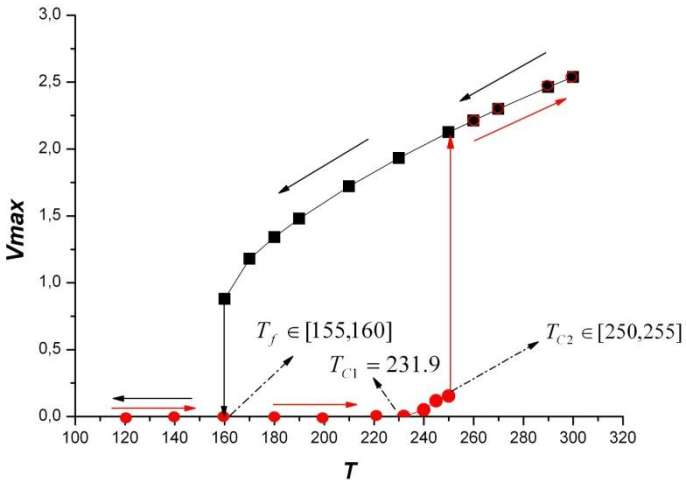

(b) A = 1.0

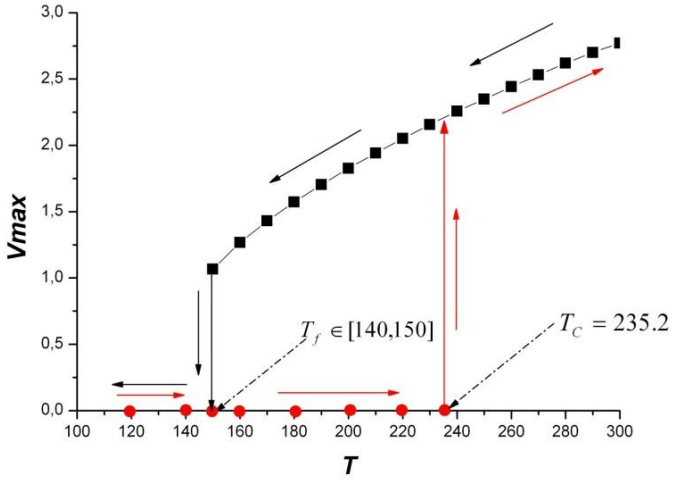

(c) A =1.1

Figure 7-24. Evolution of Vmax versus *T* for strong injection (C=10) in an enclosure with various aspect ratio; Parameters: C=10 and M = 10, the grid size is 10^{-2} in x- and y- directions; time step is 10^{-3}

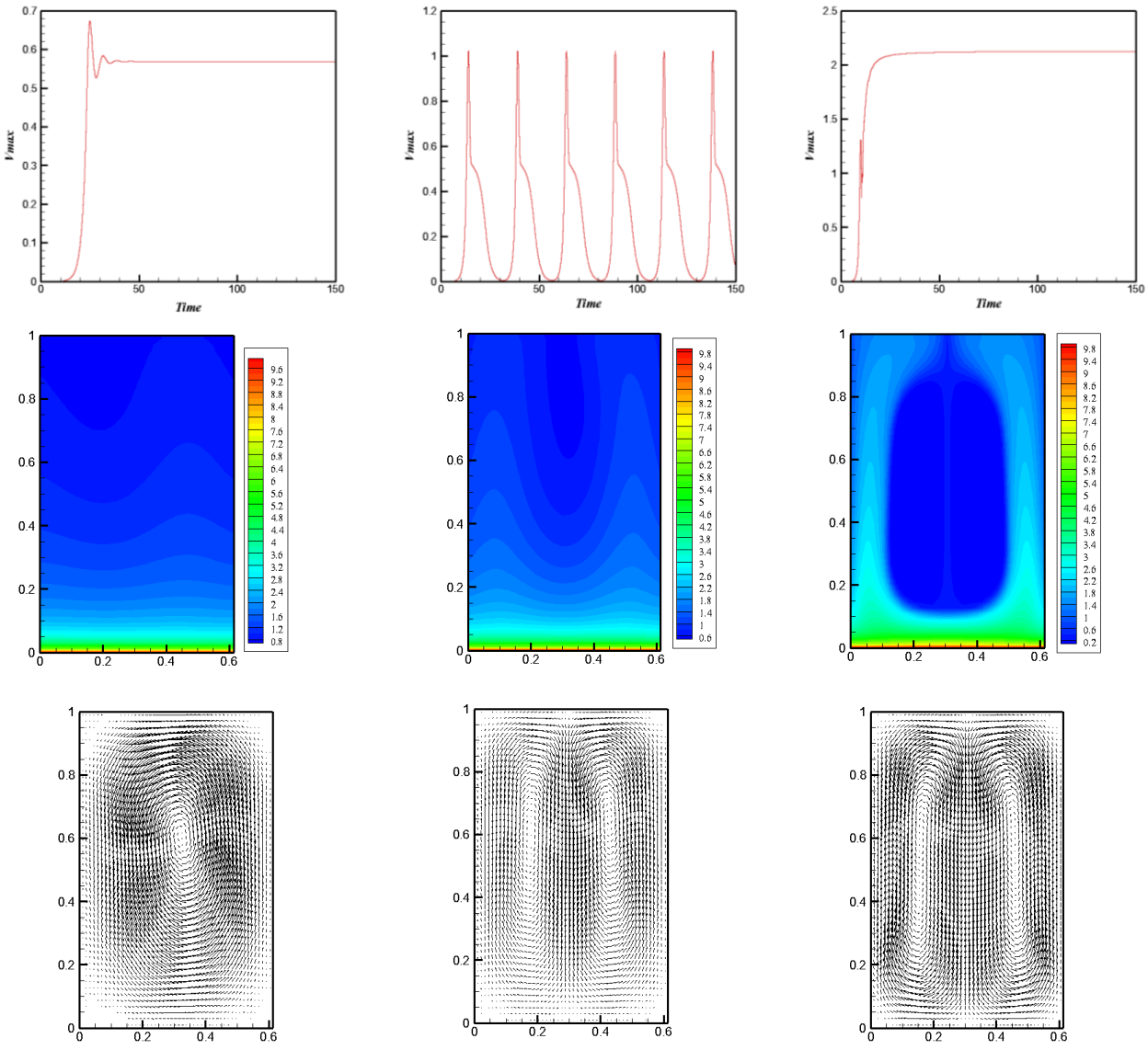

T = 400 T = 450 T = 500

Figure 7-25. Time history of the maximum of vertical velocity, contour map of the charge density and velocity field in the [0, 0.614] × [0, 1] domain for different values of T; Parameters: C = 10 and M = 50

$440 \le T \le 450$

In this range, the flow structure is quite complicated. The state of the motion is unsteady with dramatic periodical oscillation. The charge density distribution and velocity field in Figure 7-25 with T=450 correspond to a moment at which *Vmax* is at a peak value. The complex flow structure should be due to the interaction between the stabilizing effects of wall boundary and destabilizing effects of high value of T.

$460 \le T \le 550$

Increasing T till $T > T_{C2}$, the final flow state is steady again. In addition, there is a charge-free region in the charge density distribution, which makes the flow similar to the one computed with T = 290 with symmetric boundary conditions. Let us emphasize that the appearance of the charge-free region is the characteristic phenomenon of a subcritical bifurcation and a hysteresis loop. We name T_{C2} the second linear bifurcation value.

To determine the hysteresis loop, we starts with the solution obtained with T = 550 and gradually decreases T value. When T is still higher than a critical value T_f, the final state of the flow is always stable with smaller Vmax and free-charge region. When further decreasing T till $T < T_f$, the velocity reduces suddenly to zero and the solution of the system goes back to hydrostatic solution. The complete hysteresis loop is shown in Figure 7-24 (a).

7.3.2 Oscillatory and chaotic regimes of electro-convection in an enclosure

Above *T*=600, the two convective cells start to oscillate slowly and the regime becomes unsteady with regular oscillation. This behavior is depicted in Figure 7-26(b). As we increase *T*, the amplitude and the frequency of these oscillations also increase. For higher values of *T*, above 800, the regular oscillation becomes irregular and the flow is in a quasi-periodic regime.

For higher values of *T*, above 1000, the unsteadiness of the flow is more pronounced and the flow becomes chaotic. The power spectrum with *T*=700, 750 and 1000 are presented in Figure 7-27.

If we further increase *T*, we observe the electro convective plumes. Taking *T*=3000 as the example, the destabilization of the laminar sub-layer near the bottom surface induces the electro-plumes. The hydrostatic solution period will be never reached as the plumes are formed at the initial stage, see Figure 7-28 (b-1).

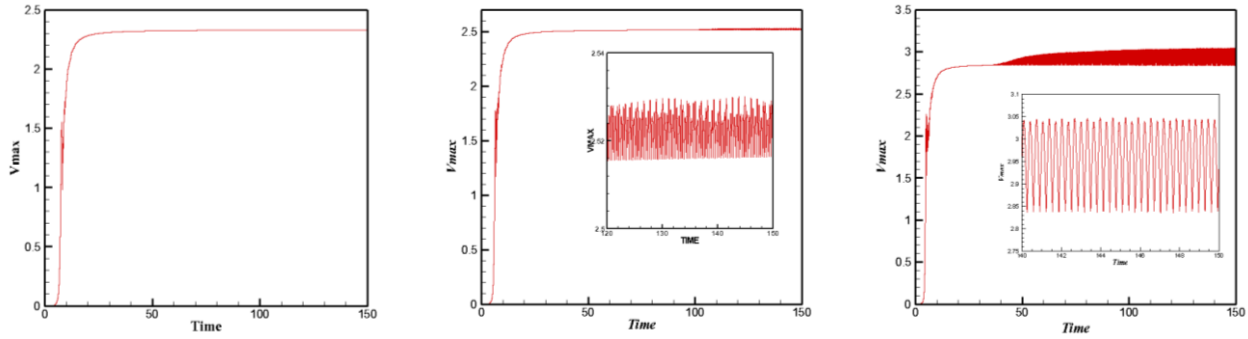

(a) T = 550 (b) T = 600 (c) T = 700

(d) T = 750 (e) T = 1000 (f) T = 3000

Figure 7-26. Time history of the maximum of velocity in the [0, 0.614] × [0, 1] domain for different values of T; Parameters: C = 10 and M = 50;

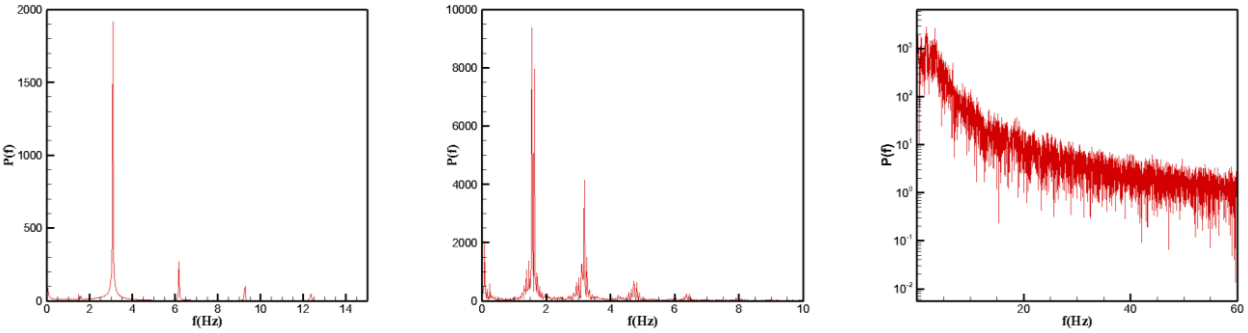

(a) T = 700 (b) T = 750 (c) T = 1000

Figure 7-27. Power spectra for numerical solution in an enclosure with different values of T; Parameters: C = 10 and M = 50;

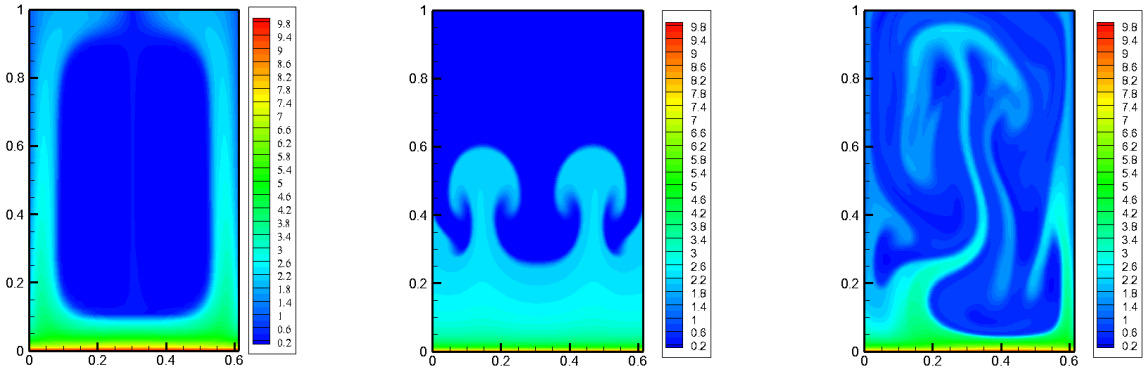

(a) T = 1000 at *time = 50* (b-1) T = 1000 at the initial stage (b-2) T = 1000 at *time = 35*

Figure 7-28. Contour map of the charge density in an enclosure with different values of T; Parameters: C = 10 and M = 50;

It is interesting to notice that the way for electro-convection flow in box is similar to the one with infinitely long parallel plates: steady – periodic - quasi-periodic – chaotic – plumes. However, some subtle difference can be found in the charge density maps. For solution with wall boundary condition at T slightly above T_t, where T_t is the transition value for the flow to become chaotic, the thickness of the charge density layer near the vertical sides is much bigger than the one of solution obtained with symmetric boundary conditions. In addition, the electro-plumes with the case of wall boundary conditions are more easily formed at the regions which are a bit far away from vertical sides; see Figure 7-28 (b-2).

7.4 Conclusions

By continuously increasing the driving T parameter in the strong injection case, the successive instabilities and the way to the chaotic state have been defined: no motion → steady one cell → periodic one cell → steady two cells →periodic two cells → pseudo-periodic two cells → chaotic (including plumes).
When diffusion mechanism for charge density is taken into account in the strong injection case, the system tends to be more stable. It is numerically shown that the linear and nonlinear stability criterion increases along with the increases of the diffusion coefficient for charge transport.

Instead the symmetric boundary conditions for vertical sides, the lateral walls may seriously affect the linear and nonlinear stability criteria and overall structure of the flow pattern that develops when the T number exceeds its critical value. It is found that the vertical walls tend to stabilize the flow especially when the aspect ratio is small.

Chapter 8 Electro-thermo-convection in a dielectric liquid layer subjected to unipolar injection and a thermal gradient

8.1 Introduction

The system under consideration in this section is a horizontal layer of a dielectric liquid enclosed between two electrodes and subjected to the combined effects of an electric field and a thermal gradient simultaneously applied.

The complex instability phenomena which result from this particular configuration have received much attention in recent years and have been studied in depth [15][16] [26][36] [181] [182][183] [290]. Another motivation for such interest is the promising way to control the fluid flow and enhance the convective heat transfer by means of externally applied electrical fields [291-293]. Indeed, it has been also shown experimentally that the heat transfer across an insulating liquid can be significantly increased [22][294][172]. With this type of active heat transfer enhancement technique, smaller and more effective thermal systems can be designed. For single-phase liquid, this noticeable increase of heat transfer is mainly due to the development of secondary motions that result from two principal body forces: Coulomb forces acting on any free charge present in the liquid and the dielectric force induced by a permittivity gradient which may result from a temperature variation. With a non-uniform distribution of charge carriers, the generation of vortices may also be enhanced. Thus, such combined effects are therefore worthy of examination not only from a fundamental point of view but also because of potential technological advantages that may result from them [295-297].

In the present study, we follow the mobility model as the charge generation mechanism. Based on this model, we consider the case of space charge only resulting from ion injection, the coupling between the conservation equations of momentum, electric charge and energy is mainly ensured via the Coulomb and buoyancy forces. This coupling results from direct interaction between the velocity, temperature and charge perturbations and from the indirect interactions between the velocity and the charge. This strong and non-linear coupling as well as the complexity of the mathematical problem has prevented the obtainment of any analytical solution. Therefore most researchers who have been working so far on electro or electro-thermo convective problems in a horizontal planar layer of dielectric liquids have mainly tackled the problem with experimental studies and stability theory. The earliest experiment evidence of the existence of electro-thermal instability of a dielectric liquid was provided by Gross and Porter [12]. By applying a DC electric field ($\geq 2\times10^5$ V/m) and a thermally stabilizing (heating from above) with a temperature difference of $12\,^{\circ}\mathrm{C}$ across a 1mm layer of transformer oil, corresponding to a Rayleigh number value of 20, they observed a steady cellular fluid motion. In [14], another type of fluid motion was presented. In this paper, Turnbull applied a temperature difference of $15\,^{\circ}\mathrm{C}$ across a corn oil layer with a thickness of 25.4 mm, corresponding to a Rayleigh number value of 240000. They observed an oscillatory fluid motion with a frequency of 0.05. The above mentioned steady cellular and

oscillatory fluid motions are representations of stationary and oscillatory instability separately. It should be pointed out that the autonomous unipolar injection associated with a appropriate choice of the injection charge density and linear assumption for the temperature-dependent mobility can predict both types of stabilities successfully [15][16][181].

The linear stability analysis has been applied to predict the onset of instability in a dielectric layer problem under weak [298] or arbitrary injection [26], and thermal constraints cooperating or competing with each other [16][181][182][290]. The effect of the temperature-dependent carrier mobility [15][182] and dielectric constant [298][182] on the stationary linear instability has also been investigated. These works greatly improved the theoretical background for the heat transfer enhancement applications.

Like for pure electro-convection, the void charge region due to the non-linear coupling between charge and electric field may also exist in electro-thermo-convection. This void region is the indicator of the nonlinear subcritical bifurcation. However, this nonlinear stability characteristic of the system has seldom been analyzed due to the complexity of the mathematical models. To our knowledge, the only nonlinear study was taken by Worraker and Richardson [15] who investigated the problem with a normal-mode cascade analysis. Typically, this analytical method requires further assumption of the system, solid mathematical operation and is only applicable to small-amplitude motions when voltages are close to critical value corresponding to the onset of the linear stability.

Besides the experimental and theoretical approaches, a direct numerical simulation of the ETHD problem is also an efficient investigation tool. Until now only a few numerical simulations have been attempted on ETHD convective problem with more or less success [299]. In [300], George S *et al.* simulate electro-thermally generated flows in closed enclosure and open channels. In this study, they consider the influence of the electric field on the electrically charged particles generated at one boundary side, which is similar to the case of unipolar injection considering by the present study. In [184] Yan *et al.* have solved the entire set of coupled Electro-Thermo-Hydro-Dynamics (ETHD) equations with a finite-difference method and have characterized EHD enhancement of heat transfer especially in the case of a uniform or non-uniform electric field. The QUICK scheme has been applied to solve the charge density equation.

More recently Traoré *et al.* have developed a direct numerical simulation based on finite volume method to solve the entire set of EHD and ETHD equations [56][57]. A core component of the numerical procedure is the original method based on total variation diminishing (TVD) scheme for solving the charge density equation. From our practical experience, the application of such high-resolution scheme to capture the void region of space charge density is necessary for an accurate prediction of the possible nonlinear stability criterion. In [57], the authors started from the viewpoint of considering the effects of buoyancy force on pure electro-convection and mainly emphasized the appearance of subcritical and supercritical bifurcations which depends on the values of Prandlt number, Pr, and a mobility-related non-dimensional parameter, M.

The main objective of this chapter is to show that our numerical approach can be used to compute the electro-thermal-convection. Both fundamental linear and nonlinear stabilities and application-related heat transfer enhancement will be considered. The reminder of this chapter is

organized as follows. The problem, the governing equations and boundary conditions have been already stated and described in chapter 2 and a brief introduction will be presented in section 8.2. The numerical method and solving chart has been explained in Chapter 3 and 4. Thus, in the section 8.3 we directly verify our numerical solvers with a complete ETHD problem which has been tackled with the linear stability approach. In section 8.4, features on the development of pure Rayleigh-Bénard and pure electroconvective instabilities are recalled and the neutral stability of the electro-thermo convection problem is presented. The conditions for which the instability develops regarding the driving parameters *Ra* and *T* are discussed. Finally a conclusion is drawn up in section 8.5.

8.2 Statement of the problem

8.2.1 Basic governing equations and their non-dimensional forms

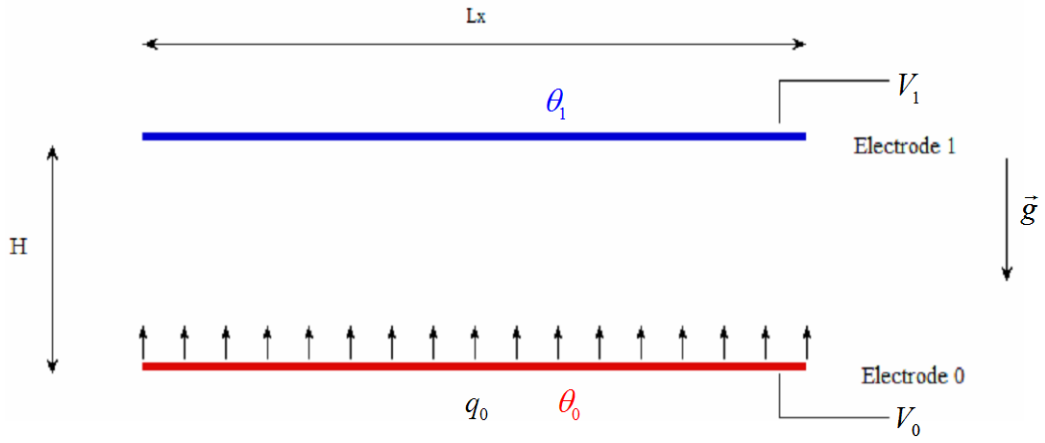

Figure 8-1. Sketch of the physical domain with electro-thermal-convection problems

We consider a dielectric liquid layer of thickness H enclosed between two electrodes of length L_x. The layer is heated either from below or above and subjected to a thermal gradient $\Delta\theta = \theta_0 - \theta_1$. Between the two electrodes a potential difference $\Delta V = V_0 - V_1$ is applied. A charge density q_0 is injected either from the below or the above electrode. The z-axis is taken perpendicular to the electrodes and the gravity is considered acting in the negative z-direction. The two-dimensional geometry is depicted on Figure 8-1. In total, there are four distinct modes representing the competition or cooperation relations between the buoyancy and Columbic forces, see Figure 2-3(1) ~ (4). The general set of equations for an incompressible fluid includes the mass and momentum conservation, energy balance equation under the Boussinesq assumption, charge density conservation, and Gauss theorem for electric potential. Electric and buoyancy forces are included as source term in the momentum equations.

In this study, we neglect the variation of kinematic viscosity and thermal diffusivity with temperature to highlight the effects of buoyancy force and temperature-dependent mobility and permittivity. We follow a simple assumption that both the mobility and permittivity varies linearly

with temperature. Taking into account all these considerations we reach the coupled partial differential equations system,

$$\nabla.\left(\vec{u}\right)=0 \tag{6-1}$$

$$\rho_0\left(\frac{\partial\vec{u}}{\partial t}+(\vec{u}.\nabla)\vec{u}\right)=-\nabla p+\nabla.\tau+\rho\vec{g}+\vec{f}_{el} \tag{6-2}$$

$$\rho_0 C_p\left(\frac{\partial\theta}{\partial t}+\vec{u}\cdot\nabla\theta\right)=\nabla\cdot\left(\lambda\nabla\theta\right)+\vec{E}\cdot\vec{j} \tag{6-3}$$

$$\nabla.(\varepsilon\vec{E})=q \tag{6-4}$$

$$\frac{\partial q}{\partial t}+\nabla\cdot\vec{j}=0 \tag{6-5}$$

$$\vec{E}=-\nabla V \tag{6-6}$$

$$\rho(\theta)=\rho_0\left[1-\beta\left(\theta-\theta_0\right)\right] \tag{6-7}$$

$$\varepsilon(\theta)=\varepsilon_0\left[1-e_1\left(\theta-\theta_0\right)\right] \tag{6-8}$$

$$K(\theta)=K_0\left[1-k_1\left(\theta-\theta_0\right)\right] \tag{6-9}$$

where $\vec{u}$ is the velocity, ρ_0 is the mass density, p is the pressure, $\vec{g}$ the gravity, $\vec{f}_{el}$ stands for the electric forces induces by the electric field $\vec{E}$, C_p the thermal capacity, θ the temperature, θ_0 is a reference temperature, λ the conductivity, ε the permittivity of the fluid, q the volumic electric charge density in the liquid. K is the ion drift velocity and V the electric potential. β is the volumetric thermal expansion coefficient, e_1 , k_1 are respectively the relative change of permittivity and mobility with temperature.

$$e_1=-\frac{1}{\varepsilon_0}\left(\frac{\partial\varepsilon}{\partial\theta}\right),\quad k_1=-\frac{1}{K_0}\left(\frac{\partial K}{\partial\theta}\right)$$

In the conservative equation (6-5) for the current density, there exists three distinct mechanisms of charge transfer: $\vec{j}=q\vec{u}+qK\vec{E}-D\nabla q$, where D denotes the charge-diffusion coefficient. Since the contribution of diffusion to the electric current is much smaller than the other two terms, it is commonly admit to ignore it [152]. The electric forces are expressed as follows: $\vec{f}_{el}=q\vec{E}-\frac{E^2}{2}\nabla\varepsilon+\nabla\left(\frac{1}{2}E^2\left(\frac{\partial\varepsilon}{\partial\rho}\right)_\theta\right)$ where the first term is the Coulomb force, the second the dielectrophoretic force and the last one the electrostriction force. The electrostriction force can be combined with the static pressure term and we define a modified

pressure: $\tilde{p} = p - \nabla\left(\frac{1}{2}E^2\left(\frac{\partial\varepsilon}{\partial\rho_m}\right)_\theta\right)$. The last term in the energy equation (6-3) represents the Joule heating, which can also be ignored due to the small amplitude of the current density [209].

The above equations are put in dimensionless form by using the following references:

$$[x,y]=H,\quad [t]=H^2/\nu,\qquad [\vec{u}\,]=\frac{\nu}{d},\qquad [\tilde{p}\,]=\rho_0(\nu/d)^2,\qquad [\theta]=\theta_0-\theta_1$$

$$[V]=V_0-V_1,\quad [\vec{E}\,]=(V_0-V_1)/d,\qquad [q]=q_0\qquad [K]=K_0,\quad [\varepsilon]=\varepsilon_0$$

We obtained a complete and fully coupled set of dimensionless equations.

$$\nabla.\vec{u}=0 \tag{6-10}$$

$$\frac{\partial\vec{u}}{\partial t}+(\vec{u}.\nabla)\vec{u}=-\nabla\tilde{p}+\Delta\vec{u}+\frac{T^2}{M^2}\left[Cq\vec{E}+\frac{E^2}{2}\nabla\varepsilon\right]+\frac{Ra}{Pr}\theta\ \vec{e}_y \tag{6-11}$$

$$\frac{\partial\theta}{\partial t}+\vec{u}.\nabla\theta=\frac{1}{Pr}\Delta\theta \tag{6-12}$$

$$\frac{\partial q}{\partial t}+\nabla.\left(q(\vec{u}+RK\vec{E})\right)=0 \tag{6-13}$$

$$\nabla.(\varepsilon\nabla V)=-Cq \tag{6-14}$$

$$\vec{E}=-\nabla V \tag{6-15}$$

$$\varepsilon=1-LRa\theta \tag{6-16}$$

$$K=1+NRa\theta \tag{6-17}$$

Several dimensionless parameters emerge in this analysis:

$$Ra=g\beta\Delta\theta d^3/\nu\kappa,\quad Pr=\nu/\kappa,\quad T=\varepsilon\Delta V/\rho\nu K,\quad C=q_0d^2/\varepsilon\Delta V,\quad M=\sqrt{\varepsilon/\rho K^2},\quad R=T/M^2,$$

$$N=\frac{e_1\nu\kappa}{\beta g d^3},\quad L=\frac{k_1\nu\kappa}{\beta g d^3}$$

are respectively the Rayleigh number with g the gravity and κ the thermal diffusivity, Pr the Prandtl number, T the instability parameter which is the ratio of Coulomb and viscous forces, analogous to the Rayleigh number in thermal convection. C a measure of the injection level with q_0 the injected charge, M the mobility parameter is decided by the fluid properties and stands for the ratio between the hydrodynamic and ionic mobility. R is the electrical Reynolds number which is defined by convenience. N and L dimensionless are temperature derivative of respectively dielectric constant and mobility.

8.2.2 Boundary and initial conditions

The boundary conditions in the case of heating and injection from lower electrode are depicted in Figure 8-2. On lateral boundaries we consider for the velocity, symmetrical boundary conditions to simulate an infinitely long cavity and no-slip boundary conditions to simulate the finite box.

In this study, we consider two typical cases where charge injection is always performed from the below emitter electrode while heating may be from either below or above. The horizontal boundaries are assumed to be rigid heat conducting electrodes. The injection is assumed autonomous which means that $q = q_0$ at $z = 0$ during the whole injection process.

The above system of equations (6-1) – (6-9) possesses a steady one-dimensional hydrostatic equilibrium ($\vec{u} = 0$), $\vec{j} = q(R\vec{E}) = [0, j(z)]^T$ and $\vec{E} = [0, E(z)]^T$. The dimensional form for this set of hydrostatic solutions has been widely provided [182] as it is the starting point for linear stability analysis.

$$\theta(z) = \theta_0 - \beta_z, \quad \rho(z) = \rho_0(1 + \beta\alpha z),$$

$$\varepsilon(z) = \varepsilon_0(1 + \beta e_1 z), \quad K(z) = K_0(1 - \beta k_1 z),$$

$$j_0 = K_0 q_0 E_0 = K(z) q(z) E(z),$$

$$E(z) = \frac{\varepsilon_0 E_0}{\varepsilon(z)}\left[1 + \left(\frac{2q_0 K_0}{\varepsilon_0^2 E_0}\right)\int_0^z \frac{\varepsilon(z)}{K(z)} dz\right]^{1/2},$$

where $\beta = (\theta_0 - \theta_1)/d$ with $\theta_1 = \theta_1(d)$. When the temperature of the above electrode is higher than the below one, β is positive. The electric field $E(z)$ satisfies $\int_0^d E(z)dz = \phi_0 - \phi_1$, where ϕ denotes the electric potential and $(\phi_0 - \phi_1)$ is the applied voltage difference.

Here, we provided a non-dimensional expression when *N=0* and *L=0*.

$$\theta = y$$

$$j = j_0 = Q_0 R E_0 = RQ(z)E(z)$$

$$Q(z) = \frac{a}{2C\sqrt{z+b}}$$

$$E(z) = aC\sqrt{z+b}$$

where a and b are two constants which depend on the injection strength C. For the strong injection case $C = 10$, the values for *a* and b are 1.4882 and 5.539×10^{-3} respectively.

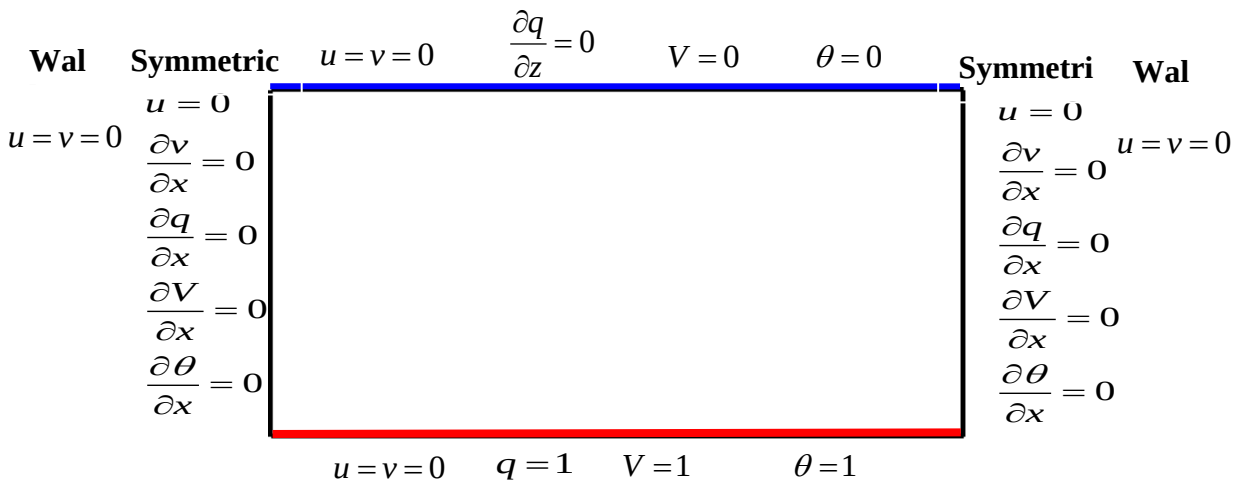

Figure. 6-2 Computational domain and boundary conditions for electro-thermal-convection problems

The validity and accuracy of our numerical solver is first checked by application to the steady hydrostatic equilibrium solution. Note that the coupling between the electric-related variables and temperature is switched off because of the zero velocity fields. The hydrostatic equilibrium solution can also be used as the starting initial field for the charge density and the electric field. In all test cases, at t=0 the liquid is heated from below and the electric potential difference between the two electrodes is applied and electric charges are injected in the bulk. In other words, the heating and charge injection always start at the same time.

8.3 Verification of the numerical ETHD solver

The numerical procedure of our numerical ETHD solver has been explained in details in Chapter 4. After the comparison tests performed with pure electro-convection problems, the SMART limiter function and second order three time level implicit time scheme are always used to solve the charge density equation.

In this section, we verify our numerical ETHD solver with two problems which have been tackled with the linear stability analysis approach. The first one is the stationary linear instability problem of unipolar injection equilibrium in the case of heating from above and injection from below. A small Ra number which means the thermal gradient weakly stabilizes the flow will be used. The mobility may not depend on temperature or depends linearly on it. This problem has been investigated in [15] and some references results like k_C and T_C are provided. It is also found two types of instability: (i) a space charge modified Bénard mode and (ii) a thermally modified space charge mode. The second one is the oscillatory instability problem with a strong stabilizing gradient.

In addition, appropriate grid convergence checks have been performed to analyze the accuracy of the code.

8.3.1 Stationary linear instability with a weakly stabilizing thermal gradient

In order to compare with published results in [15], we select the mode 3 in Figure 2-3 (heating from above and injection from below) and set the *Ra* number to 20. This *Ra* number corresponds to a weakly stabilizing temperature difference of 1°C across a layer of chlorobenzene or n-hexane of depth 0.5mm [15]. In addition, we choose $A = \Pr/M^2 = 20$ and k_1 lying in the range of [10^{-3}, 1]. The case $k_1 = 0$ is also computed. With our non-dimensional style, the value of k_1 should be converted to *N* according to Eqn.(6-17). As explained in previous chapter, a potential problem of using the direct numerical simulation to determine the linear stability criterion of a given EHD system is the size of the computational domain. In general, we set the horizontal length of the computational domain as the half of the critical wavelength of the system which has been provided through the theoretical stability analysis approach. For the ETHD problems considered in the present study, the information of the critical wavelength has been provided for various heating and injection modes. However, these information is mainly expressed through curves rather than detailed values.

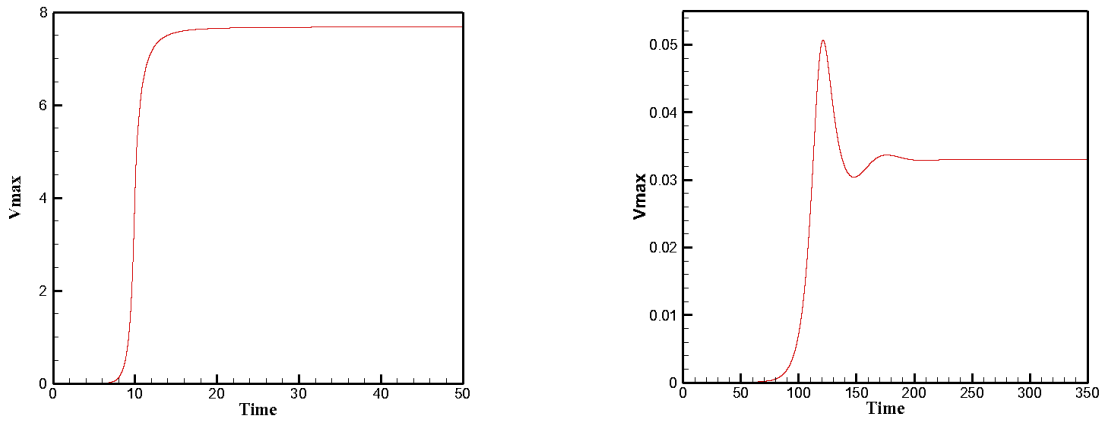

(a) (b)

Figure 8-3. Time evolution of the maximum vertical velocity component in the domain from initial state until steady state (a) T=190, N = 0 (b) T = 70, N = 5×10^{-3}

As the purpose of this subsection is to validate our numerical solver, we specially choose some cases for which the critical wavelengths have been known. In this set of computations, we fixed the values of *C, M, Pr, Ra, N* and *L*, and then ran the computations with different *T* values which are slight below or above the linear stability criterion (T_C). We observed that the system always keeps a rest state when *T* slight below T_C. If we increase *T* to a value slightly above T_C, we found the system would reach a steady state after some transition period. Two typical examples are provided in Figure 8-3 in which we use the maximum value of the vertical velocity component as the representative parameter. In both figures, the system evolved from a rest state. The system keeps the hydrostatic equilibrium solutions before an exponential interval. This exponential increasing period is induced by the tiny numerical fluctuations and can be used to compute the critical *T* value. The computation method and process are exactly the same with what we applied to the pure

electro-convection and the Rayleigh-Bénard convection, see chapter 4 and chapter 5 for more details.

In table 6-1, we compared the critical *Tc* values for the different *N* values obtained with our numerical tools with the ones provided in [15] with the linear stability analysis approach. The maximum error is less than 13%. The good agreement between our numerical results and the theoretical values highlighted the effectiveness and accuracy of our numerical approach.

Table 6-1. Comparison of numerical and analytical linear criterion for electro-thermo-convection problems, parameters: Ra = -20, A = 20 (Pr=500, M=5), C=10

κ_1	0	10^{-3}	10^{-2}	10^{-1}	1.0
N	0	5×10^{-5}	5×10^{-4}	5×10^{-3}	5×10^{-2}
$\lambda/2$	0.611	0.637	0.724	0.828	0.885
T_C_theoretical [15]	165.6	149.0	96.0	42.0	19.6
T_C_present	*168.0*	*158.4*	*99.63*	*48.0*	*22. 9*

In Figure 8-4 and Figure 8-5, we present two steady solutions with $N=0$ and $N=5\times10^{-3}$ separately. It is easy to find the two solutions showing obviously different flow structure. As the absolute value of Ra number is small, the stabilizing effect of the thermal force is limited. When *N* equals to zero, i.e., the charge carrier mobility does not vary with temperature, the results in Figure 8-4 are easy to understand as the Coulomb force is the main driving force because of high T value. The velocity field and charge void region is close to the one we obtained in pure EHD problem and the temperature can be seen as a passive transport variable. For the same strong injection strength and weak thermal force, in [15], the authors state that the mobility variation may play a dominant role. The result shown in Figure 8-5 is a good example as the thermally modified space charge flow.

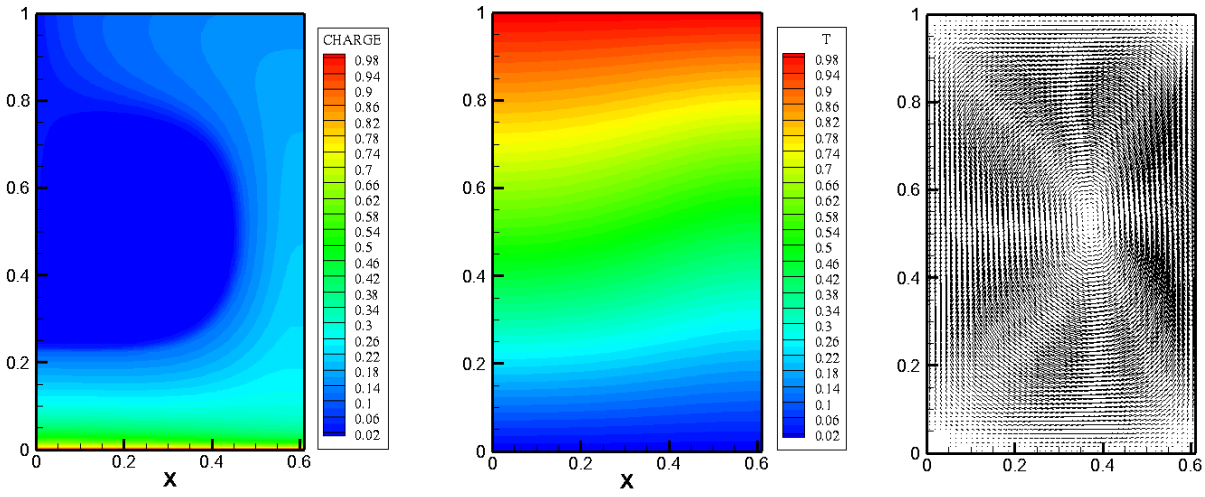

(a) Charge density isocontours (b) Temperature isocontours (c) Velocity field

Figure 8-4. Numerical results with T = 190, Ra = -20, Pr = 10, M = 50, C=10, N=0 and L=0

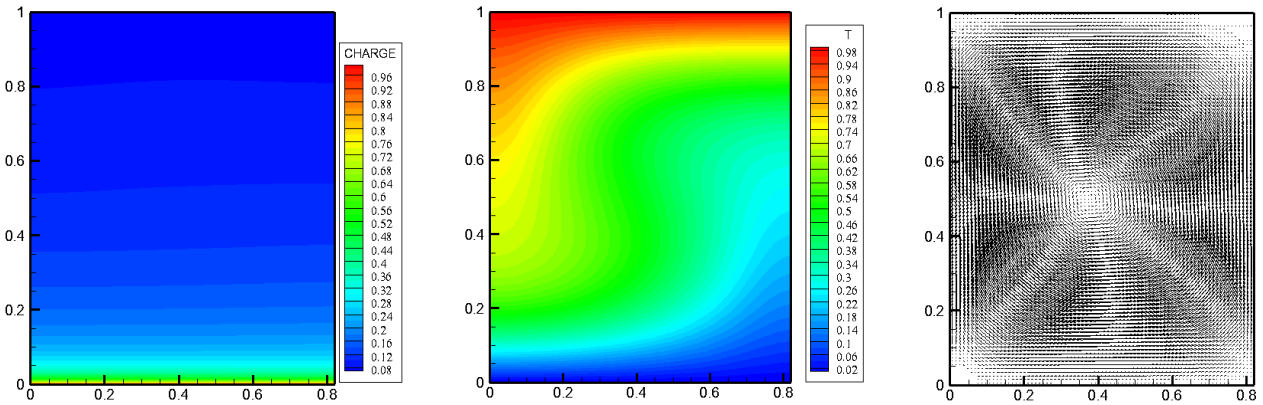

(a) Charge density isocontours (b) Temperature isocontours (c) Velocity field

Figure 8-5. Numerical results with T = 70, Ra = -20, Pr = 500, M = 5, C=10, N= 5×10^{-3} and L=0

8.3.2 Over-stable electro-thermal instability with a strong stabilizing gradient

Till now, all the problems we encountered can reach stationary pattern of motion at the onset of instabilities. The flow motion often manifests as cellular convection. On the other hand, there is another class of instability in which oscillatory motion prevails at the onset of instability. This class of marginal sate is named as overstability. In the ETHD system considered in the present study, the oscillatory instability has been observed through experiments [14] in 1968. Some attempts have been made to explain the occurrence of the oscillatory modes [14][301] based on charge conductivity model. Later, based on the mobility model for charge transport, the existence of over-stable instability has also been successfully predicted through the linear stability approach [181][182][302]. It has been shown that the over-stable mode is preferred for strongly stabilizing thermal gradient.

In this subsection, we use an example to show that our numerical tool can be used to simulate the over-stable electro-thermal convection. We choose a set of parameters for which the existence of the over-stable instability mode has been proved. In [182], the authors presented a figure showing the nature of the linear instability in corn oil for various ratio coefficients between temperature and mobility k_1 and injection strength C, see figure 2 of [182]. We selected one point from this figure, see below. The system injects ion from the below electrode and is heated from the above side. A strong Ra number is used to represent the strongly stabilizing thermal gradient.

$$C=1 \qquad T=3750 \qquad Ra=240000 \qquad \mathrm{Pr}=460$$

$$M=151.7 \qquad N=0 \qquad L=0$$

The hydrostatic equilibrium state is used as the starting condition. It is crucial to stress that the final regularly oscillatory solutions can only be obtained with this initial field rather than zero-field. The computational domain is a rectangle of size 0.988×1which is in consistent with the wavelength of the system. As the flow is oscillatory, we used a small time step 5×10^{-4}. A 100×100 uniform grid is used to discretize the domain. The point located at (0.05, 0.05) is selected as monitoring point.

In Figure 8-6 we have presented the evolution of velocity, charge density and temperature at the monitoring point. In addition, the amplitude of the velocity field of the whole system and its power spectrum analysis result are also presented. The transition from rest state to oscillatory convection is highlighted. In the power spectral curve, only one basic frequency is found.

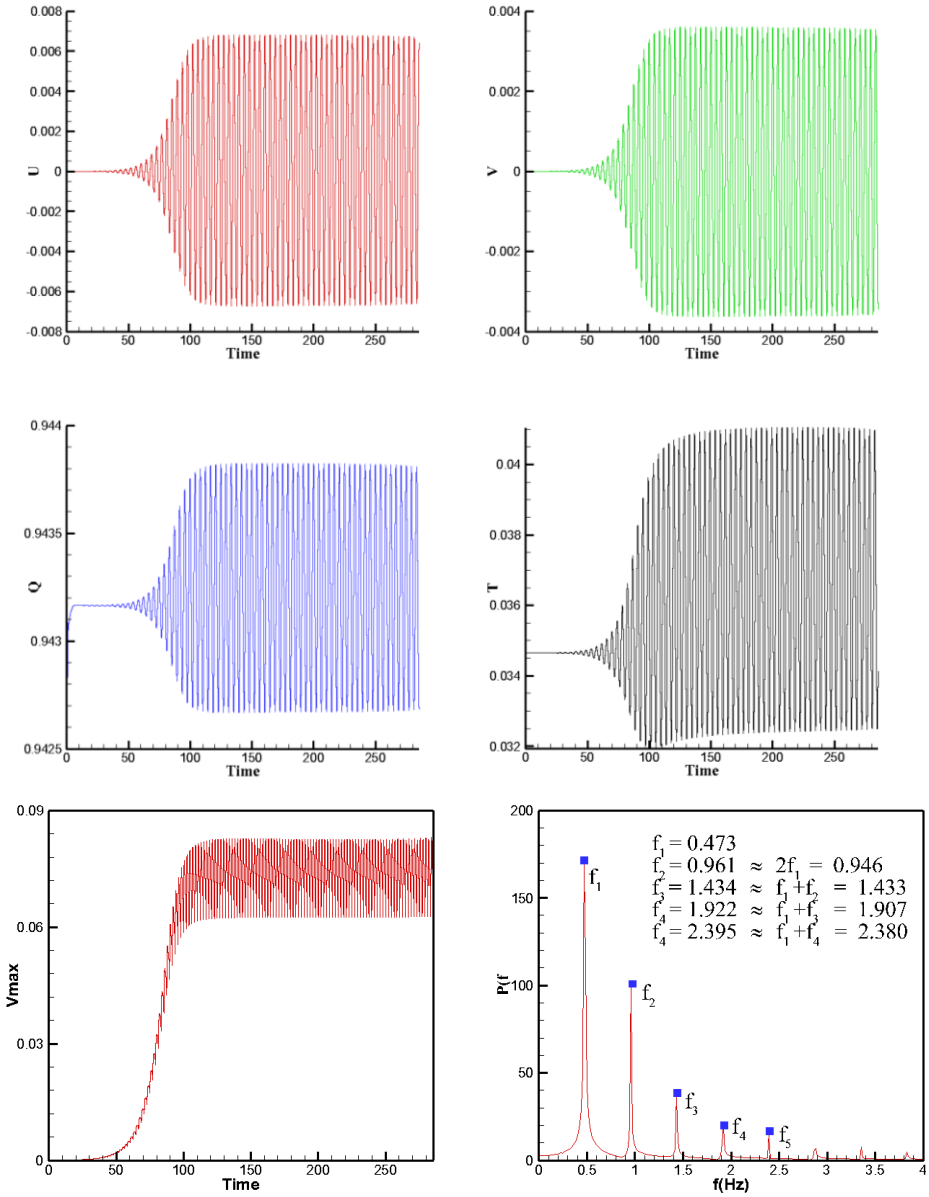

Figure 8-6. Illustration of the evolution of the horizontal velocity (U), the vertical velocity (V), the charge density (Q) and temperature (T) at the monitoring point, the evolution of the maximum velocity (Vmax) of the system and corresponding power spectrum.

Figure 8-7 shows the change of the charge density field, temperature field and stream function in a complete cycle. No charge free region is found. The convection velocity field is small, thus the transfer of the temperature and charge is limited. The successful prediction of such an over-stable motion is also a valid proof of our numerical method. It should be noticed that our results are the first numerical observation of over-stable motion in ETHD system.

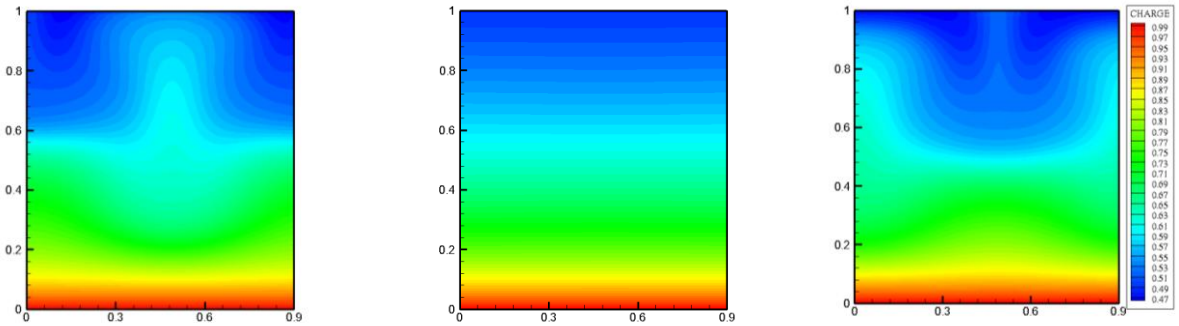

(a) Charge density field

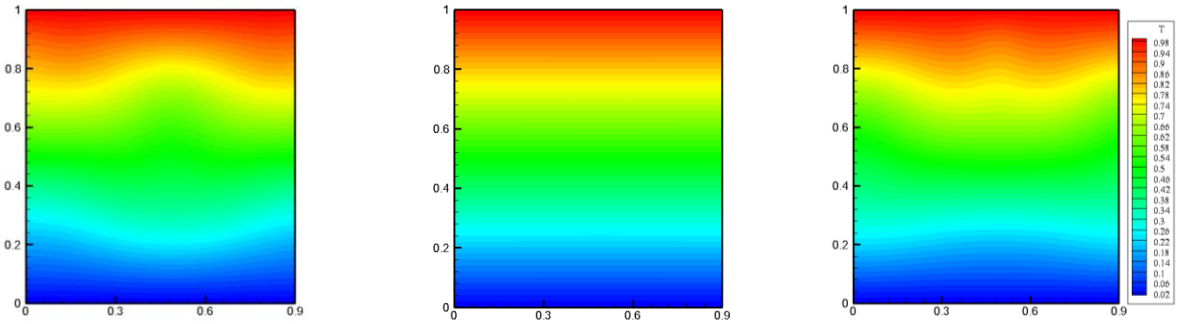

(b) Temperature field

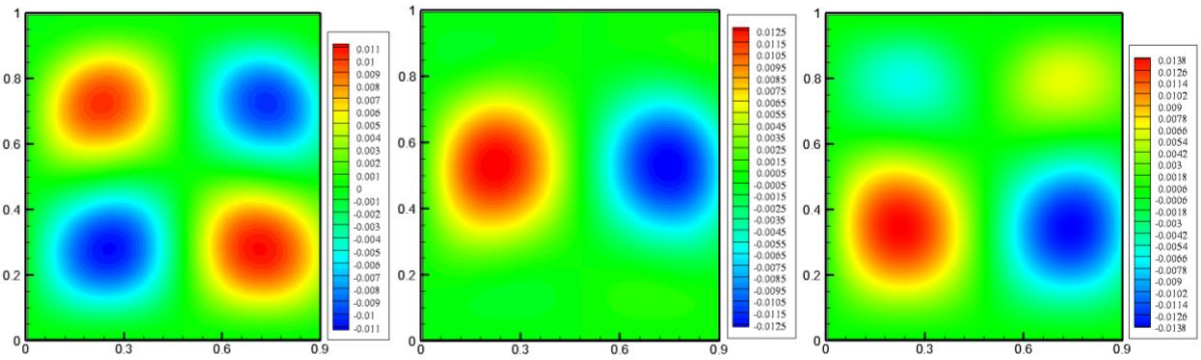

(c) Stream function

Figure 8-7. Numerical results of a over-stable linear problem in a complete cycle in a ETHD system

8.4 Subcritical feature of Rayleigh-Bénard instability induced by the presence of an electric field

In this section, we systematically investigate the problem of a dielectric liquid layer heated from below and simultaneously subjected to strong unipolar injection with our numerical tool. We try to numerically reproduce the neutral stability curve which separates the stable and unstable regions. In addition, the existence of nonlinear phenomenon and associated finite-amplitude bifurcation behaviour are highlighted in the case of the development of the Rayleigh-Bénard instability.

In the next subsection, features on the development of pure Rayleigh-Bénard and pure electro-convective instabilities are recalled and the neutral stability of the electro-thermo convection problem is analysed. The conditions for which the instability develops regarding the driving parameters *Ra* and *T* are discussed.

In this study, the featuring of subcritical bifurcations is mainly highlighted by the existence of the linear and non-linear critical instability criteria Ra_c and Ra_f respectively for thermo-convective instability and T_c and T_f for electro-convective instability. The computational strategy to determine these criteria is the same with what did with pure EHD problems and detailed in previous chapter.

For all the computations conducted in this study Pr=10 and M=10 and we are in the strong injection case with C=10. In chapter 4 and 5, we simulate the pure unipolar injection and pure Rayleigh-Bénard problems to show the effectiveness of our numerical tool in predicting both linear and nonlinear stability criteria. In principle, the nonlinear phenomenon can be expressed through discontinuous changes in heat flux, electrical current flow and the amplitude of velocity field. In the present study, the last one will be used as the indicated parameter. The second sets of simulations were to predict the Neutral stability curve in the *Ra*-*T* plane. In the concrete operation process, we fixed *T* parameters and selected several Ra numbers which were slightly above the theoretical critical one. To highlight the different bifurcation styles when unipolar injection and thermal gradient are simultaneously applied, we carefully chose three sets of (*Ra, T*) parameters to show the complete *Vmax*-*Ra* curves.

8.4.1 Recalling electro-convection and Rayleigh-Bénard convection

On Figure 8-8 we have depicted the development of the instability for the Rayleigh-Bénard instability (a) and electro-convective instability (b). The Rayleigh-Bénard instability is supercritical and the critical Rayleigh number Ra_c has been found numerically equal to 1706.6 which is very close to the critical value predicted by the linear instability of Chandrasekar: 1708 [275]. The electro-convective instability features the development of a subcritical bifurcation with a sudden jump for V_{max} from zero to 1.25 in non dimensional unit when the linear critical value T_c parameter is reached. From this state, when T is decreased the fluid stays in motion even for T under T_c. When T equals to the non-linear value T_f the flow recovers its rest state. The two particular values T_c and T_f denoted as linear and non linear critical values give rise to an hysteresis loop [153][276] which has been observed experimentally [19]. The linear and non linear phenomena are characterized respectively by a small amplitude and a finite amplitude. This basic difference between Rayleigh-Bénard and electroconvective instabilities lies with the different mechanism of transport of the temperature and of charge density respectively with the liquid at rest. For Rayleigh-Bénard heat diffuses whereas for electro-convective instability ions move with respect to the liquid with a finite velocity $K\vec{E}$ where K is the ionic mobility and $\vec{E}$ the electric field. The electric field strength increases with the distance from the emitter electrode and thus, the ion drift velocity $K\vec{E}$ increases too. As the electric charge is convected with a velocity $\vec{u}+K\vec{E}$, the regions where the liquid is moving upward will be more charged than the regions where the liquid is moving downward resulting in a electric torque and thus a convective movement in the

fluid. This convective movement will arise since the Coulomb force applied to each electric charge carrier overcomes the viscous damping friction.

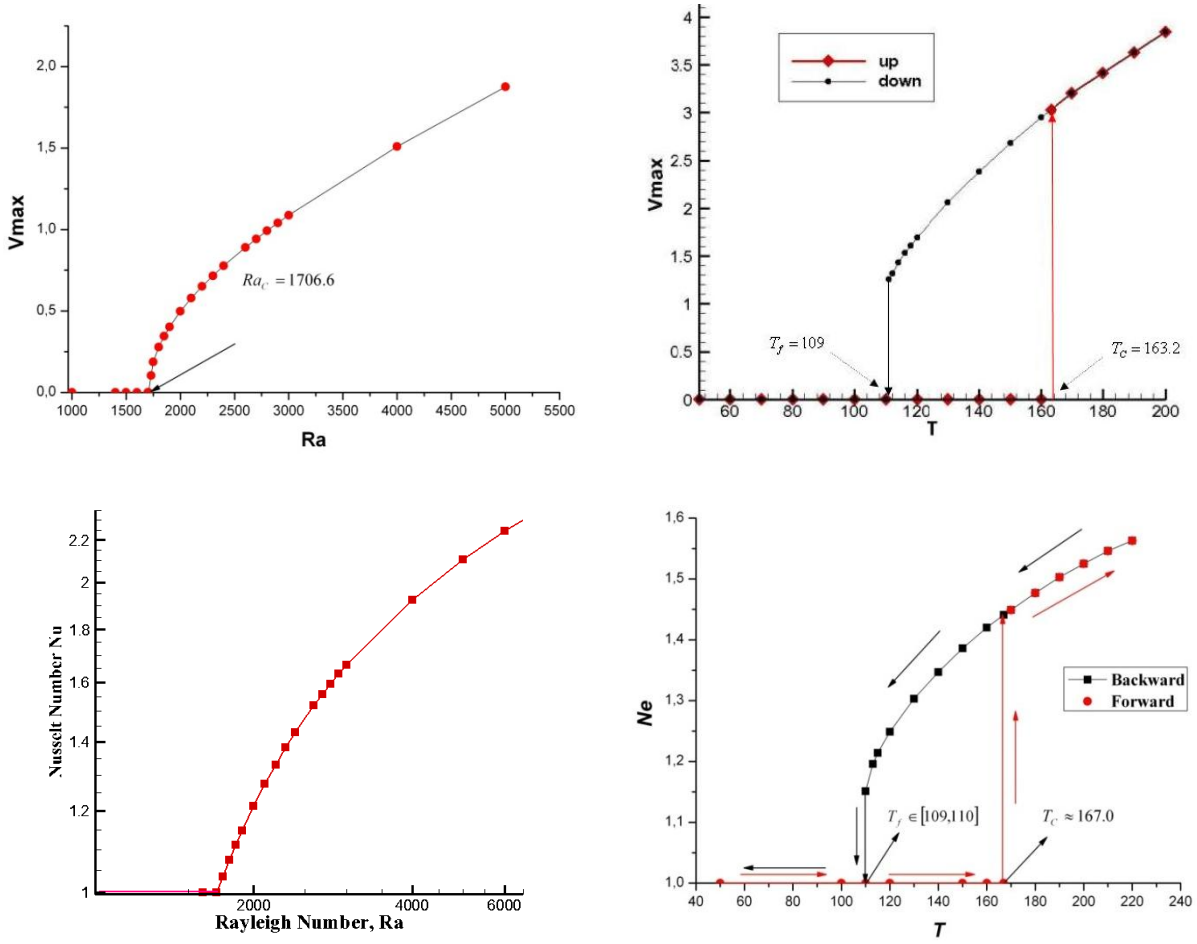

(a) supercritical thermo-convective instability (b) subcritical electro-convective instability

Figure 8-8. Maximum velocity versus *Ra* (a) and *T* parameter (b) featuring respectively the supercritical and subcritical bifurcation corresponding to pure thermo-convection and pure electro-convection flows

Once electro-convection takes place, ascending column are more charged that the descending one and ions are therefore carried by the liquid preferentially towards regions of ascending column. It results in the liquid a region void of charge [58]. It should be specified that this appearance of charged and uncharged adjacent regions is directly linked to the hyperbolic nature of the charge density transport equation. The existence of this region void of charge is responsible for the hysteresis loop and the featuring of the non linear criteria T_f [58]. This non linear instability mechanism has been also derived by Felici with its hydraulic model in the case of weak injection between two parallel plates [301]. Later Atten and Lacroix [148] extended the foregoing simplified model of Felici to the case of hexagonal cell and studied the nonlinear stability problem with a Galerkin method. They successfully predicted the existence of a nonlinear stability criterion as well as an hysteresis loop associated with the discontinuities in current and liquid velocities.

In strong injection C=10, the linear critical value T_c and non linear one T_f have been numerically found respectively equal to 163.2 and 109 while the predicted values provided by the linear

stability are 164.1 and 110 [144][148]. It is worth noting that these values are the closest one from the predicted values provided by the linear stability ever found by numerical simulations.

8.4.2 Neutral stability curve

When ion injection is from below and the liquid layer is also heated from below, it is easy to understand that the displacement of a fluid parcel is reinforced by the two mechanisms. To a simple approximation, the neutral stability curve can be expressed as a straight line,

$$Ra / Ra_C + T / T_C = 1 \tag{6-1}$$

where Ra_C corresponds to the critical Rayleigh number at $T = 0$, and T_C is the critical value in the pure EHD case. The more accurate curve deviates slightly from the above straight line considering the inconsistency of the critical wave-length at both ends. An accurate expression for the neutral stability curve is provided by Castellanos and Velarde, see Equation (11a) in [298], which has been also provided below for comparison. For the neutral stability, the following condition should be satisfied,

$$TC^2 \geq 1800 f_1(k) / k^2 - 9Ra / 98 f_2(k) \tag{6-2}$$

where k is the wave-number and

$$f_1(k) = \frac{k^4}{630} + \frac{4k^2}{105} + \frac{4}{5} \quad \text{and} \quad f_2(k) = \frac{k^2}{30} + \frac{1}{3} \tag{6-3}$$

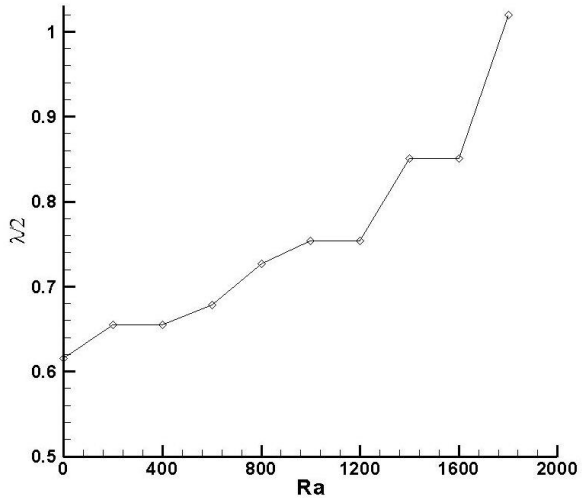

Figure 8-9. Critical wavelength versus Ra for both heating and injection from the bottom side case [57]

It should be emphasized that the variation of the critical wave-length brings some extra difficulties for the numerical determination of the neutral stability curve. It has been shown that the aspect ratio of the computational domain has an important effect on the critical T_c value in pure electro-convection [56]. With symmetrical boundary conditions, the determination of T_c would be close to the theoretical value 164.1 only when the aspect ratio will be multiples of the half

wave-length 0.614. But for a given (Ra, T) we do not know a priori the wave length of this electro-thermo convective problem which depends on the ratio Ra/T . In [57] the authors displayed the change of the wave length with Ra along the neutral curve, see Figure 8-9. It should be noted that the curve is obtained with the direct numerical approach and the curve is not smooth because of the finite computational domain. That explains why in order to limit discrepancy between numerical results and expected ones the domain has to be extended. It has been shown that this aspect ratio effect gradually fades with the increasing of L. In this study L=10 has been retained.

On Figure 8-10 is displayed the neutral stability curves obtained numerically and from expression (6-1). The maximum error is not greater than 7.2 % and the possible discrepancy is essentially due to the length L of the domain that we choose.

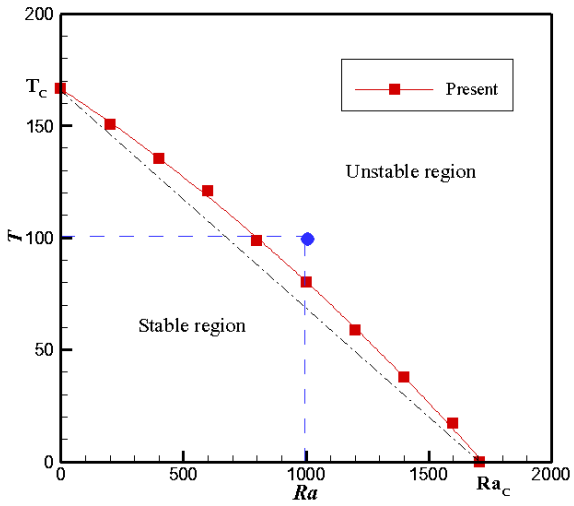

Figure 8-10. The neutral stability curve in the Ra –T plane

8.4.3 Subcritical bifurcation of the flow

On Figure 8-12 we have displayed the maximum velocity in the domain versus Ra for different values of the T parameter.

For T=80 a subcritical instability occurs, associated with a hysteresis loop highlighting a linear Ra_c and non-linear critical values Ra_f. It is worth noting that for Ra=Ra_c=1000 a convective motion takes place whereas we are under the theroretical critical value Ra_c=1708 predicted in the case of a pure thermal problem. When Ra is decreased below 1000 the convective motion still occurs until Ra_f=750 where it stops. Let's define the difference between the linear critical value Ra_c and the non linear one Ra_f as Δ and $V_{\max C}$ the maximum value of the vertical velocity obtained for Ra_c. For T=80, $\Delta = 250$ and $V_{\max C}$=1.107. For T=30, Δ decreases and equals to 4 and $V_{\max C}$=0.325. If T is further decreased the difference between Ra_c and Ra_f will vanish and $V_{\max C}$ will tend to zero. For T=10 we obtain $\Delta = 0$ which means that the fluid is suddenly put into motion from rest state with a subcritical bifurcation as the velocity jump shows it. For T=0 i.e. pure thermal problem, the subcritical bifurcation turns into a supercritical transition and we recover the classical bifurcation observed in pure Rayleigh-Bénard flow. In our simulations Ra_c in the case T=0 has

been found equal to 1706.6 and has to be compared with the theroretical critical value Ra_c=1708 provided by the linear stability analysis.

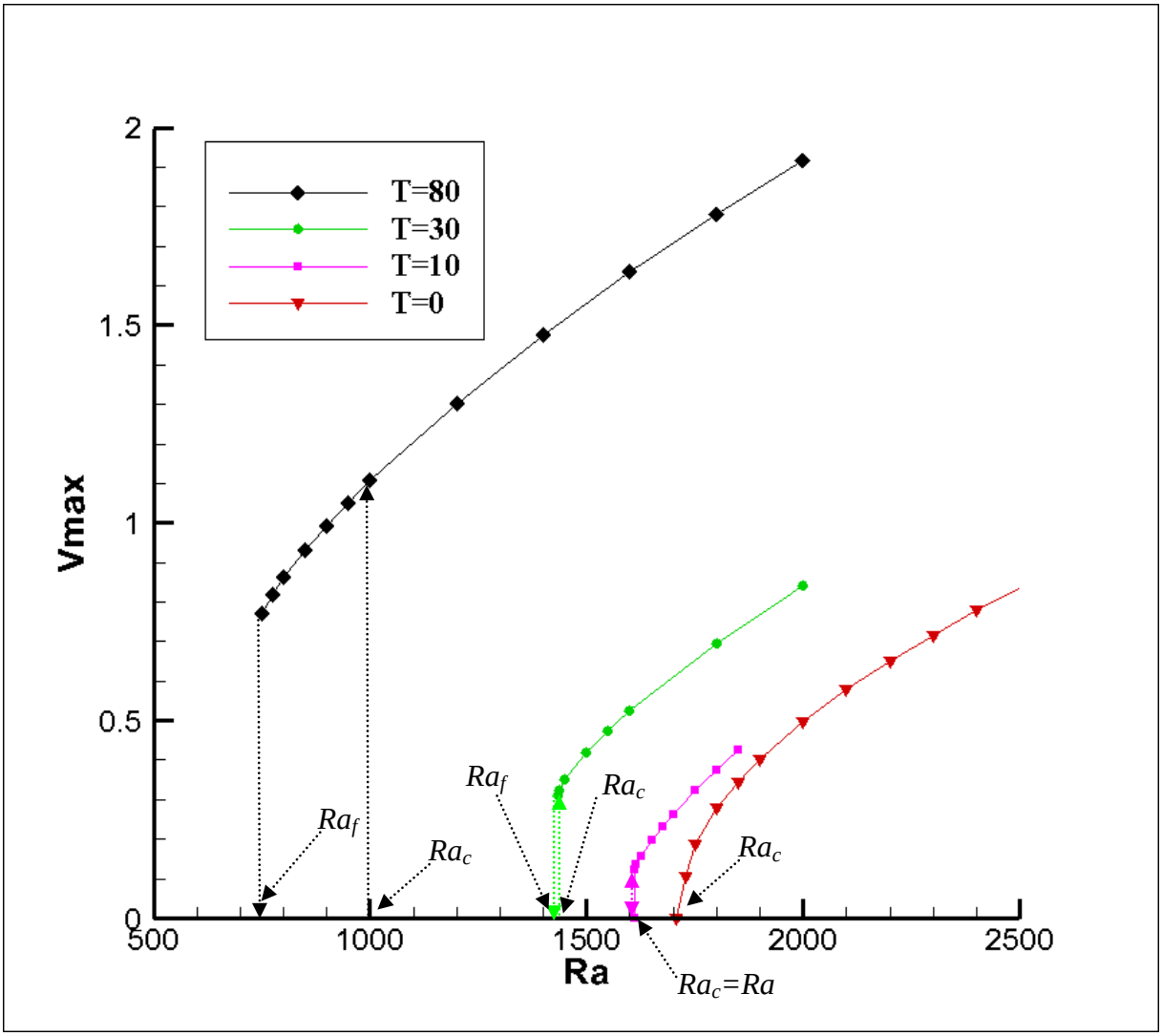

Figure 8-12. V_{max} versus *Ra* for different values of *T* parameter.

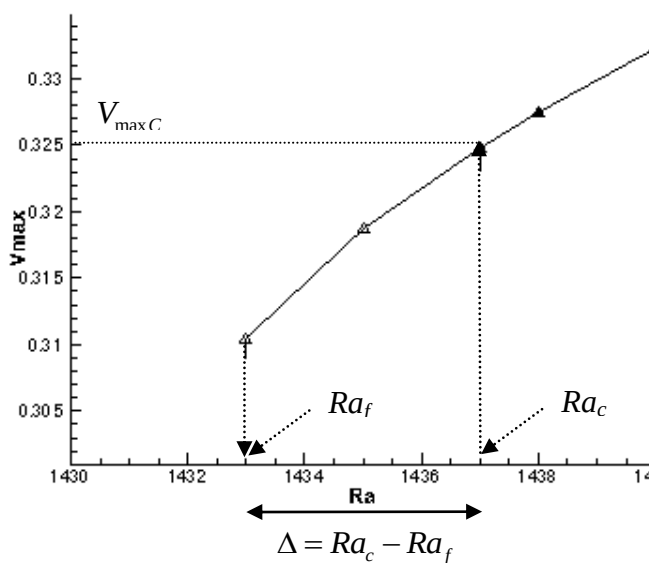

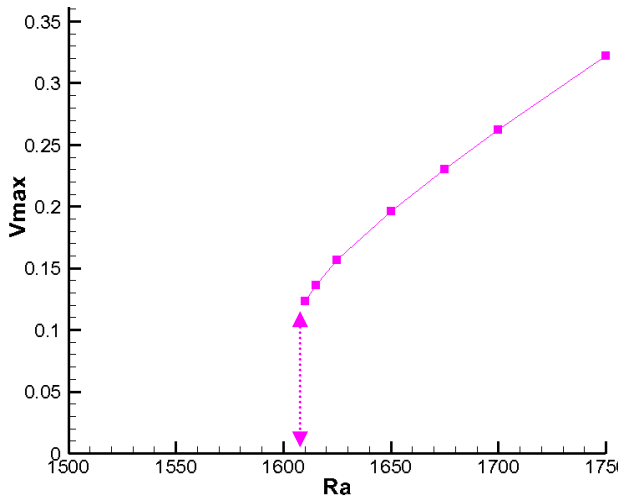

T=30 T=10

Figure 8-13. V_{max} versus Ra (*zoom* of the previous figure for cases T=30 and T=10)

8.4.4 Flow structure of electro-thermo-convection with both heating and injection from the bottom electrode case

Under the theoretical critical values provided by the linear stability analysis Ra_c=1708 for a pure thermal problem and T_c=164.1 for a pure electroconvective problem no movement occurs. The combined effects of a thermal gradient and an electric field simultaneously applied to the horizontal dielectric liquid layer leads to a complex physical flow interaction and can completely change the stability conditions. Indeed, for some particular values of the Rayleigh number and T parameter under the threshold values, one can observe convective movements.

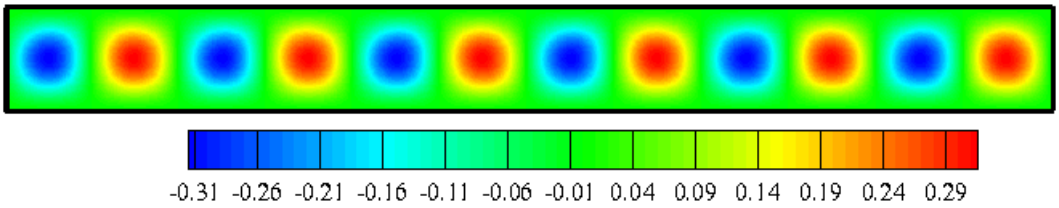

(a) Stream function

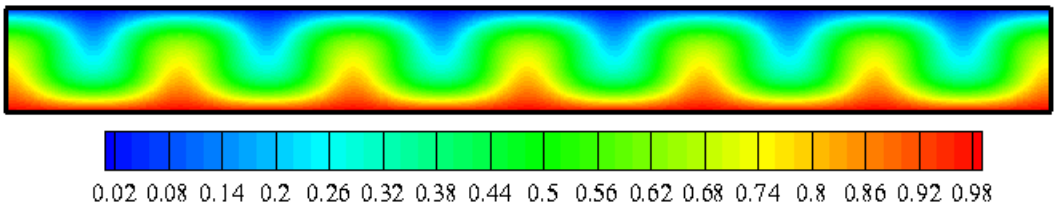

(b) Temperature field

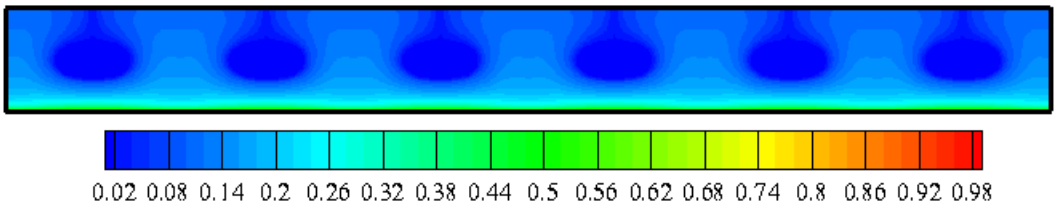

(c) Charge density field

Figure 8-14. Steady state isocontours of stream function, temperature and charge density Ra=1000, T=80.

On Figure 8-14 we have depicted the flow structure for Ra= Ra_c =1000 and T=80. Figure 8-14(a) represents the stream function, 8-14(b) the isocontours of temperature and 8-14(c) the isocontours of charge density. On this figure we clearly show the convective motion in the domain. One have to keep in mind that for the pure thermal problem with Ra=1000 there is no motion and the fluid stays at rest. It is the same for a pure electro-convective problem with T=80. The number of

convective cells in the domain depends on the width of each cell which is equal to the half wavelength $\lambda/2$ of the most unstable mode. For T=80 we observe 12 cells (Figure 8-14a) and the flow is mainly driven by the Coulomb force. For a pure electro-convective problem ($Ra=0$) the expected number of cells for this domain length, should be 16 which gives a half wave length $\lambda/2$ equal to 0.625. This value has to be compared with 0.614 the value predicted by the linear stability analysis.

For the case T=10, Figure 8-15a displays 10 cells which is the exact number of cells expected in the case of a pure thermo-convective problem (T=0) which has been shown in Figure 8-16. Indeed in this situation the half wave length is 1.0.

Between this two limit values: 1.0 and 0.614 the half wave length of the problem changes along the neutral stability curve (Ra-T) of the Figure 8-10.

It is worth to note that for both cases the Rayleigh number is below the theoretical limit 1708 but a convective motion occurs.

For the case (Ra=1000, T=80) the maximum value of the stream function is 0.29 much greater that for (Ra=1600, T=10) which is only 0.036. It indicates that for the former case the convective motion is greatly enhance compared to the latter one despite that the Rayleigh number is higher.

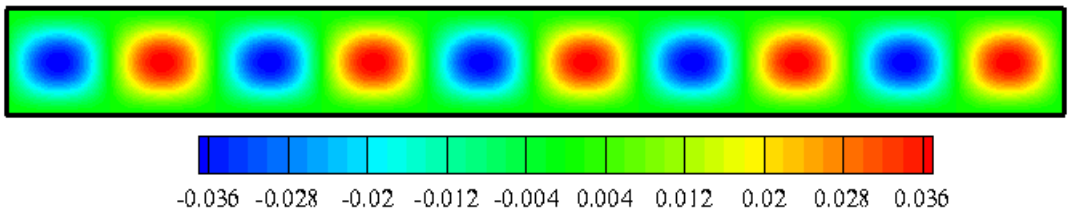

(a) Stream function

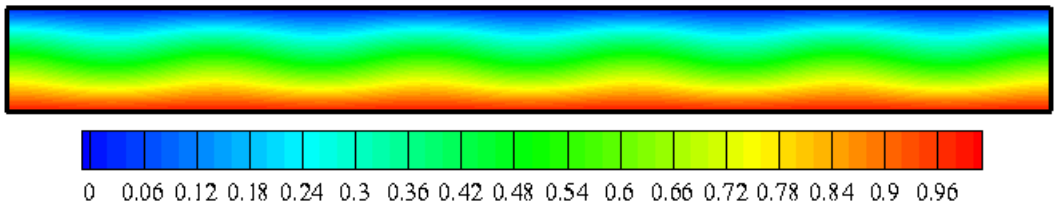

(b) Temperature field

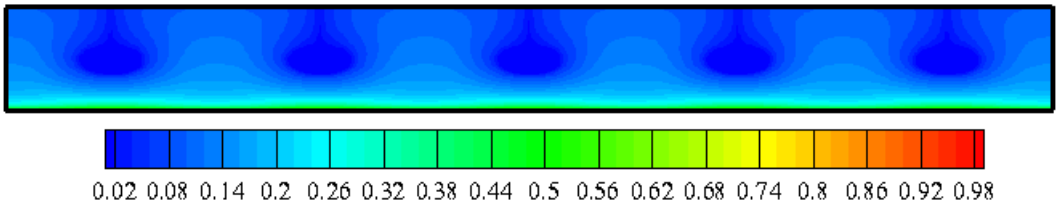

(c) Charge density field

Figure 8-15. Steady state isocontours of stream function, temperature and charge density Ra=1600, T=10.

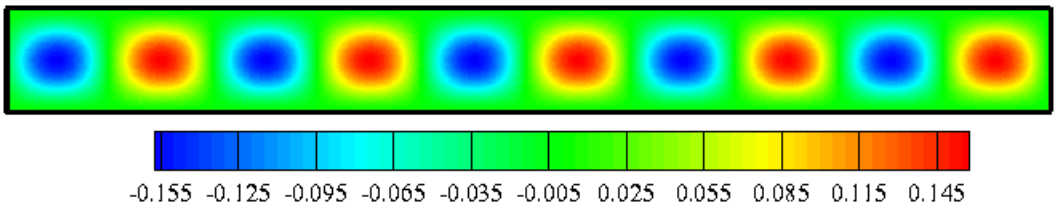

(a) Stream function

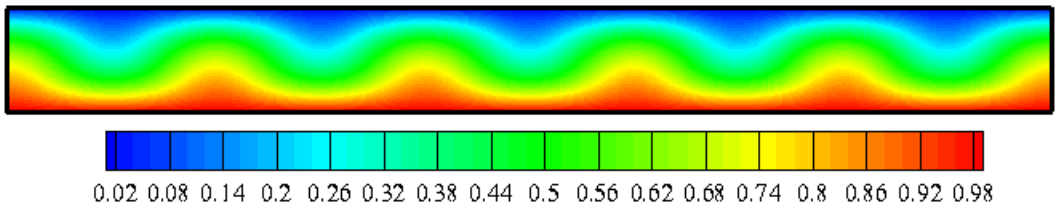

(b) Temperature field

Figure 8-16. Steady state isocontours of stream function, temperature on pure thermal problem: *Ra*=2000, *T*=0.

In the case (*Ra*=1000, *T*=80) electro-convection enforces its foot print on the flow (number of cells and temperature field figure 8-14b which matches perfectly with the charge density snapshot Figure 8-14c).

In the case (*Ra*=1600, *T*=10) the flow is mainly governed by the buoyancy force and thermo-convection.

The void region in the charge density contourmap is magnified on Figure 8-17, where only the *q*=0.05 isocontour is displayed.

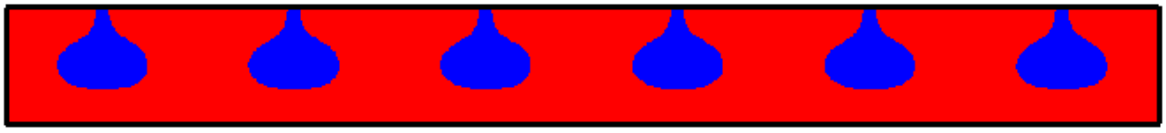

Figure 8-17. *q*=0.05 isocontours of charge density contour map *Ra*=1000, *T*=80.

It has been shown [151] that this region void of charge was responsible for the hysteresis loop and the existence of the non linear criterion T_f in pure electro-convective instability. This explanation is extended for the case of electro-thermo convective problems where a subcritical bifurcation with an associated hysteresis loop featuring a non-linear criteria Ra_f occurs as well. The existence of this non-linear criteria Ra_f is therefore also due to this region void of charge.

If we check the total amount of void region through the entire domain versus *T*, Figure 8-18, we observe that the decrease of *T* induces a decrease of this void region.

Figure 8-12 has shown that when *T* was increased the values of the non-linear and linear criteria respectively Ra_f and Ra_c decrease. In the same time Δ and $V_{\max C}$, which emphasize in a way the amplitude of the hysteresis loop, increase. This behaviour magnifies in fact the development of the

subcritical bifurcation and is directly related to the total amount of the region void of charge in the domain.

This diminishing of the void region inducing a decrease of Δ and $V_{\max C}$ has already been pointed out in [88]. In this paper the authors related the decrease of the void region to the diffusion mechanism for the charge transfer which was incorporated in their model. In our case the mechanism is different because it is only due to the value of the *T* parameter. But in any case the consequence on the subcritical bifurcation characterized by Δ and $V_{\max C}$ is the same.

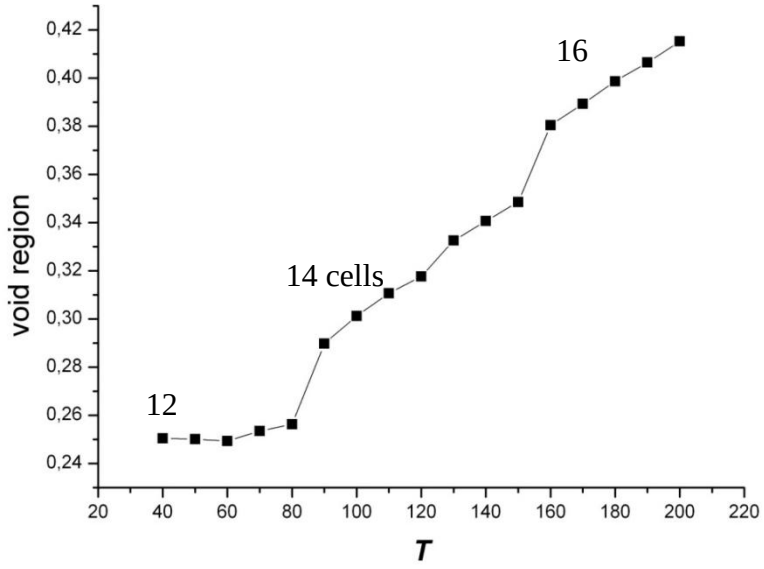

Figure 8-18. Total amount of the void region *of* the charge density contour map versus *T* for *Ra*=1000.

T = 30	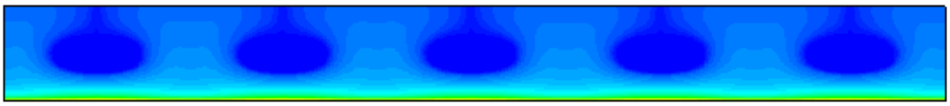
T = 70	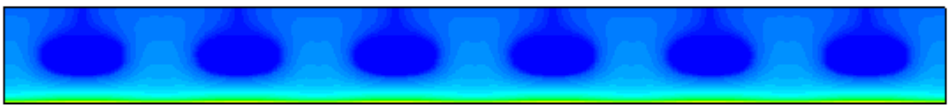
T = 140	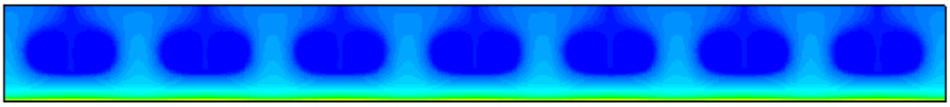
T = 200	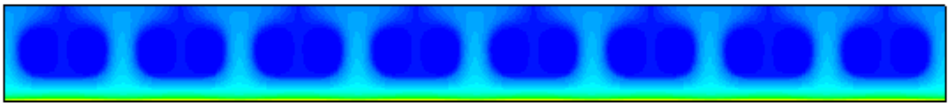

Figure 8-19. Snapshot of the charge density contour map for different T which highlights the number of cells for *Ra*=1000.

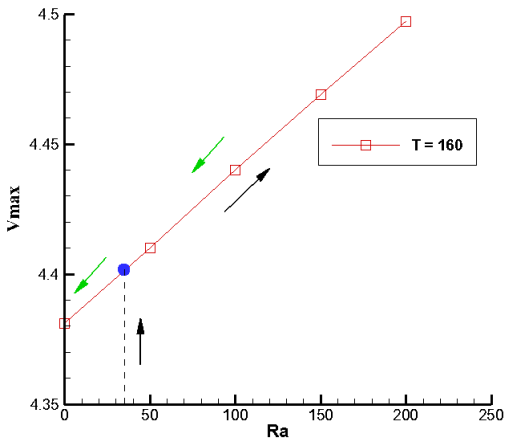

Figure 8-20. V_{max} versus *Ra* for different values of the *T=160*

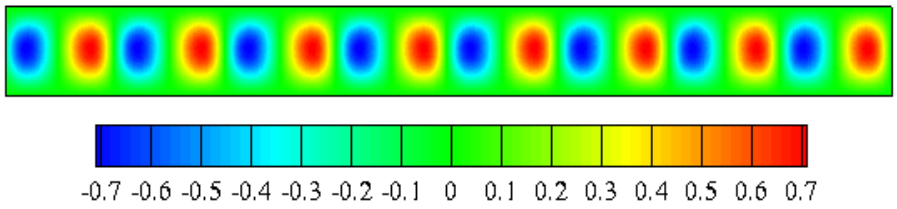

(a) Stream function

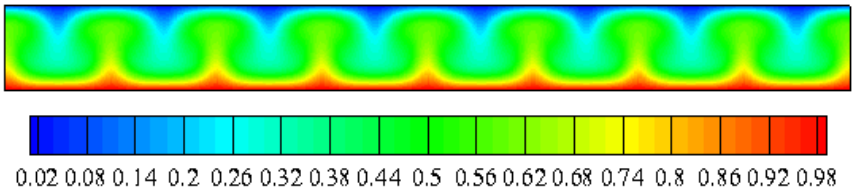

(b) Temperature field

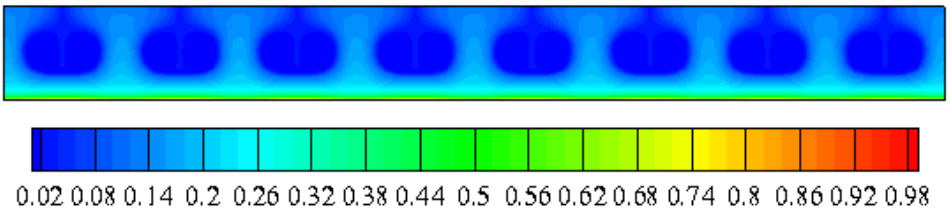

(c) Charge density field

Figure 8-21. Steady state isocontours of stream function, temperature and charge density field: *Ra*=0, *T*=160, the results are obtained by restarting the computation from *Ra = 250, T = 160*

The slight jumps which are observed on the curve for *T*=90 and *T*=160 correspond in fact to the change of wave length λ of the most unstable mode which is actually related to the number of convective cells in the domain. Indeed it is observed on Figure 8-19 that when *T* increases the number of cells in the domain increases too. Conversely when *T* is decreased the number of cells diminishes which means that the half wave length increases to reach 1. (10 cells) observed for *T*=0

which corresponds to the pure thermo-convective problem (see Figure 8-16a). We have to keep in mind that in strong injection for pure electro-convective problem the half-wave length is 0.614. (16 cells should indicate a half wave length of 0.625).

At the end of this subsection, we present an interesting result. We first started the computation with *T=160* and *Ra=250*, and we obtained a steady cell convection. Then we gradually reduce the Ra number to 0 and the results are summarized in Figure 8-20. The most interesting point is even when *Ra=0* the flow is still on motion which means the heat is completely transferred through the Coulomb force. Thus the hysteresis loop shown in Figure 8-20 is not complete. In other words, there is only up-jump part. To completely damp out the convection, we need to reduce the *T* parameter or reverse the direction of the temperature gradient. The flow structure and temperature field is shown in Figure 8-21.

8.5 Heat transfer enhancement induced by electrically generated convection

In this section, we quantitatively show the heat transfer enhancement phenomenon due to strong unipolar charge injection in a rectangular box configuration. The aspect ratio of the box is set to be 2 with no-slip boundary conditions on the lateral walls.

The case of a strong injection *C=10* is considered here. The variation of ionic mobility and permittivity is taken as independent of temperature so that *N=L=0* and the dielectric force could also be disregarded.

We start from rest and all the quantities are set to zero. At *t*=0 the liquid is heated from below and the electric potential difference between the two electrodes is applied and the electric charges are injected in the bulk.

From the linear stability analysis, it appears that when submitting the liquid layer to charge injection, it is possible to induce a convective motion whereas the Rayleigh number is under the threshold value 1708. Then the question of enhancing the heat-transfer through this mean arises naturally. We have computed the mean Nusselt number defined as below along the hot wall.

$$\overline{Nu} = \int_0^L \left(\frac{\partial \theta}{\partial y} \right)_{y=0}$$

From Figure 8-22 it is interesting to note that the mean Nusselt number is noticeably increased with *T* as it has been confirmed by [172][292][294].

Figure 8-23 (a) gives the evolution of this mean Nusselt number versus Rayleigh number for different values of *T*. Figure 8-23 (b) represents experimental results performed by Pérez et al [294]. First we observe a similar tendency for both numerical and experimental results. From these curves another important point can be emphasized. Above a given range of Rayleigh numbers around 15000, and for *T*>0 increasing the Rayleigh number does not increase the Nusselt number much. This tendency is more visible on the experimental curves (see Figure 8-23 (b)). In other words the Nusselt number becomes almost independent of the Rayleigh number for high enough values of *T*.

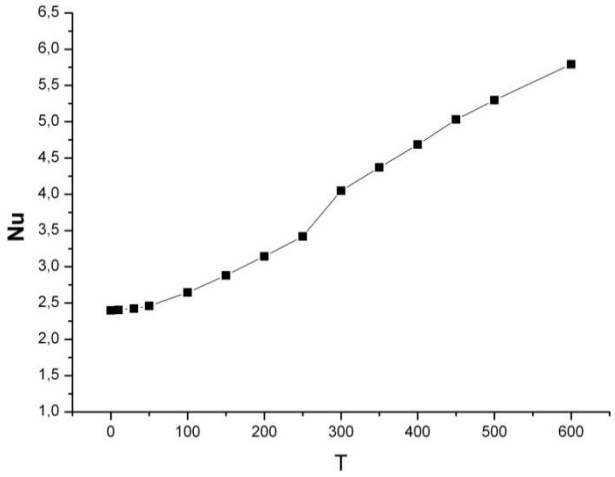

Figure 8-22. Mean Nusselt number versus *T* for *Ra*=10000, *Pr*=10.

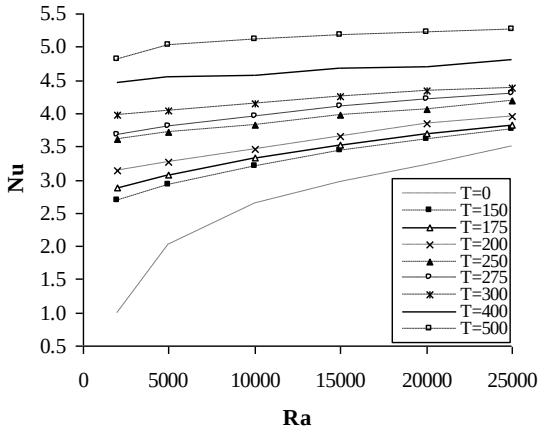

(a) numerical results

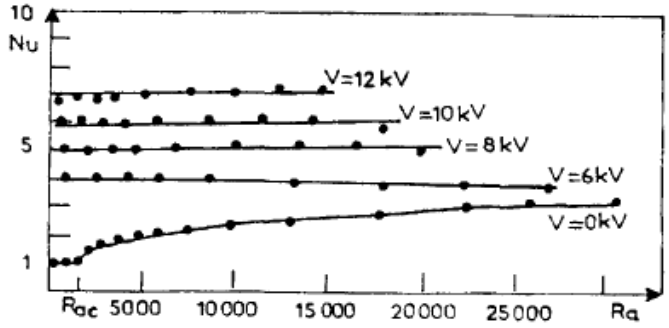

(b) experimental results Pérez et al. [12]

Figure 8-23. Mean Nusselt number versus Rayleigh for different values of the *T* parameter, *Pr*=10.

In Figure 8-24, we present the time evolution of the maximum vertical velocity component of the flow at *Ra* = 10000 for several values of *T* as well as the flow structures in terms of streamlines isocontours.

Let us notice that the aspect ratio is 2. For pure thermal problem (*T=0*) as expected we obtain a steady solution with two thermo-convective cells. When *T* is increased to 100 and 200 the steady value of the maximum velocity is visibly augmented. The increase of the velocity field explains the heat transfer enhancement in the range of $T \in (0,250]$. Indeed in natural convection in enclosure the velocities are small and when the electric force is generated these velocities are immediately and significantly augmented [161]. When we further increase *T* value to 300, the steady two-cell structure starts to oscillate. Theses oscillations indicate a better fluid mixing, which can also contribute to the heat transfer enhancement effect. A significant change is observed with *T* =350 and *T* = 400 in the flow structure. Indeed we can observe that the flow bifurcates to a four cells structure. For *T*=350 the flow is steady while for T=400 these four cells start to oscillate too as in the case *T*=300.

This four cells pattern will indubitably contributes to increase the vertical activity of the flow and hence the fluid mixing. This explain too why the heat transfer can be increased consequently.

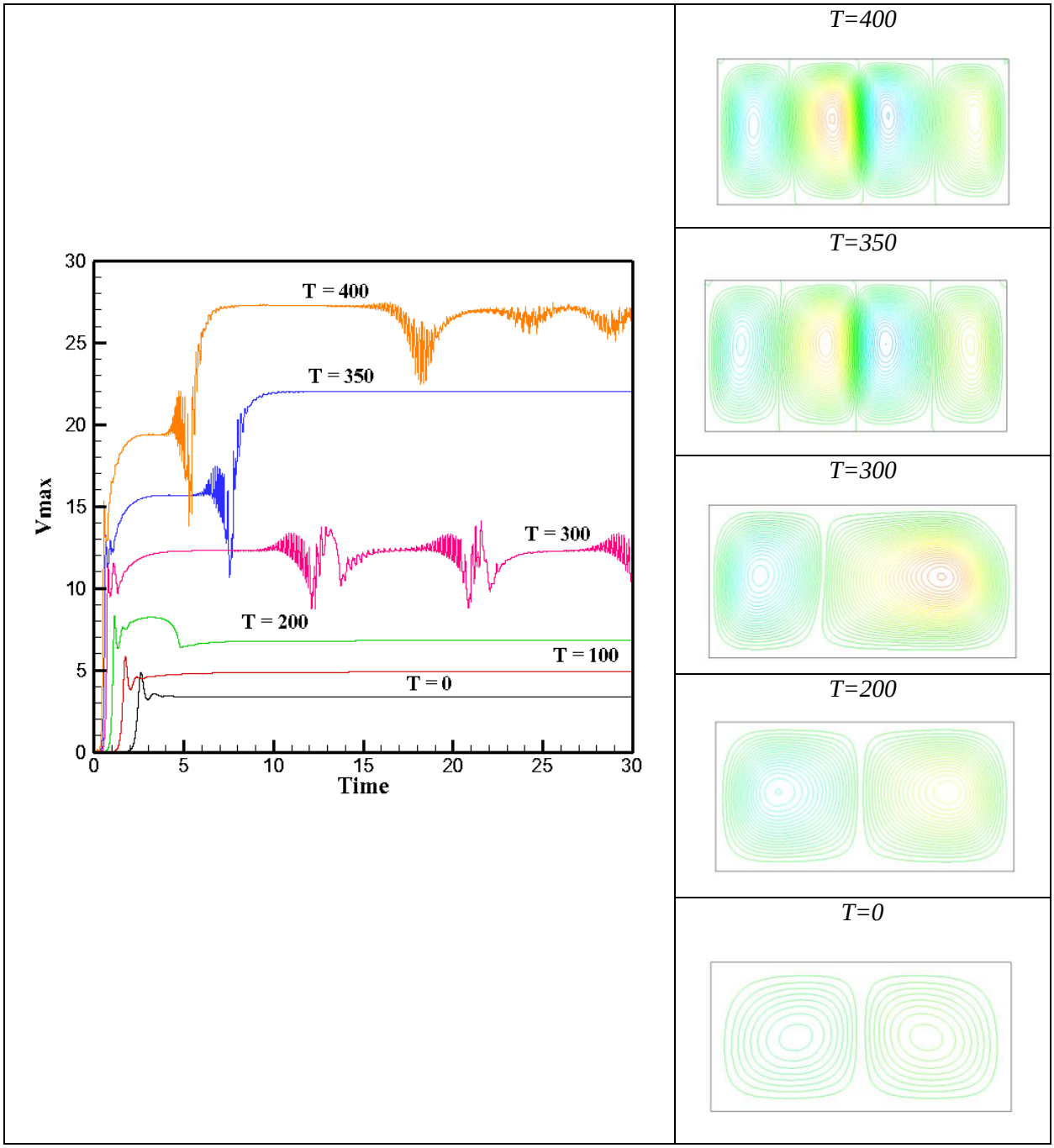

Figure 8-24. Time history of the maximum of vertical velocity with the associated flow structure depicted by the streamlines for *Ra*=10000, *Pr*=10 and different values of the *T* parameter.

In this final numerical experiment, the fluid is still heated from below and we consider electric charge injection from the bottom or the top.

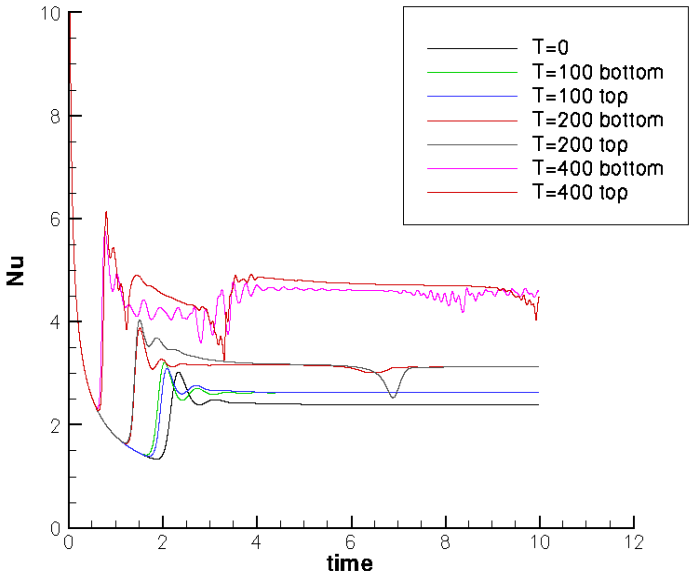

Figure 8-25. Mean Nusselt number time history for *Ra*=10000, *Pr*=10.

In Figure 8-25 the time evolution of the mean Nusselt number for *Ra* =10000 and for different *T* values is presented. We can notice that the value of the mean Nusselt number is notably increased in comparison with the reference case of the pure thermal problem for which *T*=0. For *T*=100 and *T*=200 after a brief transient period a steady state is reach and the final value of the Nusselt number is nearly the same whatever injection is from bottom or top. We observe an augmentation of the mean Nusselt number and therefore of the heat transfer of 10.4% for *T*=100, 30.96% for *T*=200 and 96.23% for *T*=400 with injection from the top. This increase of the mean Nusselt number is directly linked to the dynamic mixture induced by an increase of the vertical activity generated by the development of the electro-convective instability.

8.6 Conclusions

The typical problem considered in this chapter is a dielectric liquid layer simultaneously subjected to thermal gradient and unipolar charge injection. The whole set of governing equations associated with the electro-thermo convective phenomena is solved directly with a finite volume method. An original numerical procedure based on total variation diminishing (TVD) scheme is implemented to compute the charge density distribution.

The numerical approach was firstly verified with two stability problems (one is stationary and the other one is over-stable) which had been tackled with the linear stability analysis approach. A good agreement was found between our numerical values and theoretical ones. In addition, the over-stable flow of the ETHD system is verified with a direct numerical solver for the first time.

The numerical solver then is used to systemically analyze the linear and nonlinear stability of the injection mode when both heating and injection are from the bottom electrode. The neutral stability curve which separates the stable and unstable regions is successfully reproduced. The existence of nonlinear phenomenon and associated finite-amplitude bifurcation behaviour are highlighted in the

case of the development of the Rayleigh-Bénard instability. It is shown that subcritical bifurcation with a hysteresis loop may occurs for suitable values of the electrical parameter T. The detailed flow structure, the charge density, stream function and temperature fields involved in this problem are also presented.

Finally, the numerical approach is used to investigate the effect of the charge injection on the heat transfer in a dielectric liquid layer. The numerical results show that the charge injection significantly increases the heat transfer accordingly to several experimental results from the literature. Injection from the bottom electrode of the upper one leads to almost the same enhancement. The Nusselt number becomes almost independent of the Rayleigh number for high enough values of T. Our results are in a good qualitative agreement with the available experimental data.

Chapter 9 Summary and Conclusions

9.1 Achievements and Findings

A direct numerical tool based on finite volume method has been developed to simulate electro- and electro-thermo convective phenomena of a dielectric liquid subjected to unipolar injection and a thermal gradient. The whole set of governing equations includes charge density equation, Poisson equation, Navier-Stokes equations and energy equation. All equations are rewritten in the form of a so-called generic equation describing a general unsteady convection-diffusion transport of a conserved quantity.

The first part of this thesis consists in discussion on the discretization schemes about this generic equation. One of the aims of this study is to introduce some recently developed convective and diffusive schemes to enable numerical simulation of charged coupled problems. Considering the hyperbolic nature of the charge density equation, we focus on the Total Variation Diminishing (TVD) type high-resolution scheme which can accurately capture the possible high gradient of the charge distribution. For diffusion term and Poisson equation, we adopted a newly-developed Improved Deferred Correction (IDC) scheme which can be applied to extremely distorted meshes. The second part is to apply our numerical approach to study the flow motion of dielectric liquid due to unipolar injection and thermal gradient.

Numerical schemes

1. The unified approach for TVD-type bounded higher-resolution convection scheme is applied to the unsteady pure convection problem to compare the effectiveness, accuracy and computational cost. It is found that all these high-resolution schemes can avoid the traditional high-order schemes' oscillation problem and can largely improve the accuracy of the results in different dimensions and under different background flow fields. Moreover, there are significant differences of accuracy and computational cost among different schemes, and the MUSCL, SMART and UMIST schemes are recommended.

2. Three widely used methods for the calculation of diffusive flux: the coordinate transformation method, the surface decomposition method and direct gradient evaluation method have been revealed to be closely related to each other in two-dimensional non-orthogonal grid system. The performance of the original IDC scheme has been improved by using 2^{nd} order gradient evaluation method and appropriate boundary condition treatment.

Electro-convection

3. Numerical simulations have been undertaken to characterize the development of subcritical electroconvection instability that occurs in a plane layer of a dielectric liquid subjected to unipolar injection. The linear and non-linear stability parameter respectively T_c and T_f that we obtained numerically are very close from the ones predicted by the stability analysis. Our results have been compared with the ones computed by all the available numerical studies in the literature. It is observed that our results are significantly more accurate than the other previous ones.

4. Some difficulties were met for the weak injection case, though we can still obtain a good estimation for T_c. The flow structure is found to highly depend on M parameter. Only in the range $M \in [5,\ 10]$, the flow tends to be a quasi-steady state when T is slight above T_c. Otherwise, the motion is very chaotic and there is distinct discrepancy for the non-linear criterion T_f, between the predicted value of the hydraulic model and our result.

5. Some further studies have been undertaken with the strong injection case.

    1) The successive instabilities and the way to the chaotic state has been defined: no motion → steady one cell → periodic one cell → steady two cells →periodic two cells → pseudo-periodic two cells → chaotic (including plumes).

    2) The effect of the diffusion mechanism for charge density transport on hysteresis loop (including T_c and T_f) and the flow structure of finite amplitude convection has been shown.

    3) The stabilizing effect of the lateral walls on the linear and nonlinear stability criterion has been revealed. It is also found that the overall structure of the flow pattern that develops when the T number exceeds its critical value highly depends on the aspect ratio of the physical domain, especially when this ratio is small.

    4) A three-dimensional case has been provided to show the extension method of our numerical algorithm. The three-dimensional structures of the convection cells are shown.

Electro-thermo-convection

6. Our numerical approach for electro-thermo-convection was verified with a stationary and an over-stable stability problem which have already been tackled with the linear stability analysis approach. A good agreement was found between our numerical values and theoretical ones. The over-stable flow of the ETHD system is observed with a direct simulation approach for the first time.

7. Taking the case that both heating and charge injection are from the bottom side as the example, a detailed analysis about the linear and nonlinear stability was done. The neutral stability curve which separates the stable and unstable regions is successfully reproduced. The existence of nonlinear phenomenon and associated finite-amplitude bifurcation behaviour are highlighted.

8. Heat transfer enhancement by strong unipolar injection has been demonstrated. A good agreement has been found compared to some experimental results in literature.

9.2 Improvements and Extensions

Since our numerical solvers have been proved to be efficient, some direct application jobs can be done in near future.

1. Numerical studies with pure weak unipolar injection. Some further studies are needed to explain why the flow structure in weak injection highly depends on M parameter or electric Reynolds number.

2. The non-autonomous injection is closer to the practically physical problems. Though our numerical solver incorporates modules of non-autonomous injection based on some injection laws, numerical tests and studies have not been done yet.

3. The three-dimensional computation of strong unipolar injection. An important goal of 3D simulation is to observe the regular hexagonal cell. Till now, we only observe the irregular hexagonal cell in a rectangle of a size of $LX: LY: LZ = 4: 1: 4$. Thus we plan to further increase the computational domain to reduce the constraint of the boundary sides on the flow structure.

4. The combining effects of charge injection and thermal gradient on dielectric liquid can be divided into different situations. In this study, we only discuss one of them (both heating and injection are from below electrode) in details, some more works should be done with other heating and injection modes.

5. There exist a large number of non-dimensional parameters in a complete electro-thermo-hydrodynamics system, especially when the fluid properties, charge mobility and dielectric constant are temperature-dependent. Some extra studies are required to establish the influence of different non-dimensional parameters, especially on the flow stability.

This present study mainly concerns about the numerical aspect and the research problem is classic but simple. Some related physical problems may be taken into account in the coming future,

1. Direct numerical simulation of dielectric electrohydrodynamic convection in a blade-plane

configuration and coaxial wire cylinder geometry.

2. Numerical studies of double injection with recombination.
3. Numerical studies of linear and nonlinear electroconvection under AC electric field.
4. Dissociation-injection conductivity model for pure electro-convection and electrothermal convection.
5. Instability at the interface between two immiscible dielectric fluid layers subjected to charge injection and stability of a droplet subject to an electric field.
6. Rose-window instability in a low conducting liquid.
7. Plasma discharge numerical simulation. Our tools may be easily extended to deal with numerical simulation of plasma discharge phenomena.

Some numerical improvements and extensions have to be performed to improve the capability of the solvers.

1. To deal with fine meshes and large computational domain in 3D situation, the code must be parallelized.
2. Turbulence modeling. It has been shown that full 3D electroconvection is more chaotic in two dimensions and a length scale distribution exists. Thus some turbulence model should be taken into account to compute turbulent 3D electro- and electro-thermo- convection in dielectric liquid. Large eddy simulation (LES) approach should be attempted.

So far direct numerical simulation technique has not been extensively applied to the numerical simulation of many complex EHD and ETHD phenomena. Numerical studies are necessary to obtain insight into the applicability and usefulness of direct simulation approach for these classes of problems,.

References

[1] A. Castellanos ed, Electrohydrodynamics (New York: Springer-Verlag), 1999

[2] J. R. Melcher and G. I. Taylor, Electrohydrodynamics: a review of the role of interfacial shear stresses, Annu. Rev. Fluid Mech., 1: 111-146, 1969

[3] M. Thoma, M. Morari, Control of Fluid Flow, Springer-Verlag Berlin Heidelberg, 2006

[4] N. E. Jewell-Larsen, H. Ran, Y. Zhang, et.al, Electrodynamic (EHD) cooled laptop, Semiconductor Thermal Measurement and Management Symposium, 25th Annual IEEE, 2009

[5] Shaun Tassavur, Super Cool 'EHD Pump' by NASA Cools Devices in Space, 31st May 2011, http://onlygizmos.com/super-cool-ehd-pump-by-nasa-cools-devices-in-space/2011/05/

[6] W. Gilbert, De Magnete, Magneticisque corporibus, et de magno magnete tellure; physiologia nova, plurimis & armumentis & experimentis demonstrate, 1600

[7] T. Paillat, G. Touchard, Electrical charges and liquids motion, Journal of Electrostatics, 67, 326- 334, 2009

[8] Xiaopeng Chen, Cheng Jiusheng and Yin Xiezhen, Advances and applications of electro-hydrodynamics, Chinese Science Bulletin, Vol. 48, No. 11, 1055-1063, 2003

[9] J. R. Melcher, Continuum Electromechanics, the M.I.T. Press, 1981

[10] Jen-Shih Chang, Arnold J. Kelly and Joseph M. Crowley, Handbook of Electrostatic Processes, New York: Dekker, 2nd Edition, 1995

[11] L. D. Landau, Electrohydrodynamics of Continuous Media, New York: Oxford, 1960

[12] M. J. Gross and J. E. Porter, Electrically induced convection in dielectric liquids. *Nature*, 212, 5068, 1343 - 1345, 1966

[13] R. J., Turnbull, Electroconvective instability with a stabilizing temperature gradient. I. Theory. Phys. Fluids, 11, 2688, 1968

[14] R. J. Turnbull, Electroconvective instability with a stabilizing temperature gradient. II. Experimental results. Phys. Fluids, 11, 2597-2603, 1968

[15] W. J. Worraker and A. T. Richardson, The effect of temperature-induced variations in charge carrier mobility on a stationary electrohydrodynamic instability. J. Fluid Mech. 93, 29, 1979

[16] W. J. Worraker and A. T. Richardson, A nonlinear electrohydrodynamic stability analysis of a thermally stabilized plane layer of dielectric liquid, J. Fluid Mech. 109, 217-237, 1981

[17] P.H.G. Allen and T.G. Karayiannis, Electrohydrodynamic enhancement of heat transfer and fluid flow, Heat Recovery Systems and CHP, Vol.15, 5, 389-423, 1995

[18] G. Brière and J. P. Gosse, Injection d'ions dans les liquides polaires, J. Chim. Phys., 65, 725, 1968

[19] J. C. Lacroix, P.Atten and E. J. Hopfinger, Electro-convection in a dielectric liquid layer subjected to unipolar injection, J. Fluid Mech., Vol. 69, part 3, 539-563, 1975

[20] P. Atten, J.C. Lacroix and B. Malraison, Chaotic motion in a Coulomb force driven instability: large aspect ratio experiments, Physics Letters, Vol. 79A, No.4, 1980

[21] B. Malrasion and P. Atten, Chaotic Behavior of Instability Due to Unipolar Ion Injection in a dielectric liquid, Physical Review Letters, Vol. 49, No. 10, 1982

[22] P. Atten, F. M. J. McCluskey and A. T. Perez, Electroconvection and its Effect on Heat Transfer, IEEE transactions on Electrical Insulation, Vol. 23 No. 4, 659-667, 1988

[23] F. Pontiga, A. Castellanos and B. Malrasion, Some considerations on the instabilities of nonpolar liquid subjected to charge injection, Phys. Fluids 7 (6), 1348-1356, 1995

[24] A. Denat, B. Gosse and J. P. Gosse, Ion injections in hydrocarbons, Journal of Electrostatics, 7, 205, 1979

[25] F. Pontiga and A. Castellanos, The effect of residual conduction on weak unipolar injection and buoyancy driven instabilities, in P. Atten and R. Tobazéon, Eds., Proc. 10th Porc. Conf. Conduction and Breakdown in Dielectric Liquids, 286-290, 1990

[26] F. Pontiga and A. Castellanos, The onset of electrothermal convection in nonpolar liquids on the basis of a dissociation-injection conductivity model, IEEE Trans. and. Appl., Vol. 28, No. 3, 520-527, 1992

[27] P. Atten, Stabilité électrohydrodyanmique des liquides de faible conductivité, *J.* Mécanique**,** Vol. 14, No. 3, 461-495, 1975

[28] S. Theoleyre and R. Tobazéon, Conduction électrique aux champs très intenses dans le le carbonate de propylène, C. R. Acad. Sc. Paris, Vol. 296, part II, 241-244, 1983

[29] A. Denat, B. Gosse, and J. P. Gosse, High field dc and ac conductivity of electrolyte solutions in hydrocarbons, Journal of Electrostatics, Vol. 11, 179-194, 1982

[30] R. Tobazéon, M. Haidara and P. Atten, Ion injection and Kerr plots in liquids with blade-plane electrodes, J. Phys. D: Appl. Phys., 17, 1293-1301, 1984

[31] P. Atten and M. Haidara, Electrical conduction and EHD motion of dielectric liquids in a knife-plane electrode assembly, IEEE, Transactions on Electrical Insulation, Vol. EI-20, No.2, 187-198, 1985

[32] M. Haidara and P. Atten, Role of EHD Motion in Electrical conduction of Liquids in a blade-plane geometry, IEEE, Transactions on Industry Application, Vol. IA-21, No.4, 709-714, 1985

[33] A. Alj, A. Denat, et.al., Creation of Charge Carriers in Nonpolar Liquids, IEEE, Transactions on Electrical Insulation, Vol. EI-20, No.2, 221-231, 1985

[34] R. Chicón, A. Castellanos and E. Martin, Numerical modeling of Coulomb-driven convection in insulating liquids, J. Fluid Mech., Vol.344, 43-66, 1997

[35] F. Pontiga and A. Castellanos, Galerkin analysis of electrothermal instabilities in plane liquid layers, IEEE Transactions on industry applications, Vol. 30, No. 4, 862-876, 1994

[36] F. Pontiga and A. Castellanos, Physical mechanisms of instability in a liquid layer subjected to an electric field and a thermal gradient, Phys. Fluids 6 (5), 1684-1701, 1994

[37] A. T. Pérez, P. A. Vazquez and A. Castellanos, Dynamics and Linear stability charged jets in dielectric liquids, IEEE Transactions on industry applications, Vol.30, No. 4, 761-767, 1995

[38] P. A. Vazquez, A. T. Perez and A. Castellanos, Thermal and electrohydrodynamic plumes: A comparative study, Phys. Fluids Vol. 8, 2901-2906, 1996

[39] P. A. Vazquez, A. T. Perez, et.al, Dynamics of electrohydrodynamic laminar plumes: scaling analysis and integral model, Phys. Fluids Vol.12, NO.11, 2809-2818, 2000

[40] V. Seidl, S. Muzaferija and M. Perić, Parallel DNS with local grid refinement, Applied Scientific Research, 59: 379-394, 1998

[41] I. Demirdžić and S. Muzaferija, Finite volume method for stress analysis in complex domains, International Journal of Numerical Methods in Engineering 37, 3751-3766, 1994

[42] I. Demirdžić , S. Muzaferija and M. Perić, Beachmark solutions of some structural analysis problems using finite-volume method and multigrid acceleration, International Journal for Numerical Methods in Engineering, Volume 40, Issue 10, 1893-1908, 1997

[43] H. Jasak and H. G. Weller, Application of the finite volume method and unstructured meshes to linear elasticity, International Journal for Numerical Methods in Engineering, Vol. 48, Issue 2, 267-287, 2000

[44] I. Demirdžić, E. Džaferović and A. Ivanković, Finite-volume approach to thermo -viscoelasticity, Numerical Heat Transfer, Part B 47, 213-237, 2005

[45] C. J. Greenshields, H. G. Weller and A. Ivanković, The finite volume method for coupled fluid flow and stress analysis, Computer Modeling and Simulation in Engineering 4, 213-218, 1999

[46] L. Kadinski and M. Perić, Numerical study of grey-body surface radiation coupled with fluid flow for general geometries using a finite volume multigrid solver, International Journal of Numerical Methods for Heat and Fluid Flow, Vol. 6, Issue 3, 3-18, 1996

[47] H. K. Versteeg and W. Malalasekera, An Introduction to Computational Fluid Dynamics: The Finite Volume method, 2nd Edition, Longman Scientific and Technical, 2007

[48] Mathew N. O. Sadiku, Numerical Techniques in Electromagnetics, 2nd Edition, CRC press, 2001

[49] X. Li, I. R. Ciric and M. R. Raghuveer, Highly stable finite volume based relaxation iterative algorithm for solution of DC line ionized fields in the presence of wind, International Journal of Numerical Modelling: Electronic Networks, Devices and Fields 10, 355–370, 1997

[50] H. Lei, L. Z. Wang and Z.-N. Wu, Applications of upwind and downwind schemes for calculating electrical conditions in a wire-plate electrostatic precipitator, Journal of Computational Physics 193, 697-707, 2004

[51] A. J. Medlin, C. A. J. Fletcher and R. Morrow, A pseudotransient approach to steady state solution of electric field-space charge coupled problems, Journal of Electrostatics 43, 39-60, 1997

[52] A. M. Meroth, T. Gerber, C.D. et al., Numerical solution of nonstationary charge coupled problems, Journal of Electrostatics, 45, 177-198, 1999

[53] C. U. Bottner, The role of the space charge density in particulate processes in the example of the electrostatic precipitator, Powder Technology, Vol. 135-136, 285-294, 2003

[54] N. Neimarlija, I. Demirdžić and S. Muzaferija, Finite Volume Method for Calculation of Electrostatic Fields in Electrostatic Precipitators, Journal of Electrostatics, Vol. 67, 37-47, 2009

[55] N. Neimarlija, I. Demirdžić and S. Muzaferija, Numerical Method for Calculation of Two-Phase Electrohydrodynamic Flows in Electrostatic Precipitators, Numerical Heat Transfer, Part A: Applications, 59: 5, 321-348, 2011

[56] P. Traoré and A. T. Pérez, Two-dimensional numerical analysis of electroconvection in a dielectric liquid subjected to strong unipolar injection, Physics of Fluid, 24, 037102, 2012

[57] P. Traoré, A. T. Pérez, Koulova-Nenova and H. Romat, Numerical modelling of finite amplitude electro-thermo-convection in a dielectric liquid layer subjected to both unipolar injection and temperature gradient, Journal of Fluid Mechanics, Vol. 658, 279-293, 2010

[58] A. Castellanos, and P. Atten, Numerical modeling of finite amplitude convection of liquids subjected to unipolar injection, IEEE Trans. Ind. Appl. IA23, 825-830, 1987

[59] A. Castellanos, A., A.T. Pérez, and R. Chicón, Chaotic electroconvection in a layer of dielectric liquid subjected to unipolar injection: Maximal Lyapunov exponents, International Journal of Bifurcation and Chaos, Vol. 12, No. 11, 2523-2534, 2002

[60] Randall J. Leveque, High-Resolution Conservative Algorithms for Advection in Incompressible Flow, SIAM Journal on Numerical Analysis, Vol. 33, No. 2 , 627-665, 1996

[61] R. B. Rood, Numerical advection algorithms and their role in atmospheric transport and chemistry models, Rev. Geophys., 25, 71-100, 1987

[62] R. W. Hockney and J. W. Eastwood, Computer simulations using particles, New York: McGraw-Hill, 1981

[63] C. K. Bridsall and A. B. Langdon, Plasma Physics via Computer Simulation, Bristol: Institute of Physics Publishing, 1991

[64] S. Zalesak, Fully Multidimensional Flux-Corrected Transport Algorithms for Fluids J. Comput. Phys. 31, 335–62, 1979

[65] A. Hallac, G. E. Georghiou and A. C. Metaxas, Three dimensional algorithm for transient gas discharge processes - alidation Int. Conf. on Gas Discharges and Applications (Liverpool, England), 315 - 18, 2002

[66] P. A. Vazquez, G. E. Georghiou and A. Castellanos, Characterization of injection instabilities in electrohydrodynamics by numerical modelling: comparison of particle in cell and flux corrected transport methods for electroconvection between two plates, J. Phys. D: Appl. Phys. 39 2754–63, 2006

[67] P. A. Vazquez, G. E. Georghiou and A. Castellanos, Numerical analysis of the stability of the electro-hydrodynamic (EHD) electroconvection between two plates, J. Phys. D: Appl. Phys. 41, 1–10, 2008

[68] H. Jasak, Error Analysis and Estimation for the Finite Volume Method with Applications to Fluid Flows, Ph.D. Thesis, Imperial College, 1996

[69] B. van Leer, Upwind difference methods for aerodynamic problems governed by the Euler equations, in: Engquist, Osher and Somerville (Eds.), Lectures in Applied Mathematics, Large-Scale Computations in Fluid Mechanics, (AMS-SIAM Summer Seminar, La Jolla, CA, USA, 1983), Am. Math. Soc., vol. 22, Part 2, p. 327, 1985

[70] J. H. Fergizer and M. Peric, Computational Methods for Fluid Dynamics, Springer, 2002

[71] H. Jasak, H. G. Weller and A. D. Gosman, High resolution NVD differencing scheme for arbitrarily unstructured meshes, Int. J. Numer. Meth. Fluids, 31(2), 431-449, 1996

[72] Randall J. Leveque, Finite-Volume methods for hyperbolic problems, Cambridge University Press, 2004

[73] W. Q. Tao, Recent Advances in Computational Heat Transfer, Science Press of China, Beijing, China, pp. 125 – 138 , 2001 (in Chinese)

[74] W. Hundsdorfer, B. Koren, M. Van Loon, et al., A positive finite-difference advection scheme. J. Comput. Phys., 117, 35-46, 1995

[75] P. L. Roe, Characteristic-based schemes for the Euler equations, Ann. Rev. Fluid Mech. 18 337, 1986

[76] A. Harten, High resolution schemes for hyperbolic conservation laws, Journal of Computational Physics, 49, 357, 1983

[77] P. K. Sweby, High resolution schemes using flux limiters for hyperbolic conservation laws, SIAM J. Numer. Anal. 21, 995, 1984

[78] B. P. Leonard, Simple high-accuracy resolution program for convective modelling of discontinuities, Int. J. Numer. Methods Fluids 8, 1291, 1988

[79] P. H. Gaskell and A. K .C. Lau, Curvature-compensated convective transport: SMART, a new boundedness - preserving transport algorithm, Int. J. Numer. Methods Fluids 8, 617, 1988

[80] P. L. Roe, Finite-volume methods for the compressible Navier–Stokes equations, in: Taylor, Habashi, Hafez (Eds.), Proceedings of the Fifth International Conference on Numerical Methods in Laminar and Turbulent Flow, Montreal, July, Pineridge Press, Swansea, p. 2088, 1987

[81] Z. Wang and B. E. Richards, High resolution schemes for steady flow computation, Journal of Computational Physics, Vol.97 No.1, 53-63, 1991

[82] B. P. Leonard, SHARP Simulation of Discontinuities in Highly Convective Steady Flow, NASA Technical Memorandum 100240 ICOMP-87-9, 1987

[83] N. P. Waterson and H. Deconinck, A unified approach to the design and application of bounded higher-order convection schemes, in: Taylor, Durbetaki (Eds.), Proceedings of the Ninth International Conference on Numerical Methods in Laminar and Turbulent Flow, Atlanta, July, Pineridge Press, Swansea, p. 203. 1995

[84] N. P. Waterson and H. Deconinck, Design principles for bounded higher-order convection schemes – a unified approach, Journal of Computational Physics, 224, 182–207, 2007

[85] M. Zijlema and P. Wesseling, Higher order flux-limiting methods for steady-state, multidimensional, convection-dominated flow, Report 95-131, Faculty of Technical Mathematics and Informatics, Delft, The Netherlands, 1995

[86] Zijlema, M. and Wesseling, P, Higher-Order Flux-Limiting Schemes for the Finite Volume Computation of Incompressible Flow, International Journal of Computational Fluid Dynamics, 9: 2, 89-109 , 1998

[87] Ni Mingjiu, Recent development of modern differencing schemes, Ph.D. Thesis, Xi'an Jiaotong University, China, 1999

[88] A. Castellanos. A. T. Pérez and P. Atten, Charge diffusion versus coulomb repulsion in finite amplitude electroconvection, IEEE Industry Applications Society Annual Meeting, 1989

[89] S. Muzaferija, Adaptative finite volume method for flow prediction using unstructured meshes and multigrid approach, Ph.D. Thesis, Imperial College, 1994

[90] S. R. Mathur, and J. Y Murthy, A Pressure-Based Method for Unstructured Meshes, Numerical Heat Transfer, Part B: Fundamentals, 31: 2, 195 - 215, 1997

[91] M. S. Darwish and F. Moukalled, TVD schemes for unstructured grids, Int. J. Heat Mass Transfer 46(4), 599-611, 2003

[92] C. Bruner and R. Walters, Parallelization of the Euler equations on unstructured grids, AIAA, 97-1894, 1995

[93] Lian-xia Li, Hua-sheng Liao and Li-jian Qi, An improved r-factor algorithm for TVD schemes, Int. J. Heat Mass Transfer, 51, 610-617, 2008

[94] R. J. LeVeque, Numerical Methods for Conseruation Laws, Lecture Notes in Mathematics, ETH Zurich, Birkhauser, Basel, 1992

[95] W. Hundsdorfer and R. A. Trompert, Method of lines and direct discretization: a comparsion for linear advection, Applied Numerical Mathematics, 13, 469-490, 1994

[96] Shu, C.-W. and Osher, S., Efficient implementation of essentially non-oscillatory shock-capturing schemes, Journal of Computational Physics, **77**, 439–471, 1988

[97] Shu, C.-W., Total-variation diminishing time discretizations, SIAM J. Sci. Statist., Comput. 9, 1073–1084, 1988

[98] Hundsdorfer, W., Ruuth, S.J. and Spiteri, R.J., Monotonicity-preserving linear multistep methods, SIAM J. Numer. Anal., 41, 605–623, 2003

[99] Higueras, I., On strong stability preserving time discretization methods, J. Sci. Comput., 21, 193–223, 2004

[100] A. Harten, ENO schemes with subcell resolution, Journal of Computational Physics, 83, 148–184, 1987

[101] X. D. Liu, S. Osher and T. Chan, Weighted essentially non-oscillatory schemes, Journal of Computational Physics, 115,200-212, 1994

[102] G. Jiang and C.W. Shu, Efficient implementation of weighted ENO schemes, Journal of Computational Physics, 126, 202–228, 1996

[103] Sigal Gottlieb, On high order strong stability preserving Runge-Kutta and Multi step time discretisations, Journal of Scientific Computing, Vol. 25, Nos. ½, 2005 (review)

[104] Sigal Gottlieb, David I. Ketcheson and Chi-Wang Shu, High Order Strong Stability Preserving Time Discretizations, Journal of Scientific Computing, 38: 251–289, 2009 (review)

[105] P. Traoré, Yves Marcel Ahipo et al., A robust and efficient finite volume scheme for the discretization of diffusive flux on extremely skewed meshes in complex geometries, Journal of Computational Physics, 228, 5148-5159, 2009

[106] Yves Marcel Ahipo, Philippe Traoré, et al., A robust iterative scheme for finite volume discretization of diffusive flux on highly skewed meshes, Journal of Computational and Applied Mathematics, 231, 478-491, 2009

[107] S. Muzaferija, Adaptative finite volume method for flow prediction using unstructured meshes and multigrid approach, Ph.D. Thesis, Imperial College, 1994

[108] R. Eymard and T. Gallouet, R. Herbin, Error estimate for approximate solutions of a nonlinear convection–diffusion problem, Advances in Differential Equations 7, 419-440., 2002

[109] S. R. Mathur and J.Y. Murthy, A Pressure-Based Method for Unstructured Meshes', Numerical Heat Transfer, Part B: Fundamentals, 31: 2, 195-215, 1997

[110] D. Kim and H. Choi, A Second-Order Time-Accurate Finite Volume Method for Unsteady Incompressible Flow on Hybrid Unstructured Grids, Journal of Computational Physics, 162, 411–428, 2000

[111] M. Kobayashi, A second-order upwind least-squares scheme for incompressible flows on unstructured hybrid grids, Numerical Heat Transfer, Part B, 34 (1): 39-60, 1998

[112] M. H. Xu, Comparison of Methods for Diffusion Flux Calculation on Unstructured Grids, Jounral of Engineering Thermophysics, Vol.26, No.2, 313- 315, 2005 (in Chinese)

[113] D. C. Perez-Segarra, C. Farre, J. Cadafalch and H. Oliva, Analysis of Different Numerical Schemes for the Resolution of Convection-Diffusion Equations using Finite-Volume Methods on Three-Dimensional Unstructured Grids. Part I: Discretization Schemes, Numerical Heat Transfer, Part B: Fundamentals, 49: 4, 333-350, 2006

[114] Sun Dongliang, Qu Zhiguo, et al., Implementation of an efficient segregated algorithm IDEAL on 3D collocated grid system, Chinese Science Bulletin, Vol. 54, No. 6,929-942, 2009

[115] S. V. Patankar and D. B. Spalding A calculation procedure for heat mass and momentum transfer in three dimensional parabolic flows. International Journal of Heat and Mass Transfer, 15: 1787–1806, 1972

[116] S. V. Patankar, Numerical Heat Transfer and Fluid Flow, Hemisphere: Washington, DC, 1980

[117] S. V. Patankar, A calculation procedure for two-dimensional elliptic situations, Numerical Heat Transfer, 4: 409–425, 1981

[118] J. P. Van Doormaal and G. D. Raithby, Enhancements of the SIMPLE method for predicting incompressible fluid flows. Numerical Heat Transfer, 7: 147-163, 1984

[119] Van Doormaal J P and Raithby G D, An evaluation of the segregated approach for predicting incompressible fluid flow, ASME Paper 85-HT-9, 1985

[120] R. I. Issa, Solution of implicitly discretized fluid flow equation by operator-splitting, Journal of Computational Physics, 62: 40-65,1985

[121] R. H. Yen and C. H. Liu, Enhancement of the SIMPLE algorithm by an additional explicit corrector step, Numerical Heat Transfer, Part B, 24: 127-141,1993

[122] W. Q. Tao, Z. G. Qu and Y. L. He, A novel segregated algorithm for incompressible fluid and heat transfer problems-CLEAR (Coupled and Linked Equations Algorithm Revised) Part I: mathematical formulation and solution procedure, Numerical Heat Transfer, Part B, 45: 1-17, 2004

[123] W. Q. Tao, Z. G. Qu and Y. L. He, A novel segregated algorithm for incompressible fluid and heat transfer problems-CLEAR (Coupled and Linked Equations Algorithm Revised) Part II: application examples, Numerical Heat Transfer, Part B, 45: 19-48, 2004

[124] Y. P. Cheng and T. S. Lee, Low H T and Tao W Q, An efficient and robust numerical scheme for the SIMPLER algorithm on non-orthogonal curvilinear coordinates: CLEARER. Numerical Heat Transfer, B, 51: 433-461, 2007

[125] D. L. Sun, Z. G. Qu, Y. L. He et al., An efficient segregated algorithm for incompressible fluid flow and heat transfer problems-IDEAL (Inner Doubly-Iterative Efficient Algorithm for Linked-Equations) Part I: mathematical formulation and solution procedure. Numerical Heat Transfer, Part B, 53: 1-17, 2008

[126] D. L. Sun, Z. G. Qu, Y. L. He et al., An efficient segregated algorithm for incompressible fluid flow and heat transfer problems-IDEAL (Inner Doubly-Iterative Efficient Algorithm for Linked-Equations) Part II: application examples, Numerical Heat Transfer, Part B, 53: 18-38, 2008

[127] Dong-Liang Sun, Zhi-Guo Qu, et al., Performance analysis of IDEAL algorithm for three-dimensional incompressible fluid flow and heat transfer problems, International Journal for Numerical Methods in Fluids ,Vol. 61, Issue 10: 1132-1160, 2009

[128] M. Perić, Analysis of Pressure Velocity Coupling on Non-Staggered Grids, Numerical Heat Transfer, Part B, vol. 17, 63-82, 1990

[129] M. J. Cho and M. K. Chung New treatment of nonorthogonal terms in the pressure correction equation, Numerical Heat Transfer, Part B, 26:133–145, 1994

[130] T. Lehnhauser and M. Schafer Improved linear interpolation practice for finite-volume schemes on complex grids, International Journal for Numerical Methods in Fluids, 38:625– 645, 2002

[131] T. Lehnhauser and M. Schafer, Efficient discretization of pressure-correction equations on non-orthogonal grids, International Journal for Numerical Methods in Fluids, 42:211–231, 2003

[132] L. Onsager, Deviations from Ohm's law in weak electrolytes, J. Chem. Phys. 2, 599, 1934

[133] M. Silver, Conduction of electricity in insulating liquids, J. Chem. Phys. 42, 1011, 1965

[134] G. Briere and F. Garpard, Equilibre thermique de dissotiation et conduction ionique intrinseque en phase liquide, J. Chim. Phys. 64, 1071, 1967

[135] D. F. Blossey, One-dimensional Onsager theory for carrier injection in metal-insulator systems, Phys. Rev. B, 9, 5183, 1974

[136] A. Denat, B. Gosse, and J. P. Gosse, Ion injections in hydrocarbons, Journal of Electrostatics, **7**, 205, 1979

[137] N. Felici, Charge carrier elimination and production of electrodialytic polymers in contact with dielectric liquids, Journal of Electrostatics, 11, 131, 1981

[138] C. Louste, M. Daaboul and H. Romat, A study of vortex shedding induced by dielectric barrier injection, Journal of Electrostatics, 67, 348–53, 2009

[139] P. Traor´e, M. Daaboul and Ch. Louste, Numerical simulation and PIV experimental analysis of electrohydrodynamic plumes induced by a blade electrode, J. Phys. D: Appl. Phys. 43 , 2010

[140] F. J. Higuera and P. A. Vazquez, Coulomb-driven flow of a dielectric liquid subject to charge injection by a sharp electrode, Phys. Fluids 11, 2434, 1999

[141] F. J. Higuera, Electrohydrodynamic flow of a dielectric liquid around a blade electrode, Phys. Fluids, Vol.12, No.11, 2732, 2000

[412] F. J. Higuera, Stationary and Oscillatory Flow of a Charged Liquid Around a Blade Electrode, Coherent Structures in Complex Systems, Lecture Notes in Physics, Volume 567, 338-348, 2001

[143] Schneider J. M., Watson P. K. and H. R. Till, Electrohydrodynamic Stability of Space -Charge -Limited Currents in Dielectric Liquids, I. Theoretical Study, Phys. Fluids, 13, 1948, 1970

[144] P. Atten and Moreaur, Stabilité électrohydrodynamique des liquids isolants soumis à une injection unipolaire, J . Mécan., 11**,** 471-520, 1972

[145] J. M. Schneider, P. K. Watson and H. R. Till, Electrohydrodynamic Stability of Space -Charge -Limited Currents in Dielectric Liquids, II. Experimental Study, Phys. Fluids **13**, 1955, 1970

[146] P. Atten and J.C. Lacroix, Electrohydrodynamic stability of liquids subjected to unipolar injection: Non linear phenoma, Journal of Electrostatics, Vol. 5, 439-452, 1979

[147] J. C. Lacroix and P. Atten, Double injection with recombination: EHD linear and non linear stability study, Journal of Electrostatics, Vol. 5, 453-461, 1978

[148] P. Atten and J. C. Lacroix, Nonlinear hydrodynamic stability of liquids subjected to unipolar injection, Journal de Mécanique, Vol. 18, No.3, 1979

[149] N. Felici, Phénomènes Hydro- et Aérodynamiques dans la Conduction des Dielectriques Fluides, Rev. Gen. Electr., Vol. 78, 717-734, 1969

[150] P. Atten, B. Malraison and M. Zahn, Electrohydrodynamic plumes in point-plane geometry, IEEE Trans. Dielectrics Electrical Insulation, 4(6), 710–718, 1997

[151] A. Castellanos, P. Atten, and A. T. Perez, Finite amplitude electroconvection in liquid in the case of weak unipolar injection, PCH, PhysicoChem. Hydrodyn. **9**(3/4), 443, 1987

[152] A. T. Perez and A. Castellanos, Role of charge diffusion in finite-amplitude electro-convection, Phys. Rev. A, 40, 5844-5855, 1989

[153] A. Castellanos, Coulomb-driven convection in electrohydrodynamics, IEEE Trans. Electr. Insul., 26, 1201-1215, 1991

[154] P. Traoré, A. T. Perez, et. al.,Analysis by numerical simulation of the development of the electroconvective instability of a dielectric liquid layer to an unipolar injection [Analyse par simulation numérique du développement de l'instabilité électro-convective d'une couche de liquide diélectrique infinie soumise à une injection unipolaire, Comptes Rendus - Mecanique, 337 (9-10), 667-674, 2009

[155] P. A. Vazquez and A. Castellanos, Stability analysis of the 3D electroconvective charged flow between parallel plates using the particle-in-cell method, IEEE International Conference on Dielectric Liquids (ICDL), June 2011

[156] G. Ahsmann and R. Kronig, The influence of electric fields on the convective heat transfer in liquids, Appl. Scient. Res. A2, 235 – 244, 1950

[157] W. Eames and H. M. Sabir, Potential benefits of electrohydrodynamic enhancement of two-phase heat transfer in the design of refrigeration systems, Appl Therm Eng, 17:79–92, 1997

[158] J. Seyed-Yagoobi and J. E. Bryan, Enhancement of heat transfer and mass transport in single-phase and two-phase flows with electrohydrodynamics, Adv. Heat Transfer **33:** 95–186, 1999

[159] S. Laohalertdecha, P. Naphon and S. Wongwises, A review of electrohydrodynamic enhancement of heat transfer, Renewable & Sustainable Energy Reviews, 11(5), 858–876, 2007

[160] T. B. Jones, Electrohydrodynamically enhanced heat transfer in liquids - a review, Adv Heat Transfer, 14, 107-148, 1978

[161] D. A. Nelson and E. J. Shaughnessy, Electric field effects on natural convection in enclosures, J. Heat Transfer, Vol. 108, 749-754, 1986

[162] E. Bonjour, J. Verdier and L. Weil, Electroconvcction effects on heat transfer, Chem. Engng Prog. 58, 63-66, 1962

[163] S. D. Savkar, Dielectrophoretic effects in laminar forced convection between two parallel plates. Physics Fluids, 14, 2670-2679, 1971

[164] R. Schnurmann and M. G. C. Lardge, Enhanced heat flux in non-uniform electric fields, Proc, R. Soc. London A334, 71-82, 1973

[165] Walter Grassi, Daniele Testi and Mario Saputelli, Heat transfer enhancement in a vertical annulus by electrophoretic forces acting on a dielectric liquid, International Journal of Thermal Sciences, 44, 1072–1077, 2005

[166] R. J. Turnbull, Free convection from a heated vertical plate in a direct-current electric field, Physics Fluids, 12, 2255-2263, 1969

[167] B. R. Lazarenko, F. P. Grosu and M. K. Bologa, Convective heat transfer enhancement by electric fields, Int. J. Heat Mass Tranfer 18, 1433-1441, 1975

[168] M. Takashima and K. D. Aldridge, The stability of a horizontal layer of dielectric fluid under the simultaneous action of a vertical d.c. electric field and a vertical temperature gradient, Q. J. App. Math, 29, 71-87, 1976

[169] J. F. Hoburg and J. R. Melcher, Internal elcctrohydrodynamic instability and mixing of fluids with orthogonal field and conductivity gradients, J. Fluid Mech. 73, 333-351, 1976

[170] J. F. Hoburg and J. R. Melcher, Electrohydrodynamic mixing and instability induced by colinear fields and conductivitv gradients, Physics Fluids 20, 903-911 , 1977

[171] J. F. Hoburg, Internal electrohydrodynamic instability of liquids with colinear field and conductivity gradients, J. Fluid Mech., 84, 291-303, 1978

[172] F. M. J. Mccluskey, P. Atten and A. T. Perez, Heat transfer enhancement by electroconvection resulting from an injected space charge between parallel plates, Int. J. Heat Mass Transfer, Vol. 34, No. 9, 2237-2250, 1991

[173] J. L. Fernandez and R. Poulter, Radial mass flow in electrohydrodynamically-enhanced forced heat transfer in tubes, Int. J. Heat Mass Transfer 30, 2125-2136, 1987

[174] T. Mizushina, F. Ogino, T. Matsumoto, M. Yokoyama and N. Kitano, Effect of radial electrical field on heat and momentum transfers in dielectric organic liquid for laminar flow through concentric annuli, Int. J. Heat Mass Transfer, 23, 1105-1115, 1980

[175] A. Castellanos, N. Agrait, Unipolar injection induced instabilities in plane parallel flows, IEEE Trans. Industry Appl. 28 (3) , 513-519, 1992

[176] I. Demirdžić and S. Muzaferija, Numerical method for coupled fluid flow, heat transfer and stress analysis using unstructured moving meshes with cells of arbitrary topology, Computer Methods in Applied Mechanics and Engineering 125, 235–255, 1995

[177] N. Agrait and A. Castellanos, Linear convective pattern in cylindrical geometry for unipolar injection, Physics of fluids, 2(1), 37-44, 1990

[178] R. F. Bradley and J. F. Hoburg, Elcctrohydrodynamic augmentation of forced convection heat transfer, IEEE. Trans. Ind. Application, IA-21(6), 1373-1376, 1985

[179] J. S. Paschkewitz and D. M. Pratt, The influence of fluid properties on electrohydrodynamic heat transfer enhancement in liquids under viscous and electrically dominated flow conditions, Exp. Therm. Fluid Sci. 21: 187–97, 2000

[180] N. Felici, D.C. conduction in dielectric liquids Part I: A survey of recent progress, Direct Current 2, 90-99, 1971

[181] P. J. Martin and A. Richardson, Overstable electrothermal instabilities in a plane layer of dielectric liquids, Journal of Electrostatics, 12, 435, 1982

[182] A. Castellanos, P. Atten and M. G. Velarde, Oscillatory and steady convection in dielectric liquid layers subjected to unipolar injection and temperature gradient, Phys. Fluids 27, 1607-1615, 1984

[183] L. Rodrigues, A. Castellanos and Richardson, A, Stationary instabilities in a dielectric liquid layer subjected to an arbitrary unipolar injection and adverse thermal gradient. J. Phys. D: Appl. Phys. **19**, 2115–2122, 1986

[184] Y. Y. Yan, H. B. Zhang and J. B. Hull, Numerical modeling of electrohydrodynamic (EHD) effect on natural convection in an enclosure, Numerical Heat Transfer, Part A, 46: 453-471, 2004

[185] P. Traoré, D. Koulova, H. Romat, et al., Caractérisation de l'augmentation des transferts thermiques dans une couche de liquide diélectrique soumise à une injection unipolaire de charges électriques; Characterization of the increase in heat transfer in a dielectric liquid layer under unipolar injection of electric charge, Comptes Rendus Mécanique, Vol.337, Issue 3, 150-157, 2009

[186] D. Koulova, A. Perez and P. Traoré et al., Influence Of The Dielectric Force On A Thermoelectric Convection Phenomena In Case Of Weak Injection, IEEE International Conference Dielectric Liquids, ICDL, 2008

[187] D. Koulova, P. Traoré P. et al., Influence of the characteristic parameters on flow patterns and heat transfer in electro-thermo-convection, IEEE International Conference Dielectric Liquids, ICDL 2011

[188] Fortin M and Glowinski R, Méthodes de Lagrangien Qugmenté, Dunod, Pairs, 1982

[189] P. Atten and T. Honda, The electroviscous effect and its explanation I-the electrohydrodynamic origin; study under unipolar d. c. injection, Journal of Electrostatics, 11, 225-245, 1982

[190] N. J. Felici, Electrostatics and Hydrodynamics, Journal of Electrostatics, 4, 119-129, 1977/1978

[191] N. J. Felici, A tentative explanation of the voltage-current characteristic of dielectric liquids, Journal of Electrostatics, 12, 165 -172, 1982

[192] R. Tobazeon, in Phénomènes de conduction dans les liquides isolants, Colloque N ° 179, Centre National de la Recherche Scientifique, 15, Quai Anatole France, Paris, See p. 407 to 421

[193] P. J. Martin and A. T. Richardson, Conductivity Models of Electrothermal Convection in Plane Layer of Dielectric Liquid, *Trans. ASME,* J. Heat Transfer, Vol. 106, No. 1, 131–136, 1984

[194] L. Onsager, Deviations from ohm's law in weak electrolytes, Journal of Chemical Physics, 2: 599-614, 1934

[195] P. Debye, Reaction rates in ionic solutions, Trans. Electrochem. Soc., 82, 262-272, 1942

[196] R. M. Fuoss, Ionic association, III, the equilibrium between ion pairs and free ions, J. Am. Chem. Soc., 80(5), 5059-5061, 1958

[197] Thomson J. J. and Thomson G. P., Coundction of Electricity through Gases, Cambridge University Press, 3rd Edition, 1928

[198] G.Briere and J. P. Gosse, Injection d'ions dans les liquides polaires, J. Chim. Phys. 65, 725, 1968

[199] H.L.F. von Helmholtz, Studien űber electrische Grenzschichten, Ann. Phys. Chem. 7,337 -382, 1879

[200] G. Gouy, Sur la constitution de la Charge Electrique à la surface d'un Electrolyte, J. Phys. 9, 457-468, 1910

[201] D.L. Chapman, A contribution to the theory of electrocapillarity, Philos. Mag. 25, 475-481, 1913

[202] O. Stern, Zur Theorie der Electrolytischen, Z. Elektrochem, 30, 508–516, 1924

[203] Lyklema J., Fundamentals of Interface and Colloid Science, Vol.2, 1995

[204] A. Castellanos, Entropy production and the temperature equation in Electrohydrodynamics, IEEE Transactions on Dielectrics and Electrical Insulation, 10(1), 22-26, 2003

[205] J. C. Lacroix, Doctoral Thesis, Université de Grenoble, 1976

[206] J. C. Lacroix and P. Atten, Double injection with recombination: EHD Linear and non linear stability study, Journal of Electrostatics, 5, 453-461, 1978

[207] P. Atten, B. Malrason and S. Ali Kani, Electrohydrodynamic stability of dielectric liquids subjected to A.C. fields, Journal of Electrostatics, 12, 477-488, 1982

[208] A. I. Zhakin and I. E. Tarapov, Instability and flow of a weakly conducting fluid in the presence of oxidation-reduction reactions at electrodes and recombination, Fluid dynamics, Vol. 16, No. 4, 505-510, 1981

[209] Juan L. Lara, Francisco Pontiga and A. Castellanos, Stability analysis of a Taylor-Coutte flow of insulating fluid subjected to radial unipolar injection of charge, Physics Fluids, Vol. 10, No. 12, 1998

[210] Gallagher, T. J., Simple Dielectric Liquids, Oxford: Clarendon, 1975

[211] A. Denat. Etude de la conduction électrique dans les solvants non polaires. State Thesis, Grenoble. France, 1982

[212] Felici, N.J. and Gosse, J. P. Injection d'ions par des électrodes métaliques dans les hydrocarbures liquides de résistivité élevée. Re. Phys. Appl., 14, 629, 1979

[213] A. I. Zhakin, Electrohydrodynamics of liquid dielectrics on the basis of a dissociation -injection conductivity model, Izv. Akad. Nauk SSSR, Mekh. Zhidk. Gaza, No. 4, 3, 1986

[214] E. L. Tarunin and Yu. A. Yamshinina, Bifurcation of stationary solutions of the system of equations of electrohydrodynamics for unipolar injection, Izv. Ross. Akad. Nauk, Mekh. Zhidk. Gaza, No. 3, 23, 1994

[215] A. I. Zhakin, Investigation of electroconvection and electroconvective transfer in liquid dielectrics for unipolar injection conductivity,Izv. Akad. Nauk SSSR, Mekh. Zhidk. Gaza, No. 2, 14, 1988

[216] John Shrimpton, Charge injection systems: physical principles, experimental and theoretical work, Springer, 2009

[217] Kourmatzis A. and Shrimpton J., Electrohydrodynamics and charge injection atomizer: a review of the governing equations and turbulence, automization and sprays, 19, 1045-1063, 2009

[218] Tobazéon, R., Electrohydrodynamic instabilities and electroconvection in the transient and A.C. regime of unipolar injection in insulating liquids: a review, Journal of Electrostatics 15, 359-384, 1984

[219] J.S. Paschkewitz, D.M. Pratt, The influence of fluid properties on electrohydrodynamic heat transfer enhancement in liquids under viscous and electrically dominated flow conditions, Exp Therm Fluid Sci, 21, 187-197, 2000

[220] Peric, M., A finite volume method for the prediction of three dimensional flow in complex ducts, PhD Thesis, University of London, 1985

[221] Zhang Hanxin, He Guohong and Zhang Lei, Some important problems for high order accurate difference scheme solving gas dynamic equations, ACTA Aerodynamica SINICA, Vol.11, No.4, 347-356 , 1993, (in Chinese)

[222] Panos Tamamidis and Dennis N.Assanis, Evaluation of various high-order-accuracy schemes with and without flux limiters, International Journal for Numerical Methods in Fluids, Vol. 16, 931-948, 1993

[223] Jameson A., Artificial Diffusion, Upwind Biasing, Limiters and their Effect on Accuracy and Multigrid Convergence in Transonic and Hypersonic Flows, AIAA paper 93-3359, 1993

[224] H. C. Yee, A class of high–resolution explicit and implicit shock - capturing methods, Technical Memorandum 101088, NASA Ames Research Center, 1989

[225] N. P. Waterson, A symmetric formulation for flux-limited convection schemes, International Journal for Numerical Methods in Fluids, 56: 1575-1581, 2008

[226] Miroslav Čada and Manuel Torrilhon, Compact third-order limiter functions for finite volume methods, J. Comput. Phys., 228, 4118-4145, 2009

[227] G.D. van Albada, B. van Leer and W.W. Roberts, A comparative study of computational methods in cosmic gas dynamics, Astron. Astrophys. 108, 76, 1982

[228] Wu Jian, Philippe Traoré and Romat Hubert, The Extension of Convective Boundedness Criterion, International conference of numerical analysis and applied mathematics, vol.1, 91-94, 2010

[229] Qin Qian, Heinz G.Stefan and V.R.Voller, A physically based flux limiter for QUICK calculations of advective scalar transport, Int. J. Numer. Meth. Fluids, 55, 899 – 915, 2007

[230] Wu Jian, Philippe Traoré and Romat Hubert, A Simple 2nd-order Physically Bounded Convective Scheme, International conference of numerical analysis and applied mathematics, Vol.1, 143-147, 2010

[231] M. S. Darwish and Moukalled, F. H., Normalized variable and space formulation methodology for high-resolution schemes, Numerical Heat Transfer, Part B: Fundamentals, 26: 1, 79 -96, 1994

[232] Jian chun Liu, Gary A. Pope and Kamy Sepehrnoori, A high-resolution finite-difference scheme for nonuniform grids, Applied Mathematical Modeling, Volume 19, Number 3, 162-172(11), 1995

[233] J. B. Goodman, R.J. Leveque, On the accuracy of stable schemes for 2D scalar conservation laws, Math. Comput., 45, 15, 1985

[234] R. J. Leveque, Numerical Methods for Conservation Laws, second ed., Lectures in Mathematics, ETH Zűrich, Birkhaűser, 1992.

[235] S. R. Mathur, J. Y. Murthy, A pressure-based method for unstructured meshes, Numerical Heat Transfer, Part B: Fundamentals, 31(2), 195-215, 1997

[236] John Thuburn, Multidimensional flux-limited advection schemes, Journal of Computational Physics, 123**,** 74–83, 1996

[237] Personal communication with Mr. Dhiraj V. Patil of Indian Institute of Science

[238] P. K. Khosla and S.G., Rubin, A diagonally dominant second-order accurate implicit scheme, Computers and Fluids, 2, 207-209, 1974

[239] John Thuburn, TVD schemes, positive schemes, and the universal limiter, Monthly Weather Review, Vol.125, 1990-1993, 1997

[240] Wu Jian, Philippe Traoré and Hubert Romat, Similarity and relationship between three methods for diffusive flux computation on nonorthogonal meshes, submitted to Computer Methods in Applied Mechanics and Engineering, September, 2012

[241] Panos Tamamidis and Dennis N. Assanis, Evaluation of various high-order-accuracy schemes with and without flux limiters, Int. J. Numer. Method in Fluid, Vol. 16, No.10, 931-948, 1993

[242] Courant, R., Friedrichs, K.O., and Lewy, H.: Uber die partiellen dierenzgle-ichungen der matematishen Physik, Matematishe Annalen, 100:32-74, 1928

[243] Williamson, J. H., Low –storage Runge-Kutta schemes, Journal of Computational Physics 35, 48-56, 1980

[244] Hundsdorfer, W. Ruuth S. J. and Spiteri, R.J., Monotonicity-preserving linear multistep methods, SIAM J. Numer. Anal., 41, 605–623, 2003

[245] Higueras, I., On strong stability preserving time discretization methods, J. Sci. Comput. 21, 193–223, 2004

[246] Sigal Gottlieb and Shu, C.-W.: Total-variation diminishing Runge-Kutta schemes, Mathematics of Computation, Vol. 67, NO. 221, Jan. 73-85, 1998

[247] Sigal Gottlieb, Shu, C.-W. and Eitan Tadmor, Strong stability-preserving high-order time discretization methods, SIAM review, Vol. 43, No. 1, Mar, 89-112, 2001

[248] Traoré Ph, Simulation numérique en mécanique des fluides et en dynamique des milieux granulaires Modélisation des phénomènes Electro-Fluido-Dynamiques, Habilitation à diriger les recherches, Université de Poitiers, 2011

[249] Rhie, C.M. and Chow, W.L.,Numerical study of the turbulent flow past an airfoil with trailing edge separation, AIAA J., Vol. 21, 1523–1532, 1983

[250] S. Majumdar, Role of Underrelaxation in Momentum Interpolation for Calculation of Flow with Nonstaggered Grids, Numer. Heat Transfer, Vol. 13,125-132, 1988

[251] M. H. Kobayashi and J. C. F. Pereira, Numerical Comparison of Momentum Interpolation Methods and Pressure-Velocity Algorithm Using Nonstaggered Grids, Commun. Appl. Numer. Meth., vol. 7, 173-196, 1991

[252] S. K. Choi, Note on the Use of Momentum Interpolation Method for Unsteady Flows, Numerical Heat Transfer A, Vol. 36, 545-550, 1999

[253] B. Yu, Y. Kawaguchi, W. Q. Tao, and H. Ozoe, Checkerboard Pressure Predictions Due to the Underrelaxation Factor and Time Step Size for a Nonstaggered Grid with Momentum Interpolation Method, Numer. Heat Transfer B, vol. 41, no. 1, 85-94, 2002

[254] B. Yu, Y. Kawaguchi, W. Q. Tao and H. Ozoe, Checkerboard pressure predictions due to the underrelaxation factor and time step size for a nonstaggered grid with momentum interpolation method, Numerical Heat Transfer B, 41, 85-94, 2002

[255] H. L. Stone, Iterative Solutions of Approximations of Multidimensional Partial Differential Equations, SIAM J. Numer, Anal., vol. 5, 530-558, 1968.

[256] R.M. Smith, A.G. Hutton, The numerical treatment of advection: a performance comparison of current methods, Numerical Heat Transfer 5, 439-461, 1982

[257] Song B, Liu GR, Lam KY, Amano RS. On a higher-order bounded discretization scheme. International Journal for Numerical Methods in Fluids, 32: 881- 897, 2000

[258] Alves MA and Oliveira PJ, Pinho FT., A convergent and universally bounded interpolation scheme for the treatment of advection, Int J Numer Methods Fluids, 41:47-75, 2003

[259] Wu Jian, Philippe Traoré, et al., Evaluation of various high-resolution schemes with flux limiters, The 8th Euromech Fluid Mechanics Conference, Bad Reichenhall, Germany, Sep.2010

[260] Wu Jian, Traoré P. et al., A finite volume method for electric field-space charge coupled problems, submitted to the international conference on electrostatics, 2013, Budapest, Hungary

[261] C. H. Tai, D. C. Chiang and Y. P. Su, Explicit Time Marching Methods for the Time-Dependent Euler Computations, Jounral of Computational Physics, 130, 191-202, 1997

[262] H.A. Van der Vorst, Bi-CGSTAB: a fast and smoothly converging variant of BiCG for the solution of nonsymmetric linear systems, SIAM Journal on Scientific and Statistical Computing 13, 631–644, 1992

[263] I.Gustafsson, On First and Second Order Symmetric Factorization Methods for the Solution of Elliptic Difference Equations, Chalmers University of Technology, 1978

[264] M. Shashkov, S. Steinberg, Solving diffusion equations with rough coefficients in rough grids, Journal of Computational Physics 129, 383–405, 1996

[265] Personal communication with Mr. Riccardo Rossi, Università di Bologna

[266] J.E. Morel, Michael, L. Hall, and Mikhail J. Shashkov, A Local Support-Operators Diffusion Discretization Scheme for Hexahedral Meshes, Journal of Computational Physics 170, 338-372, 2001

[267] H.J. Leister and M. Peric, Vectorized strongly implicit solving procedure for a seven-diagonal coefficient matrix, Int. J. Meth. Heat Fluid Flow, Vol. 4, 159–172, 1994

[268] K. Lipnikov, D. Svyatskiy and Y.Vassilevski A momotone finite volume method for advection-diffusion equations on unstructured polygonal meshes, Journal of Computational Physics 229, 4017 – 4032, 2010

[269] Communication with Pro. Kazimierz Adamiak, University of Western Ontario, Canada

[270] Paria Sattari, FEM-FCT based dynamic simulation of Trichel pulse corona discharge in point-plate configuration, Ph.D. Thesis, University of Western Ontario, 2011

[271] Demirdzic, I., Likek, Z. and Peri, M., Fluid flow and heat transfer test problems for non-orthogonal grids: benchmark solutions, International Journal of Numerical Methods in Fluids, Vol. 15, 329–354, 1992

[272] S. Davis, Convection in a Box: Linear Theory, Journal of Fluid Mechanics, Vol. 30, No. 3, 465-478, 1967

[273] K. Stork and U.Muller, Convection in a Box: Experiments, Journal of Fluid Mechanics, Vol. 54, No. 4, 599-611, 1972

[274] *Wu Jian*, Traoré P. et al., Direct numerical simulation of dielectric electrohydrodynamic convection in blade-plane configuration, submitted to the international conference on electrostatics, 2013, Budapest, Hungary

[275] S. Chandrasekhar, Hydrodynamic and hyrdomagnetic stability, Oxford Press, 1961

[276] P. Atten, Electrohydrodynamic instability and motion induced by injected space charge in insulating liquids, IEEE, Transaction on dielectric insulation, Vol. 3 No. 1, 1996

[277] P. Atten, Role de la diffusion dans le probkème de la stabilité hydrodynamique d'un liquid diélectrique soumis à une injection unipolaire forte, C. R. Acad. Sci. Paris, Vol. 283 B, 29-32, 1976

[278] E. J. Hopfinger and J. P. Gosse, Charge transport by Self-generated turbulence in insulating liquid submitted to unipolar injection, Physics of Fluids, Vol. 14, No. 8, 1671-1682, 1971

[279] L D Landau and E. M. Lifshitz, Fluid Mechanics,Course of Theoretical Physics, Vol6, 2nd Edition, 1987

[280] V.V. Gogosov and V.A. Polyansky, Shock waves in electrohydrodynamics, Prog. Aerospace Sci. 20, 125-216, 1983

[281] V.A. Polyansky and I. L. Pankratieva, Electric current oscillations in low conducting liquids, Journal of Electrostatics, 48, 27-41, 1999

[282] Traoré P, Wu J. and Pérez A., Numerical analysis of the subcritical electroconvective instability in a dielectric liquid subjected to strong or weak unipolar injection, submitted to Journal of Electrostatics, Feb. 2012

[283] P. Atten and L. Elouadie, EHD convection in a dielectric liquid subjected to unipolar injection: coaxial wire/cylinder geometry, Journal of Electrostatics 34, 279-297, 1995

[284] Leonard, B. P., A Stable and Accurate Convective Modelling Procedure Based on Quadratic Upstream Interpolation, Comput. Methods Appl. Mech. Eng., Vol. 19, 59–98, 1979

[285] Mohit Arora and Philip L. Roe, A Well-Behaved TVD Limiter for High-Resolution Calculations of Unsteady Flow, Journal of Computational Physics 132, 3-11, 1997

[286] R. Enns and G. McGuire, Nonlinear physics with mathematics for scientists and engineers, Birhkäuser, 2011

[287] A. T. Perez, P. Traoré , D. Koulova-Nenova and H. Romat, Numerical study of an electrohydrodynamic plume between a blade injector and a flat plate, IEEE Trans. Dielectr. Electr. Insul. **16** 448–55, 2009

[288] Marcello Lappa, Thermal convection: Patterns, Evolution and Stability, John Wiley & Sons, 2010

[289] A. Kourmatzis and J. S. Shrimpton, Turbulent three-dimensional dielectric electro-hydrodynamic convection between two plates, Journal of Fluid Mechanics, Vol. 696, 228-262, 2012

[290] A. Castellanos, P. Atten and M. G. Velarde, Electrothermal Convection: Felici's Hydraulic Model and the Landau Picture of Non-Equilibrium Phase Transitions. J. Non-Equilib. Thermodyn. 9, 235–244, 1984

[291] S. D. George and J. C. Marcelo, Convective heat transfer control using magnetic and electric fields, Journal of Enhanced heat transfer, 13 (2) 139 – 155, 2006

[292] Derek Dunn-Rankin and Felix J. Weinberg, Using large electric fields to control transport in microgravity, Annals of the New York Academy of Sciences, Interdisciplinary Transport Phenomena in the space sciences, Vol. 1077, 570-584, September 2006

[293] A. Yabe, Y. Mori and K. Hijikata, Active heat transfer enhancement by utilizing electric fields, Chang-Lin Tien (Ed.), Annual Review of Heat Transfer, Vol. 7 Begell House, New York, chap. 4, 1995

[294] A. T. Perez, P. Atten et al.. Heat transfer augmentation induced by electrically generated convection in liquids. In: Experimental heat transfer, fluid mechanics and thermodynamics, Eds. Shah, Ganic and Yang, 941–947, Elsevier, 1988

[295] B. Suman, A steady state model and maximum heat transport capacity of a electro-hydrodynamic augmented micro-grooved heat pipe. Int. J. Heat Mass Transfer 49, 3957-3967, 2006

[296] J. E. Bryan and J. Seyed-Yagoobi, Heat transport enhancement of monogroove heat pipe with electrohydrodynamic pumping, J. Thermophys. Heat Transfer 11(3), 454–460, 1997

[297] J. E. Bryan and J. Seyed-Yagoobi, Influence of flow regime, heat flux, and mass flux on electrohydrodynamically enhanced convective boiling. J. Heat Transfer 123(2), 355-367, 2001

[298] A. Castellanos and M. G. Velarde, Electrohydrodynaamic stability in the presence of a thermal gradient, Phys. Fluid, 24, 1784-1786, 1981

[299] Tsai P. Daya Z. A., Deyirmenjian V. B. and Morris S. W., Direct numerical simulation of supercritical annular electroconvection, Phys. Rev. E. 76, 026305, 2007

[300] George S. Dulikravich, Vineet Ahuja and Seungsoo Lee, Simulation of electro-hydrodynamic enhancement of laminar flow heat transfer, Enhanced Heat Transfer, Vol. 1, No. 1, 115-126, 1993

[301] R. Bradley, Overstable electroconvective instabilities, Quart. J. Mech. Appl. Math. 31, 381-390, 1978

[302] F. Pontiga and A. Castellanos, The onset of overstable motions in a layer of dielectric liquid subjected to the simultaneous action of a weak unipolar injection of charge and a thermal gradient, Quart. J. Mech. Appl. Math., vol. 45, part. 1, 25-46, 1992

[303] N. Felici, Phénomènes hydro et aérodynamiques dans la conduction des diélectriques fluides, Rev. Gen. Electr., Vol. 78, 717-734, 1969

Appendix A

Limiter function for TVD-type High-Resolution schemes

In this section, we listed all the TVD schemes we summarized. It should be stressed here that the expressions of various schemes in the following table are not entirely the same with the schemes in Appendix A of [84]. The reason is the definitions of the gradient ratio r are different (in a reciprocal relationship). However, the expressions of the five classical limiter functions: Minmod [A6], Superbee [A7], MUSCL [A2], van Leer [A1] and van Albada [A3], are the same because of their symmetric property.

Table A-1. Limiter functions of various TVD-type HR schemes

Scheme	Limiter function	Author & Year
Van Leer	$\frac{r+\lvert r\rvert}{r+1}$	van Leer, 1974 [A1]
MUSCL	$\max[0, \min(2r, \frac{1}{2}r+\frac{1}{2}, 2)]$	van Leer, 1977 [A2]
Van Albada-1	$\frac{r^2+r}{r^2+1}$	van Albada, et al., 1982 [A3]
Osher	$\max[0, \min(r, \beta)], (1 \le \beta \le 2)$	Chatkravathy and Osher, 1983 [A4]
Sweby	$\max[0, \min(\beta r, 1), \min(r, \beta)], (1 \le \beta \le 2)$	Sweby, 1984 [A5]
Min-mod	$\max[0, \min(r, 1)]$	Roe, 1986 [A6]
Superbee	$\max[0, \min(2r, 1), \min(r, 2)]$	Roe, 1986 [A7]
SMART	$\max[0, \min(4r, \frac{1}{4}r+\frac{3}{4}, 2)]$	Gaskell & Lau, 1988 [A8]
UMIST	$\max[0, \min(2r, \frac{3}{4}r+\frac{1}{4}, \frac{1}{4}r+\frac{3}{4}, 2)]$	Lien & Leschziner, 1994 [A9]
CHARM	$\frac{r+\lvert r\rvert}{2}\frac{3+r}{(r+1)^2}$	Zhou, 1995 [A10]
OSPRE	$\frac{3}{2}\frac{r^2+r}{r^2+r+1}$	Waterson & Deconinck, 1995 [A11]
SPL-1/3	$\max[0, \min(2r, \frac{1}{3}r+\frac{2}{3}, \frac{1}{3}+\frac{2}{3}r, 2)]$	Waterson& Deconinck, 1995 [A11]
Gamma	$\max[0, \min(1, \frac{1}{\beta_m}\frac{r}{1+r})], \frac{1}{10} \le \beta_m \le \frac{1}{2}$	H. Jasak,, 1999 [A12]

STOIC	$\begin{cases} 0 & r \le 0 \\ 4r & 0 < r \le \frac{1}{4} \\ 1 & \frac{1}{4} < r \le 1 \\ \frac{3}{4}+\frac{1}{4}r & 1 < r \le 5 \\ 2 & 5 < r \end{cases}$	Lin & Lin, 1997 [A13]
Van Albada-2	$\frac{2r}{r^2+1}$	Kermani, 2003 [A14]
HOAB	$\begin{cases} 0 & r \le 0 \\ 5r & 0 < r \le \frac{1}{5} \\ 1 & \frac{1}{5} < r \le 1 \\ \frac{1}{2}+\frac{1}{2}r & 1 < r \le 3 \\ 2 & 3 < r \end{cases}$	J. J. W, et al., 2003 [A15]
SPL-max-$\frac{1}{2}$	$\max\left[0, \min(2r, \max(\frac{3}{4}r+\frac{1}{4}, \frac{1}{4}r+\frac{3}{4}), 2)\right]$	Waterson& Deconinck, 2007[A16]
SPL-max-$\frac{1}{3}$	$\max\left[0, \min(2r, \max(\frac{2}{3}r+\frac{1}{3}, \frac{1}{3}r+\frac{2}{3}), 2)\right]$	Waterson& Deconinck, 2007 [A16]
M. Cada & M. Torrihon	$\max\left[0, \min\left(\frac{2+r}{3}, \max\left[-0.5r, \min\left(2r, \frac{2+r}{3}\right) 1.6\right]\right)\right]$	M. Cada & M. Torrihon, 2009 [A17]

References of Appendix A

[A1] Van Leer, B., Towards the ultimate conservative difference scheme II. Monotonicity and conservation combined in a second order scheme, J. Comp. Phys. 14 (4): 361–370, 1974

[A2] B. van Leer, Towards the ultimate conservative difference scheme. IV. A new approach to numerical convection, J. Comput. Phys. 23, 276, 1977

[A3] G.D. van Albada, B. van Leer, W.W. Roberts, A comparative study of computational methods in cosmic gas dynamics, Astron. Astrophys., 108, 76, 1982

[A4] S.R. Chakravarthy and S. Osher, High resolution applications of the Osher upwind scheme for the Euler equations, AIAA Paper 1983-1943, in: Sixth AIAA CFD Conference, Danvers, MA, USA, pp. 363, 1983

[A5] Sweby, P.K., High resolution schemes using flux-limiters for hyperbolic conservation laws, SIAM J. Num. Anal. 21 (5): 995–1011, 1984

[A6] P.L. Roe, M.J. Baines, Algorithms for advection and shock problems, in: Viviand (Ed.), Proceedings of the Fourth GAMM Conference on Numerical Methods in Fluid Mechanics, Vol. 5, pp.281, 1982

[A7] P.L. Roe, Some contributions to the modelling of discontinuous flows, in: Engquist, Osher, Somerville, (Eds.), Lectures in Applied Mathematics, Large-scale Computations in Fluid Mechanics (AMS-SIAM Summer Seminar, La Jolla, CA, USA, Am. Math Soc., 1985, Vol. 22, Part 2, p. 163, 1983

[A8] P.H. Gaskell and A.K.C. Lau, Curvature-compensated convective transport: SMART, a new boundedness-preserving transport algorithm, Int. J. Numer. Methods Fluids 8, 617, 1998

[A9] F.S. Lien, M.A. Leschziner, Upstream monotonic interpolation for scalar transport with application to complex turbulent flows, Int. J. Numer. Methods Fluids 19, 527, 1994

[A10] Zhou, G., Numerical simulations of physical discontinuities in single and multi-fluid flows for arbitrary Mach numbers (PhD Thesis), Sweden: Chalmers Univ. of Tech., 1995

[A11] N.P. Waterson and H. Deconinck, A unified approach to the design and application of bounded higher-order convection schemes, in:Taylor, Durbetaki (Eds.), Proceedings of the Ninth International Conference on Numerical Methods in Laminar and Turbulent Flow, Atlanta, July, Pineridge Press, Swansea, pp. 203, 1995

[A12] H. Jasak, H.G. Weller, A.D. Gosman, High resolution NVD differencing scheme for arbitrarily unstructured meshes, Int. J. Numer. Methods Fluids, 31 431, 1999

[A13] M.S. Darwish, A new high-resolution scheme based on the normalized variable formulation, Numerical Heat Transfer, Part B 24, 353, 1993

[A14] Kermani, M.J.; Gerber, A.G.; Stockie, J.M., Thermodynamically Based Moisture Prediction Using Roe's Scheme, 4th Conference of Iranian AeroSpace Society, Amir Kabir University of Technology, Tehran, Iran, January 27–29, 2003

[A15] J.-J. Wei, B. Yu, W.-Q. Tao, Y. Kawaguchi and H.-S. Wang, A new high-order accurate and bounded scheme for incompressible flow, Numerical Heat Transfer, Part B 43, 19, 2003

[A16] N.P. Waterson, H. Deconinck, Design principles for bounded higher-order convection schemes – a unified approach, Journal of Computational Physics 224, 182–207, 2007

[A17] Miroslav Čada, Manuel Torrilhon, Compact third-order limiter functions for finite volume methods, J. Comput.Phys., 228, 4118-4145, 2009

Appendix B

Various gradient evaluation methods

One important contribution of present study is the highlighting of the importance of appropriate gradient evaluation methods for both high-resolution convection schemes and improved deferred correction (DFC) diffusion scheme. Several widely used gradient evaluation methods have been incorporated in our numerical solvers. The algorithms of these evaluation methods are explained in

details in the following which will be helpful to understand their performance on different non-orthogonal grid systems.

Method 1: Simple Gauss Formula

One of the simplest methods can be expressed by the simple Gauss formula,

$$(\nabla\phi)_P = \frac{1}{V_P}\sum_f \vec{S}\phi_f \qquad \text{(B-1a)}$$

$$\phi_f = f_x\phi_P + (1-f_x)\phi_K \qquad \text{(B-1b)}$$

where V_P indicates the volume of the control volume P and $\vec{S}$ is the outward-pointing surface area vector.

It is worth pointing out that the above simple Gauss formula is only first order when there is skewness on the surfaces, as Eqn. (B-1b) couldn't ensure the value at surfaces is evaluated at the surface centroid. If strict second-order accuracy is to be maintained, some corrections must be introduced, see method 2 and method 3.

Method 2: Two-Step Gauss Formula

A second order method for Gradient computation can be developed basing on the modification of the simple Gauss formula. It contains two steps. Firstly, the same equation as Eqn. (B-1b) is used to get the approximation of ϕ_f. Then a correction is applied to obtain the improved value of $\phi_{f'}$ from ϕ_f,

$$\phi_{f'} = \phi_f + (\nabla\phi)_f \cdot \overrightarrow{ff'} \qquad \text{(B-2a)}$$

where a simple interpolation expression can be used to decide gradient at surface,

$$(\nabla\phi)_f = f_x(\nabla\phi)_P + (1-f_x)(\nabla\phi)_K \qquad \text{(B-2b)}$$

Then the new value of $\phi_{f'}$ is used for gradient computation,

$$(\nabla\phi)_P = \frac{1}{V_P}\sum_f \mathbf{S}\phi_{f'} \qquad \text{(B-2c)}$$

Method 3: One-step Gauss Formula

A one-step method is reported in [B1]. In this approach, the value of $\phi_{f'}$ is directly computed by a single equation,

$$\phi_{f'} = \frac{1}{2}(\phi_P + \phi_K) + \frac{1}{2}\left((\nabla\phi)_P \cdot \overrightarrow{Pf'} + (\nabla\phi)_K \cdot \overrightarrow{Kf'}\right) \qquad \text{(B-3)}$$

After getting the estimation of $\phi_{f'}$, Eqn. (B-2c) can be used for gradient calculation.

For method 2 and method 3, the gradients at CV nodes are unknown at the beginning and to be decided by $\phi_{f'}$. Thus, an extra iteration loop is necessary for better accuracy. We name the new iteration Gradient Iteration Loop. And the initial estimation of the cell gradients can be obtained by some symmetric schemes, like

$$\phi_{f'} = \frac{1}{2}\left(\phi_P + \phi_K\right) \qquad \text{(B-4a)}$$

and

$$\phi_{f'} = \frac{|Kf'|}{|Pf'|+|Kf'|}\phi_P + \frac{|Pf'|}{|Pf'|+|Kf'|}\phi_K \qquad \text{(B-4b)}$$

Both Eqn. (B-4a) and Eqn.(B-4b) were applied to the numerical test cases, little difference was found. For simplicity, only the numerical results with Eqn. (B-4b) will be present in all test cases.

By observing Eqn.(B-2a), (B-2b) and (B-3), there is gradient value in the final expressions, which means an extra loop may be needed to improve the accuracy for both one-step and two-step Gauss Formula. However, from the numerical tests, the effect of the addition of the extra loop for one-step and two-step Gauss Formula are completely different, which is an interesting finding.

Both Method 2 and Method 3 are based on simple Gauss formula, but with correction to obtain a better approximation of values at the surfaces' centroids. In addition, the method which plays no restrictions on cell irregularity could also be effective to overcome the difficulty mentioned in Method 1. The Least-squares approach belongs to this method.

Method 4: The Simple Least-squares approach

The Least-squares approach is very attractive when skewness is distinct, as the estimation of values on the surfaces is avoided. The key idea of the Least-squares approach is to reconstructs the solution in the neighborhood of the cell in a least-squares sense [B2].

For example, by assuming a locally linear variation of ϕ, each neighboring element cell centre value may be expressed as,

$$\phi_K = \phi_P + \nabla\phi_P \cdot \Delta\mathbf{r}_K \qquad \text{(B-5a)}$$

where $\Delta\mathbf{r}_K$ is the vector from the centroid of cell P to the centroid of neighboring cell, see Figure B-a.

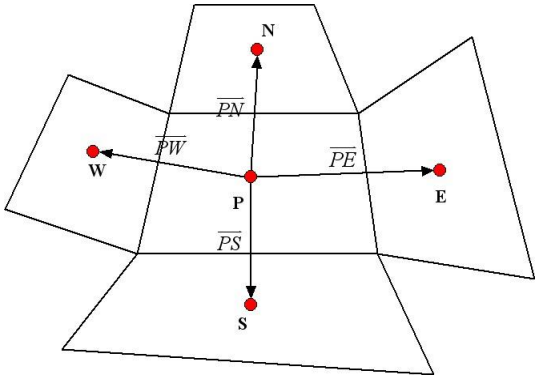

Figure B-a. Nodal notation and locations used in the Least-squares calculation of CV gradient

Substituting coordinate position expression of $\Delta\mathbf{r}_K$ for all cells around P, an overdetermined system of linear equations is obtained,

$$\mathbf{Md} = \Delta\phi \qquad \text{(B-5b)}$$

where $\mathbf{M}$ is the 4×2 matrix for quadrilateral meshes, $\mathbf{d}$ is the vector of the components of gradients of ϕ at nodal P and $\Delta\phi$ is the vector of the difference of ϕ,

$$\mathbf{M} = \begin{bmatrix} x_E - x_P & y_E - y_P \\ x_N - x_P & y_N - y_P \\ x_W - x_P & y_W - y_P \\ x_S - x_P & y_S - y_P \end{bmatrix}; \quad \mathbf{d} = \begin{bmatrix} \left.\frac{\partial\phi}{\partial x}\right|_P \\ \left.\frac{\partial\phi}{\partial y}\right|_P \end{bmatrix}; \quad \Delta\phi = \begin{bmatrix} \phi_E - \phi_P \\ \phi_N - \phi_P \\ \phi_W - \phi_P \\ \phi_S - \phi_P \end{bmatrix}$$

The overdetermined system may be solved in a least square sense, which means the sum of the squares of the errors over all neighboring cells,

$$R = \sum_K R_K^2$$

$$R_K = \nabla\phi_P \cdot \Delta\mathbf{r}_K - \left(\phi_K - \phi_P\right)$$

is minimized.

By differencing R with respect to $\left.\frac{\partial\phi}{\partial x}\right|_P$ and $\left.\frac{\partial\phi}{\partial y}\right|_P$ and equating to zero, we obtain

$$\mathbf{M}^T\mathbf{Md} = \mathbf{M}^T\Delta\phi \qquad \text{(B-5c)}$$

Then by inverting $M^T M$, the final expression for gradient $\Delta\phi$ evaluation is obtained as,

$$\mathbf{d} = \left(\mathbf{M}^T\mathbf{M}\right)^{-1}\mathbf{M}^T\Delta\phi \qquad \text{(B-5d)}$$

Method 5: The Improved Least-squares approach [B3][B4]

In terms of one-dimensional Taylor Series Truncation Error, the gradient computed by simple Least-squares approach is second-order accurate on a uniform grid only. In order to achieve an approximation of second-order on a non-uniform grid, then the influence of the distance vector modulus has to be taken into account, and then an improved version of the simple Least-squares approach is obtained.

$$R = \sum_K \frac{1}{|\Delta \mathbf{r}_K|} \left(\frac{\phi_K - \phi_P}{|\Delta \mathbf{r}_K|} - (\nabla \phi)_P \cdot \frac{\Delta \mathbf{r}_K}{|\Delta \mathbf{r}_K|} \right)^2 \qquad \text{(B-6a)}$$

The above expression is equivalent to the requirement that the projection of $(\nabla \phi)_P$ onto $\Delta \mathbf{r}_K$ fits the gradient based on the values of variable ϕ in that direction and the influence of neighboring point K on the gradient is weighted by the modulus of the distance vector.

By differencing R with respect to $\left.\frac{\partial \phi}{\partial x}\right|_P$ and $\left.\frac{\partial \phi}{\partial y}\right|_P$ and equating to zero, we obtain,

$$\mathbf{Gd} = \mathbf{H} \qquad \text{(B-6b)}$$

where $\mathbf{H}$ is a 2×1 matrix and $\mathbf{G}$ is a 2×2 matrix with the members expressed as,

$$h_i = \sum_K \frac{\phi_K - \phi_P}{|\Delta \mathbf{r}_K|} \frac{\Delta \mathbf{r}_K{}^i}{|\Delta \mathbf{r}_K|^2} \qquad i = 1,2 \qquad \text{(B-6c)}$$

$$g_{ij} = \sum_K \frac{\Delta \mathbf{r}_K{}^i \Delta \mathbf{r}_K{}^j}{|\Delta \mathbf{r}_K|^3} \qquad i = 1,2 \quad j = 1,2 \qquad \text{(B-6d)}$$

where $\Delta \mathbf{r}_K{}^i$ is the i$^{\text{th}}$ Cartesian component of vector $\Delta \mathbf{r}_K$.

For 2D problems with different types of meshes, $M^T M$ and $\mathbf{G}$ are always 2×2 matrix, they can easily be inverted analytically, which brought convenience for programming. While for 3D problems, $M^T M$ and $\mathbf{G}$ are become 3×3 matrix, a special subroutine for matrix inverting is inevitable.

It should be pointed out that the members of matrix $M^T M$ and $\mathbf{G}$ are concerned with positions of CV nodes, thus it is enough to calculate $(M^T M)^{-1}$ and $\mathbf{G}^{-1}$ once.

Some more accurate but complicated methods for gradient computation are available, see [B5][B6]. All these methods utilize more CV nodes, or vertexes points, or extra constructed points' information, which require more storage and introduce difficulties for programming procedure.

References of Appendix B

[B1] Riccardo Rossi, Direct numerical simulation of scalar transport using unstructured finite-volume schemes, Jounral of Computational Physics 228, 1639 – 1657, 2009

[B2] W.J. Minkozycz, E. M. Sparrow and J. Y. Murthy, Handbook of Numerical Heat Transfer, 2nd ed., Wiley, pp.22-25, 2006

[B3] S. Muzaferija, Adaptative finite volume method for flow prediction using unstructured meshes and multigrid approach, Ph.D. Thesis, Imperial College, pp.33-3, 1994

[B4] Jasak, H. and Weller, H.G, Application of the Finite Volume Method and Unstructured Meshes to Linear Elasticity, Int. J. Num. Meth. Engineering, 48 (2):267-287, 2000

[B5] Perez-Segarra, C. D., Farre, C., Cadafalch, J. And Oliva. Analysis of Different Numerical Schemes for the Resolution of Convection-Diffusion Equations using Finite-Volume Methods on Three-Dimensional Unstructured Grids. Part I: Discretization Schemes, Numerical Heat Transfer, Part B: Fundamentals, 49: 4, pp. 333-350, 2006

[B6] D. J. Mavriplis, Revisiting the least-squares procedure for gradient reconstruction on unstructured meshes, AIAA-Paper 2003-3986, June 2003.

Appendix C

Coordinate Transformation Method and Direct Gradient Evaluation Method

In this appendix, we try to deduce the final formulae for diffusive flux estimation with thecoordinate transformation method (CTM) and the direct gradient evaluation method (DGEM) using available information such as values of adjacent nodes and geometry information.

C.1 Coordinate Transformation Method

For two-dimensional problem, the outward-pointing face area vector, $\vec{S}_f = S_f \vec{n}_f$ can be determined as,

$$\vec{S}_f = \left(S_x, S_y\right) = \left(y_b - y_a, x_a - x_b\right) \tag{C-1}$$

And the diffusion flux at the cell face can be directly expressed as,

$$S_f \left(\nabla\phi\right)_f \cdot \vec{n}_f = \phi_x S_x + \phi_y S_y \tag{C-2}$$

where $\phi_x = \frac{\partial\phi}{\partial x}$ and $\phi_y = \frac{\partial\phi}{\partial y}$. The difficulty is that the $x-$, $y-$directional derivatives cannot be explicitly expressed in terms of nodal values P and K.

First, we define a generalized coordinate system with covariant bases $\left(\mathbf{e_1}, \mathbf{e}_2\right)$ locally on each cell face, where $\mathbf{e_1}$ and $\mathbf{e}_2$ are unit vectors from f (the cross-section point of $\overline{PK}$ and $\overline{ab}$) to K

and from f to b, respectively. By the chain rule, the $\mathbf{e_1}-$, $\mathbf{e}_2-$ directional derivatives are obtained,

$$\begin{cases} \phi_{e_1} = \phi_x x_{e_1} + \phi_y y_{e_1} \\ \phi_{e_2} = \phi_x x_{e_2} + \phi_y y_{e_2} \end{cases} \tag{C-3}$$

By simple operation,

$$\begin{cases} \phi_x = \dfrac{\phi_{e_1} y_{e_2} - \phi_{e_2} y_{e_1}}{\Delta} \\ \phi_y = \dfrac{\phi_{e_2} y_{e_1} - \phi_{e_1} x_{e_2}}{\Delta} \end{cases} \tag{C-4}$$

where, $\Delta = x_{e_1} y_{e_2} - x_{e_2} y_{e_1}$.

So Eqn.(C-2) turns to

$$S_f \left(\nabla\phi\right)_f \cdot \vec{n}_f = \phi_x S_x + \phi_y S_y = \frac{\phi_{e_1} y_{e_2} - \phi_{e_2} y_{e_1}}{\Delta} S_x + \frac{\phi_{e_2} y_{e_1} - \phi_{e_1} x_{e_2}}{\Delta} S_y \tag{C-5}$$

Then the key problems switch to compute ϕ_{e_1}, ϕ_{e_2}, $x_{e_1}, x_{e_2}, y_{e_1}$ and y_{e_2} with available information. The calculation is straightforward through the following expressions,

$$\begin{cases} x_{e_1} = \dfrac{x_K - x_P}{\xi} \quad x_{e_2} = \dfrac{x_b - x_a}{\eta} \\ y_{e_1} = \dfrac{y_K - y_P}{\xi} \quad y_{e_2} = \dfrac{y_b - y_a}{\eta} \end{cases} \tag{C-6.a}$$

$$\phi_{e_1} = \frac{\phi_K - \phi_P}{\xi} \quad \phi_{e_2} = \frac{\phi_b - \phi_a}{\eta} \tag{C-6.b}$$

where ξ and η represent the distances from P to K and a to b, respectively. In fact, η is equal to S_f. Putting Eqn.(C-1), Eqn.(C-6.a) and Eqn.(C-6.b) into Eqn.(C-5), the final expression is obtained,

$$S_f \left(\nabla\phi\right)_f \cdot \vec{n}_f = S_f \frac{\phi_K - \phi_P}{\xi \cdot \cos\theta} - S_f \frac{\phi_b - \phi_a}{\eta} \tan\theta \tag{C-7}$$

where θ is the angle between $\vec{n}$ and $\mathbf{e_1}$. It should be noted that the right hand side of Eqn.(C-7) includes two parts: the first part corresponding to the principal diffusion and the second one to the cross diffusion as in the curvilinear coordinate system [c1]. When the mesh is orthogonal, the second term vanishes.

The same or similar derivation processes appeared in [C1][C2]C3].

The left problem lies in how to evaluate the values at the nodal points, ϕ_a and ϕ_b. The universal interpolation approach can be expressed as,

$$\phi_n = \frac{\sum_{i=1}^{N} W_i \phi_i}{\sum_{i=1}^{N} W_i} \tag{C-8}$$

where $n = a$ or b, N is the number of the cells sharing the node, ϕ_i is the i th cell value, and W_i is the weighting factor. The two simplest methods are,

$$W_i = \frac{1}{r_i} \text{ or } W_i = \frac{1}{A_i} \tag{C-9}$$

where r_i is the distance from the centroid of the i th cell to the nodal point and A_i is the i th cell area. In particular, the accuracy of the interpolation method of Eqn.(C-8) and Eqn.(C-9) is limited. As pointed out in [C2], this interpolation method is second-order accurate only on "regular" triangular grids and is equivalent to the bilinear interpolation on rectangular grids. For common grids, some better methods, like Lagrangian multiplier method, need to be incorporated [C4][C5].

Another potential error comes from the skewness. It is obvious that the above method does not take into account this source of error. In fact, this mesh-induced error is not easy to overcome.

So, the main error of the coordinate transformation method contains two parts: (1) Skewness-induced error, (2) nodal value interpolation error.

C.2 Direct Gradient Evaluation Method: DGEM

The direct gradient evaluation method for diffusion flux computation appeared for the first time in [C6]. The core of this method is to construct two virtual points on the mid-perpendicular line of surface S_f.

Checking Fig. C-2(a), the point f is defined as the midpoint of the surface S_f. We draw a line which passes through f and is perpendicular to the surface. Then if the location of the two virtual points P' and K', belonging to the mid-perpendicular line is known and if the value of ϕ at this node can be interpolated, the diffusion flux through the face can be expressed as,

$$S_f \left(\nabla\phi\right)_f \cdot \vec{n} \approx S_f \frac{\phi_{K'} - \phi_{P'}}{\left|K'P'\right|} \tag{C-10}$$

Then the new problem which arises is how to choose the location of the virtual points as infinite ways are possible? Different options can be developed. In that sense DGEM can also be seen as a family of methods only different in the way the virtual points are chosen.

In [C6], for unstructured grids the location of the virtual points is the intersection between the line connecting two CV nodes and the mid-perpendicular line, see Figure C-1(b). Then the second-order-accurate central differencing scheme can be used to compute the values of virtual points from the values of the cell center points. The method is second-order accurate even for general meshes. Nevertheless one drawback remains, it is not easy to define the intersection locations for general polygon meshes.

To overcome this difficulty, Peric developed a similar method in [C7] following the same idea of virtual point construction. The positions of their virtual points can be seen in Figure C-1(c). The virtual point is the orthogonal projection of CV nodes onto the mid-perpendicular line. The idea is to choose the point on the mid-perpendicular line which minimizes the distance between the virtual point and the CV node. This supposed short distance should help to increase the accuracy of the overall algorithm.

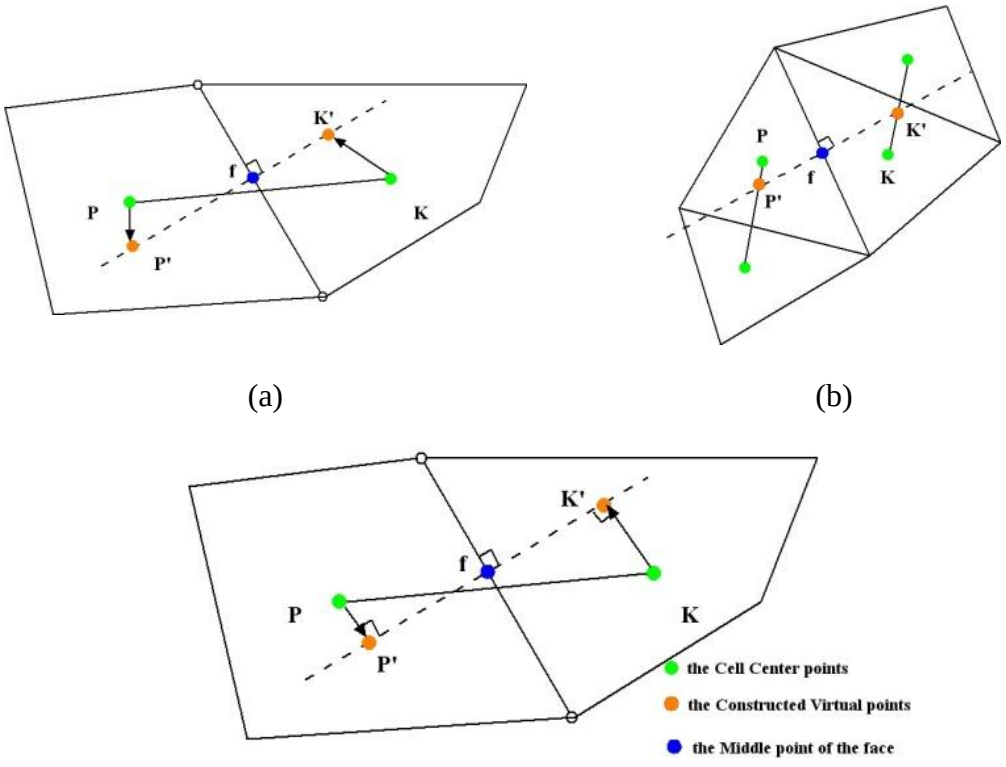

Figure C-1. Detail of the grid and geometric parameters for direct gradient evaluation method (a) the general positions of virtual points (b) Virtual points of Kobayashi M [C6] (c) Virtual points of Ferziger and Peric [C7]

Thus, once the locations of the virtual points have been determined, the values of ϕ at these nodes can be interpolated using the following second order expression from Taylor series.

$$\phi_{P'} = \phi_P + (\nabla\phi)_P \cdot \overrightarrow{PP'} \qquad \text{(C-11a)}$$

$$\phi_{K'} = \phi_K + (\nabla\phi)_K \cdot \overrightarrow{KK'} \qquad \text{(C-11b)}$$

Introducing Eqn. (C-11a) and Eqn. (C-11b) into Eqn. (C-10), the following expression is obtained,

$$S_f \left(\nabla\phi\right)_f \cdot \vec{n} = S_f \frac{\phi_K - \phi_P}{\left|\overrightarrow{K'P'}\right|} + S_f \frac{\left(\nabla\phi\right)_K \overrightarrow{KK'} - \left(\nabla\phi\right)_P \overrightarrow{PP'}}{\left|\overrightarrow{K'P'}\right|} \qquad \text{(C-12)}$$

Noting that the relationship between the length of line PK and line $\left|\overrightarrow{P'K'}\right| = \xi\cos\theta$, Eqn.(C-12) can be rewritten as,

$$S_f \left(\nabla\phi\right)_f \cdot \vec{n} = S_f \frac{\phi_K - \phi_P}{\xi\cos\theta} + S_f \frac{\left(\nabla\phi\right)_K \overrightarrow{KK'} - \left(\nabla\phi\right)_P \overrightarrow{PP'}}{\xi\cos\theta} \qquad \text{(C-13)}$$

It is interesting to point out that the first term of the right hand side of Eqn.(C-13) is exactly the same as the primary-diffusion term in Eqn. (3-24) and that it will also be evaluated implicitly. The second one will be explicitly computed from the values of the previous iteration in the source term.

As the skewness has no impact on this method, the error introduced by DGEM in the interpolation process, see Eqn (C-11.a) and (C-11b), becomes the main error source.

References of Appendix C

[C1] Dongjoo Kim and Haecheon Choi, A Second-Order Time-Accurate Finite Volume Method for Unsteady Incompressible Flow on Hybrid Unstructured Grids, Journal of Computational Physics 162, 411–428, 2000

[C2] Mathur, S. R. and Murthy, J. Y., A Pressure-Based Method for Unstructured Meshes, Numerical Heat Transfer, Part B: Fundamentals, 31: 2, 195-215, 1997

[C3] Gao Wei, Duan Ya-li and Liu Ru-xun, The finite volume projection method with hybrid unstructured triangular collated grids for incompressible flows, Journal of Hydrodynamics, 21 (2) : 201 - 211, 2009

[C4] Tao, W.Q. Recent Advances in computational heat transfer, Science Press of China, Beijing, China, pp.194–197, 2000 (in Chinese)

[C5] Vapnyarskii, I.B., Lagrange multipliers, in Hazewinkel, Michiel, Encyclopaedia of Mathematics, Springer, 2001

[C6] Kobayashi M., A second-order upwind least-squares scheme for incompressible flows on unstructured hybrid grids. Numerical Heat Transfer, Part B, 34 (1): 39-60, 1998

[C7] H. Fergizer, and M. Peric, Computational Methods for Fluid Dynamics, Springer, 2002

Appendix D

Numerical method for the determination of the linear stability criterion

In the present study, a great many critical values have been computed numerically for stability analysis and checking of the accuracy of the developed numerical codes. The method with an example will be explained in details here.

In the case of the electro-convective instability of a dielectric liquid layer to a strong unipolar injection, it is well known that a convective motion of liquid arises at the critical non-dimensional T number (T_c) for fixed M and C. Generally speaking, the numerical diffusion decreases with increasing number of control volumes N. For a fixed value of N, tiny numerical fluctuations or an asymmetric perturbation introduced artificially can be used to develop the flow. If the value of T number is high enough, the fluctuations or perturbation will start growing. The maximal velocity or any other physical quantity of convective motion will increase exponentially in time with some growth constant.

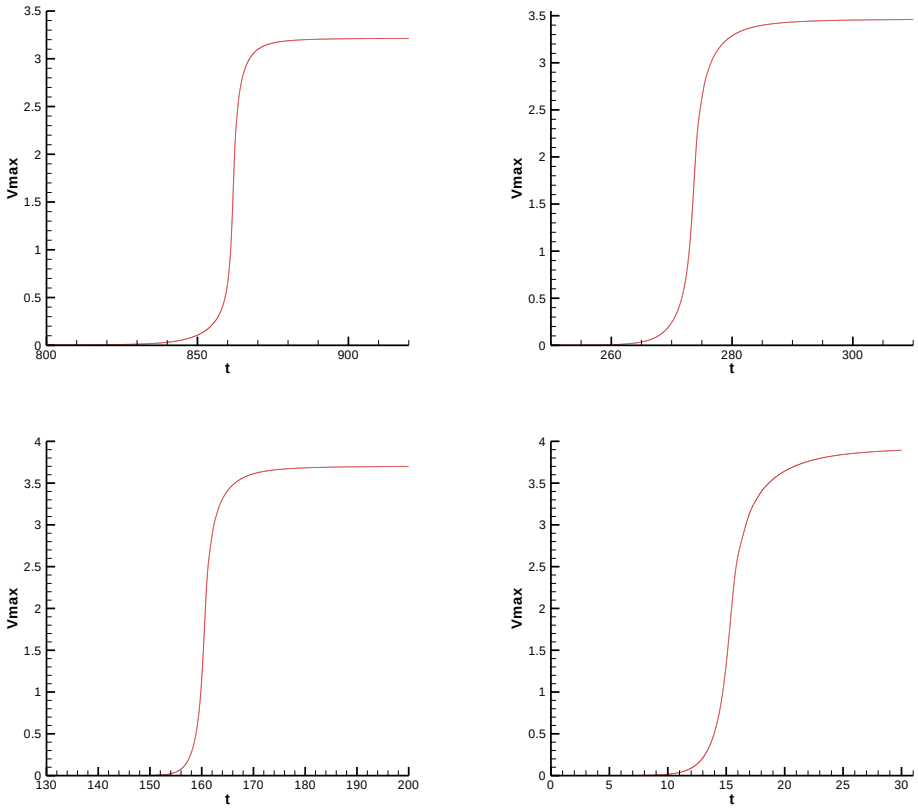

Figure D-1. The non-dimensional maximal vertical convection velocity as a function of dimensionless time for four values of T number (170, 180, 190 and 200). Grid: 100×100.

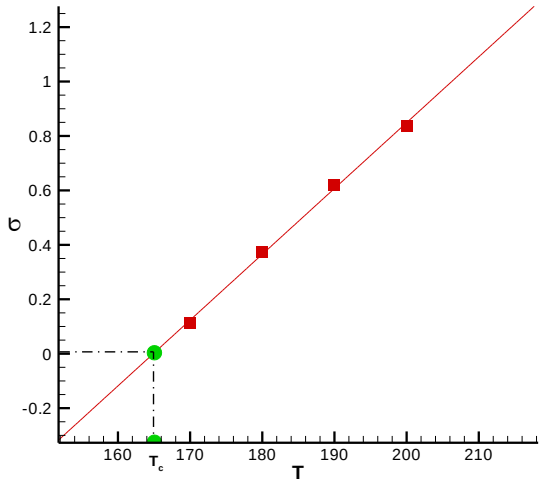

Figure D-2. Non-dimensional growth constants found by Figure D-1. as a function of T number and the critical T number for 100×100 grid system, Tc = 164.9. M=10, C=10.

In Figure D-1, we plotted the numerical results of a strong injection problem with different T number. Note that the complete proof of the method is given in [D1].

In addition, the true critical T number should be computed with the grid system of indefinitely small size. Obviously, as the grid size decrease, the critical value will tend to its true critical value, to see Table D1 as an example. Thus, another extrapolation is needed.

Table D-1. The critical T number versus mesh size

Grid	The critical T number
50×50	158.3
80×80	161.9
100×100	163.1
150×150	163.2

It is interesting to note that a very exact value of critical T number T_c = 163.2 is obtained at N = 100×100, which differs from the theoretical value Tc = 164.1 by more or less 0.55%. In addition, there is some tiny manual error when computing growth constant and interpolation error. Thus, in practical, we can use the critical value obtained at 100×100 grid system to represent the final limiting numerical value. The same strategy will be used throughout present dissertation. Another important detail is the selection of T values to compute growth constants. Normally, the selection should be close to the final critical values.

References of Appendix D

[D1] Landau, L.D. and Lifshitz, E.M., Elektrodinamika sploshnykh sred (Electrodynamics of Continua), Moscow: Nauka, Vol. VIII, 1982